AERODYNAMICS OF RECIPROCATING ENGINES

CONSTANTINOS VAFIDIS
Dipl-Ing

Thesis submitted for the degree of
Doctor of Philosophy
in the University of London
and for the
Diploma of Membership of the Imperial College

Imperial College of Science and Technology
Department of Mechanical Engineering

December 1985

TO MY PARENTS

ABSTRACT

The thesis is concerned with an experimental investigation of the isothermal in-cylinder flowfield in motored model and production reciprocating engines. Detailed velocity measurements were obtained by laser Doppler anemometry with emphasis on the induction flowfield, including the flow at the exit of the intake valve, and its evolution during compression.

A series of steady and unsteady flow simulations of a model engine have been studied; the results established that the geometric details of the intake port/valve assembly determine the discharge capacity and velocity characteristics of the intake valve. These characteristics were not influenced by the flow unsteadiness or valve operation for an engine speed of 200 rpm but were sensitive to the valve confinement by the cylinder wall and, in extreme cases, by its proximity to the operating piston. In all cases the flowfield downstream of the valve was strongly influenced by flow unsteadiness and piston confinement.

The axial flow structures generated during induction in the model engine were found to decay shortly after the closure of the intake valve with simultaneous redistribution of the intake generated turbulence which, in the absence of compression squish, decayed to intensities of less than 0.5 times the mean piston speed at TDC of compression. In contrast to the axial flow, the induction generated swirl persisted during compression with a simultaneous decay of its angular momentum by 30-50%, depending on initial swirl level, swirl velocity distribution and combustion chamber geometry. The swirl centre was found to oscillate around the cylinder axis throughout induction and compression performing a helical motion which was reduced when a squish piston was used. The in-bowl flow pattern at TDC of compression was also found to depend strongly on the initial swirl level. The dependence of TDC turbulence on the induction generated flowfield was further investigated with a shrouded valve which produced a strong tumbling motion during induction. This flow pattern persisted throughout compression and resulted in nearly double turbulence intensity at TDC of compression.

The influence of engine speed on the in-cylinder flowfield was investigated in a modified production engine with similar geometric characteristics to those of the model engine. It was established that, in the absence of swirl and squish, the average TDC turbulence intensity increased more than linearly with engine speed in the range of 300 to 2000 rpm.

The valve exit and in-cylinder flow development was also examined under steady and operating conditions in a production Diesel engine incorporating a helical intake port and motored at 900 rpm. The results revealed that the relationship between the valve flow under steady and operating conditions, the collapse of the induction generated axial flow pattern and the decay of the swirl motion and in-cylinder turbulence were similar to those of the simplified engine and justified the model engine configuration as a good simulation of a realistic engine.

ACKNOWLEDGEMENTS

I would like to express my sincere gratitude to my supervisor Professor J.H. Whitelaw for his guidance, constructive criticism and continuous support throughout the course of this work.

I am grateful to Dr. C. Arcoumanis and Dr. A.F. Bicen for their valuable assistance and advice and to Dr. A.D. Gosman and Dr. B. Ahmadi-Befrui for their continuous interest in my work.

I have benefitted from my association with all my colleagues, particularly Dr. M. Founti and Dr. A.M.K.P. Taylor who guided me during the first stages of my research.

I am pleased to acknowledge the contribution of Messrs. N. Frost, M. Roper and W. Crew with respect to the manufacture of the mechanical hardware and Messrs. J.R. Laker and O. Vis for their technical support and construction of the electronic and optical equipment.

I would like to thank Miss J. Tromans for her valuable assistance and Cathy Maxwell for her excellent and speedy typing of the thesis.

I am grateful to all my friends in London who shared my good and bad times and, above all, to my parents who encouraged me and accepted uncomplainingly my long absence.

Finally, I take the opportunity to acknowledge the financial support provided by the Atomic Energy Research Establishment Harwell, the Joint Research Committee of European Engine Manufacturers and Ford Motor Co.

TABLE OF CONTENTS

LIST OF TABLES

LIST OF FIGURES

(*)NOTE: In all figures, open symbols (o) denote mean velocities and closed symbols (●) r.m.s. velocities, unless otherwise stated.

LIST OF SYMBOLS

Roman characters

a	distance between measurement volume and collecting lens L_4
A	cross-section area
A_E	effective valve flow area
A_L	valve-lift curtain area ($\pi D_V L$)
A_M	minimum valve passage area
A_P	port area
b	bumping clearance; distance between lens L_4 and photomultiplier pinhole
b_o	beam diameter at laser exit at $1/e^2$ intensity points
b'_o	laser beam diameter before imaging lens L_3
b_x	diameter of measurement volume at $1/e^2$ intensity points
b_y	length of measurement volume at $1/e^2$ intensity points
c	piston clearance at TDC
C	orifice plate discharge coefficient
C_L	valve discharge coefficient based on A_L
C_M	valve discharge coefficient based on A_M
d_b	piston-bowl diameter
d_e	re-entrant piston-bowl entry diameter
d_f	fringe spacing in the measurement volume
d_{Ph}	photomultiplier pinhole diameter
d_r	line-pair width of diffraction grating
d_s	valve stem diameter
D	nominal engine bore
D_c	engine cylinder diameter
D_p	piston diameter
D_v	valve head diameter
e	valve eccentricity
E	velocity of approach factor; beam expansion ratio
f	frequency of scattered light
f_1, f_2, f_3, f_4	focal lengths of the focusing, collimating, imaging and collecting lenses (L_1, L_2, L_3, L_4)
f_D	Doppler frequency
f_r	frequency of rotation of diffraction grating
f_s	frequency shift
f_t	frequency of turbulent velocity fluctuations

G	diffraction grating
h	pressure in mmWg
h_b	piston-bowl depth
i	counter index: engine cycles, data points
K	proportionality constant
ℓ	connecting rod length; characteristic length
L	valve lift
L_{max}	maximum valve lift
m	order of diffracted beam
$\dot{m}$	mass flow rate
$\dot{m}_i$	isentropic mass flow rate
$\dot{m}_\infty$	mass flow rate for infinite valve lift
M	magnification of collecting optics
n	engine speed (rpm); polytropic process exponent
N	total number of samples
N_f	number of fringes in the measurement volume
N_ℓ	number of line-pairs on the grating
p	static pressure
p_o	total pressure
p_θ	absolute pressure at crank angle θ
p_{TDC}	absolute pressure at TDC of compression
r	radial co-ordinate
R	radius of rotation of the air charge
R_c	cylinder radius ($D_c/2$)
Re	Reynolds number
Re_L	Reynolds number based on L (UL/ν)
s	beam separation
S	piston stroke; Strouhal number ($f_t\ell/V$)
t	valve seat width
T_o	total temperature (K)
u,v,w	axial, radial and tangential turbulent velocity components
$\tilde{u},\tilde{v},\tilde{w}$	r.m.s. of the axial, radial and tangential turbulent velocity components ($\sqrt{\overline{u^2}}$, etc.)
U,V,W	instantaneous axial, radial and tangential (swirl) velocity components
$\overline{U},\overline{V},\overline{W}$	mean axial, radial and tangential (swirl) velocity components

$\overline{U}_e(\theta)$	ensemble-average mean velocity at crank angle θ
$\tilde{u}_e(\theta)$	ensemble-average r.m.s. velocity at crank angle θ
$\overline{U}_t(i)$	time-average mean velocity over interval $\Delta\theta$ of the i^{th} cycle
V_p	instantaneous piston speed
$\overline{V}_p$	mean piston speed ($S\omega_e/\pi$)
V_θ	charge volume at crank angle θ
V_{TDC}	clearance volume at TDC
X	error estimator
z	axial co-ordinate
z_D	pipe size correction factor
z_p	instantaneous piston position
z_R	Reynolds number correction factor

Greek characters

γ	specific heat ratio
Δh	pressure drop across the valve (mmWg)
Δp	pressure difference
$\Delta\theta$	crank angle window
$\Delta\overline{\Omega}$	angular momentum loss
ε	expansibility factor
η	angular momentum conversion efficiency
θ	crank angle
θ_B	Bragg-angle
θ_m	m-order diffraction angle
λ	laser wavelength
λ^*	Doppler frequency to velocity conversion factor
Λ	ultrasonic wavelength at the Bragg-cell
μ	viscosity ; area ratio of the orifice meter
ν	kinematic viscosity
ρ	density
ϕ	beam intersection angle
ψ	valve seat angle
ω	rotational speed of air charge
$\overline{\omega}$	mean rotational speed of air charge
ω_e	engine rotational speed (rad/s)

Ω	angular momentum of air charge
$\overline{\Omega}$	mean angular momentum of air charge

Abbreviations

CR	compression ratio
SN	swirl number
SR	swirl ratio
IVO	inlet valve opening
IVC	inlet valve closure
EVO	exhaust valve opening
EVC	exhaust valve closure
TDC	top-dead-centre
BDC	bottom-dead-centre
BTDC	before TDC
ATDC	after TDC
BBDC	before BDC
ABDC	after BDC
OR	orientation of measurement plane
(e),(m),(ℓ)	denote results referring to early, mid- and late induction, respectively
(U),(V),(W)	denote results referring to axial, radial and tangential velocity components, respectively

CHAPTER 1

INTRODUCTION

1.1 BACKGROUND AND OBJECTIVES OF ENGINE RESEARCH

The development and production of modern internal combustion engines is subject to market and legislation requirements which call for low cost, high performance engines with low fuel consumption and reduced emission of pollutants. The last three factors are directly related to the in-cylinder combustion process and, consequently, a major research effort has been launched to identify the parameters influencing the combustion efficiency and pollutants formation.

The role of the in-cylinder air motion in the combustion process has been recognised since the early days of engine development. The pioneering works of Clerk (1921), Ricardo (1922) and Alcock (1934) showed the possibility of improving combustion efficiency through the control of the in-cylinder air or mixture motion, namely its turbulent and bulk flow characteristics prior to combustion. The beneficial influence of these parameters on fuel mixing and combustion duration subsequently allowed the use of higher compression ratios and leaner fuel-air mixtures leading to improvements in engine power output and reduction of the pollutants emission. Understanding of the qualitative relationships between precombustion flowfield and in-cylinder combustion resulted in the development of semi-empirical design rules which brought engine development to its current state. Further improvements are not expected to be spectacular and every detail of the in-cylinder processes must be exploited in order to gain a small percentage in engine performance. In this context the previously employed empirical design methods cannot be considered as adequate and cost-effective. The development of new design methods, with a-priori knowledge of the resulting engine performance is desirable and, to this end, detailed knowledge and in-depth understanding of the engine flow and combustion processes is necessary. This calls for a combined experimental and theoretical research effort which faces the formidable task of probing and analysing a three-dimensional, turbulent, time dependent and strongly compressible combusting flowfield in the hostile environment of a reciprocating engine. The "classical" measurement techniques (see for example Amann, 1985) and the "phenomenological" analysis methods (Blumberg et al, 1979) had to be supplemented with new

measurement and analysis methods capable of resolving in detail the complex engine flows.

Although attempts to obtain detailed in-cylinder velocity measurements have been made as early as in 1958 (Semenov, 1963), it is mainly during the last decade that the development of the laser-based diagnostics and particularly of laser Doppler anemometry (see for example Dyer, 1985 and Rask, 1984) made it possible following the pioneering works of Trolinger et al (1974) and Melling and Whitelaw (1976). In the theoretical front, the advent of the large main-frame computers enabled the development of the "multi-dimensional" prediction methods (see for example Gosman, 1985) which, in principle, are capable of resolving the in-cylinder flowfield in space and time. The simultaneous development of these theoretical and experimental research tools was of paramount importance since they depend on each other for the provision of boundary and validation data, and the feedback of the insight of the flow mechanisms respectively. The laser-based diagnostics however, due to their faster pace of development and their ability to handle real engine configurations, have already been adopted by the automotive industry as practical "post-dictive" and development methods.

Although the research efforts during the last years have produced a large amount of information and some useful conclusions,the complexity of the flows under investigation and their dependence on a large number of parameters have been a significant obstacle to the understanding of the basic in-cylinder processes. As will be shown in the following sections, a large number of questions await answers and the details of the in-cylinder flow dependence on engine geometry and operating conditions are, to a certain extent, unknown. Furthermore, the basic mechanisms of the flow evolution throughout the engine cycle have not yet been thoroughly investigated while its influence on and interaction with the combustion process are not well understood.

The present thesis aims to contribute to the understanding of the in-cylinder flow mechanics, and particularly to the influence of engine geometry and operating conditions on the induction-generated flowfield and its evolution throughout compression, by describing velocity field measurements in motored model and production engines. The main objective of this research is the detailed quantification of the effect of individual geometric and flow parameters on the precombustion flowfield. The

experimental approach is that of detailed LDA velocity measurements in a variety of engine configurations which gradually introduce an increasing complexity in the in-cylinder flowfield. The results are also intended for use as input conditions and testing grounds for a series of relevant multi-dimensional calculations which have been carried out in parallel with this work.

1.2 PREVIOUS WORK

Following the interest shown by industry and research establishments in the in-cylinder flow processes, the last decade has witnessed the appearance of a large number of experimental and theoretical works related to the isothermal and combusting flowfields in reciprocating internal combustion engines. Lately the realisation of the complexity of the problem led to some re-organisation and co-ordination of research in the engine community. This was expressed by the appearance of several review works (for example, Witze, 1981, Tabaczynski, 1983, Gosman, 1983, Arcoumanis and Whitelaw, 1985, Borman, 1985), which summarise the findings of previous investigations and attempt to indicate the areas requiring further research. Similar reviews of the experimental and modelling techniques have also been made (for example, Rask 1984, Amann, 1985, Dyer, 1985, Gosman, 1985) in an effort to summarise their achievements and future potential. A summary of these review works and their main conclusions is given in Table 1.1.

The following sub-section outlines the current trends of engine research methodology as it emerges from a general overview of the relevant literature. Sub-section 1.2.2 describes the experimental methods used in engine flow studies in order to give the background for the discussion of the findings of previous research presented in sub-section 1.2.5. In view of the wide availability of extensive review studies on the subject, an effort is made in the following sub-sections to discuss only the most relevant and more recent research works so as to highlight the areas requiring further research and to put the present work into perspective.

TABLE 1.1

Summary of review studies

1. Witze, 1981

Research targets: Induction-generated ring-vortex structures; Piston-induced vortex roll-up; Turbulence behaviour during compression; Decay of swirl during compression; Exhaust-pipe flow.
Conclusions: Little is known about the intake process to permit assessment of the significance of its sub-processes; Initial and boundary conditions are required; HWA data of turbulence behaviour during compression are of questionable reliability; Precession of swirl centre causes difficulties in turbulence measurements; In-cylinder swirl and secondary swirl-induced flows require further research; Although predictions of the mean and especially turbulence quantities are not very satisfactory, the results are encouraging.

2. Tabaczynski, 1983

Vortices during induction scale with instantaneous piston position and are highly unstable breaking down after IVC; Small scale flame structures are related to turbulence microscales. Uncertainties exist in the separation of turbulence and cyclic variations because of comparable time scales, and in the adequacy of k-ε models to predict turbulence behaviour. A large scale co-operative effort is required to advance knowledge in engine flows.

3. Gosman, 1983

An unambiguous method of characterising in-cylinder turbulent flows is required; Inlet ports should be characterised by detailed velocity measurements at their exit; Engine flow calculations should commence at the very beginning of induction; Induction flow does not scale directly with engine speed; During compression and expansion the principal factors determining the flow behaviour are the chamber geometry, the initial swirl distribution and, to a lesser extent, the initial turbulence level. Turbulence during compression in a disc-type chamber decreases to 0.4 - 0.5 $\bar{V}_p$ and may be further attenuated by swirl. Differences between air motion in motored and firing engines are confined to the periods of "post-start-of-injection" or "post-ignition"; Parallel experimental and calculation programmes should be conducted.

4. Arcoumanis and Whitelaw, 1985

Suggested areas for further research: Flow in inlet manifolds and ports; Correlation between cyclic velocity variations and combustion; Methods for increasing turbulence through the induction flowfield; Effect of engine speed on mean and turbulent flowfields prior to ignition; Structure of fuel sprays, interaction with the pre-injection flowfield.
Recommendations: Co-operative research with parallel experimental and theoretical studies in "standard" engine configurations.

5. Borman, 1985

Comprehensive review of engine research needs. Suggested areas for further work: Improve experimental techniques for engine flow mapping; Study the flow in ports and around valves; Study the mechanisms of turbulent flame propagation, transient spray behaviour, engine knock, turbulent mixing in heterogeneous charge engines; Evaluation studies for numerical global and multidimensional calculations; Improved droplet vapourisation models.

Cont'd

Table 1.1 (cont'd)

6. Rask, 1984

Future directions for the experimental methods: Simultaneous multi-component velocity measurements; Cycle-resolved analysis for turbulence measurements should be used, combined with conditional sampling techniques; Photon correlation techniques are promising for high data rates; Combination of LDA with global diagnostics results in a powerful technique for combustion studies; Global diagnostics can greatly assist understanding of the cyclic variations.

7. Amann, 1985

Extensive historical review of classical (non-laser based) probe and optical diagnostics and critique of their relative merits and shortcomings. Optical techniques are considered as intrusive since they require engine modifications to gain optical access into the cylinder.

8. Dyer, 1985

Comprehensive review of laser based diagnostics. Suggested directions: Improve techniques for turbulent time- and length-scales measurements; Develop imaging techniques to study the role of fuel droplets in Diesel combustion and mixture homogeneity in homogeneous charge engines; Combine multiple simultaneous measurement with conditional sampling techniques; Develop the point-measurement techniques towards multi-dimensional spatial mapping.

9. Gosman, 1985

Comprehensive review of multi-dimensional modelling methods. Main conclusions: Reasonably accurate predictions of the in-cylinder flow are possible with statistical turbulence representations, provided that numerical and boundary condition uncertainties are reduced; 3-D calculations for practical engine chambers are feasible but costly and subject to limitations; Evaluation studies and applications have increased with generally positive outcomes; Cycle-to-cycle variations are a turbulence definition/modelling issue and are not unique to engine flows.

1.2.1 Methods of engine flow research

The complexity of the in-cylinder flowfield in reciprocating internal combustion engines, due to its three-dimensional, turbulent, time dependent, compressible and combusting nature, is further increased by the wide variety of the existing engine types and designs. A general approach followed in both experimental and theoretical research is the simplification of the problem by the elimination of several of these parameters at a time.

The first parameter to be eliminated was combustion, (Semenov, 1963). It was believed that the effect of combustion is not carried over from one cycle to the next and that the precombustion flowfield is not influenced by its presence. This assumption was first verified by spark discharge swirl velocity measurements obtained near top-dead-centre (TDC) of compression in a motored and firing engine by Ohigashi et al (1972). Further confirmation regarding both mean and turbulent flowfield was provided later by LDA measurements obtained in motored and firing Diesel (Wigley et al, 1981) and spark-ignition engines, (Rask, 1979, Witze et al, 1984a, Witze et al, 1984b). It is now generally accepted (see for example Gosman, 1983) that the flowfield during induction and compression is essentially similar in motored and firing engines.

Further simplifications introduced in the past in order to eliminate parameters such as three-dimensionality and compressibility resulted in the adoption of the so-called "model engines" as a basic research tool. A series of experimental investigations has been carried out in axisymmetric model engines in the absence of compression and with a variety of inlet flow conditions (see for example Gosman et al, 1978, Morse et al, 1979, Morse et al, 1980a, Arcoumanis et al, 1982c). The effect of three-dimensionality was also introduced by off-setting the idealised intake port with respect to the cylinder axis, (Morse et al, 1980b). The next parameter to be introduced was that of compression; the results of the non-compressing engines investigations were extended to four-stroke engine configurations operating in speeds up to 200 rpm and low compression ratios of 3.5 to 7:1. (see for example Gany et al, 1980, Arcoumanis et al, 1982a, b). Again these studies were later extended to include a variety of intake flow conditions and combustion chamber geometries (Arcoumanis, 1983, Bicen, 1983, Arcoumanis et al, 1984a).

An alternative experimental approach is the direct measurement of the precombustion flowfield in motored production engines. A large number of such investigations were conducted using a variety of measuring techniques such as hot-wire anemometry (e.g. Witze, 1977, Tindal et al, 1974), spark discharge anemometry (e.g. Wakisaka et al, 1979) and laser Doppler anemometry (e.g. Renshaw and Wigley, 1979, Morse and Whitelaw, 1981, Liou et al, 1984 etc.). These investigations were conducted with realistic compression ratios and in relatively high engine speeds but the detail of the measurements obtained is limited and their interpretation difficult due to the combined effect of several operating and geometric parameters on the in-cylinder flowfield.

The former experimental approach allows the understanding of the effect of individual parameters on the in-cylinder processes and, at the same time, it enables the development and assessment of both experimental and analytical methods. The experiments conducted in production engines, however, provide information on the real flow processes, validate the simplifications made in the model engines and indicate the parameters which require closer investigation. It is concluded that the two methods are complementary and that a gradual transition from the model engine experiments to more complex practical geometries is the best experimental approach and this is the one followed in this study.

1.2.2 Review of the experimental methods

The parameters which define the in-cylinder flowfield relate to its thermodynamic state (pressure, temperature and density), its chemical composition (species concentration) and fluid dynamic conditions (mean velocity, turbulence intensity and turbulence scales). Some additional parameters of interest in internal combustion engines are the fuel preparation and injection and the flame front speed. Ideally all these parameters should be quantified to fully define the engine flowfield and, to a certain extent, techniques exist for their measurement.

The measurement techniques can be classified in two main categories; the global methods which provide information on bulk quantities, such as cylinder pressure, swirl angular momentum and flow patterns, and the local

methods which provide detailed information on local characteristics such as velocity, turbulence and concentration. The measurement methods are also classified as intrusive or non-intrusive; in general the intrusive methods rely upon the use of probes or other measuring devices interfering with the flow (with the exception of cylinder pressure measurements), while the non-intrusive methods are mainly optical techniques. An argument exists as to the non-intrusiveness of the optical techniques since they require optical access with consequent modifications of the engine geometry (Amann, 1985). The use or not of lasers by the measurement methods also classifies them into laser-based and classical diagnostics.

These experimental techniques have been extensively reviewed by, for example, Arcoumanis (1983), Witze and Dyer (1984), Amann (1985) and Dyer (1985). A summary of their applications, advantages and shortcomings is given in Table 1.2 in order to provide a background for the discussion of the previous experimental work presented in sub-section 1.2.5.

One of the objectives of this experimental work is the provision of detailed data of the velocity characteristics in motored engines. This requires a local velocity measurement technique and, as shown in Table 1.2, the two more likely candidates are the hot-wire and laser Doppler anemometers. A brief description of these techniques is given below together with their advantages and limitations in order to justify the choice made in the present study.

Hot-wire anemometry (HWA)

The principle of HWA is based on the relationship between the convective heat transfer from the surface of a thin heated wire and the gas velocity past it. This heat loss is a non-linear function of the cooling velocity and also depends on the temperature difference between the wire and the fluid, the properties of the fluid (density, thermal conductivity) and the flowfield itself. Furthermore, the effective cooling velocity is a function of flow direction with respect to the sensor. The determination of velocity magnitude is made by direct calibration and in cases of varying fluid properties, as in motored engines, theoretical or experimentally defined corrections have to be incorporated in the calibration function.

The suitability of the HWA for engine applications has been carefully assessed by Witze (1980a) and his main conclusions can be summarised as follows

Advantages:	Continuous output signal
	Good frequency response
	Good spatial resolution
	Good signal-to-noise ratio
Disadvantages:	Intrusive method
	Delicate probe
	Requires calibration
	Flow properties dependent
	Relatively insensitive to flow direction
	Limited to relative turbulence intensities <20%
	Not applicable in combusting flows.

A large number of engine flow data have been obtained by HWA but the results of Witze (1980a) cast doubt on the accuracy of the mean velocity and turbulence intensity measurements, particularly during compression and expansion; careful calibration is essential and some methods have been developed recently to overcome these difficulties (Kyriakides, 1984). The time correlation and turbulence time scale measurements, however, are not affected by the changes of fluid properties (Haghgooie et al, 1982).

Laser Doppler anemometry (LDA)

The principle of LDA is based on the Doppler frequency shift of light scattered by moving particles. In dual-beam (differential or fringe mode) laser anemometry, the difference of the Doppler shift from two intersecting laser beams is used to determine the velocity of the scattering particle crossing the intersection (measurement) volume. This frequency difference is independent of the observer's position and directly proportional to the velocity component of the particle which lies on the plane of the beams and is normal to the bisector of their angle of intersection. The proportionality constant is a function of laser wavelength and beam intersection angle. The velocity direction is resolved by imposing a known frequency difference (shift) between the two laser beams which is added or subtracted from the Doppler frequency depending on the direction of motion of the scattering particle. The scattering particles

are deliberately introduced in a flow and their size and density characteristics are chosen so that they accurately follow the local velocity fluctuations.

The suitability of LDA for engine flow measurements has been extensively investigated by, for example, Trolinger et al (1974) and Witze (1980a). Their main conclusions can be summarised as follows:

Advantages:	Non-intrusive technique - Good spatial resolution
	No calibration required - Linear response
	Independent of fluid properties
	Independent of flow characteristics
	Good directional sensitivity
	Applicable in combusting flows.
Disadvantages:	Intermittent output signal
	Limitations in time resolution
	Requires optical access
	Requires appropriate seeding particles
	Relatively low signal-to-noise ratio.

Most of the recent investigations in motored and firing engines have been conducted by laser anemometry techniques. Their advantages are particularly suited for in-cylinder measurements and efforts are being made to extend their application to situations with limited optical access by using fibre-optics probes (Durst and Krebs, 1984) and to provide turbulence scale measurements (Cole et al, 1980, Fraser et al, 1984, Liou and Santavicca, 1985).

For the reasons outlined above the LDA technique has been used almost exclusively in the present investigation in a variety of optical and signal processing configurations to match the flow requirements; these configurations will be described in the appropriate chapters.

TABLE 1.2

Summary of experimental techniques

A) GAS VELOCITY FIELD

1. Pressure probes (Pitot tubes)

Classical method for the measurement of mean velocities in steady and constant property flows. Multi-hole pitot tubes can provide both direction and magnitude of the velocity vector. Limited to low turbulence flows, intrusive and non-applicable to engine flows.

2. Hot-wire anemometry

Well-established technique for turbulence measurements. Good time and space resolution, fluid properties dependent, requires calibration. Laborious data processing, limited to low turbulence flows. Intrusive method, non-applicable to firing engines.

3. Spark discharge anemometry

Involves time-of-flight measurement of a spark discharge convected between two electrodes to deduce gas velocity. Variants of this method include repetitive discharge and simultaneous photography (spark tracing). Intrusive methods, require calibration, in principle applicable to firing engines.

4. Laser Doppler anemometry

Non-intrusive technique for velocity and turbulence measurements. Good directional resolution, fluid properties independent, applicable to firing engines. Limited time resolution, requires optical access. Powerful technique, especially when combined with global laser diagnostics for combustion studies.

5. Vane and Impulse swirl meters

Global, intrusive techniques used for the characterisation of swirl-producing intake ports under steady flow conditions by measuring the rotational speed and angular momentum of the air flow respectively. The impulse swirl meter is less sensitive to velocity distribution than the vane swirl meter.

6. Particle streak photography

Flow visualisation method based on the imaging of the light scattered by seed particles in the flow. Processing of the still or video images can provide local velocity information of the precombustion flowfield ("particle image displacement velocimetry").

B) FLAME CHARACTERISTICS

1. Shadowgraph and Schlieren visualisation

Global methods for the two-dimensional flow visualisation of combustion phenomena, based on the refraction of light due to density gradients. Combined with strobed light source and video imaging or high speed cinematography they provide time-resolved information on the flow and flame structure, spray penetration, combustion cyclic variations and turbulence scales (microschlieren photography).

2. Holographic interferometry

A family of optical methods based on the interference of a reference light source with that scattered or refracted in the flow to provide three-dimensional flow or flame mapping. Techniques in a development stage; also used for scalar field studies in vapourised and non-vapourised Diesel sprays.

3. Multibeam laser refraction

Non-intrusive, inexpensive technique based on the refraction of a laser beam crossed by the propagating flame front. Combined with photodiode arrays can provide flame arrival time and flame front speed measurements.

4. Ionisation probes

Local method for the detection of flame arrival, based on the ionisation of the gas between two electrodes at the presence of the flame front. Simple, inexpensive but intrusive technique.

Cont'd

Table 1.2 (cont'd)

C) PRESSURE

1. Pressure transducers

A variety of piezoelectric and diaphragm-type pressure transducers exist which can give accurate measurements of in-cylinder pressure. Local pressure fluctuations cannot be resolved with these transducers.

D) TEMPERATURE AND SPECIES CONCENTRATION

1. Thermocouples and Resistance wires

Traditional methods for local measurements of temperature and its fluctuations. Resistance wires can also be used for binary mixture concentration measurements after a suitable calibration. Lack of durability and low frequency response are the main disadvantages.

2. Rayleigh scattering

Optical, non-intrusive technique based on the elastic molecular scattering. Suitable for concentration measurements in binary mixtures and temperature measurements when gas mixture composition and scattering properties are known. Requires calibration and clean research environment. Distinction between Mie and Rayleigh scattering signals is the main difficulty for in-cylinder measurements.

3. Spontaneous Raman Spectroscopy

Optical method based on the inelastic molecular scattering to measure the rotational-vibrational Raman spectra of a gas to infer local temperature or concentration in gas mixtures. Very low intensity signal and influence of Mie-scattered and background light are the main disadvantages of this technique.

4. Coherent Anti-Stokes Raman Spectrocopy (CARS)

Similar to Raman spectroscopy but non-linear scattering technique, overcoming the problems of background luminosity and particle presence. Expensive and difficult to implement but applicable to I.C. engine environments.

5. Laser-induced fluorescence

Visualisation technique making use of a fluorescent tracer gas to map its spatial distribution. Used for the study of the mixing of fresh charge with the residual gases or the homogeneity of a mixture.

E) FUEL SPRAY CHARACTERISTICS

1. Laser Doppler anemometry

The LDA signal can be processed in terms of amplitude and/or visibility to provide information about both fuel droplet velocity and size. Limited to very dilute sprays. As an amplitude-based technique sensitive to concentration of the surrounding droplet field.

2. Phase Doppler interferometry

Similar optical system to LDA but droplet size is deduced from the phase difference of the reflected or refracted light at two scattering angles. Limited to spherical transparent/opaque droplets.

3. Fraunhofer diffraction

Provides average droplet size along the line-of-sight of a single laser beam. Limited to situations with low droplet number density.

1.2.3 Review of theoretical methods

The existing methods of analysis and prediction of the in-cylinder flow processes are classified in two main categories: the phenomenological (or global) and the multi-dimensional methods. The first category consists of simplified, mainly thermodynamic, zero- and one-dimensional models which concentrate on the temporal in-cylinder variation of bulk quantities such as cylinder pressure and swirl angular momentum. The zero-dimensional models are used mainly to describe the "filling and emptying" process of the cylinder charge while the one-dimensional models attempt to resolve the spatial distribution of the in-cylinder flow in one direction. Examples of such models include the one-dimensional compression or expansion, (Watkins, 1973), the axisymmetric squish theory (Fitzgeorge and Allison, 1962) and the simple swirl theories (see Davis and Kent, 1979). The simplicity of these methods is achieved at the expense of their accuracy but makes them useful for simple parametric studies and preliminary calculations for multi-dimensional methods.

The multi-dimensional methods are based on the solution of the partial differential equations of mass, momentum and energy conservation and calculate the full spatial and temporal evolution of the in-cylinder flow processes. The instantaneous flow equations are ensemble- (or time-) averaged and supplemented with additional closure equations (mathematical models) representing processes such as turbulence, heat transfer and chemical reaction. The solution of these equations is performed by computer-based numerical methods starting either from the beginning of induction (e.g. Ahmadi-Befrui et al, 1982) or the beginning of compression (e.g. El Tahry, 1982); both procedures require detailed initial conditions at the intake valve and cylinder space respectively. The main difficulties encountered in the use of multi-dimensional methods are related to the assumptions made by the mathematical models and to the uncertainties and computer storage requirements of the numerical solution procedures. Recent progress in the mathematical modelling of turbulence has been slight; several variants of the original "k-ε" model, which include compressibility, (e.g. Ahmadi-Befrui et al, 1982, Grasso and Bracco, 1983) have been tested in axisymmetric engine geometries, (Ahmadi-Befrui, 1985b) followed by the "Reynolds stress" model (El Tahry, 1984). These evaluation studies revealed moderate agreement with relevant

experimental data which was attributed to the imperfections of the turbulence models as well as numerical errors and lack of appropriate boundary conditions. Future developments of the numerical solutions may include some aspects of "Large Eddy Simulation" models (Witze, 1981) which, in principle, are capable of resolving flow parameters in individual cycles rather than their ensemble-averaged values, but the massive computer storage and computational effort required makes the task prodigious.

Recent developments in numerical methodology have improved the computational grid arrangement, the discretisation of the differential equations and the solution algorithms. The early versions of the "cylindrical-polar, expanding-contracting" grids (Watkins, 1973, Griffin et al, 1976) and "curvilinear-orthogonal" grids (Gosman and Johns, 1978, Ramos and Sirignano, 1980a, b) are now replaced by "body-fitting" coordinate frames (Butler et al, 1979) to provide flexibility for the description of complex three-dimensional geometries; still, a number of severe limitations exist related to the requirements of simultaneous detailed "meshing" of valves and piston recesses in practical engine geometries. The use of "higher-order" differencing schemes for the discretisation of the flow equations has also improved the grid-independence of the numerical solutions and the use of implicit solution methods (such as EPISO, Gosman et al, 1984) allowed a reduction of the number of iterations and computing cost. These achievements, together with growing computer power, enabled the development of three-dimensional prediction codes for the in-cylinder flow in realistic engine geometries, (e.g. Mukerjee et al, 1984, Gosman et al, 1984, Johns, 1984, Butler et al, 1985). The accuracy of these methods is low for moderate mesh densities and the computing times are long, typically 80 minutes for a rather coarse grid of 28 x 16 x 28 (Gosman et al, 1984). Despite these shortcomings these methods can provide valuable insight into the complex flow mechanisms, as demonstrated by a combined experimental and theoretical study of Gosman et al, (1985).

A comprehensive review of the multi-dimensional methods and their achievements is given by Butler et al, (1981) and Gosman (1985). It is generally concluded that numerical and modelling uncertainties have to be reduced and more efficient solution methods devised. Furthermore it

is pointed out that more evaluation studies must be undertaken and uncertainties related to the boundary conditions must be removed; one of the objectives of this study is to provide such boundary conditions and evaluation data for both axisymmetric and practical three-dimensional engine geometries.

1.2.4 Statistical characterisation of the in-cylinder flow

The in-cylinder velocity field in reciprocating engines exhibits temporal variations due to the periodic piston and valve motions and its turbulent nature. Additionally, there is evidence of non-repeatability of some in-cylinder flow processes which is usually manifested in firing production engines as "cyclic variations" of peak cylinder pressure. The experiments of Patterson (1967), Winsor and Patterson (1973) and Cole and Swords (1980) in spark-ignition engines revealed a strong correlation between the cyclic variations of the combustion process and the instantaneous velocity of the fuel-air mixture near the spark plug at the time of ignition and indicated that the precombustion flowfield is also non-repeatable from one cycle to the next. This phenomenon was treated as a unique characteristic of the reciprocating engines and was initially attributed to non-repeatability of the induction process, (Reynolds, 1980). It is known, however, that the ignition process and flame propagation are not exactly repeatable phenomena even in stationary turbulent flows, such as in pipes (Ballal and Lefebvre, 1975) and fan-stirred combustion bombs (Abdel-Gayed et al, 1984). It appears that these non-repeatabilities are bound to occur in any phenomenon which is triggered by a short duration intermittent process imposed on a random process with larger time scale, (Gosman, 1983). Whatever the cause of the cyclic combustion variations, their significance cannot be underestimated since they affect the maximum power output and smooth operation of the internal combustion engines. Furthermore, their possible correlation with the precombustion flowfield indicates that close investigation and proper characterisation of the latter is required.

The characterisation of the turbulent non-stationary in-cylinder flowfield is not straightforward since the conventional decomposition of instantaneous velocities into time-average mean and fluctuating components is not applicable to non-stationary flows. The additional feature of the apparent non-repeatability of the precombustion flowfield (see for example Lancaster, 1976, Rask, 1981, Liou and Santavicca, 1983) raises questions regarding the proper definition of its mean and turbulent quantities and has been a matter of controversy for the last few years. Several methods have been proposed for the processing of the instantaneous velocity data to provide meaningful parameters, characterising the in-cylinder flows. They can be classified as ensemble-averaging, filtering and conditional sampling methods and are described and discussed in the following paragraphs.

Ensemble-averaging methods

In these methods the instantaneous velocity at a crank-angle θ in the i^{th} engine cycle, $U(\theta, i)$, is decomposed as

$$U(\theta, i) = \overline{U}_e(\theta) + u(\theta, i)$$

where $\overline{U}_e(\theta)$ is the ensemble-averaged mean velocity over N cycles and $u(\theta, i)$ is the deviation from the mean, usually expressed as ensemble-averaged rms, $\tilde{u}_e(\theta)$:

$$\overline{U}_e(\theta) = \frac{1}{N} \sum_{i=1}^{N} U(\theta, i)$$

$$\tilde{u}_e(\theta) = \left[\frac{1}{N} \sum_{i=1}^{N} u(\theta, i)^2\right]^{1/2}$$

When the velocity data are not continuous, as in the case of LDA measurements, the use of a finite sampling "window" (crank angle window, $\Delta\theta$) is necessary. The resulting "window ensemble-averaged" quantities become a function of the crank angle window, as well as crank angle:

$$\bar{U}_e(\theta \pm \frac{\Delta\theta}{2}) = \frac{1}{N} \sum_{i=1}^{N} U(\theta \pm \frac{\Delta\theta}{2}, i)$$

$$\tilde{u}_e(\theta \pm \frac{\Delta\theta}{2}) = \left[\frac{1}{N} \sum_{i=1}^{N} u(\theta \pm \frac{\Delta\theta}{2}, i)^2\right]^{1/2}$$

The effect of the crank angle window on the ensemble-averaged quantities (crank angle broadening) has been quantified by Morse (1977) and Arcoumanis et al (1984b). It was established that its effect can be rendered negligible by appropriate choice of its size, depending on the particular phase of the engine cycle.

The ensemble-average method inherently assumes that the mean velocity at a crank angle θ is independent of the engine cycle, thus implying repeatability of the process. It has the definite advantage of being simple and unambiguous but at the same time it suppresses information related to individual cycles, by incorporating the effects of possible cyclic variations in the ensemble-averaged quantities $\bar{U}_e(\theta)$ and $\tilde{u}_e(\theta)$. The measurements of Johnston et al (1979), for example, showed that a cyclic precession of a swirl flow pattern gave rise to abnormal values of $\tilde{u}_e(\theta)$ near the cylinder axis, which had little in common with the "in-cycle" turbulence.

An alternative method involving ensemble- and time-averaging was proposed by Lancaster (1976) who attempted to eliminate the non-stationary component of the instantaneous velocity by subtracting from it the ensemble-average velocity and by time-averaging the difference over a crank angle (time) interval $\Delta\theta$. In this case the instantaneous velocity is decomposed as:

$$U(\theta, i) = \bar{U}_e(\theta) + \bar{U}_t(i) + u(\theta, i)$$

where $\bar{U}_t(i)$ is the time-average mean velocity over an interval $\Delta\theta$ of the i^{th} cycle. This method introduces the notion of cyclic variations in the mean velocity but the choice of averaging interval is arbitrary ($\Delta\theta = 45^o$ in Lancaster's case) and may well influence the results.

Filtering methods

The inability of the ensemble-average methods to provide information related to individual engine cycles together with the observation that the cyclic variations of the instantaneous velocity appear mainly as variations of its low frequency components resulted in the adoption of filtering techniques for the determination of the in-cylinder flow quantities. The earliest methods, related to the use of hot-wire anemometers, employed electronic filters to eliminate the low frequency periodicity of the velocity signal, thus producing a stationary signal which is amenable to time-averaging, (Semenov, 1963, Dent and Salama, 1975). The cut-off frequency, however, and the crank angle interval over which the time-averaging is performed are arbitrary; these investigations do not give information on the sensitivity of their methods to the choice of these parameters which undoubtedly influence the results.

A more recent processing method, which is suitable for LDA in-cylinder velocity measurements, was proposed by Rask (1979). The instantaneous velocity in this method is decomposed in a more general form as:

$$U(\theta, i) = \overline{U}(\theta, i) + u(\theta, i)$$

which implies that both mean and fluctuating components are functions of crank angle as well as individual engine cycle. The instantaneous data $U(\theta, i)$ over each cycle are divided in 1^{o} windows and an arithmetic mean is calculated for each window. These values are subsequently fitted by a smooth curve which is assumed to represent the variation of the mean value $\overline{U}(\theta, i)$ for the specific engine cycle, while the deviation of the instantaneous data from this curve is considered as the turbulent fluctuation $u(\theta, i)$. The curve fitting is performed with a cubic-spline routine using the standard deviation of the data as the weighting factor in an iterative manner. The procedure of curve-fitting is essentially similar to filtering and the degree of smoothness equivalent to a cut-off frequency. This method treats turbulence as a random error in the measurement of the mean velocity and was criticised by Ahmadi-Befrui (1985b) as incorrect since the turbulent motions are spatially and temporally correlated and should not be treated as random. Despite this deficiency the method can resolve the turbulent characteristics of each cycle and allows a variable degree of filtering to be used in individual cycles.

Possible cyclic variations of the turbulence intensity, however, cannot be accounted for and a high data rate is required to resolve the high frequency velocity fluctuations.

An alternative filtering method was proposed, and extensively applied in various engine configurations, by Liou and Santavicca (1982, 1983, 1985). With this method the instantaneous velocity data are averaged within 1^{o} crank angle windows and the spectrum of the resulting velocity variation in each cycle is calculated using an FFT analysis. The objective is to find a distinct frequency cut-off point between the "true" turbulence spectrum and the "low frequency" cyclic variations. The experiments of Liou and Santavicca did not reveal any obvious cut-off frequency and for this reason the upper limit of the ensemble-average mean velocity spectrum was used as the filtering criterion. This was found to depend on engine speed and flow characteristics and to vary between 300 - 900 Hz in an engine speed range of 1200 - 2400 rpm. Once the cut-off frequency was chosen, the components of the instantaneous velocity spectra above this limit were set to zero and the inverse Fourier transform taken, yielding a mean velocity variation for each cycle. Again, a high data rate is required for the application of this method and the absence of any clear cut-off frequency between the low and high frequency regions of the velocity spectra indicates that a significant amount of low frequency turbulent energy may be assigned to the mean velocity variations resulting in a possible underestimation of the "true" turbulence intensity.

From the above it is concluded that the filtering methods suffer from an ambiguity in the definition of turbulence. The FFT analysis method is more strict than the curve-fitting method but does not allow the variation of frequency cut-off points in individual cycles. Both methods conclude that the so-defined cyclic variations are usually reduced in regions of strong, well-directed flow and give estimates of the in-cylinder turbulence which in some cases may be between 50 to 100% lower than those obtained with the ensemble-average methods.

Conditional sampling methods

Conditional sampling techniques have been used in firing internal combustion engines to investigate the correlation between the precombustion flowfield and the combustion characteristics (Cole and Swords, 1980,

Swords, et al, 1982). Similar techniques can be used to resolve the cyclic velocity variations in firing engines, as demonstrated by Witze et al (1984a) and Martin et al (1984). This method inherently assumes that there is a cause-and-effect relationship between the fluid motion and the combustion process. It involves the selection of one or more combustion parameters, such as flame speed, flame arrival time and cylinder pressure, to identify individual engine cycles which are similar to each other; this permits statistical ensemble-averages to be obtained for groups of engine cycles which are described as having only stohastic differences. The effectiveness of the method depends on the choice of the conditioning parameters which involves a degree of arbitrariness; it is also argued (Rask, 1984) that these parameters usually result from space- and time-averaged processes and may disguise important cyclic differences. In this context it has been proposed that combinations of filtering and conditional sampling methods may be used to decrease the ambiguities involved in both methods. The advantages of the conditional sampling methods include the possibility of obtaining measurements with low data rates and resolving turbulence quantities in individual (similar) cycles. The main disadvantage is that, in their present form, they can only be applied in firing engines.

The variety of the data processing methods described above and the substantial differences between them indicate the uncertainties related to the proper characterisation of the flow in reciprocating engines. In firing engines the description of the flowfield on an individual cycle basis is desirable, since the intermittent combustion process is governed by the flow parameters of the individual cycle rather than their average values. For this purpose the most suitable methods for flow characterisation seem to be the multi-parameter conditional sampling techniques.

The "cyclic variations" of the precombustion flowfield are turbulent in nature; they appear as variations of the "mean" flowfield because of the comparable time scales of the low frequency turbulent fluctuations and the engine stroke. The comparison of relatively small segments of any instantaneous velocity trace obtained in a steady turbulent flow would probably produce a similar impression of varying mean velocity if the time scales of the flow were comparable to the length of the segment. Any attempt to reduce the "cyclic variations" in an engine flow is equivalent

to reduction of the low frequency turbulent fluctuations and to this end the filtering methods for the flow characterisation may be useful.

The multi-dimensional calculations of the isothermal in-cylinder flowfield cannot cope, at present, with cycle-resolved analysis; they solve the ensemble-averaged equations which inherently include the turbulent phenomenon described as cyclic variations. In this context validation data obtained with filtering methods are not relevant and the ensemble-average methods should be used for the flow characterisation. However, when comparative experimental studies between various engine configurations are involved there is a need for, at least, qualitative investigation of the low frequency turbulence behaviour.

Based on the above discussion and considering the objectives of the thesis the method of ensemble-averaging is adopted in this work supported, when necessary, by cycle-resolved instantaneous velocity measurements.

1.2.5 Review of the in-cylinder flow processes

This section reviews the current state of knowledge of the characteristics of the in-cylinder flow processes. It is divided into three main parts dealing with the induction, compression and power/exhaust strokes of the engine cycle, respectively. Most of the discussion is based on the results of relevant experimental studies with emphasis on the pre-combustion flowfield. The objective of this review is to highlight areas requiring further research for better understanding of the in-cylinder flow processes and to provide the background for the discussion of the results of the present study.

1.2.5.1 The induction process

The induction process consists of the filling of the engine cylinder with fresh charge through the inlet manifold and port/valve assembly. In homogeneous-charge gasoline engines the charge is the fuel-air mixture

prepared in the carburator while in Diesel and stratified-charge gasoline engines it consists of compressed or preheated air, depending on the particular engine type. The main role of the inlet manifold is the uniform distribution of the charge to the engine cylinders where the intake port/valve assemblies shape its mean and turbulent flow characteristics as it enters the cylinder. The amount of charge trapped in the cylinder during induction is controlled by the flow characteristics of the induction system and the valve timing and it is directly related to the power output of the engine. The parameter used for the characterisation of this "breathing capacity" of the engine is termed "volumetric efficiency", (η_v), and is defined as the ratio of the mass of fresh charge which passes into the cylinder during the induction stroke to the mass of charge which would fill the piston displacement volume at inlet density (Taylor, 1977). The induction-generated flowfield, on the other hand, determines the mean and turbulent motion of the charge prior to ignition which, in turn, controls the efficiency of the combustion process. These features of the induction system make its design an important factor influencing the overall engine performance; this is reflected on the large variety of existing induction systems and the continuing effort to improve their performance.

The more representative investigations of the flowfield in the induction system are reviewed in the following paragraphs with emphasis on the flow at the exit of the intake valve. This is followed by a review of the flow evolution inside the cylinder throughout induction, until the closure of the intake valve.

Flow in the inlet manifold

The main objective in the design of a conventional inlet manifold is the uniform distribution of charge to the engine cylinders with minimum pressure loss. The first requirement is related to the smooth operation of the engine while the second is meant to improve its volumetric efficiency, since up to 20% of the pressure loss in the induction system occurs in the manifold (Tabaczynski, 1982). Modern inlet manifolds, however, face an increasing demand for high charge pressure in order to compensate for the pressure losses of the swirl producing ports and to increase the power output of small engines. These requirements are usually met by turbochargers or by "tuned intake manifolds" (see for example

Engelman, 1973) which take advantage of the pressure waves generated in the induction system to deliver higher charge pressure during induction. The role of the inlet manifold is thus becoming more important and its design more complicated.

Little attention has been paid to the detailed flowfield in manifolds since it is further transformed by the intake port while its global dynamic characteristics can be estimated with reasonable accuracy with thermodynamic and one- or two-dimensional models (see for example Tabaczynski, 1982 and Chapman, 1979). The development of the multi-dimensional methods, however, indicates that the possibility of predicting the flowfield in the induction system must not be excluded and some first attempts in simple geometries have already started.

Flow in the intake port/valve assembly

The inlet manifold is followed by the intake port which usually forms part of the cylinder head block of the engine. The design of the intake port has similar requirements for low pressure losses and good dynamic behaviour as the inlet manifold but its major role is the shaping of the charge flow structure as it enters the cylinder via the valve passage. The importance of the intake flow structure on engine performance has been demonstrated by a large number of investigations. The simplest experiment was performed by Clerk (1921) who compared the combustion characteristics in an engine in the presence and absence of induction-generated flow; in the latter case the combustion duration was twice as long and the peak cylinder pressure only a fraction of that obtained with the normally operating engine. A particular flow structure which is of importance in direct-injection Diesel and stratified-charge gasoline engines is the rotational motion of the charge, referred to as "swirl"; this is a major parameter controlling the fuel-air mixing after injection and the combustion duration. The beneficial influence of swirl on combustion efficiency was recongised by Dicksee (1949) and, since then, a variety of swirl-producing intake ports have appeared; they can be classified into two categories depending on whether they produce swirl downstream or upstream of the intake valve. The first category comprises the "directed" or "tangential" ports and the second a variety of "helical" ports.

The directed ports have a flow passage with varying cross-section arranged at an angle with respect to the cylinder head such as to produce

a non-uniform exit flow with a preferential direction. During induction the linear momentum of the flow emerging from the port is partly transformed into angular momentum by its deflection on the cylinder wall. The strength of the resulting swirl depends on the angle between the port axis and the cylinder head (Fitzgeorge and Allison, 1962) and its eccentricity with respect to the cylinder axis (Watts and Scott, 1969). Some directed ports incorporate a "deflector" or "shroud" at their exit or on the valve itself (masked or shrouded valve), covering part of the flow exit area; this configuration enhances the directional characteristics of the port and was extensively used in earlier Diesel engines. The obstruction of the flow caused by the shroud, however, reduces the volumetric efficiency of the engine and, at present, this type of port is mainly used for research purposes (for example Witze, 1980b).

The helical ports produce swirl by their spiral shape which forces the charge to rotate around the valve axis before entering the cylinder. There is a variety of helical ports classified according to the shape of their spiral ramp (steep or shallow, Monaghan and Pettifer, 1981) and their orientation (Tindal and Williams, 1977). The current high swirl ports often combine the characteristics of helical and directed ports (Uzkan et al, 1983) and are extensively used in high speed direct-injection (HSDI) Diesel engines. The advantages offered by the helical ports are: high swirl at low and medium valve lifts (Tindal and Williams, 1977), more ordered swirl motion during compression, higher swirl inside the piston bowl (Tindal et al, 1982), lower flow obstruction than the directed ports for equivalent swirl levels (Brandl et al, 1979) and small performance variations caused by manufacturing tolerances.

Other induction system configurations used in production engines include the "side-valve" (L-head) geometries (Rask, 1978, Witze, 1978) and the "ported" engines (Liou and Santavicca, 1983). These configurations are convenient for use in research engines but they are not representative of the current trends in engine design. Axisymmetric idealised cylindrical ports are also used in research engines (see for example Arcoumanis et al, 1983) where the induction swirl is generated by guide vanes located upstream of the intake valve. In all cases described above, however, the generation of induction swirl results in a reduction of the discharge capacity of the induction system; the optimum balance between these characteristics is always a major concern in engine design.

Experimental data of the flowfield within the intake ports and at the exit of intake valves are rather limited. A large number of investigations have been performed, however, to determine the discharge and swirl producing capabilities of the intake port/valve assemblies. A review of the most important findings of these investigations is presented in the following paragraphs.

Mass flow through the intake valve

The volumetric efficiency of an engine depends largely on the discharge characteristics of the intake port/valve assembly. The difficulties associated with the measurement of its instantaneous flow characteristics in an operating engine prompted the use of steady flow simulations of the induction process. Usually, the performance of an intake port/valve assembly is characterised by a "discharge coefficient" which is defined as the ratio of the mass flowrate through the valve to the mass flowrate through an ideal nozzle under the same pressure ratio (or pressure drop, see Appendix 2.2). It has been shown by Annand and Roe (1974) and Wood et al (1942) that the performance of a non swirl-producing intake port/valve assembly is mainly determined by the geometric details of the valve and valve seat. For this reason most of the relevant investigations were carried out with valves assembled in idealised cylindrical ports.

The influence of valve lift, L, (see Figure 1.1) on the discharge coefficient of a typical valve has been investigated by Tanaka (1929), Kastner et al (1963) and Annand (1969) who observed discontinuities in the variation of discharge coefficient with valve lift and postulated the presence of four distinct flow patterns (regimes) at the valve exit: At low lifts the flow remains attached to the valve passage (regime I, Figure 1.2) and separates at higher lifts, initially from the valve sealing face (regime II) and later from the valve seat (regime III) to reattach on the valve head at even higher lifts (regime IV). In general, the discharge coefficient was found to decrease with valve lift and it was assumed by Kastner et al (1963) that the transition from one flow regime to the other causes variations in the flow angle at the valve exit. It was also suggested by Annand (1969) that flow regimes II and III are unstable and in several cases direct transition from flow regime I to IV may occur.

The influence of valve seat angle, ψ, on the discharge coefficient was investigated by Tanaka (1929) and Annand (1969). Their results showed that with a 45^{o} seat angle the transition from one flow regime to another occurs at larger valve lifts than with a 30^{o} seat angle; the 45^{o} seat angle was therefore recommended for high lift and the 30^{o} for low lift engines. Both, 45^{o} and 30^{o} seat angles were found to give better performance than a 60^{o} seat angle.

The valve seat width, t, influences the transition from one flow regime to the other and the frictional losses in the valve passage. Although its influence is not significant, a small seat width gives better overall flow characteristics.

The most effective way to improve the discharge coefficient of a typical valve was found to be the rounding of the sharp corners at the valve head and seat, which makes the flow passage like a convergent-divergent nozzle and sustains flow regime I for larger lifts (Tanaka, 1929). All investigations (for example Tanaka, 1929, Annand, 1969, Wood et al, 1942 and Kastner et al, 1963) support the view that rounding of these corners may result in an increase of the discharge coefficient by up to 30%. This approach however is not very practical for production engines where machining should be as simple as possible.

The effect of pressure drop across the valve on the discharge coefficient is directly related to the Reynolds number and compressibility effects and has been investigated by Luck (1906), Nutting and Lewis (1918) and Tanaka (1929). It was found that the discharge coefficient increases with pressure drop to an asymptotic value and is more sensitive to pressure drop variations when flow transition occurs (Kastner et al, 1963) and at small valve lifts (Woods and Khan, 1965).

The interaction of the outflow from the valve with the cylinder wall and its effect on the discharge coefficient has not been adequately investigated (Annand, 1969). Woods and Khan (1965) reported that at high valve lifts the cylinder confinement of the valve flow decreases the discharge coefficient of the valve by about 3% and by less at small lifts. Kastner et al (1963) also reported a minor effect on the discharge coefficient but suggested that the confinement of the flow may alter the valve lifts where change of flow regime occurs.

The valve operation is expected to have an effect on its discharge characteristics due to inertia and resonance effects in the induction system, (see for example Luck, 1906). However due to lack of relevant data, an assumption was often made that the flow at the valve passage responds quickly enough to the lift variations so that steady flow data can be used to calculate the volumetric efficiency of the engine, (assumption of induction quasi-steadiness). More recent investigations, however, indicated that the mean "dynamic" discharge coefficient of an operating valve may be up to 20% lower than the corresponding "static" discharge coefficient under steady flow conditions, at high engine speeds and large pressure drops across the valve, (Kastner et al, 1963, Fukutani and Watanabe, 1982). The effect of engine speed on the volumetric efficiency of an engine was demonstrated by the measurements of Davis and Kent (1979) who showed a decrease of 20% in the amount of fresh charge drawn in the cylinder when the engine speed increased from 1000 to 3500 rpm. The above data suggest that the characteristics of the induction process do not vary linearly with engine speed; furthermore they relate to cycle-averaged quantities and no information is available for the instantaneous flowrate through the intake valve.

Velocity field characteristics at the valve exit

Early steady-state measurements at the exit of an intake valve were obtained by Kastner et al (1963) using Pitot probes and confirmed the postulations of Tanaka (1929) regarding the change of flow pattern at the valve exit with increasing valve lift. Similar measurements obtained by laser Doppler anemometry (Bicen, 1983) confirmed and quantified the findings of Kastner et al and further revealed that the flow pattern at the exit of a stationary valve under pulsating flow conditions was identical to that under steady flow conditions. They also showed that, for a given mass flowrate, the separation at the valve passage results in exit flow velocities which are significantly larger than those anticipated by the assumption of uniform (plug) velocity distribution.

Several attempts have been made to describe the valve exit velocity field in practical helical and directed ports using hot-wire anemometry. The measurements of Uzkan et al (1983) and Haghgooie et al (1984) showed that the velocity magnitude and distribution vary considerably around the valve periphery, depending on the particular port/valve geometry. These

measurements were obtained under steady flow conditions and did not provide information about the valve exit flow angle.

The most comprehensive measurements of the valve exit flowfield in helical and directed ports were obtained by laser Doppler anemometry by Wigley and Glanz (1984a, b) and Brandstatter et al (1985). They obtained measurements of three velocity components under steady flow conditions and used them as boundary conditions in a multi-dimensional analysis. They also reported radial velocity measurements at the exit of an operating valve in an L-head engine motored at 1790 rpm (Wigley and Glanz, 1984b). No comparison was made between steady and unsteady flow measurements with the same port, and the results served mainly as a demonstration of the ability of their system to measure the valve flow characteristics under operating conditions.

From the above discussion it is concluded that the discharge characteristics of intake port/valve assemblies have been extensively investigated while the flowfield characteristics at the valve exit are not well documented. Very little is known of the influence of valve operation and engine speed on the valve exit flowfield and the value of relevant steady flow data is still in question. Furthermore, the interaction of the valve flow with the descending piston or the neighbouring cylinder walls has not been examined. In view of the increasing need of the multi-dimensional prediction codes for boundary conditions, the availability of such data appears to be essential.

In-cylinder flow structure

The flow structure generated during induction inside the cylinder of reciprocating engines is generally complex and three-dimensional due to the intake port and combustion chamber geometries. The exception to this is the flow in axisymmetric model engines which have been used in fundamental studies, (see for example Yianneskis, 1982, Bicen, 1983 and Arcoumanis, 1983).

The induction flowfield in axisymmetric engine geometries is characterised by a system of vortices generated by the interaction of the annular jet emerging from the valve passage with the cylinder walls and the piston face. In the absence of induction swirl, the usual flow pattern is that of a main toroidal vortex behind the valve and a secondary ring

vortex formed at the corner of the cylinder head. The valve jet usually issues at an angle similar to that of the valve seat, although in some cases of small seat angle it may attach to the cylinder head, eliminating the corner vortex (Arcoumanis et al, 1982b). The size of the main vortex varies with the instantaneous piston position during early induction and later scales with the valve diameter. This vortical structure decays rapidly after bottom-dead-centre (BDC) and becomes near uniform at inlet valve closure (IVC). Turbulence is generated mainly in the shear layers of the valve jet and the wall impingement region and is gradually transported to the rest of the cylinder by convection and diffusion. At early induction turbulence is far from homogeneous and decays rapidly, as the mean flow becomes weaker, towards the end of induction showing tendencies towards homogeneity.

When vane-induced swirl is present, its distribution at early induction is far from solid body rotation (Arcoumanis et al, 1982b). The angular momentum of the incoming jet is rapidly transported towards the cylinder axis by the mean flow. This affects the axial mean motion and results in enlargement of the main vortex or even the formation of a smaller vortex within it, immediately behind the valve, as a result of the swirl-induced radial pressure gradient. (Morse et al, 1980a). The decay of the swirl motion is much slower than that of the axial flow and this has a significant effect on the carry-over of swirl to the compression stroke. The influence of parameters such as valve lift, valve seat angle and compression ratio was also examined by Arcoumanis et al (1982b) and (1984b) who found that, although the details of the induction flow structure depend to a certain extent on these variables, the flow near IVC is similar in all cases with the exception of a very low lift case, where turbulence intensity was slightly increased.

The induction flow structure in non-axisymmetric geometries is less well documented. The most detailed measurements are those of Arcoumanis (1983) and Arcoumanis et al (1984a) obtained in model engines with offset intake ports. These studies show that the axial flow pattern is essentially similar to that in axisymmetric geometries with the main vortex displaced from the cylinder axis and the corner vortex varying in size around the cylinder periphery. The tangential flow structure consists of a pair of counter-rotating vortices which decay, together with the axial flow structure, towards IVC. When swirl is introduced, however, the organised

tangential motion persists throughout induction into the compression stroke. The turbulence levels at IVC are essentially the same as in the axisymmetric cases.

Most of the data related to the induction flowfield generated by practical ports come from steady flow experiments or from measurements of a few points in the cylinder of motored production engines. Several methods have been used to study the "induction" flowfield under steady flow conditions; they include flow visualisation (Ekchian and Hoult, 1979, Hirotomi et al, 1981, Uzkan et al, 1983), hot-wire anemometry (Tindal and Williams, 1977, Tindal et al, 1982) and laser Doppler anemometry (Wigley and Hawkins, 1978, Wigley and Glanz, 1984a, b, Coghe et al, 1985). A traditional method of characterising the flow generated by swirl-producing intake ports is by measuring the average rotational speed and the angular momentum of the in-cylinder flow under steady flow conditions. This involves the use of "vane swirl meters" or "paddle-wheels" (see for example Tanabe et al, 1978) and "impulse swirl meters" (Davis and Kent, 1979), which give estimates of characteristic parameters such as the swirl ratio, SR, and the swirl number, SN, (see Appendix 3.1). A comparative study of these methods was made by Monaghan and Pettifer (1981) who showed that the swirl angular momentum obtained by the impulse swirl meter was in good agreement with that calculated from LDA velocity measurements. The hot-wire data were found to be in error in regions of high turbulence intensity and both, impulse and vane swirl meters to affect the in-cylinder flow, the latter giving also erroneous measurements in regions of flow recirculation. A more recent work of Pettifer (1982), however, revealed that various intake port geometries, giving the same swirl ratio in the steady flow tests, had different performance in a firing engine. This indicates that the characterisation of the induction flow-field with bulk quantities such as swirl number or swirl ratio is not sufficient and that the details of the velocity distribution must be taken into account; the only unambiguous method for that purpose appears to be the laser Doppler anemometry.

The features of the induction flowfield vary considerably depending on the specific intake port geometry. The helical and directed ports produce a complex axial flow pattern with an extended main vortex whose position changes with valve lift (Coghe et al, 1985). Turbulence is more or less uniformly distributed in both axial and tangential planes, (Wigley and Hawkins, 1978). The swirl flow pattern consists of two counter-

rotating vortices whose relative strengths depend on the flow asymmetry; their presence is attributed to the generation of angular momentum flux in the main swirl direction as well as the opposite direction due to the eccentricity of the intake valve (Uzkan et al, 1983). This structure becomes a single vortex swirl pattern with increasing valve lift and distance from the cylinder head. The swirl distribution is rarely solid body rotation and the swirl centre does not coincide with the cylinder axis, following a helical locus along the cylinder.

Little information is available regarding the comparison of the induction generated flowfield in production engines with steady flow simulations. The axial flow structure is not expected to be simulated well with steady flow tests, mainly due to the scaling of the axial flow with piston position (Bicen, 1983). The swirl flow pattern is expected to be better simulated but, in this respect, the results of Hirotomi et al (1981) and Gerber et al (1985) are contradictory. The latter also proposes a "correction" method for transforming the steady flow swirl measurements to simulate the flowfield in the operating engine. The relative ease of measuring in a steady flow configuration and the possibility of extrapolating these results to the operating engine is a strong incentive for a further investigation of this aspect of the induction-generated flow.

1.2.5.2 Compression process

The closure of the intake valve finds the mean and turbulent flow fields in a state of continuing decay. The evolution of the in-cylinder flow during compression is purely determined by the combustion chamber geometry and the remains of the induction flowfield.

The compression process in an axisymmetric engine with flat piston and cylinder head (disc-type combustion chamber), in the absence of induction swirl, is almost one-dimensional. The induction-generated axial flow structures have decayed considerably by IVC (Bicen, 1983, Arcoumanis, 1983) and the turbulence field is near homogeneous and isotropic, due to the effect of convection and dissipation following the break-down of the intake-generated vortices. During compression, however, turbulence generation

is sustained by the compression-induced stresses and is balanced by dissipation resulting in an almost constant turbulence intensity of about 0.7 to 0.5 $\overline{V}_p$ (Ahmadi-Befrui, 1985b, Arcoumanis, 1983). Near the end of compression turbulence generation peaks but so does dissipation which dominates and results in a decrease of TDC turbulence to values around 0.4 to 0.5 $\overline{V}_p$ (El Tahry, 1982, Arcoumanis, 1983, Bicen, 1983).

The measurements of Arcoumanis et al (1982b) in an axisymmetric engine with induction swirl indicate that the tangential flow pattern persists during compression, organised in a near solid body rotation, and does not influence the axial flowfield. The turbulence intensity in the axial direction seems to decrease slightly when swirl is present and this is attributed to a decrease of the radial normal stresses due to the stabilising effect of swirl (Gosman, 1983). Similar effects of swirl on turbulence intensity have also been reported by Rask (1979) and Liou and Santavicca (1983) for non-axisymmetric engine geometries. Other studies, however, using shrouded valves to generate swirl reported an increase of turbulence intensity during compression (Wakisaka et al, 1979 and Daneshyar and Fuller, 1982) and this may be attributed to the more complex vortical pattern induced in the cylinder with such intake port configurations (Witze,1980b). An interesting aspect of turbulence in the tangential direction is the abnormally high ensemble-average values, often measured near the swirl centre, even in cases of solid body velocity distribution where, normally, shear is not present. This phenomenon has been reported by Johnston et al (1979) and Witze (1980b) and was attributed to a broadening of the turbulence measurements due to a helical motion of the swirl centre (Rask, 1979) which is not exactly repeatable from cycle to cycle (cyclic precession of the swirl centre). Johnston et al (1979) suggested that it is a result of the eccentricity of the intake valve which remains open during part of the return stroke. Similar phenomena, however, have been reported for axisymmetric engines (Arcoumanis et al, 1983) and even in stationary swirling flows (see for example Chanaud, 1965).

Little experimental data exist with respect to the axial flow pattern during compression in non-axisymmetric engine geometries. This is mainly due to the limitations of the back-scatter mode of laser Doppler anemometry, often used to measure the in-cylinder flowfield through a transparent piston or a window on the cylinder head, which allows only velocity com-

ponents on the tangential plane to be resolved, (see for example Rask, 1979, Witze et al, 1984a, b, Liou et al, 1984). The most detailed velocity measurements available in three-dimensional model engine geometries with disc type combustion chamber are those of Arcoumanis (1983) and Arcoumanis et al (1984a). These results show that the induction-generated axial vortex persists longer during compression than in the axisymmetric case resulting in a weak vortex at TDC of compression; the behaviour of turbulence, however, is essentially the same in both cases.

In order to enhance fuel mixing prior to ignition, most of the stratified charge, direct-injection engines incorporate a recess (bowl) on the piston crown and have a small clearance between the piston face and the cylinder head (bumping clearance). This combustion chamber geometry induces during compression an inwards radial motion, termed "squish", which results in a strong shear flow near the lip of the piston-bowl as it approaches top-dead-centre. When swirl is present the piston-bowl enhances the rotational speed (swirl ratio) of the charge which tends to conserve its angular momentum in a smaller radius of gyration. The resulting flow pattern inside the piston bowl is highly turbulent and complex in structure (see for example Brandl et al, 1979, Williams and Tindal, 1980, Rask, 1984). A comprehensive experimental study of this effect of piston geometry on the in-cylinder flow and of the interaction of swirl with squish has been carried out in an axisymmetric model engine by Arcoumanis et al (1983). Their results show that, in the absence of swirl, the squish motion generates a toroidal vortex inside the piston-bowl and results in a moderate increase of turbulence intensity relative to that in a disc-chamber. The interaction of squish with swirl usually results in a reversal of the direction of rotation of the in-bowl vortex or even in the generation of a double vortex, depending on bowl geometry, accompanied by a significant increase in turbulence intensity at TDC of compression. The influence of induction swirl level on the in-bowl flow structure has been theoretically investigated by Gosman and Johns (1978) and El-Tahry (1982). Their results show that there is a strong dependence of in-bowl flow structure on induction swirl level but there is no detailed experimental data to confirm their conclusions.

The angular momentum of the rotating charge decays during compression, mainly due to frictional losses at the wall of the combustion chamber.

This is a rather important mechanism since it determines the induction swirl angular momentum which is required in order to obtain the optimum swirl level at TDC of compression. In addition, it is a convenient parameter for assessing the performance of prediction methods, such as those of Davis and Kent (1979) and El Tahry (1982). Experimental information on this aspect of the in-cylinder swirl motion is scarce but the results of Tanabe et al (1978) and Asanuma and Obokata (1972) indicate angular momentum losses of the order of 45%, independent of swirl ratio and combustion chamber geometry. These results however concern angular momentum decay from bottom-dead-centre (BDC) to TDC of compression and therefore include the momentum exchange through the intake valve from BDC to IVC.

The ability of internal combustion engines to operate efficiently in a wide speed range, when considered with the linear dependence of combustion duration on turbulence (Lancaster et al, 1976, Mattavi et al, 1979, and Coghe and Ghezzi, 1981), suggests that there should be a near monotonic increase of TDC turbulence intensity with engine speed. Semenov (1963) reported on exponential increase of TDC turbulence with engine speed ($\tilde{u} \sim n^{1.5}$) in a motored engine with a disc-type combustion chamber. Later Winsor and Patterson (1973), Lancaster (1976), Witze (1977) and Coghe and Ghezzi (1981) showed that the TDC turbulence is near homogeneous and isotropic, its intensity depends on the induction system geometry and that it scales almost linearly with engine speed. The results concerning the influence of engine speed on the TDC mean flowfield, however, were contradictory indicating either linear scaling with engine speed (e.g. Horvatin and Hussman, 1969, Witze, 1977, Brandl et al, 1979) or no scaling at all (e.g. Arnold et al, 1972). The above results, however, were obtained using hot-wire anemometry which, as shown by Witze (1980a), may give erroneous measurements near TDC of compression.

More recent investigations, conducted by laser Doppler anemometry (Cole and Swords, 1978, Rask, 1979, Coghe et al, 1980, Liou and Santavicca, 1983 and Liou et al, 1984), confirmed the near homogeneity (depending on induction system) and isotropy of TDC turbulence and, to a lesser extent, its linear dependence on engine speed. Other investigations by Witze et al (1983) and Fansler (1985) revealed a non-perfectly linear dependence of TDC turbulence on engine speed. The results regarding the mean flowfield are even more contradictory, with those of Rask (1979) and Fansler

(1985) scaling with engine speed and those of Cole and Swords, (1978). Monaghan and Pettifer (1981) and Liou et al (1984) indicating dependence of the scaling on the particular induction system and the specific velocity component under consideration.

A summary of the more important results, concerned with the dependence of TDC turbulence on engine speed, is given in Figure 1.3. The horizontal axis in this figure represents mean piston speed ($\overline{V}_p$) in order to take into account both, the stroke and engine speed used in these investigations. This diagram shows that only in a few cases the turbulence scaling is perfectly linear. Furthermore, the slope of the curves ($\tilde{u}/\overline{V}_p$) varies considerably due to specific engine geometries, measurement methods and data reduction used by the various investigators. An additional feature of these results is that they consist of few data over a wide speed range representing measurements obtained at one only point in the TDC clearance volume, while the details of the in-cylinder flow development throughout induction and compression have not been studied in the corresponding investigations.

The ambiguities and contradictions, revealed by the discussion above, suggest that a systematic and detailed investigation of the dependence of TDC flowfield on engine speed is necessary. This could be of value for the assessment of the performance of the multi-dimensional prediction methods and, with their assistance, can provide a better understanding of the turbulence production and decay mechanisms in the reciprocating engines.

1.2.5.3 Combustion/expansion and exhaust processes

The combustion process and its interaction with the precombustion flowfield is determined by the particular engine type. A comprehensive review of combustion in homogeneous-charge engines is given by Lancaster et al (1976) and Smith (1982). The more complex combustion processes in stratified-charge spark-ignition and direct-injection Diesel engines are described in detail by Tierney et al (1975) and Brandl et al (1979), respectively. A brief overview of the combustion mechanisms and their dependence on the precombustion flowfield is given below.

The combustion process in a homogeneous-charge spark-ignition engine can be divided into four phases (Lancaster et al, 1976). During the "initial" phase the ignition of the fuel-air mixture establishes a flame kernel with propagation determined by the spark and local turbulence characteristics; it is at this stage that combustion cyclic variations may be initiated (Patterson, 1967). The scale and intensity of turbulence determine the flame front speed during the "transition" phase by distorting (wrinkling) the flame front and increasing its reaction area. The burning of the reactants reaches a steady state or "turbulent" phase during which most of the charge is burnt, until the "final" phase where the flame reaches the boundaries of the combustion chamber. The flame front speed during the turbulent phase of combustion is linearly proportional to the local turbulence intensity (Lancaster et al, 1976, Mattavi et al, 1979) which may be enhanced by the combustion-induced pressure field (Witze et al, 1984b).

In stratified-charge engines the initial phase of combustion is similar to that in homogeneous-charge engines; however, the presence of a strong mean flow structure influences the combustion rate during the main burning phase which is now controlled mainly by convection. The location and number of spark plugs, combined with the magnitude of swirl are the main parameters influencing the combustion duration and, to a certain extent, the cyclic combustion variations (Witze and Vilchis, 1981 and Witze, 1982).

The combustion in direct-injection Diesel engines is controlled by the fuel-injection characteristics and its interaction with the precombustion flowfield. The relative strength of the fuel spray and pre-injection flowfield determine whether combustion is spray or flow controlled (Greaves et al, 1980), while the method and timing of injection and the magnitude of swirl velocities near the edges of the spray control the fuel evaporation and combustion rate during its initial stages (Brandl et al, 1979).

The combustion rate is particularly important in all engine types since it determines the engine performance and the emission of unburned hydrocarbons. It becomes more crucial in modern engines which operate with lean fuel-air mixtures to improve fuel economy and nitrogen oxides (NO_x) emission; the resulting low temperature combustion leads to low combustion rates which must be balanced by controlling the precombustion flowfield. Smoke formation, a characteristic feature of Diesel engines,

can also be reduced by increasing turbulence and swirl velocities in the combustion chamber (Brandl et al, 1979) and matching the injection characteristics to the particular engine (Fisher, 1983).

The expansion stroke in a motored engine with a disc-type combustion chamber is accompanied by a continuous decay of turbulence (Arcoumanis et al, 1982a, Witze et al, 1983) and in the absence of swirl, the mean flow is nearly one-dimensional; similar trends of turbulence decay are observed in firing engines after the end of the combustion process (Witze et al, 1984b). The, mainly unburned, gases trapped in the crevice between piston and cylinder wall expand and emerge as a weak annular wall jet; their presence is considered to be a major contributor to the emission of unburned hydrocarbons and to the power loss of the engine (Namazian and Heywood, 1982). The expansion stroke in engines with cylindrical or re-entrant type piston-bowls is characterised by an outflow from the bowl and redistribution of swirl angular momentum (reverse squish). The local turbulence production can play an important role in the final stages of the combustion process, (Watts and Scott, 1969).

The opening of the exhaust valve causes a purge of the high pressure combustion products from the cylinder. The evacuation process is controlled by the cylinder pressure and the discharge characteristics of the exhaust system, the performance of which is now attracting attention due to its importance in turbocharged engines (see for example Oldfield and Watson, 1983). The in-cylinder axial flow is nearly one-dimensional and when swirl is present its level decreases continuously due to wall shear effects; at the end of the exhaust stroke a "residual swirl" may still persist and contributes to the induction swirl level, (Davis and Kent, 1979).

1.3 PRESENT CONTRIBUTION

The review of the flow processes in reciprocating internal combustion engines has demonstrated the direct link between the precombustion flowfield and the combustion process itself. It also revealed that the mechanisms involved in the shaping of the precombustion flowfield and their dependence on the operational and geometric characteristics of the engine are not well understood. The most systematic information of the in-cylinder flows comes from experiments and computational work in simplified model engines but the relevance of these results to practical engine configurations has yet to be demonstrated.

The purpose of the present work is to contribute to the understanding of the in-cylinder flow processes with the further objective to assist the development of more efficient methods for the design of high performance, fuel efficient and clean exhaust gas internal combustion engines. To achieve this purpose an experimental investigation has been carried out with the following specific objectives:

- To investigate the dependence of the induction-generated flow on the geometric and operating characteristics of the intake port/valve assembly and to assess the possibility of its simulation by steady flow tests. The former investigation provides guidelines for better aerodynamic design of the induction system while the latter examines the possibility of testing their performance with simple experiments.

- To examine the effect of the intake flow characteristics on the flowfield near TDC of compression. The results of this investigation provide the link between the design of the induction system and the resulting flow conditions prior to combustion and, when considered together with the aerodynamic performance of the induction system, they assist the optimum overall design of the intake port/valve assembly.

- To bridge the gap between the information available in model and production engines by gradually introducing more realistic features in a basic simplified engine configuration. This approach provides systematic information and in-depth understanding of the individual as well as combined effect of these parameters on the in-cylinder flowfield.

- To compare the results of the simplified engine investigation with similar results obtained in production engines. This helps to quantify the extent to which the conclusions drawn from the model engine investigations can be extrapolated to realistic configurations and provides the basis for the planning of future research.

- To describe the velocity field in model and production engines in sufficient detail for the data to be used as boundary conditions and for the evaluation of the performance of multi-dimensional calculation methods. The combination of the experimental findings with the theoretical analysis leads to better understanding of the in-cylinder flow processes, particularly with respect to turbulence generation and decay mechanisms, and should eventually lead to improvement of both, flow modelling and engine design methods.

The experimental technique selected for the characterisation of the in-cylinder velocity field is laser Doppler anemometry. The LDA optical and signal processing systems are always adjusted to the flow requirements so that the measurements are not limited by system configuration. Various transparent cylinder engines are also developed and the possibility of obtaining detailed velocity field measurements in motored production engines is demonstrated.

1.4 THESIS OUTLINE

The remainder of the thesis is divided into five chapters. Chapter 2 describes an investigation of the flow through a simplified intake port/valve assembly and compares the valve exit and in-cylinder velocity field characteristics under steady and unsteady flow conditions for axisymmetric and three-dimensional flow configurations. The results of this investigation are compared in Chapter 3 with similar measurements obtained in a low speed (200 rpm) model engine and are followed by a study of the effect of the induction-generated flow on the TDC flowfield with various idealised intake port and combustion chamber geometries.

Chapter 4 is devoted to the study of the effect of engine speed on the TDC flowfield which is carried out in a modified production engine with similar geometric characteristics to those of the model engine but motored in the speed range from 300 to 2000 rpm.

Chapter 5 presents an investigation of the flow generated by the helical intake port of a modern production Diesel engine motored at ~900 rpm and compares the results with those obtained in the model engine configuration.

All chapters have a similar structure: the purpose of the specific investigation is first analysed and is followed by a description of the flow configurations examined and the experimental systems used. A detailed analysis of a basic LDA configuration is given in sub-section 2.3.2 of Chapter 2, followed by an extended error analysis in sub-section 2.3.3. The various LDA systems used in the following investigations are described only briefly in the appropriate chapters together with the associated measurement uncertainties. The following sections present and discuss the results of each investigation and, where necessary, a brief summary of the main findings is given at the end of the discussion. All chapters close with a section summarising the main conclusions.

A review of the achievements of the thesis and a summary of the main conclusions is given in Chapter 6 and is followed by a section highlighting the areas which require further research.

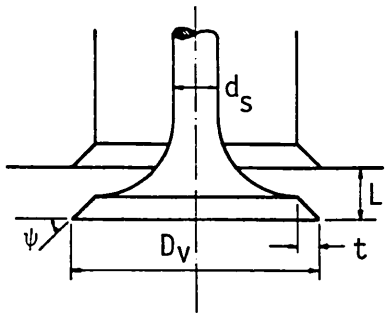

Fig. 1.1 Typical valve geometry and notation

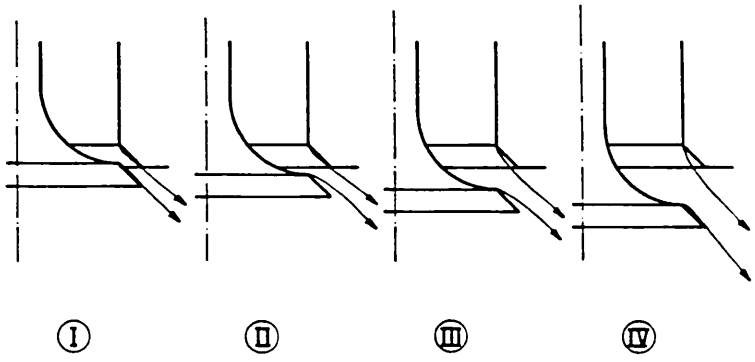

Fig. 1.2 Flow patterns at the valve exit

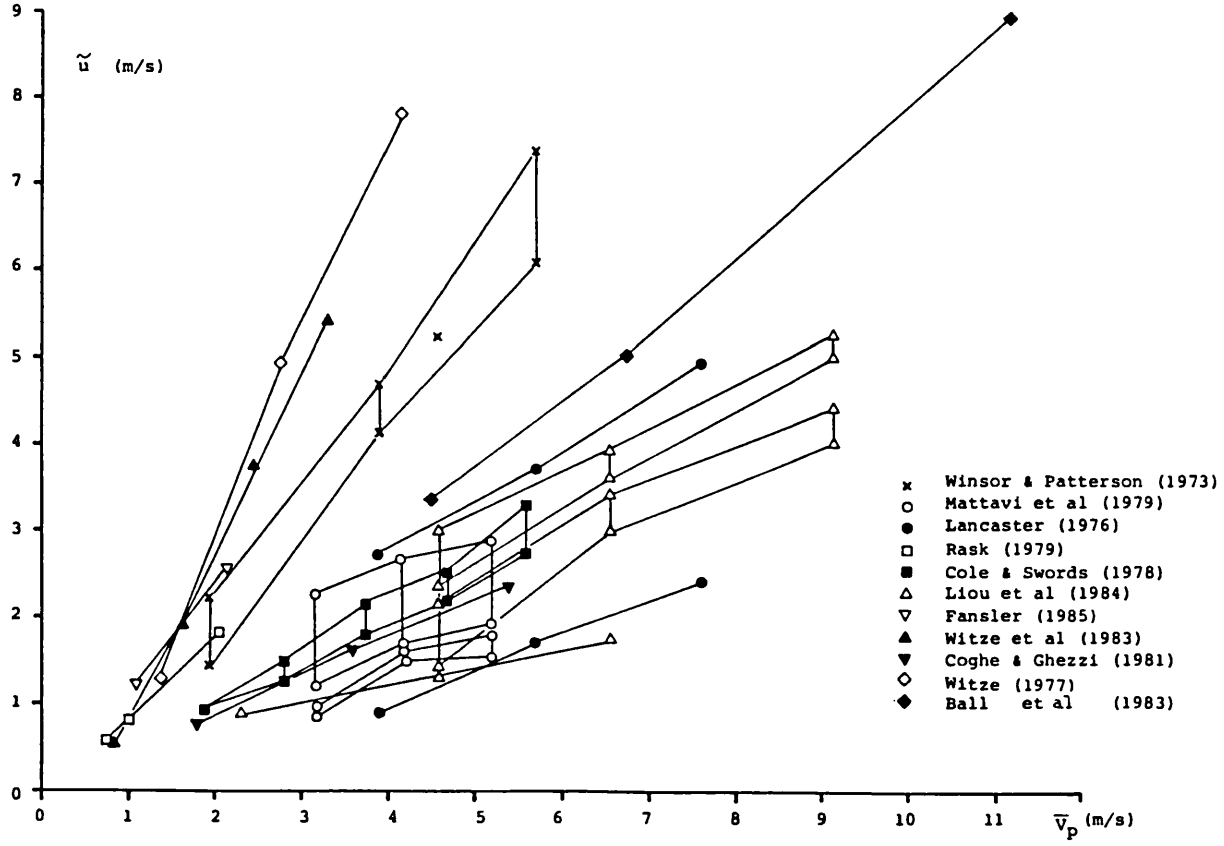

Fig. 1.3 Variation of TDC turbulence intensity with mean piston speed: Previous investigations

CHAPTER 2

INLET FLOW SIMULATIONS

2.1 INTRODUCTION

This chapter describes an experimental investigation of the flow-field at the exit plane and downstream of a stationary valve under steady and unsteady flow conditions, simulating the induction stroke in a simplified model engine. The purpose of these experiments is to quantify the influence of geometric and flow parameters on the flow field at the intake valve, to examine its interaction with the cylinder boundaries and to investigate the relationship between the steady and unsteady flow-field at the exit and downstream of the intake valve.

The performance of two idealised intake valve configurations is studied by means of discharge coefficient and velocity measurements at their exit under steady flow conditions. The valve with the best performance is subsequently tested for the sensitivity of its exit flow-field to the confinement imposed by the cylinder wall in axisymmetric and off-axis valve-cylinder arrangements. The in-cylinder flowfield is characterised in these configurations by three velocity component measurements obtained under both steady and unsteady flow conditions, the latter being imposed by a piston operating upstream of the stationary valve.

The following two sections describe the flow configurations and experimental systems. The results of the steady flow experiments are presented in section 2.4 followed by the results obtained with the unsteady flow configuration in section 2.5. The chapter ends with a summary of the most important findings in section 2.6.

2.2 FLOW CONFIGURATIONS

A versatile experimental rig was constructed for both steady and unsteady flow tests. It consisted of a cylinder followed by an axisymmetric contraction with area ratio 7.5 leading to a short cylindrical section simulating an idealised cylindrical port (Fig. 2.1). The valve

stem was supported by two thin spiders and the valve lift could be adjusted with a simple cam mechanism within 0.01 mm, measured by a dial gauge micrometer. Both the valve seat and valve head were interchangeable to allow the study of various valve/seat geometries. The valve discharged in an open-ended cylinder with 74 mm bore made of cast acrylic with wall thickness of 3 mm and extending downstream as well as upstream of the cylinder head. The cylinder head was fabricated from a thin transparent acrylic sheet of high optical quality and 0.8 mm thickness. This arrangement allowed axial velocity LDA measurements to be performed at the valve exit plane as shown in Figure 2.2 and described in sub-section 2.3.2.

The relative position of the cylinder with respect to the valve axis could be easily changed to simulate off-centre valve geometries or removed to study the behaviour of the isolated valve. Pressure tappings were provided at the cylindrical port, cylinder head and wall for measurements of the wall static pressure.

The above assembly could be mounted on a plenum chamber connected with the compressed air supply for the steady flow tests (Fig. 2.1a) or on top of a reciprocating piston/cylinder assembly, operating at 200 rpm for the unsteady flow tests (Fig. 2.1b).

The two valve/seat geometries examined are shown in Fig 2.3. The first was a typical valve with 45^{o} seat angle and sharp corners and will be referred to as valve Type I; the second was an identical valve but with corners rounded by a 1.8 mm radius at both sealing faces (valve Type II).

In both steady and unsteady flow configurations the valve discharged through the cylinder into atmosphere so that no piston confinement was imposed in either case.

2.3 MEASUREMENT METHODS

2.3.1 Discharge coefficient measurements

The steady flow arrangement (Fig. 2.4) could provide air mass flow rates up to 100 kg/h, controlled by a series of pressure and flow regulators and measured with a standard B.S. orifice meter. Three

orifice plates were used to cover the flow range. The pressure upstream of the orifice was monitored with a single limb mercury manometer and the pressure drop across the orifice was measured either with a Betz micromanometer or a mercury manometer depending on the flow rate. The air temperature was measured inside the settling chamber with a mercury thermometer. The accuracy of the mass flow rate measurements is estimated to be better than 2% as shown in Appendix 2.1. The flow rate was constant with maximum long term variations of 0.4%, while the large settling chamber of 0.6 m^3 almost eliminated short term fluctuations.

The total pressure upstream of the valve was assumed to be equal to the stagnation pressure in the settling chamber and was measured with a Betz micromanometer with an accuracy of 0.1 mmWg, while the static pressure downstream of the valve was assumed to be atmospheric. The measured discharge coefficient of the intake port assembly without the valve head was 0.99 and the wall static pressure measurements in the vicinity of the valve exit gave magnitudes very close to the atmospheric pressure, thus justifying these assumptions with an estimated error of 1% in pressure drop measurement.

The discharge coefficient C_L is defined as the ratio of the measured mass flow rate through the valve to the theoretical isentropic mass flow rate through an ideal nozzle with throat area equal to the valve lift "curtain" area ($\pi.D_V.L$), under the same pressure difference (Appendix 2.2). The theoretical air mass flow rate was calculated according to equation (4) of Appendix 2.2, although the compressibility effects in the flow range of interest were very small.

Some of the results are given as discharge coefficients C_M based on the minimum port area (Appendix 2.2) and comments on this definition are made in sub-section 2.4.1.

The overall accuracy of the discharge coefficient measurements as described above is estimated to be 3%.

2.3.2 Velocity measurements

At least two velocity components were measured in the cylinder space under both steady and unsteady flow conditions with laser Doppler anemometry. Particular emphasis was given to the flowfield at the exit plane of the valve and a special effort was made to measure the axial velocity component along the valve gap. The limitations imposed by the finite intersection angle of the laser beams on the axial velocity measurements at these locations were overcome by passing one of the beams through the transparent cylinder head as illustrated in Figure 2.2. In order to avoid total reflection of this beam from the cylinder head a large beam intersection angle had to be used (see Table 2.1). The resulting Doppler signal, although of good quality, had a reduced visibility of approximately 0.7 due to the lower intensity of the beam crossing the cylinder head. This technique allowed measurements of the axial velocity component to be obtained in the valve gap up to 0.5 mm away from the cylinder head.

A detailed description of the optical configuration of the LDA system and the signal processing system is given in the following paragraphs.

LDA optical system

The laser Doppler anemometer was operated in the dual-beam (fringe mode) forward-scatter mode. The laser source was a 5 mW He-Ne laser (Spectra Physics model 120 S). The laser beam was focused by a plano-convex lens (L_1) onto a rotating diffraction grating (G) (Technisch Physische Dienst, Type H) where it was diffracted into zero-order and pairs of higher order beams. The rotation of the diffraction grating provided a frequency shift between the diffracted beams, proportional to its rotational speed and the diffraction order of the beam. (see Oldengarm et al, 1976). The two first order beams, which contain about 60% of the laser power, were subsequently collimated by a plano-convex lens (L_2) and focused by a similar imaging lens (L_3) to form the intersection (measurement) volume. The imaging lens was changeable to provide the appropriate beam intersection angle and measuring volume dimensions for each particular set of measurements. The light collecting optics comprised a bi-convex lens (L_4) which focused the light scattered by the

TABLE 2.1

Optical characteristics of the laser Doppler anemometer

Laser:	Wavelength, nm		632.8
	Power, mW		5
	Beam diameter at $1/e^2$ intensity, mm		0.8
Lenses:	L_1, focal length, mm	150	100
	L_2	300	300
	L_3	200	300
Beam separation, (s) mm		63	63
Beam intersection half-angle ($\phi/2$), deg.		8.95	5.99
Measurement volume dimensions ($1/e^2$ intensity)			
	diameter, (b_x), μm	100	100
	length, (b_y), μm	635	953
Fringe separation , (d_f), μm		2.034	3.032
Number of stationary fringes, (N_f)		49	32
Frequency to velocity conversion factor, (λ^*), ms^{-1}/MHz		2.034	3.032
Diffraction grating:			
Number of line pairs (N_ℓ)		Track 1:16384	
Line pair width (d_r), μm		6	
Frequency of rotation (f_r), Hz		variable	0 - 200
Frequency shift (1st order beams), (f_s), MHz		variable	0 - 6.55
Receiving optics:			
Collecting lens (L_4), focal length, mm		100	100
Magnification (M)		2.5	2.5
Pinhole diameter (d_{Ph}), mm		0.5	0.5

seeding particles onto a pinhole, located in front of the photo-sensitive area of a photomultiplier tube (PM), (EMI, type 9817 B). An analysis of the optical configuration is given in Appendix 2.3 and the details of the optical system in Table 2.1 and Figure 2.5.

The flow was seeded by 2 μm average diameter silicone-oil particles generated in a blast type atomiser. In the steady flow tests the seeded air was fed into the settling chamber and its flow rate, which was about 1% of the total mass flow rate, was monitored with a rotameter located upstream of the blast atomiser. In the unsteady flow tests the seeding was supplied through a low velocity jet issuing at the exit of the open-ended cylinder.

The transmitting and receiving sections of the LDA system were mounted on a traversing mechanism with three degrees of freedom and allowed scanning of the whole flowfield. The effect of refraction of the laser beams at the curved optical boundaries on the measurement location and beam intersection angle has been taken into account by correcting the results according to the procedure outlined in Appendix 2.4.

Signal processing systems

The output of the photomultiplier was amplified and band-pass filtered in the range 0.5 to 20 MHz by a Harwell 95/2153 - 1/6 amplifier and subsequently high-pass filtered, if necessary, by a variable active filter (Krohnhite, model 3200). The conditioned signal was fed to an oscilloscope (HP 1740 A) and then to a fixed-gate 1 ns resolution frequency counter (HP 5360 A), operating in the "external arming" mode. A combination of the main and delayed time base threshold controls was used to recognise the rising part of the Doppler signal envelope and the gate output pulse of the delayed time base was used to arm the frequency counter and enable it to measure over the selected part of the signal. The measurement duration was selected externally through the counter controls and was monitored on the second channel of the oscilloscope, which was added to the original signal. A detailed analysis of this system, which was used for the steady flow measurements, is given by Durão (1976).

The same counter system was used for the unsteady flow measurements with the additional feature of an optical shaft encoder (Digitech DR 1034) mounted on the crankshaft of the piston/cylinder assembly and providing 1000 pulses per revolution. The pulse train output of the shaft encoder

was processed in a "gating circuit" which provided a "gate pulse" over a preselected and variable crank angle window. This pulse was electronically compared with the delayed gate output pulse of the oscilloscope indicating the presence of an amplitude-validated Doppler burst. When both conditions were met the resulting AND pulse was used to externally arm the frequency counter. This system ensured that only amplitude-validated Doppler signals occurring within the preset crank angle window were processed by the frequency counter.

The frequency counter was interfaced to a 6502 microprocessor-based microcomputer (ITT 2020 or APPLE IIe) where its binary-coded-decimal (BCD) output was processed to yield decimal frequency values. The cycle time of the system was variable from 3 ms upwards. The sampling rate in the steady flow measurements was chosen according to the flow conditions while, in the unsteady flow measurements it was set to ensure that one only measurement was performed within each window. The individual Doppler frequency measurements were processed with the ensemble-averaging method as described in section 1.2.4 to yield ensemble-averaged mean and r.m.s. velocity measurements which, in the steady flow case, correspond to time-averaged quantities. The data processing software also provided the probability density distribution of the measured frequencies. This allowed the sample to be digitally filtered by rejecting the obviously erroneous data. These data usually come from low amplitude signals failing to satisfy the amplitude threshold of the counter and were readily distinguishable by having values an order of magnitude lower than the majority of the data. A typical rejection ratio was 0.5% of the sample size.

A number of cycle-resolved velocity measurements were also performed at the exit of the valve under unsteady flow conditions. For these measurements a purpose-built 10 ns resolution frequency counter was used, interfaced to a microcomputer (ITT 2020). This counter, which is described in detail by Founti (1983), validated the Doppler signals in the amplitude domain (Doppler envelope recognition) as well as in the frequency domain by comparing the frequency information over two overlapping parts of each burst (8/16 cycles comparison). This measurement system had a 80 μs cycle time and allowed for gated measurements through an "external request" input. The software controlling the data acquisition made use of the microcomputer's clock to obtain time-elapsed between Doppler signals, thus providing real-time velocity measurements. The results obtained with this

system are presented as plots of instantaneous velocity against crank angle and are used to illustrate the "cyclic variations" of the unsteady flowfield.

2.3.3 Error sources and measurement uncertainties

A brief analysis of the errors involved in the in-cylinder LDA measurements is made and their contribution to the measurement uncertainty discussed and, when possible, quantified.

A laser Doppler anemometer measures the instantaneous velocity of the seeding particles and assigns this velocity to the fluid by assuming that they accurately follow the flow oscillations. The blast-type atomiser used here, generates silicone-oil droplets with diameters ranging between 1 - 3 μm, (Melling and Whitelaw, 1975). The smaller droplets of this range are known to have a "velocity fidelity" of 97% in frequencies of flow fluctuations of about 10 kHz (Melling and Whitelaw, 1975, Ball et al, 1983). Since most of the turbulence energy during induction is contained in frequencies below 5 kHz (Dent and Salama, 1975) it is concluded that the seeding material used in this study was appropriate and did not introduce errors in the turbulence measurements.

The finite dimensions of the measuring volume may give rise to a broadened and sometimes skewed velocity probability distribution when measuring along a steep velocity gradient. The resulting "velocity gradient broadening" error in the mean and r.m.s. velocity measurements is a function of the size of the measuring volume and the particular velocity distribution and can be estimated according to the procedure described by Melling (1973). This error was minimised here by the small dimensions of the measuring volume used and by positioning its long axis parallel to the velocity gradients. The maximum uncertainty in the mean and rms velocity measurements is expected to be 3 and 10% respectively and to occur only in regions of steep and non-linear velocity gradients.

The uncertainty related to the requirement of the counter-type processors to measure over a finite number of Doppler cycles, which may not always be present (fringe bias), has been discussed extensively by

Buchhave (1979). It can be minimised by increasing the frequency shift and the number of fringes in the measuring volume. In this study most of the velocity measurements were obtained with a "fixed-gate" counter which is less prone to this error than the "fixed zero-crossings" counters. In all cases, however, the frequency shift used was at least twice as large as the maximum Doppler frequency and, according to Buchhave's analysis, this should eliminate the "dead zone" of the measuring volume and consequently the fringe bias.

Velocity bias errors may be present in individual-realisation LDA systems using ensemble-averaging methods for data reduction, since a larger number of high rather than low velocity particles cross the measuring volume over the measurement time. Many theoretical and experimental studies have been carried out in order to quantify this statistical error but their results are often contradictory. Several correction methods have been proposed, such as the one-dimensional correction (McLaughlin and Tiederman, 1973), residence time weighting (George, 1975, Hoesel and Rodi, 1977) and time-averaging (Dimotakis, 1976). Durão et al (1980) suggested that if the sampling time is larger than the particle-arrival time the velocity bias may be minimised. This method, however, does not eliminate the statistical dependence of the sampling process on the presence of a particle. In the present study a comparison was made between the time-averaging method of Dimotakis, using the counter system described by Heitor et al (1984), and the "slow sampling" procedure proposed by Durão et al using the counter system described in sub-section 2.3.2. The maximum differences observed were about 2 and 5% in the mean and r.m.s. velocities respectively in regions of high turbulence intensity. Assuming that the time-averaging results represent a good approximation of the true quantities, the above mentioned differences may be considered to be the maximum uncertainty of the present measurements due to velocity bias in the steady flow experiments. Quantification of this uncertainty in the unsteady flow measurements is not equally simple; it is expected, however, that it should be of similar magnitude.

An important source of error in the window ensemble-averaged measurements in unsteady flows can be the "window-size" or, more appropriately here, "crank angle" broadening (Morse, 1977). This error is equivalent to the velocity gradient broadening but in the time, rather than space, domain and increases with the window size. The effect of

crank angle broadening on the mean and r.m.s. velocity measurements has been experimentally investigated by Arcoumanis et al (1984b) who suggested the use of appropriate crank angle windows ($\Delta\theta$ = 1 - 10^{o}) depending on the particular phase of the engine cycles. The crank angle window used in the present measurements was 1.44^{o} and, according to this analysis, the contribution of the crank angle broadening to the measurement uncertainty should be negligible.

The measurement accuracy of the 1 ns (1 GHz clock) resolution frequency counter, in the range of frequencies encountered, was approximately 0.05% and led to an average systematic error of 2 kHz, equivalent to a negligible error of 0.006 ms^{-1} in terms of velocity. The frequency shift was stable within 0.3% r.m.s. and, in the unsteady flow measurements, the rotational speed of the crank driving the piston/cylinder assembly was constant within ±1%, both leading to negligible errors in the velocity measurements (Melling and Whitelaw, 1976).

The uncertainties introduced by the finite sample size have been theoretically investigated by Yanta (1973). The typical sample size in this study was 1000 data points which, according to Yanta's analysis, allows an estimation of the r.m.s. of the turbulent fluctuations within 4% with a confidence level of 95%. The uncertainty in the estimation of the mean velocity depends on the local velocity fluctuations; for typical relative turbulence intensities of 40 and 10% the corresponding uncertainties are less than 3 and 1% respectively.

The uncertainty of the positioning of the measuring volume in the cylinder space is related to the precision of the traversing mechanism and the dimensions of the measuring volume. The maximum systematic error is estimated to be ±0.05 mm and the corresponding random error 0.3 mm. The error associated with the timing of the measurement system with the reciprocating piston in the unsteady flow measurements is related to the resolution of the optical shaft encoder and the accuracy of its initial setting, and is estimated to be ±0.1%, equivalent to ±0.36^{o} of crank-angle.

Considering the discussion above, the average overall uncertainty of the steady flow velocity measurements is estimated to be less than 3 and 5% for the mean and r.m.s. velocities, respectively. The maximum uncertainty in regions of steep velocity gradients and high turbulence intensity may be up to 5 and 12% respectively. The average uncertainties in the unsteady flow measurements are estimated as 4 and 8% in the mean and r.m.s. velocities with maximum values of 10 and 15% respectively in

areas of steep spatial and temporal velocity gradients and high turbulence intensity.

2.4 STEADY FLOW RESULTS

2.4.1 Discharge coefficient measurements

The air mass flow rate through the valves under investigation has been measured as described in section 2.3.1 and the results are presented in Figure 2.6 as curves of mass flow rate versus valve lift with the pressure drop across the valve as a parameter. Both valves were confined by a cylinder axisymmetrically located with the valve. From these results it can be seen that the flow through valve Type I exhibits four flow regimes indicated by singular points in the flow curves and by changes in curve slope between the change-over points. Valve type II exhibits only two (or three) flow regimes for the same valve lift range and gives larger slope in the first regime, when compared with valve I. The interpretation of these results is similar to that made by Tanaka (1929) and is supported by the radial velocity measurements at the exit plane of the valves, shown in Figure 2.7. In the case of valve I, (Fig. 2.7a) the flow is initially attached to both sealing faces of the valve (not shown here) and this corresponds to flow regime I of Figure 2.6a. For L/D_v greater than 0.1 the flow detaches from the valve sealing face, effectively reducing the actual flow area and thus the slope of the flow curve corresponding to flow regime II. For L/D_v greater than 0.17, as shown in Figure 2.7a, the flow also separates from the seat face and later on ($L/D_v > 0.2$) reattaches on the valve face. The transition from flow regime III to regime IV is not very clear in the flow curves but its existence is proved by the velocity measurements of Figure 2.7a.

From similar velocity measurements for valve II, shown in Figure 2.7b, it can be concluded that the valve with rounded corners exhibits only flow regimes I and IV, with flow regime I sustained up to larger lifts ($L/D_v \simeq 0.15$) when compared with valve I. However, the shape of the flow curve in the region of transition for pressure drops greater than 150 mmWg, (Fig. 2.6b), when compared with the corresponding region for valve I,

Fig. (2.6a), may indicate that a hybrid flow regime exists at large Reynolds numbers, similar to regime III detected with valve II. This shows a smaller dependence of flow pattern on Reynolds number for the valve I, probably due to the well defined detachment points at its sharp edges.

The influence of pressure drop on the flow rate through the valves is shown in Figure 2.8 by normalising the actual mass flow rate with the theoretical isentropic flow rate corresponding to the port area under the same pressure drop (Eqn. (4) of Appendix 2.2). From these results it can be seen that the influence of pressure drop is more apparent in regions of flow transition, as also reported by Kastner et al (1963), especially with valve II.

The discharge coefficient C_L, based on the valve lift area ($\pi.D_v.L$), is shown in Figures 2.9a and 2.9b for valves I and II respectively. Comparing the two figures it becomes clear that the discharge coefficient of valve II is generally higher than that of valve I at low and medium lifts ($L/D_v < 0.15$) with differences up to 15% or more. It can be firmly stated that the rounding of the valve edges improves its discharge coefficient. An increase in pressure drop increases the discharge coefficient and its influence is shown to be stronger at small lifts and low pressure drops as a result of increased contribution of viscous effects under these conditions. For pressure drops greater than 200 mmWg the discharge coefficient curves almost collapse into one. These trends agree with those reported by Kastner et al (1963), Woods and Khan (1965) and Fukutani and Watanabe (1982) but show a greater dependence of the discharge coefficient on pressure drop as they concern lower flow rates.

Figures 2.10a and b show the discharge coefficient C_M, based on the minimum port area as defined in Appendix 2.2, for the two valves under investigation. This discharge coefficient takes values near to or greater than unity and shows a recovery towards high valve lifts. Although the results are still valid, there are two points against the use of C_M. The first applies to the inconvenience of using three equations to describe the minimum port area for the whole range of valve lifts (Appendix 2.2). The second, and probably more important, is the arbitrary assumption that the static pressure at the throat is equal to the pressure downstream of the valve. It is more likely that the pressure at the valve exit plane (as used in the definition of C_L) satisfies better this assumption. This

arbitrary choice must be the reason for the unrealistic values of C_M obtained even with standard (no venturi-type) valves.

In an attempt to validate an assumption, usually made for convenience in the prediction codes, that the flow through the valve can be approximated with a simple function of Reynolds number, the discharge coefficient C_L of valve II is given in Figure 2.11 as a function of Reynolds number based on valve lift (Re_L). The results show that C_L correlates well with Re_L only for non-dimensional lifts (L/D_v) smaller than 0.15. This indicates that the valve behaves almost as an ideal nozzle only as long as the flow is attached to both valve and seat sealing faces. These findings imply that such assumptions should be avoided for predictions in practical engine configurations.

The measurement of the discharge coefficient at a constant pressure drop is performed in order to estimate the actual discharge characteristics of the valve under normal operating conditions. For high speed practical engine configurations these measurements are made with large pressure drops where the discharge coefficient is almost Reynolds independent. In the low speed model engine of interest, however, the Reynolds effects are significant and for this reason an appropriate method to estimate the discharge coefficient of the operating valve should be established. For this purpose the instantaneous mass flow rate through the valve was calculated based on the instantaneous piston speed and on the assumption of incompressible flow. As the valve lift diagram of the specific engine is known a relationship was established between calculated instantaneous mass flow rate and valve lift. The discharge coefficient C_L of valve II was then measured under steady flow conditions and for the appropriate mass flow rate for each lift. The results are shown in Figure 2.12 and, when compared with the lowest curve of Figure 2.9b, show differences up to 8%, especially in the medium lift range, indicating that measurements of the discharge coefficient under a low pressure drop, (here 50 mmWg), overestimate the actual discharge coefficient. However, measurements of the discharge coefficient with a constant mass flow rate of 12 kg/h corresponding to the mean piston speed (Fig. 2.12) revealed that they represent better the "actual" discharge coefficient during both opening and closing periods of the valve, except for very small lifts ($L/D_v < 0.05$) where, as expected, the discharge coefficient is overestimated. This observation also prompted the decision to perform the valve exit velocity

measurements, presented in the following sections, with this constant mass flow rate and for non-dimensional valve lifts (L/D_v) greater than 0.05, ($L > 1.7$ mm).

2.4.2 Velocity field measurements

2.4.2.1 Unconfined valve

Measurements of mean axial and radial velocity components and of the corresponding normal stresses were obtained under steady flow conditions at the exit plane of valve II, mounted on a flat plate and in the absence of cylinder confinement. The velocity measurements were made for valve lifts L = 2,4,5, 6 and 8 mm at a radial distance r = 17 mm from the valve axis to allow the radial velocity component to be measured at the plane containing the valve face. Additional radial velocity component measurements were made inside the valve gap at radial distance r = 14.5 mm. The results are shown in Figure 2.13.

Comparison of the radial velocity distribution at L = 6 and 8 mm with that of Figure 2.7b for the axisymmetrically confined valve shows that flow separation from the seat face is of lesser extent and occurs at larger lift (L = 8 mm) for the unconfined than for the confined valve (L = 6 mm). Further examination of the relative magnitudes of axial and radial velocity components over the valve lift range (Fig. 2.13) indicates that the flow angle varies with valve lift. The flow at small lifts (L = 2 mm) emerges from the valve gap at 45^{o} and later, at L = 4 and 5 mm, deviates towards the cylinder head. Increasing the valve lift at L = 6 mm causes the flow to return at 45^{o} while at larger lifts (L = 8 mm) it separates from the seat face and deviates towards the cylinder axis. This small variation of flow angle is probably due to the entrainment of air from the surroundings in the region between the cylinder head and the valve jet. This effect decreases the pressure in this region causing the flow to deviate towards the cylinder head until it separates from the valve seat. This also explains the delay in flow separation observed with the unconfined valve. The radial velocity components inside the valve gap do not indicate flow separation and reattachment as suggested by Tanaka (1929). Turbulence intensity is relatively low with similar

magnitudes for both normal stresses and the main production of turbulence is observed at the edges of the valve jet.

The results obtained with the unconfined valve indicate that it is not advisable to extrapolate information from an unconfined valve to a confined one, as far as the flow pattern at its exit and the discharge coefficient curves are concerned. This comment emphasizes the observations of Kastner et al (1963) who reported changes in the position of the change-over points of the discharge coefficient curve with valve confinement.

2.4.2.2 Axisymmetrically confined valve

Axial and radial velocity component measurements were also obtained at the exit plane and downstream of the valve II, axisymmetrically confined by a cylinder, for valve lifts L = 2.15, 4.25, 6 and 8 mm. Flow symmetry was examined at z = 15 mm with valve lift L = 8 mm and was found to be better than 5% (Fig. 2.16d).

The velocity distribution measured at the valve exit (r = 17 mm) for the above lifts is given in Figure 2.14. Comparison of the relative magnitudes of the axial and radial velocity components shows similar trends of flow angle variation with valve lift for the confined as with the unconfined valve, described in section 2.4.2.1. The flow initially issues at 45^{o} to the axis, and seems to deviate slightly towards the cylinder head at medium lifts. Once the flow detaches from the valve seat at L = 6 mm, as predicted by the discharge coefficient measurements, it inclines towards the cylinder axis. The velocity vector plots of Figure 2.15 are deduced from the above measurements and indicate that valve II gives a well defined jet-like flow, especially near the valve head, issuing at $\sim 45^{o}$ to the cylinder axis for all practical lifts. In the context of the present study this point was important because it simplified the boundary conditions used in a parallel theoretical investigation. From Figures 2.14 and 2.15 it can be concluded that, although the length of the recirculation region is not small when compared with the valve lift, the amount of recirculating mass is very small with respect to the valve's

outflow. Thus, as the discharge coefficient of the valve is known, the valve flow pattern at high lifts could be approximated by a plug-type velocity distribution at 45^{o} to the axis over a length smaller than the valve lift, as appropriate. Existing computational results (Ahmadi-Befrui et al, 1982) underpredict the maximum velocities during the induction stroke. One possible reason for that could be the lower velocities through the valve used as boundary conditions by assuming the whole valve lift area as effective, (Bicen, 1983).

Figure 2.16 shows the mean axial and radial velocity distribution at the valve face plane (z = L) and further downstream (z = 15 mm) together with the corresponding turbulence intensity for valve lifts L = 2.15, 4.25, 6 and 8 mm. From these results it can be seen that, although the flow at small valve lifts (L = 2.15 mm) issues from the valve at 45^{o} to the axis, it immediately deviates towards the cylinder head as indicated in Figure 2.16a by the relative magnitudes of the axial and radial components at both measurement planes. This stems from the low pressure created by the strong recirculation at the corner of the cylinder head with the cylinder wall. For medium and high valve lifts, L = 4.25, 6 and 8 mm (Figs. 2.16b, c, d) the axial and radial velocity components at the shear layer are of similar magnitude, indicating that the flow is directed at almost 45^{o}, especially at the valve face plane, while a considerable radial spread of the jet is observed further downstream. The length of the recirculation region on the cylinder wall increases with valve lift and the width of the recirculation zone behind the valve at z = 15 mm decreases. Turbulence inside this recirculation zone is almost homogeneous and decreases towards the valve head, where the back flow also decelerates. The main turbulence production occurs at the shear layer around the recirculation zone, where normal stresses are up to ten times larger than those measured at the valve exit plane, indicating that turbulence upstream of the valve is insignificant when compared with that generated during the induction process.

2.4.2.3 Off-centre valve

Similar velocity measurements were obtained with the same intake port located 12 mm off the cylinder axis (Fig. 2.3). The pressure drop across the valve was the same as in the axisymmetric case for all valve lifts and a constant flow rate of 12 kg/h, indicating that the discharge coefficient of the off-centre valve was unaffected by wall proximity, as suggested by Kastner et al (1963) and Woods and Khan (1965). The velocity results were obtained at three radial planes perpendicular to each other (planes 0^{o}, 90^{o} and 180^{o} in Fig. 2.3). The axial flow field on the 90^{o} plane was tested for symmetry at z = 20 mm and L = 4.25 mm and was found to be satisfactory (Fig. 2.19d).

The mean axial and radial velocity distribution and the corresponding normal stresses measured at the exit plane of the valve at the three radial planes are presented in Figures 2.17a, b, c and d for valve lifts L = 2.15, 4.25, 6 and 8 mm respectively. For small and medium lifts (L = 2.15 and 4.25) it can be seen (Fig. 2.17a, b) that the radial velocities tend to decrease with wall proximity while the axial velocities increase. This effect of wall proximity should be expected as the flow issuing from the valve tries to accommodate itself in the imposed boundaries, affecting also the upstream flow at the valve exit. For larger valve lifts (L = 6 and 8 mm, Figs. 2.17c, d), where separation of the flow from the seat face has already occurred, the cylinder wall influences the recirculation at the valve seat. The reverse velocities at the valve exit and the length of the recirculation region increase with wall proximity. The flow direction is less affected and remains roughly 45^{o} to the axis for L = 6 mm and slightly less for L = 8 mm, as also observed in the axisymmetric case. The results obtained with the axisymmetric configuration, (Fig. 2.14), compare well with those obtained on the 90^{o} plane in the off-centre configuration as the distance of the valve from the wall is comparable for the two cases.

Detailed measurements of the three velocity components were made at the valve face plane (z = L) for a valve lift L = 4.25 mm and are presented in Figure 2.18. The valve jet direction at this axial plane varies with wall proximity with the maximum deviation from the 45^{o} angle on the 90^{o} plane where the radial component is much higher than the axial The flow structure at the corner of the cylinder head is complex and

consists of a recirculation region whose length and strength vary with wall proximity, as shown in Figures 2.18a, b. The tangential velocity distribution at the 90^{o} plane (Fig. 2.18e) shows minimum velocities near the valve exit and a local minimum at the point of reversal of the axial flow. The vector addition of the axial with the corresponding radial velocities (Fig. 2.18d) indicates that the flow from the valve is initially directed towards the wall and then progressively deviates towards the cylinder axis (Fig. 2.18f). This mechanism creates a vortical flow pattern further downstream of the valve (Fig. 2.19) consisting of two counter-rotating vortices on the tangential plane, (Fig. 2.19c), superimposed to the two toroidal vortices on the axial planes (Fig. 2.19a).

Similar results are presented in Figures 2.20a, b and c for valve lifts L = 2.15, 6 and 8 mm at z = 15 mm respectively. The general flow pattern remains essentially the same for all valve lifts with differences in velocity magnitudes and recirculation regions size. The corner vortex at the valve head increases in length with valve lift on the 90^{o} plane where the radial velocities are higher than the axial indicating that the low pressure in the corner vortex region forces the flow to deviate towards the cylinder head. In contrast, the valve jet in the 180^{o} plane deviates towards the cylinder axis as a result of higher pressures in this region due to the lower velocities in the corner vortex. This effect becomes more apparent with increasing valve lift. For all valve lifts the small magnitude of radial velocity component measured near the wall on the 0^{o} plane indicates that although the flow emerges from the valve at 45^{o} to the axis it quickly turns to become parallel to the cylinder wall. The radial velocity component inside the wake of the valve goes to zero near the cylinder axis rather than near the valve axis, as would probably be expected. This shows that the presence of the cylinder wall affects the radial velocity distribution, especially at small valve lifts where the valve jet velocity is high.

Turbulence inside the wake of the valve is near homogeneous as the three normal stresses are of similar magnitude and uniformly distributed. Turbulence intensity at the shear layers around the wake of the valve increases with decreasing valve lift due to the steeper velocity gradients associated with the higher jet exit velocities. This also leads to higher normal stresses inside the wake as a result of turbulent diffusion.

2.5 UNSTEADY FLOW RESULTS

The intake port/valve configurations described in the previous section were also examined under unsteady flow conditions. The flow was pulsating by means of a piston operating upstream of the valve which discharged in the open-ended cylinder as described in section 2.2. Although the piston motion was almost sinusoidal (see Fig. 3.6) and its instantaneous speed over half a cycle was roughly symmetric around its maximum value, the air velocity through the valve was not, as indicated by the cycle-resolved velocity measurements shown in Figure 2.21. This is due to the compressibility of the air and the relatively large air volume between the piston face and valve exit which led to a phase lag between instantaneous piston speed and valve exit velocity. The results were obtained at three different instants in the cycle covering the accelerating and decelerating periods of the flow, as indicated in Figure 2.21, and will be referred to as early, mid- and late induction.

2.5.1 Axisymmetrically confined valve

The velocity distribution measured at the exit plane of the valve is shown in Figures 2.22a, b, c and d for valve lifts L = 2.15, 4.25, 6 and 8 mm respectively. As can be seen from Figures 2.22c and d, the length of the recirculation region at the seat face changes slightly from early to mid-induction probably due to Reynolds number effects related with the curvature of the rounded corners, as already shown by the discharge coefficient measurements. Surprisingly the magnitude of the reverse velocities does not scale with the instantaneous bulk velocity but the mean flow pattern remains similar throughout the cycle. The normal stresses increase towards mid- and late induction especially for the larger valve lifts due to the gradual development of the flow through the valve passage to fully turbulent. This is also apparent in the cycle-resolved measurements of Figure 2.21.

Comparison of the above results with those obtained under steady flow conditions (Fig. 2.14) shows that both radial and axial velocity

distributions at the valve exit are similar for both cases especially at mid-induction and large lifts where even the recirculation region near the valve seat is almost identical for the steady and unsteady flow configurations. Normal stresses, however, are generally lower for the unsteady flow case reaching values similar to those of the steady flow towards mid-induction, where the instantaneous Reynolds number is closer to that of the steady flow configuration. Thus the velocity distribution at the exit plane of a valve under unsteady flow conditions can be predicted adequately from steady flow experiments provided that the appropriate Reynolds number is used for the steady flow tests. These results, however, were obtained in a low speed engine. Possible resonance and chocking effects in the intake port of a high speed engine may reduce the accuracy of the corresponding steady flow simulation. The overprediction of normal stresses at the valve exit is not considered to be very significant as the main production of turbulence takes place downstream of the valve as discussed earlier.

Axial velocity components were measured downstream of the valve at z = 15 mm for two medium valve lifts L = 4.25 and 6 mm and at early, mid- and late induction. The results are presented in Figure 2.23 and show that the velocity distribution in the wake of the valve at early induction is different from that later in the stroke, apparently due to residual effects from the previous (exhaust) stroke and to the delay of the development of the wake behind the valve. Comparison of the mean velocity distribution at mid-induction with the corresponding steady flow results (Figs. 2.16b, c) shows a general similarity, especially for the larger valve lift. The axial normal stresses, however, inside the wake of the valve are lower although their magnitudes at the shear layer are comparable. In addition the axial normal stresses in the wake of the valve increase by up to four times from early to late induction. These two observations lead to the conclusion that turbulence produced in the shear layer takes time to diffuse inside the wake. (Roughly 100^{o} of crank angle, or 80 ms, to become comparable with the normal stresses measured under steady flow conditions). The same phenomenon is shown in Figures 2.24 and 2.25 by cycle-resolved and temporal ensemble-averaged axial velocity measurements, which also illustrate the residual effects of the previous stroke up to crank-angle $\theta = 30^{o}$ of induction. As

can be seen from these figures the turbulence intensity on the centre-line is constant and low during early induction and starts increasing 80 crank angle degrees after the start of the stroke reaching a maximum at late induction.

By comparing the relative magnitudes of axial and radial velocity components in the same axial plane (z = 15 mm, Figs. 2.23 and 2.26) for the two valve lifts at mid-induction, it is concluded that the flow emerges from the valve at 45^{o} to the axis and deviates further downstream towards the cylinder head. This observation does not agree with the corresponding results under steady flow conditions, (sub-section 2.4.2.2, Fig. 2.16b, c), indicating that this is a feature of the transient flow field consistent with the development of the corner vortex at the cylinder head. In addition the radial normal stresses inside the wake of the valve are up to 25% lower than the axial ones, while under steady flow conditions and for the same valve lifts they were found to be almost equal.

The results obtained downstream of the valve under unsteady flow conditions indicate that, although the unsteady flow at the valve exit can be accurately predicted by steady flow measurements, the flow characteristics downstream of the valve cannot. The reason for that is the residual effects of the previous (exhaust) stroke and the developing nature of the transient flow.

2.5.2 Off-centre valve

The off-centre valve geometry was tested under similar unsteady flow conditions and, as expected from the results obtained with the axisymmetric geometry, no significant difference was found between steady and unsteady flow at the exit plane of the valve. In fact the radial velocity component measurements obtained with valve lift L = 6 mm during mid-induction at the 0^{o} and 180^{o} planes, (Fig. 2.27), when compared with the corresponding steady flow results, (Fig. 2.17c), show very good agreement in both mean and turbulent velocity distributions.

Three velocity components were measured downstream of the valve (z = 15 mm) on the three azimuthal planes for valve lifts L = 4.25 and

6 mm at mid-induction (Figs. 2.29b and 2.30) as well as at early induction with the 2.15 and 4.25 mm valve lifts, (Figs. 2.28 and 2.29a). The mean axial velocity distribution at early induction for valve lifts L = 2.15 and 4.25 mm shows significant differences from the corresponding steady flow results. The velocity distribution inside the wake of the valve is characteristic of the early induction as found in the axisymmetric geometry and the corner vortex on the 180^{o} plane is larger than in the steady flow configuration. The radial velocity distribution for valve lift L = 4.25 mm, when compared with the corresponding axial velocities, shows that the valve jet has a similar trajectory as under steady flow conditions on the 0^{o} and 180^{o} planes but not on the 90^{o} plane, where its direction is almost 45^{o}. Radial velocities inside the wake of the valve are near zero and normal stresses significantly lower than the corresponding under steady flow conditions and uniformly distributed.

At mid-induction with the 4.25 mm valve lift (Fig. 2.29b) the axial and radial velocity distributions show greater similarities with the steady flow case on the 0^{o} and 180^{o} planes but again not on the 90^{o} plane, where the axial velocity component is now much larger than the radial. The size of the corner vortex at the cylinder head on the 180^{o} plane has now decreased and the valve jet has deviated more towards the cylinder axis. Radial velocities inside the wake of the valve increase significantly and go to zero nearer to the valve axis rather than near the cylinder axis as would be expected from the steady flow results. The tangential flow pattern, being a result of complex interaction of the valve jet with the cylinder wall, shows greater dependence on the axial flow development as indicated by the differences in tangential velocity distributions between early and mid-induction. Turbulence is not homogeneous inside the wake of the valve, where the radial and tangential normal stresses are generally lower than the axial ones, as also found with the axisymmetric geometry. Additionally there is a trend for higher radial and tangential normal stresses towards the shear layer on the 180^{o} plane which, when compared with the corresponding steady flow results, indicates that an equilibrium state has not yet been achieved at mid-induction.

Finally, for a valve lift L = 6 mm at mid-induction (Fig. 2.30) the comparison between steady and unsteady flow improves. The main differences lie in the magnitude of normal stresses which are generally lower than those under steady flow conditions but uniformly distributed inside the wake of the valve.

From the above results it can be concluded that the three-dimensional flowfield downstream of a valve under unsteady flow conditions is not accurately represented by steady flow tests. The differences in the mean flowfield decrease with increasing valve lift and towards mid-induction. The tangential flow pattern shows greater differences than the axial one and the normal stresses are generally lower under unsteady flow conditions.

2.6 CONCLUSIONS

The pressure drop and velocity field measurements obtained under steady and pulsating flow conditions through a stationary intake valve revealed the following:

1. Four different flow regimes have been identified over the useful valve lift range of a typical intake valve. Rounding of the sharp edges of the valve resulted in fewer flow regimes and significant overall improvement of its discharge coefficient. The transition from one flow regime to another was affected by cylinder confinement and pressure drop across the valve. The influence of pressure drop on discharge coefficient was found to be greater at low pressure drops and small valve lifts. Under these conditions the discharge coefficient increased with pressure drop up to an asymptotic value.

2. The direction of the flow at the exit plane of the valve was influenced by valve lift and cylinder confinement. The distance of the cylinder wall from the off-centre valve influenced the size and strength of the vortex at the corner with the cylinder head and affected the velocity distribution and flow angle at the valve exit but did not alter its discharge coefficient.

3. The mean velocity distribution and the flow angle at the exit plane of the stationary valve under unsteady flow conditions were found to be accurately predicted by steady flow tests for both the axisymmetric and off-centre valve configurations. The agreement of these results was better when the instantaneous Reynolds number of the unsteady flow was closer to that of the steady flow tests. Normal stresses, however, were generally lower under unsteady flow conditions and increased towards the end of the induction stroke.

4. The comparison of the mean flowfield downstream of the valve under steady and unsteady flow conditions was not satisfactory, especially at early induction. The residual effects from the previous stroke and the developing nature of the transient flow influenced the development of the corner and valve vortices which also affected the valve jet direction. Normal stresses downstream of the valve were found to be lower in the unsteady flow case increasing towards late induction.

These results were obtained in steady and unsteady flow configurations simulating the induction stroke in a low speed model engine where the valve flow was still Reynolds dependent. The validity of the "quasi-steady" assumption for the valve flow was confirmed at this low engine speed; this conclusion, however, should not be extrapolated to higher engine speeds where inertia and compressibility effects may become important. Finally, the interaction of the valve jet with the downstream reciprocating piston and the effect of valve operation on the flowfield at its exit have still to be investigated in order to determine the extent to which the valve exit flow under engine operating conditions can be simulated by steady flow tests. This investigation is presented in section 3.3 of the following chapter.

APPENDIX 2.1

Error analysis of the flowrate measurements

The maximum error in the air mass flowrate measurements is estimated according to the procedure of B.S. 1042 (1964). The working equation for the measurement of mass flow rate with an orifice meter is

$$\dot{m} = K.C.z_R.z_D.\varepsilon.E.d^2\sqrt{h\rho}$$

The overall error X_m in the mass flow rate measurement is thus given by:

$$X_m = \left[X_c^2 + X_{zR}^2 + X_{zD}^2 + X_\varepsilon^2 + \left(\frac{2}{1-\mu^2}\right)^2 X_d^2 + \left(\frac{2\mu^2}{1-\mu^2}\right)X_D^2 + \frac{1}{4}(X_h^2 + X_\rho^2)\right]^{1/2}$$

Where

X_c = ±0.7% : Error in the discharge coefficient of the orifice
X_{zR} = ±0.3% : Error in the Reynolds number correction factor
X_{zD} = ±1.0% : Error in the pipe size correction factor
X_ε = ±0.2% : Error in the expansibility factor
μ : Area ratio of orifice meter
X_d = ±0.05%: Error in orifice size
X_D = ±0.8% : Error in pipe size
X_h = ±1.0% : Maximum error in pressure drop measurement
X_ρ = ±0.5% : Error in air density calculation.

Thus, the maximum error in the mass flowrate measurement is estimated to be:

$$X_m \simeq \pm 1.3\%$$

APPENDIX 2.2

Calculation of discharge coefficient

The integrated form of the Bernoulli equation for frictionless adiabatic (i.e. isentropic) discharge from a reservoir where conditions are given by p_o. ρ_o, T_o ($V_o = 0$) through a nozzle for subsonic flow is:

$$\frac{V^2}{2} = \frac{\gamma}{\gamma - 1}\left(\frac{p_o}{\rho_o} - \frac{p}{\rho}\right) \tag{1}$$

where p, ρ and V the static pressure, density and velocity of the fluid at any section of the nozzle and are related to the initial conditions for the adiabatic process as:

$$\rho = \left(\frac{p}{p_o}\right)^{1/\gamma} \cdot \rho_o \tag{2}$$

Given the continuity equation:

$$\dot{m}_i = \rho.V.A \tag{3}$$

where A the area of the corresponding section, the three equations above reduce to:

$$\dot{m}_i = A.\sqrt{2.p_o.\rho_o \frac{\gamma}{\gamma - 1}\left(\frac{p}{p_o}\right)^{2/\gamma} \cdot \left[1 - \left(\frac{p}{p_o}\right)^{\gamma-1/\gamma}\right]} \tag{4}$$

giving the isentropic mass flowrate discharging from a reservoir with stagnation conditions p_o, ρ_o through a nozzle where the static pressure at a cross section A is p.

The discharge coefficient, C, of a nozzle is defined as the ratio of the actual mass flow rate to the theoretical under identical pressure ratio $(\frac{p}{p_o})$. (Or pressure difference, $(p_o - p)$, if the downstream static pressure is constant):

$$C = \frac{\dot{m}}{\dot{m}_i} \tag{5}$$

where $\dot{m}$ is the actual mass flowrate.

For the calculation of the isentropic mass flow rate the area A must be chosen. In the case of a valve this choice varies considerably (e.g. port area, valve head area, valve lift area and minimum port area).

The discharge coefficient C_L, used in this study is based on the valve lift ("curtain") area:

$$A_L = \pi . D_v . L \tag{6}$$

A comparison is also made with the discharge coefficient C_M, based on the minimum port area A_M. For a 45^o seat-angle valve the minimum port area is given by the following equations for the whole valve lift range:

For $0 < L \leq 2t$

$$A_M = \pi \frac{L}{\sqrt{2}} \left(D_v - \frac{L}{2}\right) \tag{7a}$$

For $2t < L \leq t + \sqrt{\left[\frac{(D_v - 2t)^2 - d_s^2}{4(D_v - t)}\right]^2 - t^2}$

$$A_M = \pi (D_v - t) \sqrt{L^2 + 2t^2 - 2Lt} \tag{7b}$$

For $t + \sqrt{\left[\frac{(D_v - 2t)^2 - d_s^2}{4(D_v - t)}\right]^2 - t^2} < L$

$$A_M = \frac{\pi}{4} \left[(D_v - 2t)^2 - d_s^2\right] \tag{7c}$$

APPENDIX 2.3

Optical characteristics of LDA systems

a) Diffraction grating optics (Fig. A1)

λ	laser wavelength
b_o	laser beam diameter at $1/e^2$ intensity points
f_1, f_2, f_3, f_4	focal lengths of lenses L_1, L_2, L_3, L_4
m	order of diffracted beam ($0, \pm1, \pm2, \ldots$)
d_r	line-pair width of the grating
$\theta_m = \arcsin(m\lambda/d_r)$	m-order diffraction angle
$b_o' = b_o(f_2/f_1)$	beam diameter after lens L_2
$s = 2f_2\tan\theta_m$	m-order beam separation
ϕ	beam intersection angle
$b_x = 4\lambda f_3/\pi . b_o'\cos(\phi/2)$	diameter of measurement volume at $1/e^2$ intensity points
$b_y = b_x/\tan(\phi/2)$	length of measurement volume at $1/e^2$ intensity points
$d_f = \lambda/2\sin(\phi/2)$	fringe separation in the measurement volume
$N_f = b_x/d_f$	number of stationary fringes
$\lambda^* = \lambda/2\sin(\phi/2)$	frequency to velocity conversion factor
f_r	frequency of rotation of the diffraction grating
N_ℓ	number of line pairs on the grating
$f_s = 2mN_\ell f_r$	frequency shift between the $\pm$m-order beams
$M = \frac{b}{a}$	magnification of collecting optics (L_4)
d_{Ph}	pinhole diameter

b) Bragg-cell optics (Fig. A2)

E	beam expansion ratio (here $E = 1$)
$b_o' = Eb_o$	beam diameter after the beam splitter
Λ	ultrasonic wavelength in the Bragg-cell
$\theta_B = \arcsin(\lambda/2\Lambda)$	Bragg-angle
$b_x = 4f_3\lambda/\pi b_o'\cos(\phi/2)$	diameter of measurement volume at $1/e^2$ intensity points

$b_y = b_x/\tan(\phi/2)$ length of measurement volume at $1/e^2$ intensity points

- Other parameters as above.

The doppler frequency f_D of the light scattered by a particle crossing the measurement volume is proportional to the magnitude of its instantaneous velocity component which lies on the plane of the beams, normal to the bisector of their angle of intersection (U_N). The relationship between velocity and light frequency shift, f, (including possible frequency shift, f_s, of the intersecting beams), is given by:

$$U_N = \lambda * f_D = \lambda * (f - f_s)$$

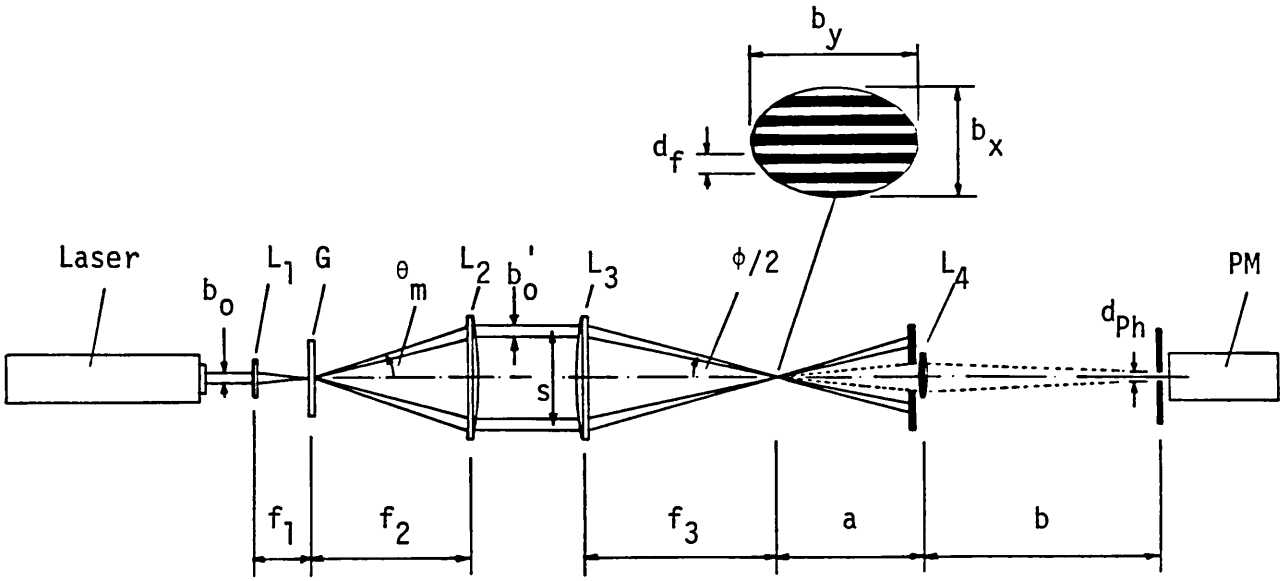

Fig. A1 Schematic of the diffraction grating LDA optics

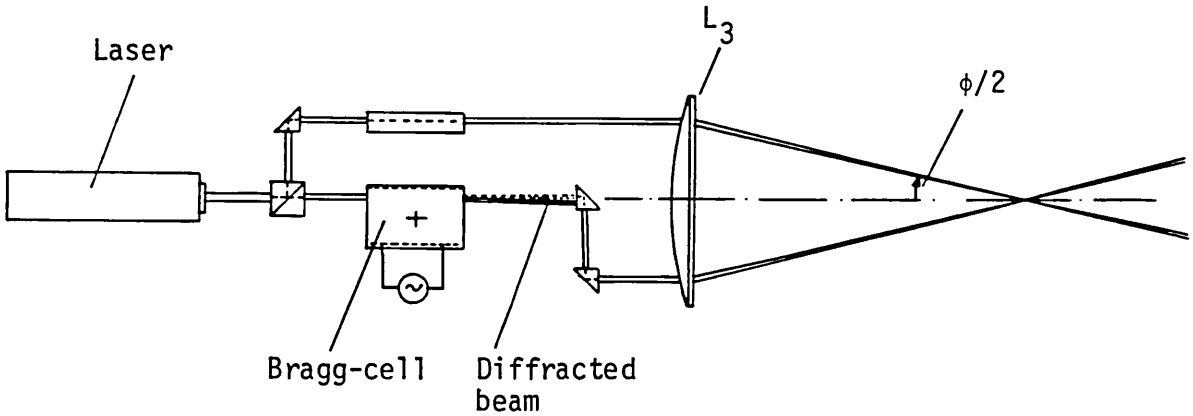

Fig. A2 Schematic of the Bragg-cell LDA optics

APPENDIX 2.4

Refraction corrections for cylindrical optical boundaries

The actual position (x_N, y_N) of the measuring volume inside the engine cylinder is calculated from the position of the optical system (x, y) relative to the cylinder axis as follows:

1 - Tangential plane (V, W components, Fig. A3)

$$\tan k = \frac{y}{x}$$

$$r = \sqrt{y^2 + x^2}$$

$$\sin a_{f1} = \frac{\sin(a_a - k)}{R_1} r$$

$$\sin a_{f2} = \frac{\sin(k - a_a)}{R_1} r$$

$$\frac{\sin a_{f1}}{\sin a_{w1}} = \frac{\sin a_{f1}'}{\sin a_{w1}'} = \frac{n_w}{n_a} \qquad \frac{\sin a_{w1}}{\sin a_{w2}} \equiv \frac{\sin a_{w1}'}{\sin a_{w2}'} = \frac{R_2}{R_1}$$

$$\frac{\sin a_{w2}}{\sin a_{f2}} = \frac{\sin a_{w2}'}{\sin a_{f2}'} = \frac{n_f}{n_w}$$

$$\sigma = a_a + (a_{f1} - a_{w1}) - (a_{f2} - a_{w2})$$

$$\rho = a_a - (a_{f1}' - a_{w1}') + (a_{f2}' - a_{w2}')$$

$$\phi = \sigma + \rho$$

$$\frac{1}{\tan\theta} = \frac{1}{\sin\phi} \left(\frac{\sin a_{f2}}{\sin a_{f2}'} + \cos\phi\right)$$

$$r' = R_2 \frac{\sin a_{f2}'}{\sin \theta}$$

$$k' = - a_a + a_{f1}' - a_{w1}' + a_{w2}' - a_{f2}' + \pi - \theta$$

$$y_N = r'.\sin k'$$

$$x_N = r'.\cos k'$$

From the above relations the actual position of the measuring volume (x_N, y_N), the actual beam intersection angle (ϕ) and the angle of the sensitivity vector (σ, ρ) can be calculated.

2 - Plane parallel to the axis (U component, Fig. A4)

$$\tan a_{f1} = \frac{y}{R_1}$$

$$\frac{\sin a_{f1}}{\sin a_{w1}} = \frac{n_w}{n_a} \qquad \frac{\sin a_{w1}}{\sin a_{w2}} = \frac{R_2}{R_1} \qquad \frac{\sin a_{w2}}{\sin a_{f2}} = \frac{n_f}{n_w}$$

$$\rho = (a_{f1} - a_{w1}) - (a_{f2} - a_{w2})$$

$$t' = R_2 . \frac{\sin(a_{w2} - a_{w1})}{\sin a_{w1}} . \cos(a_{f1} - a_{w1})$$

$(t' = R_1 - R_2 \quad \text{for} \quad y = 0)$

$$t = R_1 - R_2$$

$$A = \sqrt{\frac{n_f^2}{n_a^2} - \sin^2 a_a} \qquad B = \sqrt{\frac{n_w^2}{n_a^2} - \sin^2 a_a}$$

$$d_e = (1 - \frac{A}{B}).(t' - t)$$

$$x_N = x - d_e$$

$$y_N = R_2.\sin(\rho - a_{f2}) - | R_2 \cos(\rho - a_{f2}) - x_N | .\tan \rho$$

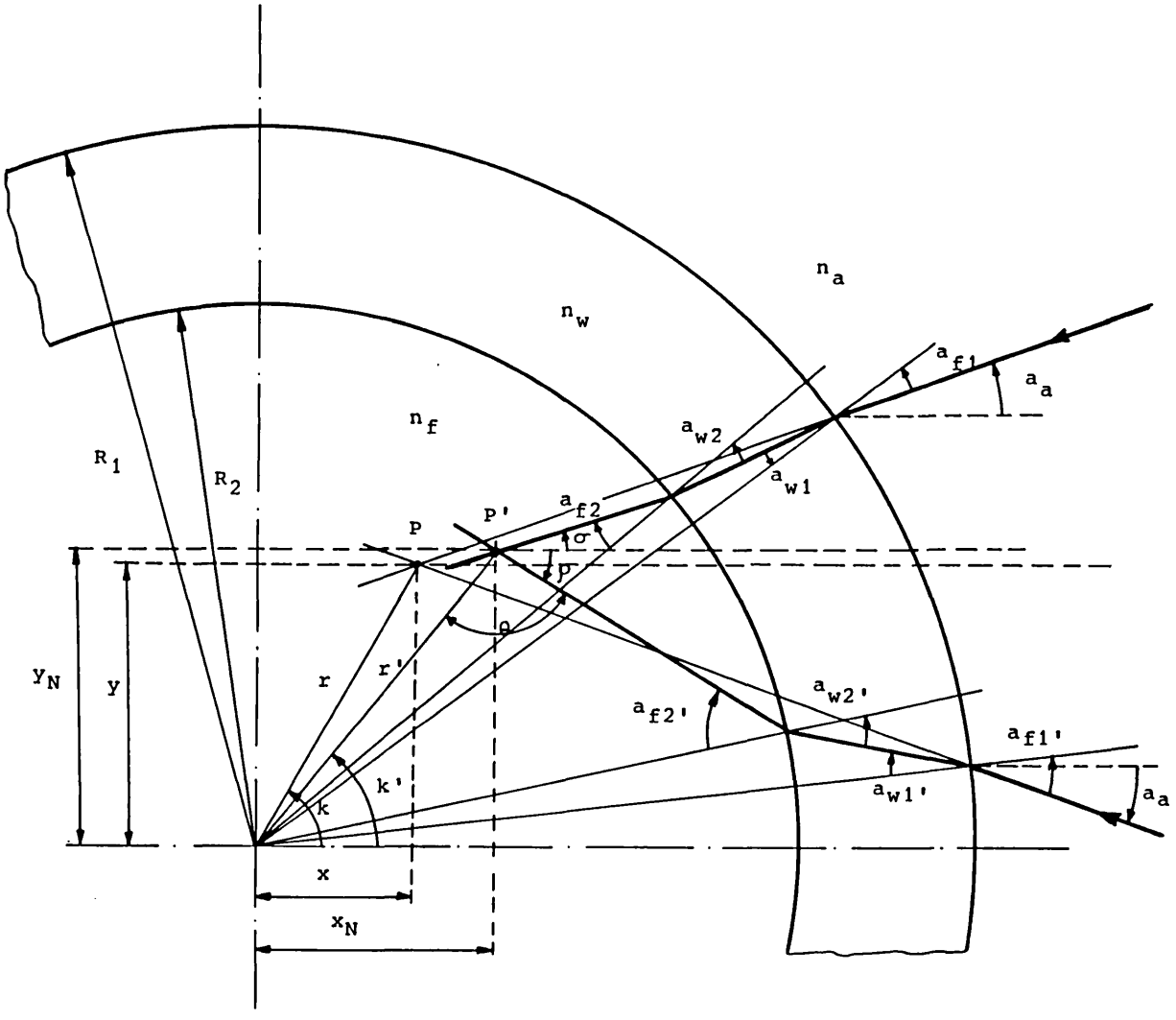

Fig. A3 Refraction of the laser beams on a plane normal to the cylinder axis

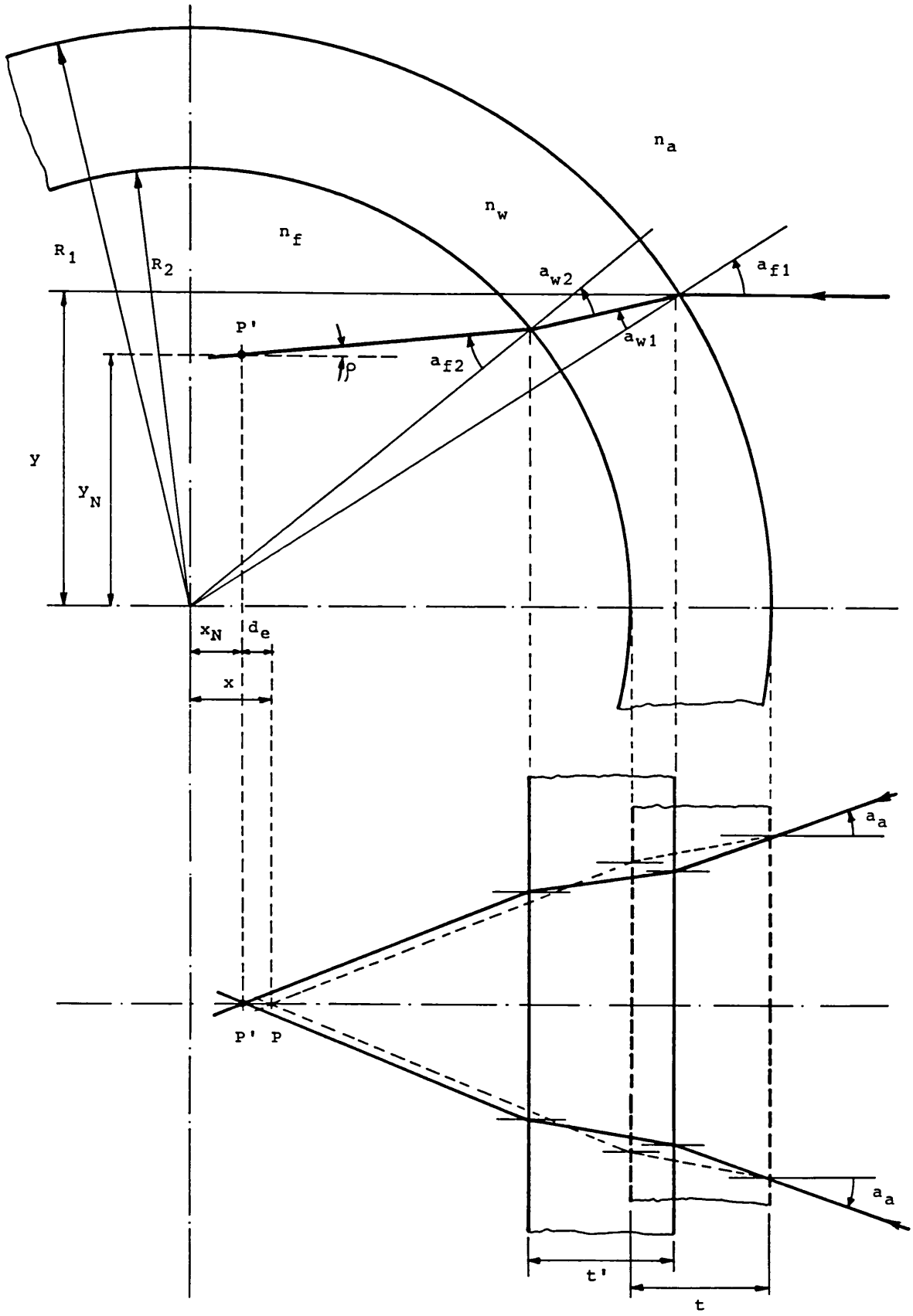

Fig. A4 Refraction of the laser beams on a plane parallel to the cylinder axis

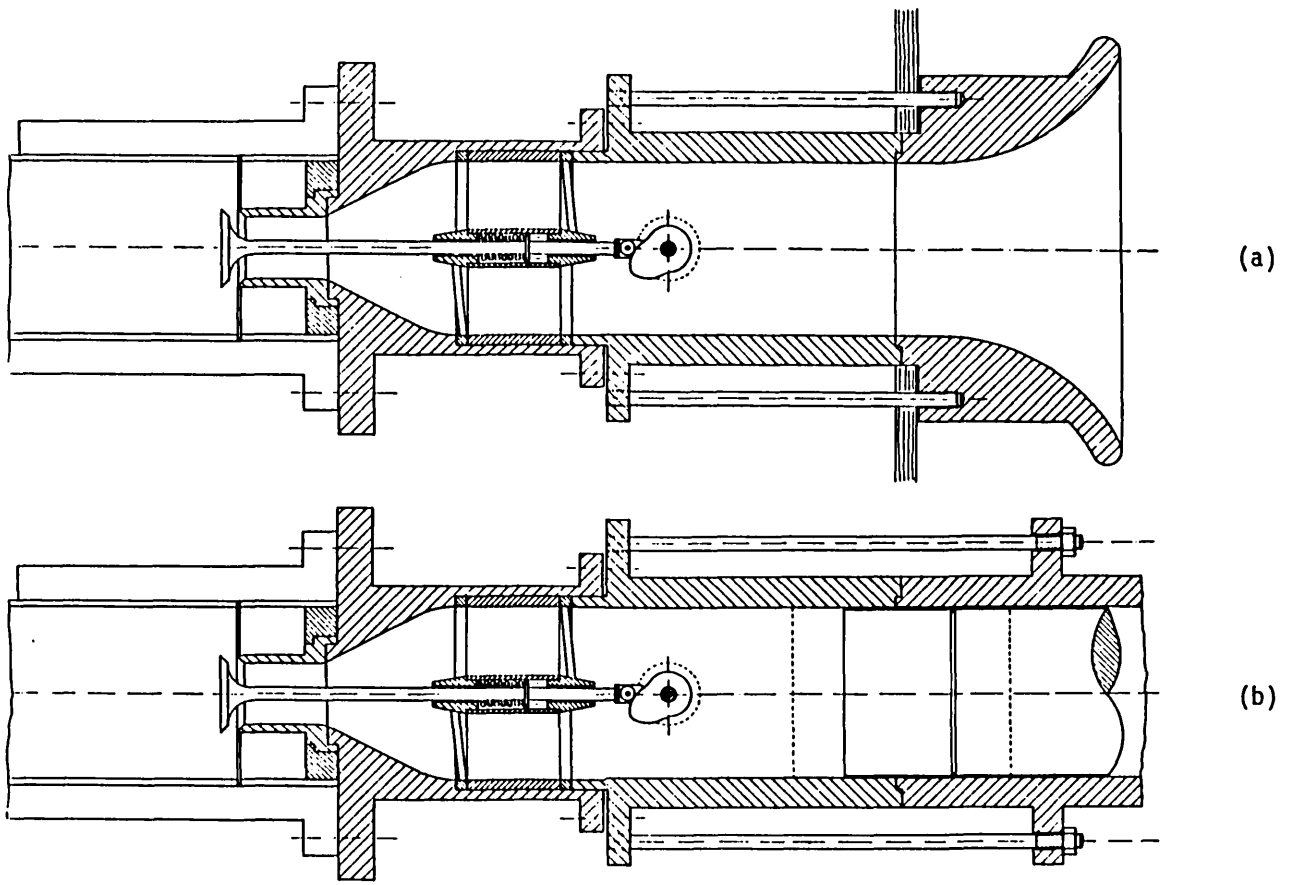

Fig. 2.1 Steady (a) and unsteady (b) flow rigs

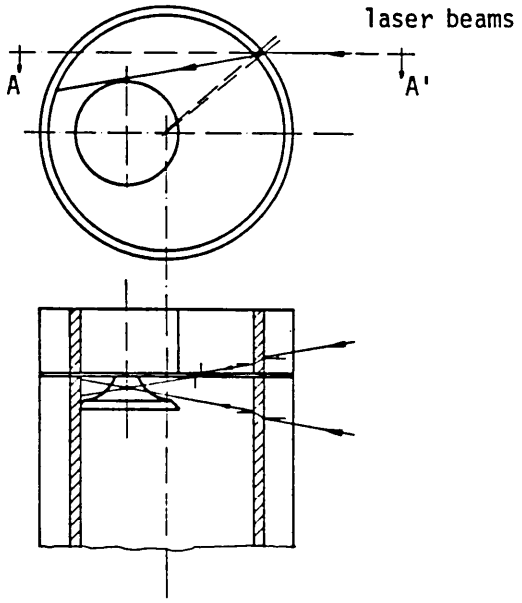

Fig. 2.2 Optical access to the valve gap

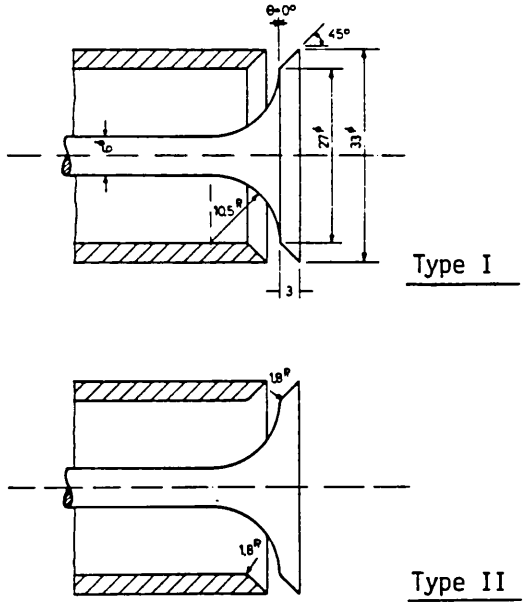

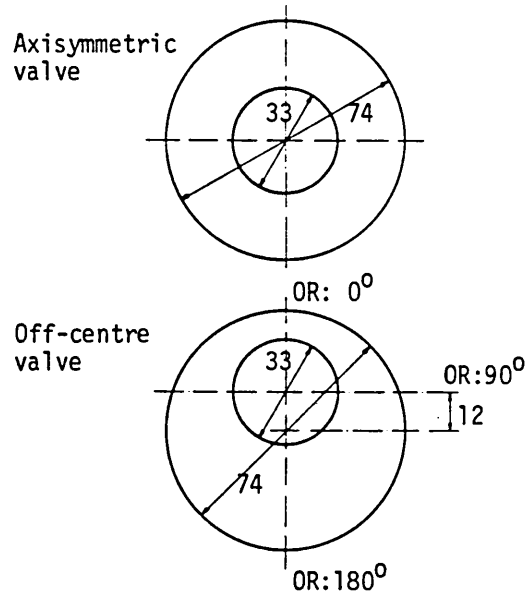

Fig. 2.3 Valve geometries and location; definition of measurement planes

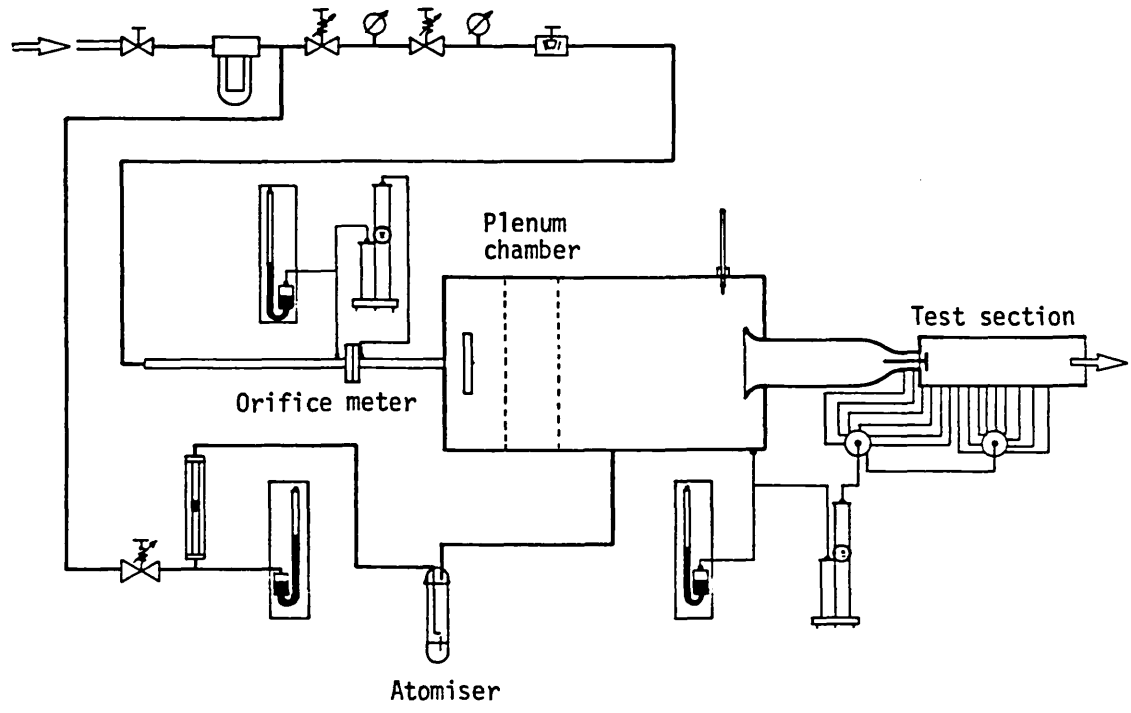

Fig. 2.4 Schematic diagram of the steady flow rig

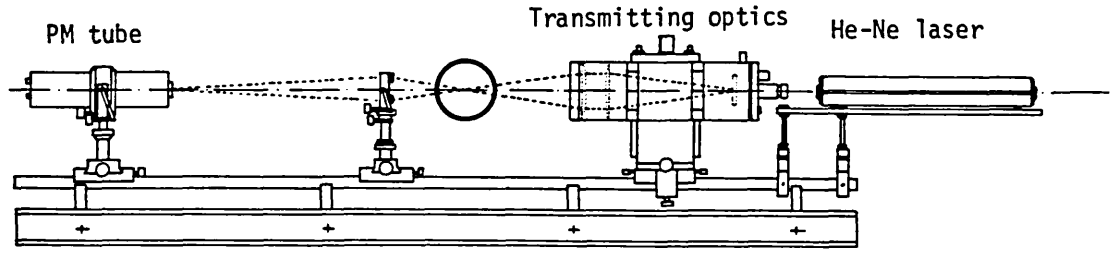

Fig. 2.5 General arrangement of the laser Doppler anemometer

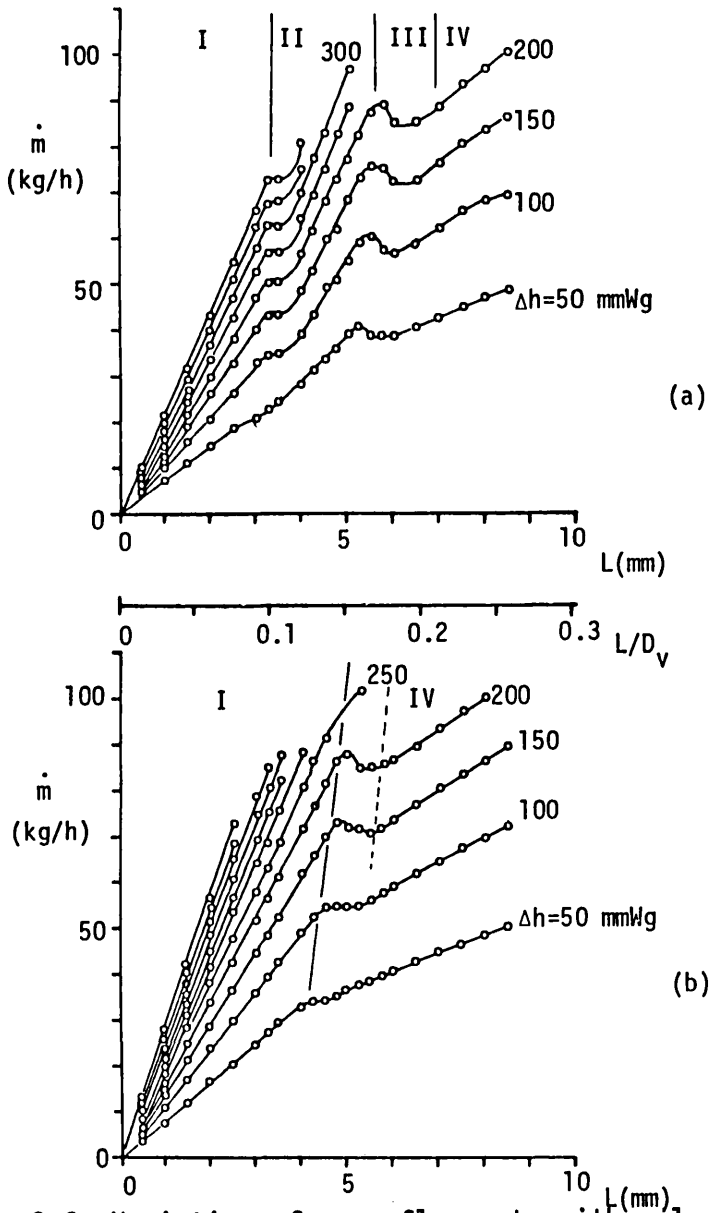

Fig. 2.6 Variation of mass flow rate with valve lift.
a) Valve I, b) Valve II

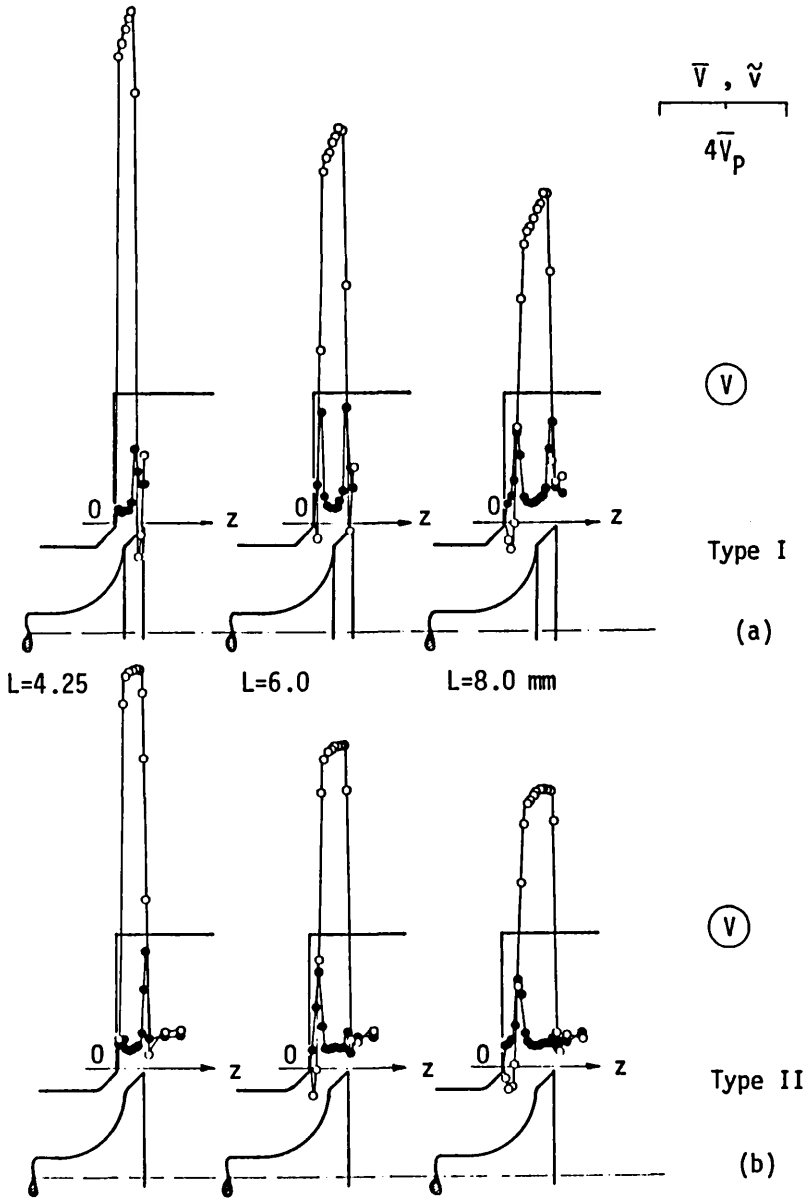

Fig. 2.7 Radial velocity distribution at the valve exit. a) Valve I, b) Valve II

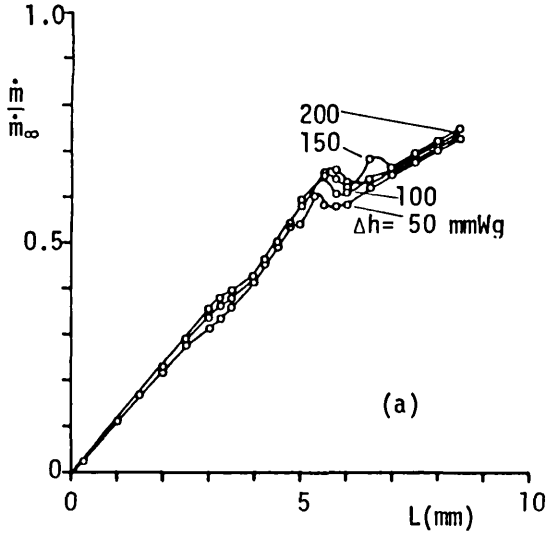

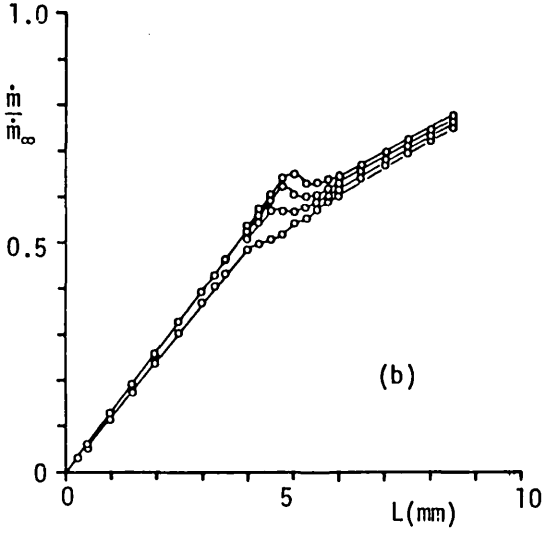

Fig. 2.8 Non-dimensional mass flow rate vs. valve lift. Valve a) I, b) II

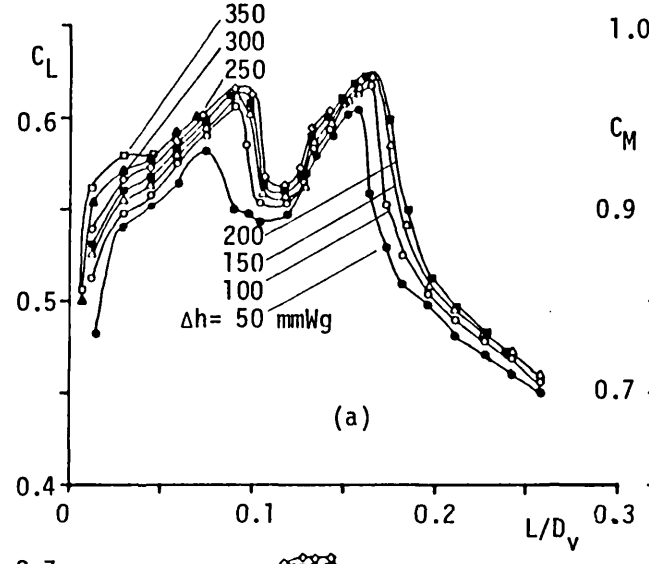

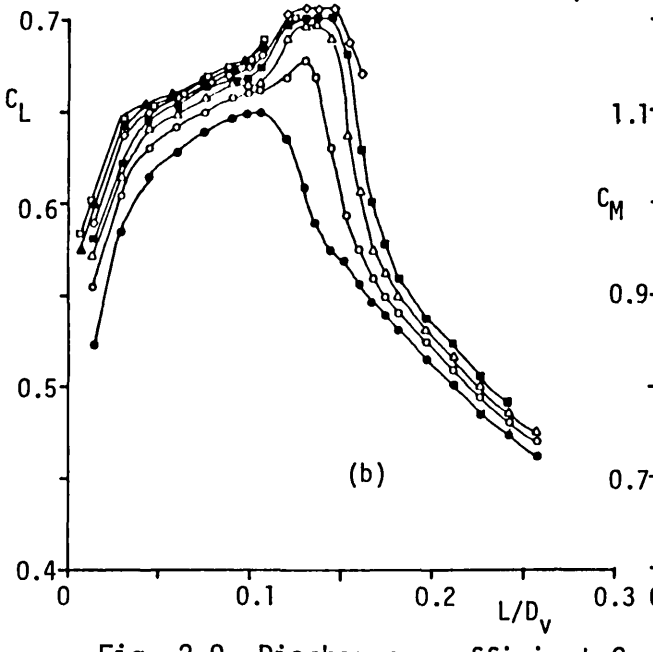

Fig. 2.9 Discharge coefficient C_L. a) Valve I, b) Valve II

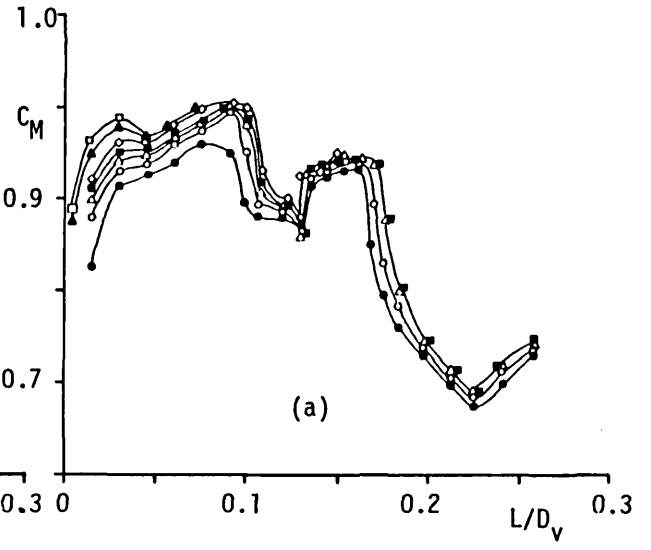

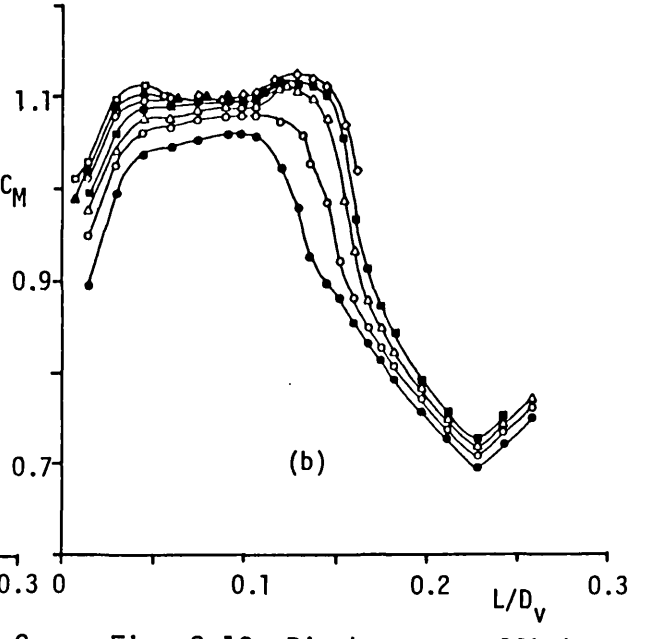

Fig. 2.10 Discharge coefficient C_M. a) Valve I, b) Valve II

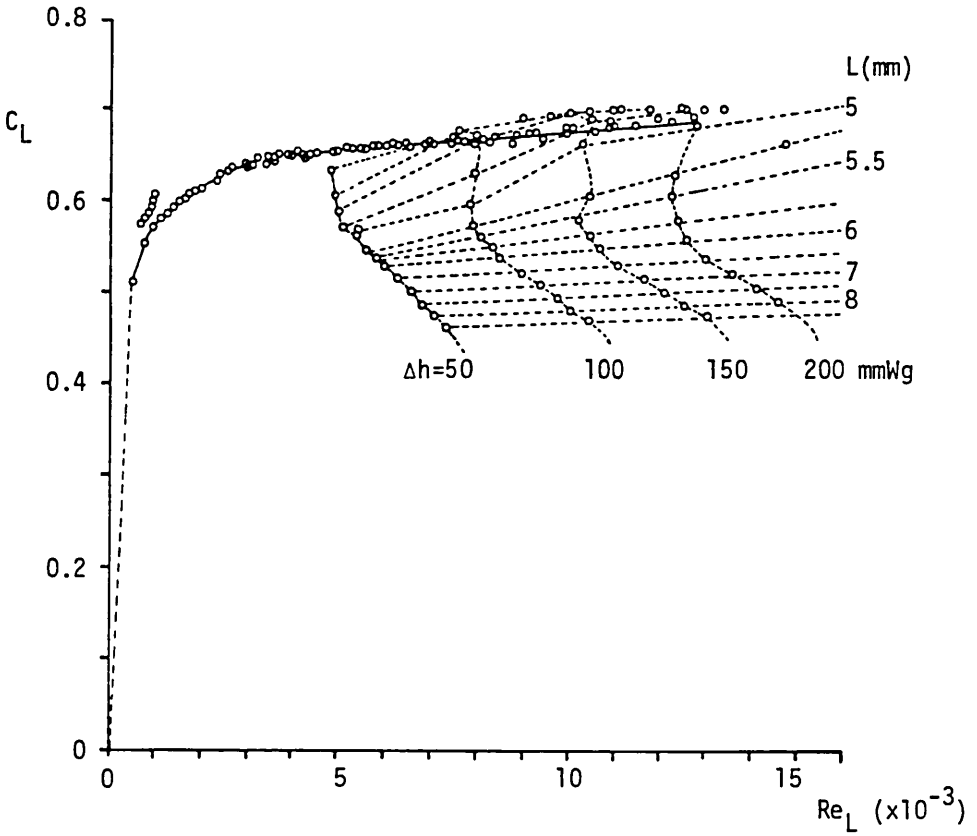

Fig. 2.11 Variation of discharge coefficient C_L of Valve II with Re_L

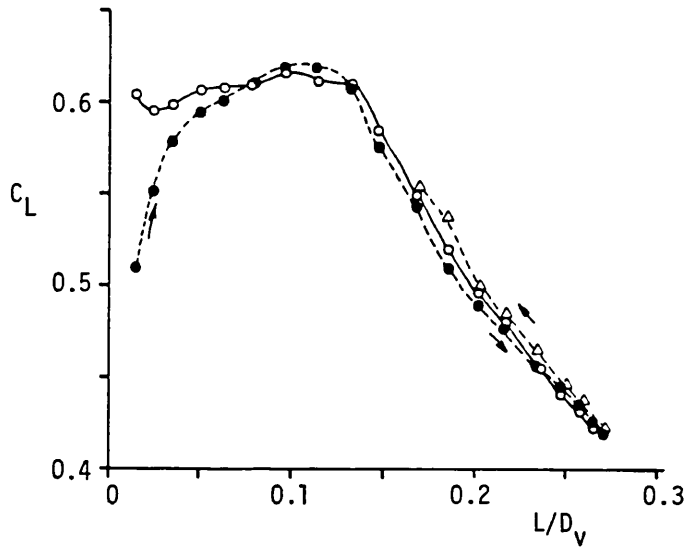

Fig. 2.12 Discharge coefficient C_L of Valve II for:
(o) constant mass flow rate corresponding to $\overline{V}_p$
(●) instantaneous mass flow rate (opening valve)
(Δ) instantaneous mass flow rate (closing valve)

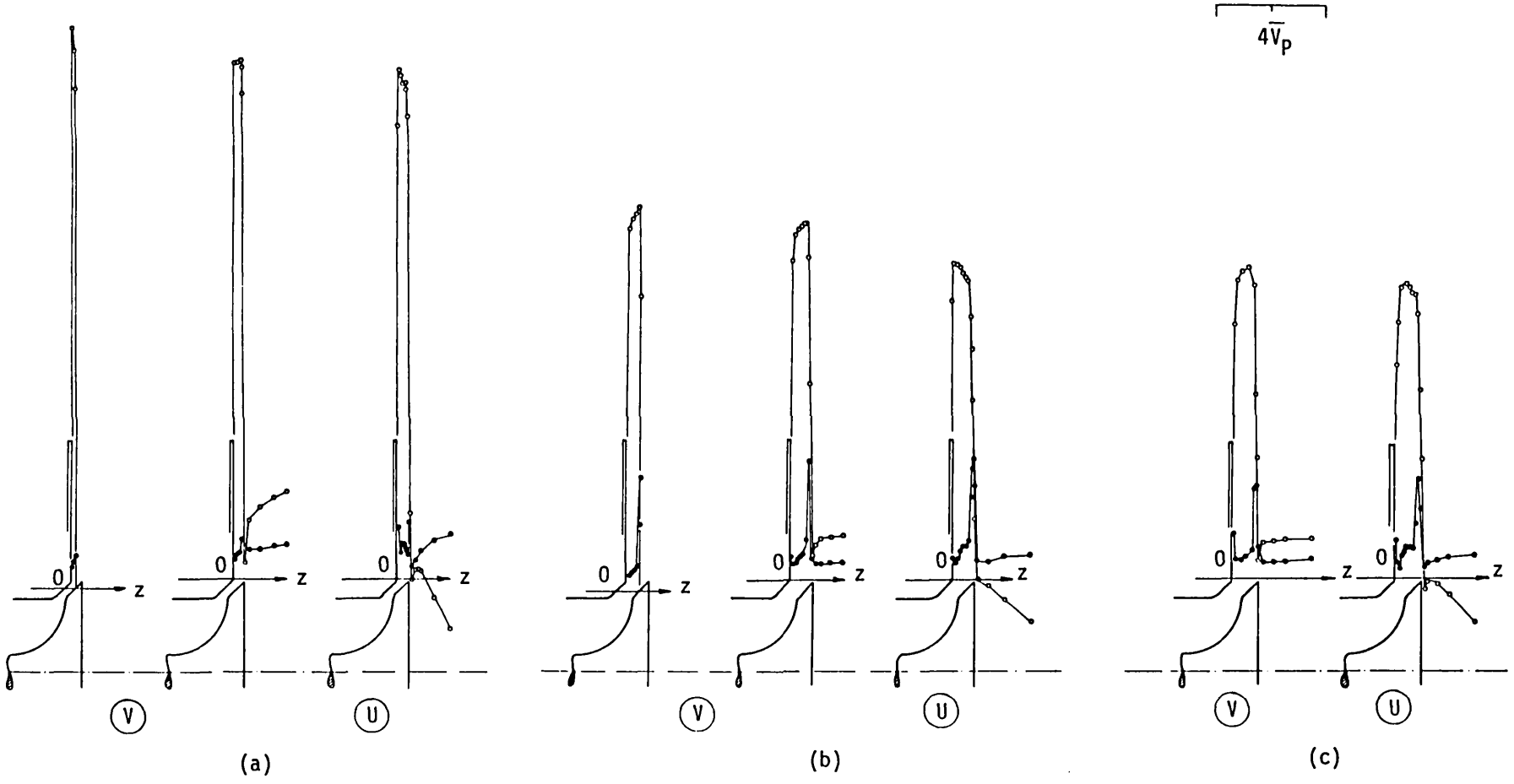

Fig. 2.13
(Cont'd)

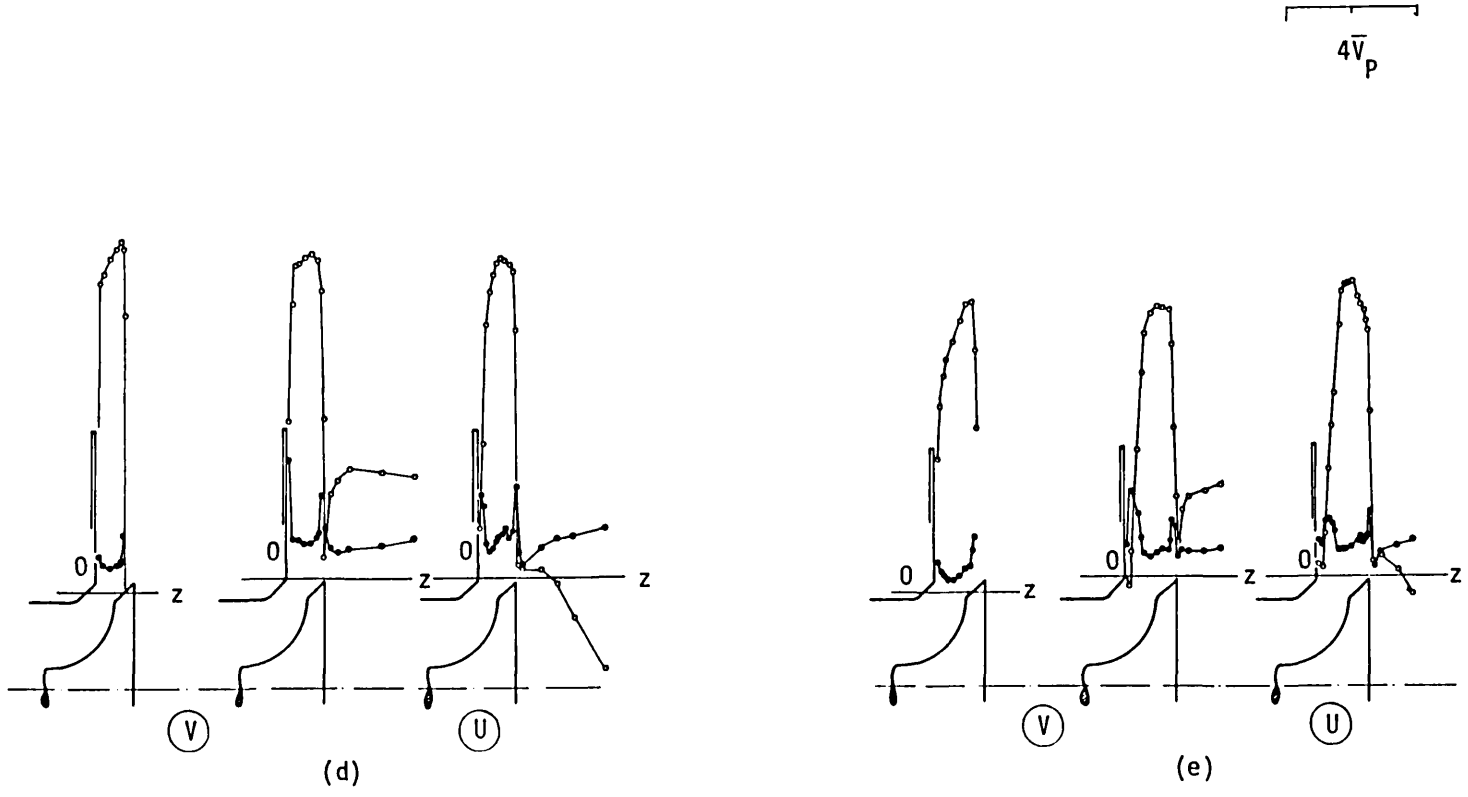

Fig. 2.13 Radial and axial velocity distribution at the exit plane and inside the valve gap. Unconfined valve. a) L = 2 mm, b) L = 4 mm, c) L = 5 mm, d) L = 6 mm, e) L = 8 mm

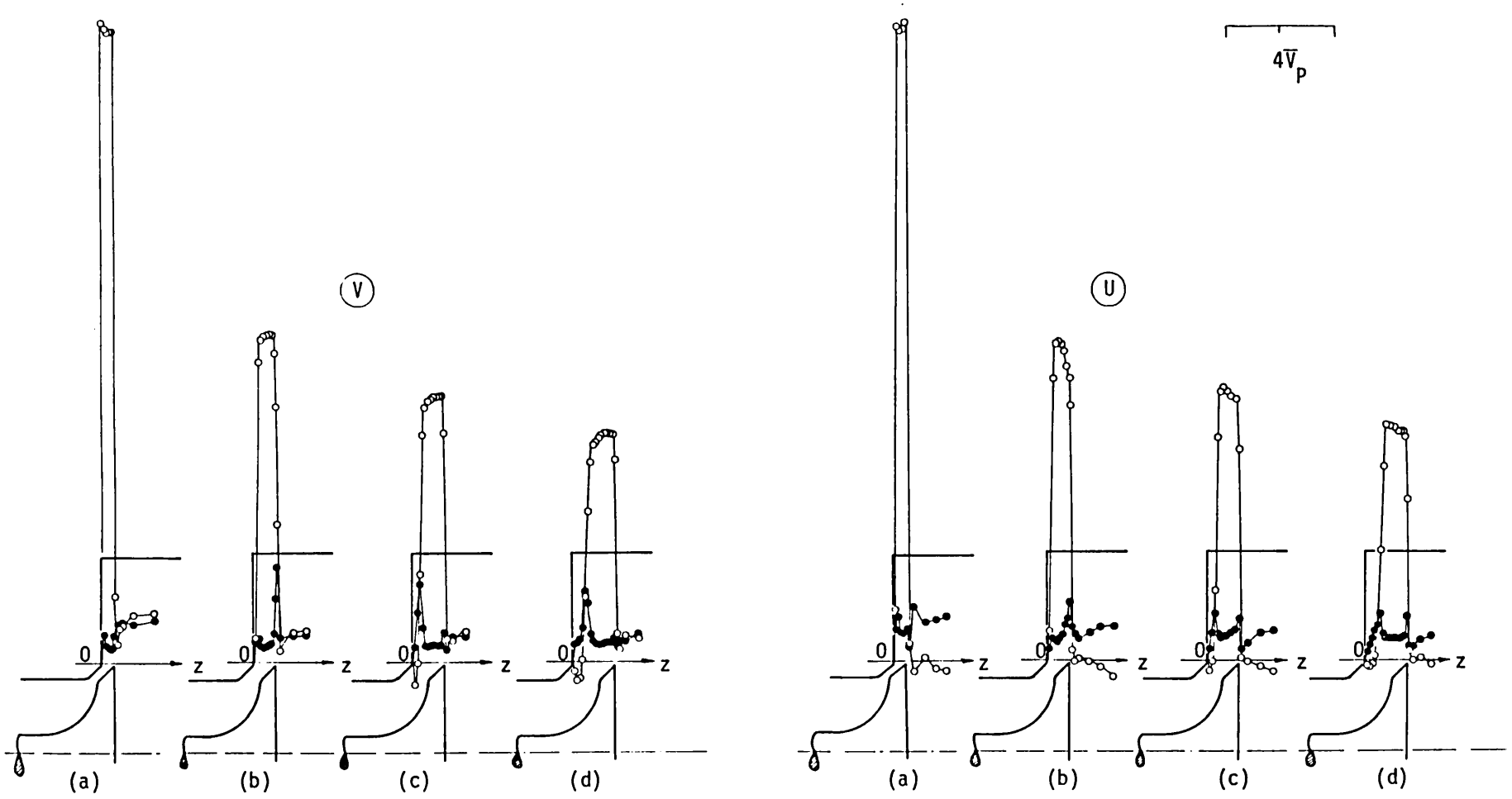

Fig. 2.14 Radial and axial velocity distribution at the exit of the axisymmetrically confined valve. Steady flow. a) L = 2.15 mm, b) L = 4.25 mm, c) L = 6 mm, d) L = 8 mm

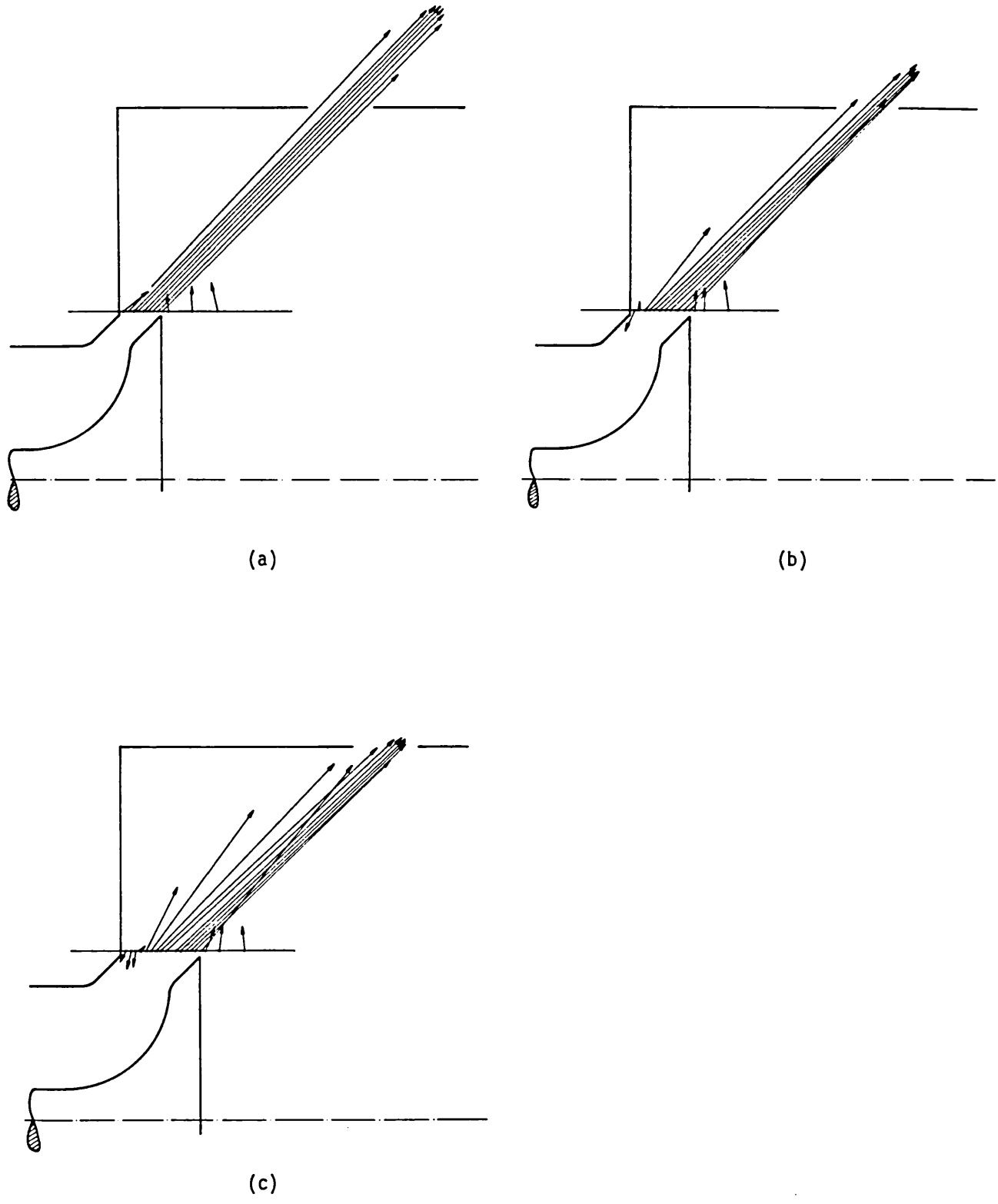

Fig. 2.15 Velocity vectors at the exit of the axisymmetrically confined valve. Steady flow. a) L = 4.25 mm, b) L = 6 mm, c) L = 8 mm

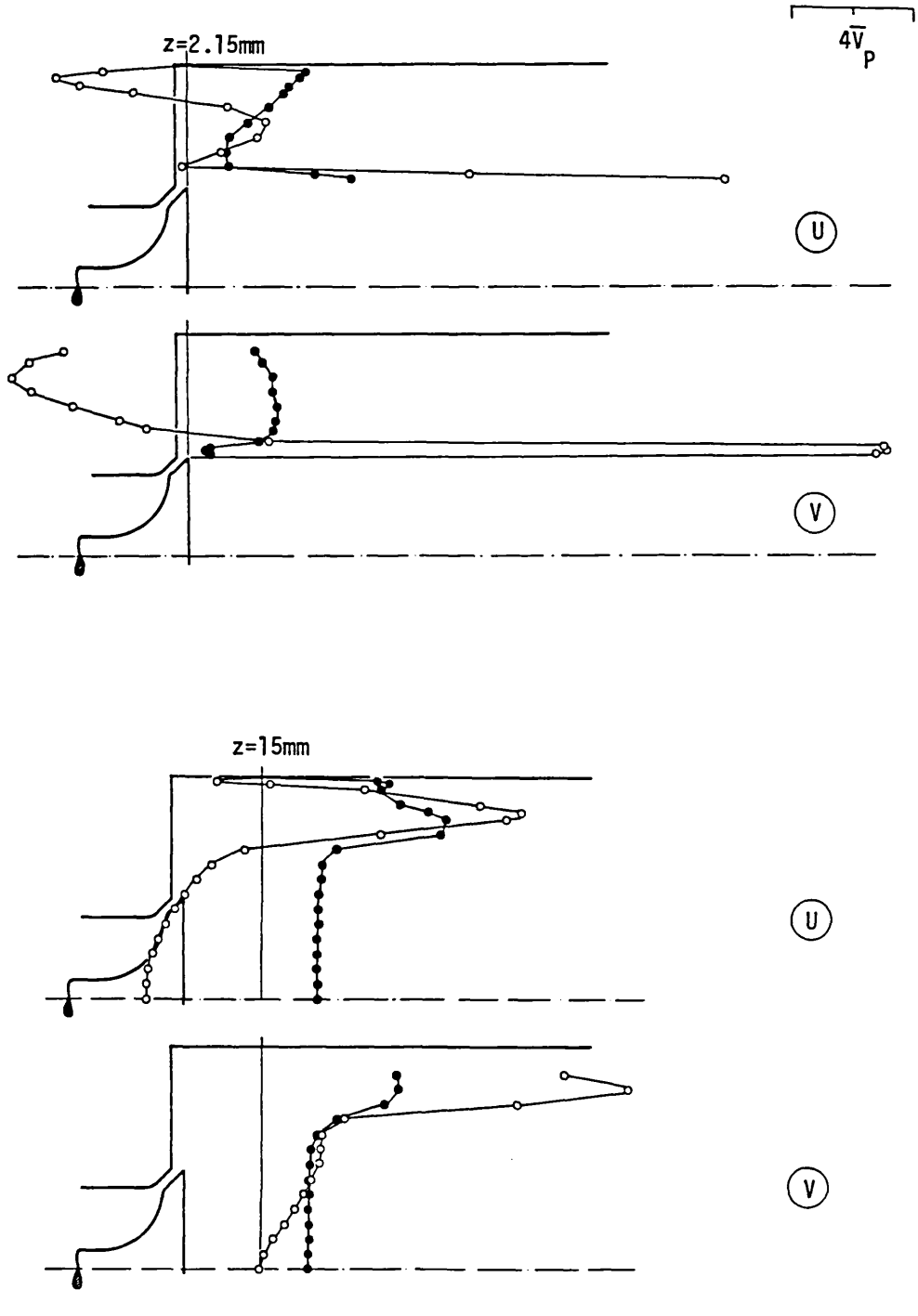

(a)

Fig. 2.16
(Cont'd)

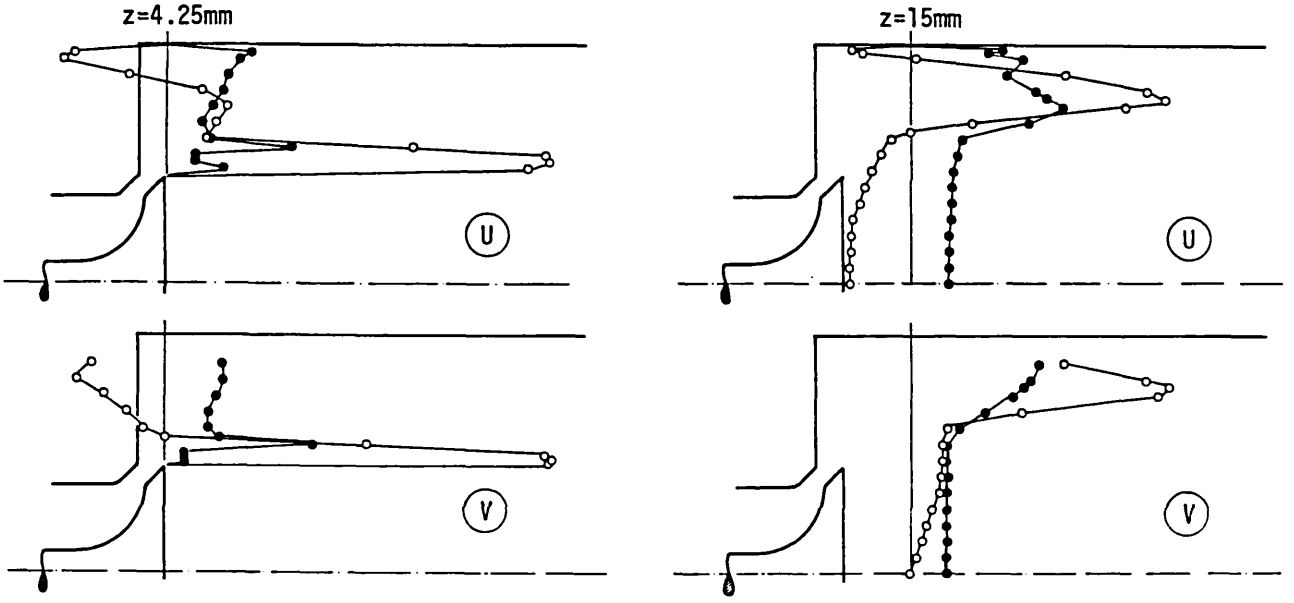

(b)

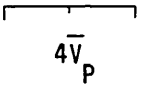

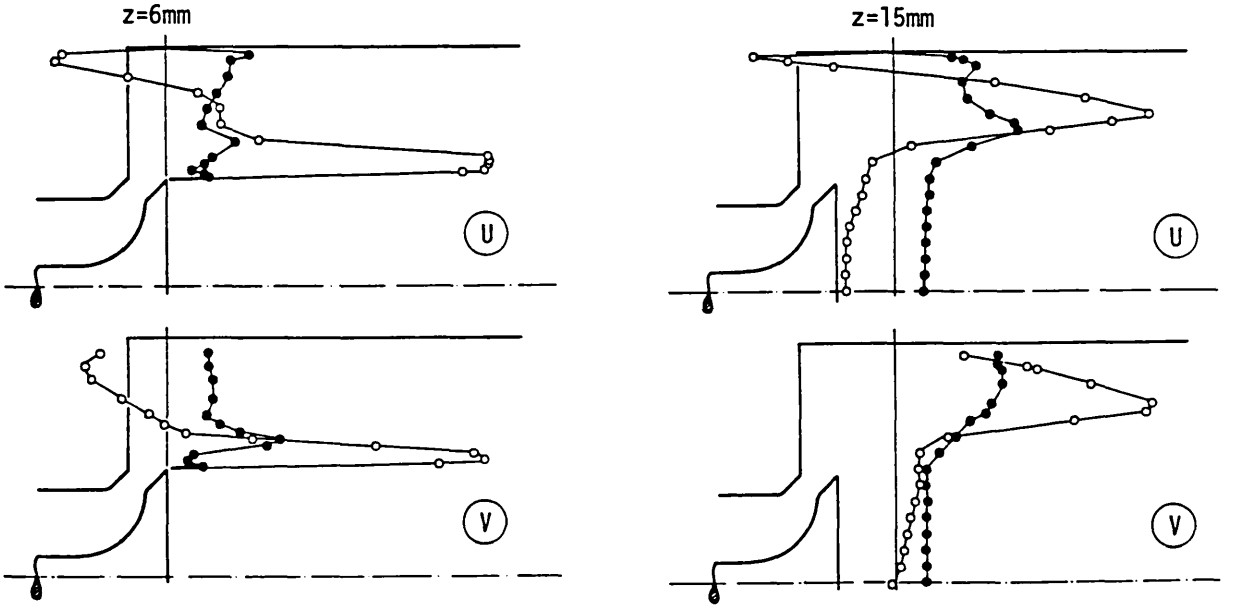

(c)

Fig. 2.16
(Cont'd)

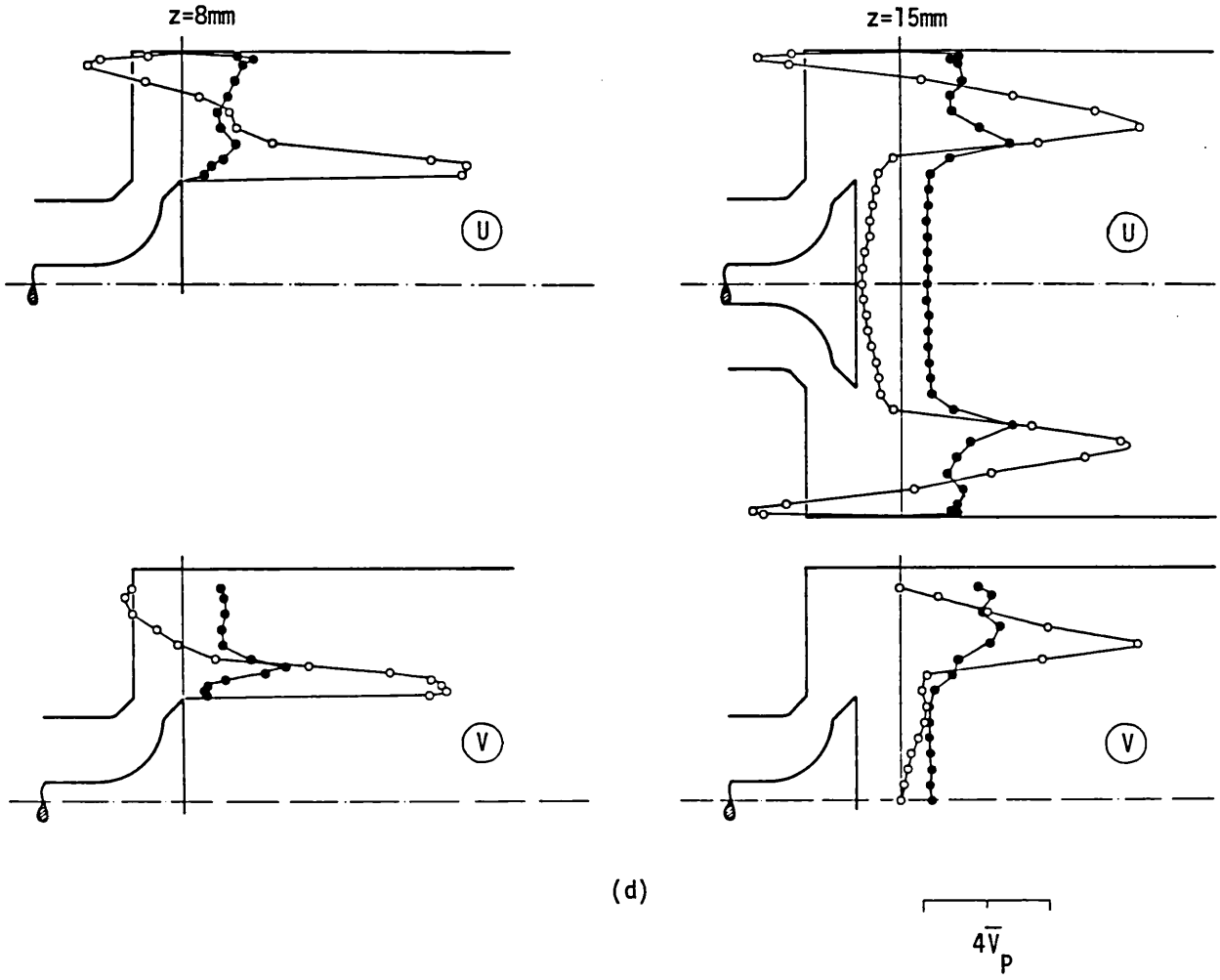

Fig. 2.16 Axial and radial velocity distribution at z = L and z = 15 mm. Axisymmetrically confined valve, steady flow. a) L = 2.15 mm, b) L = 4.25 mm, c) L = 6 mm, d) L = 8 mm

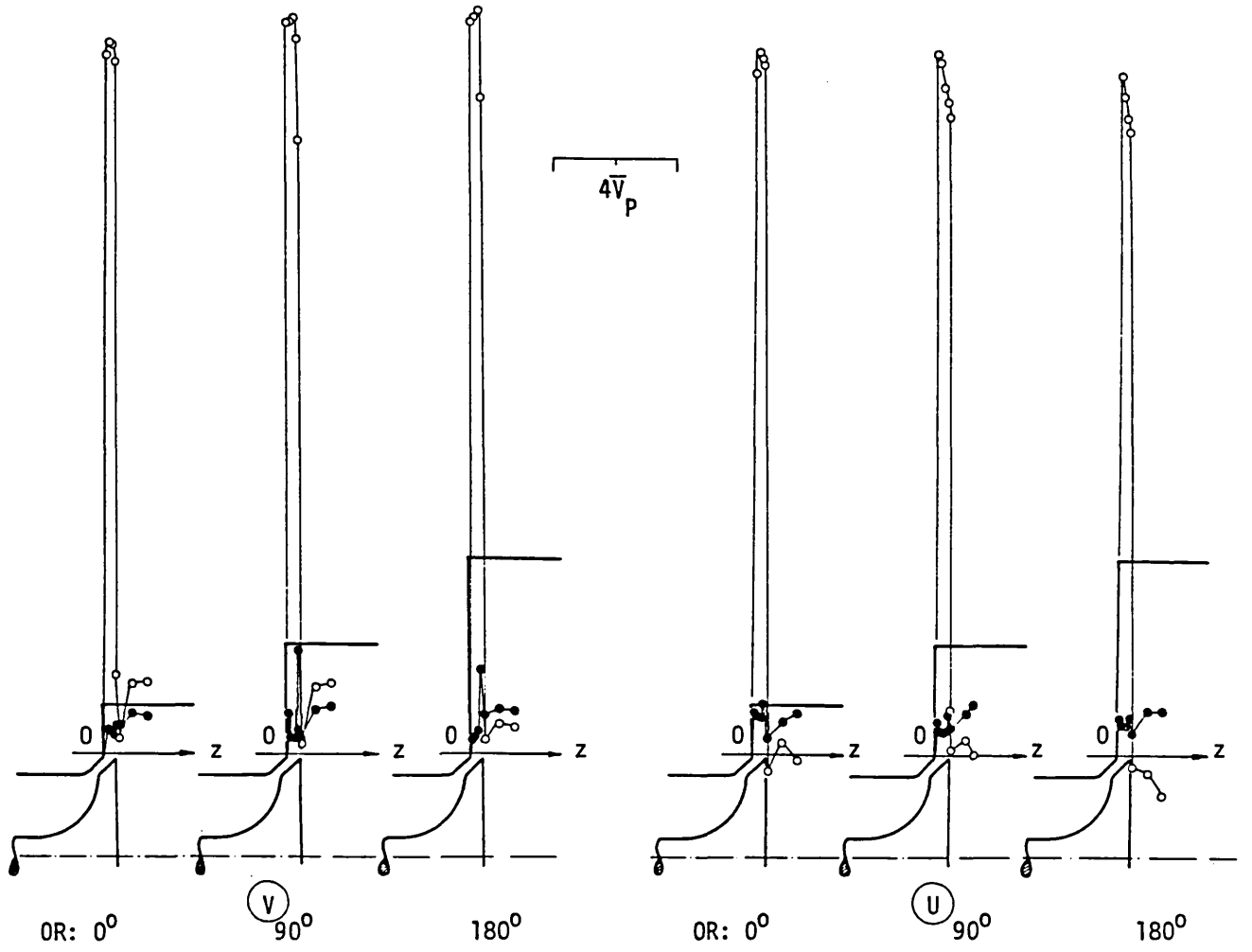

(a)

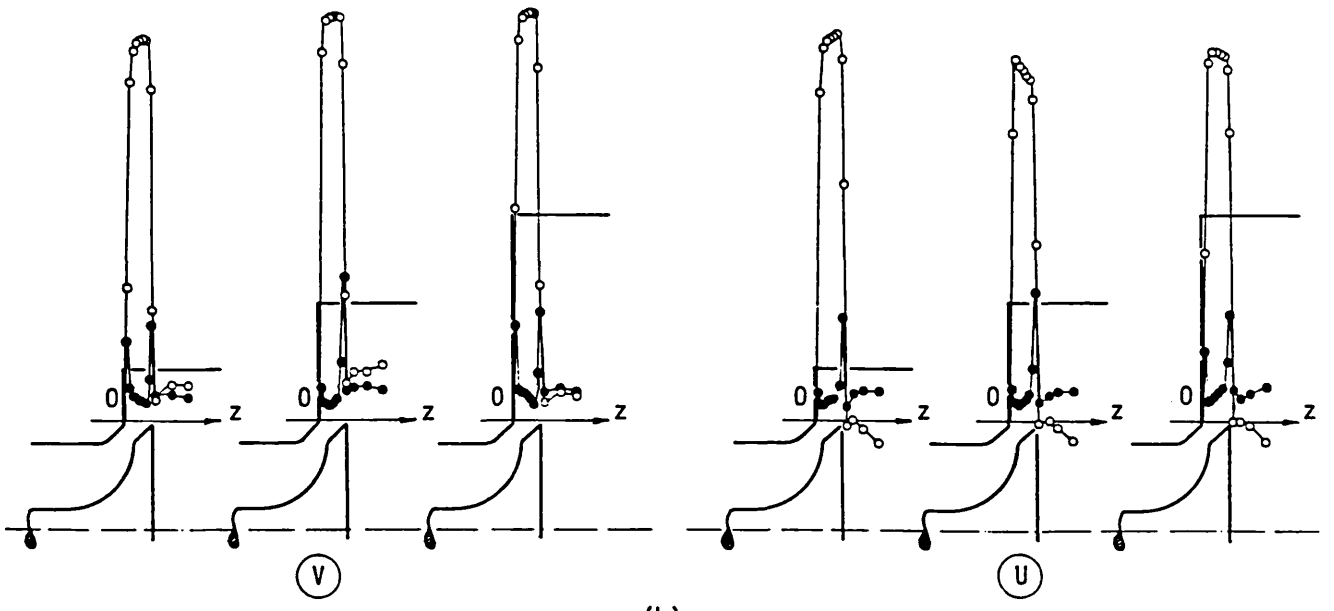

(b)

Fig. 2.17
(Cont'd)

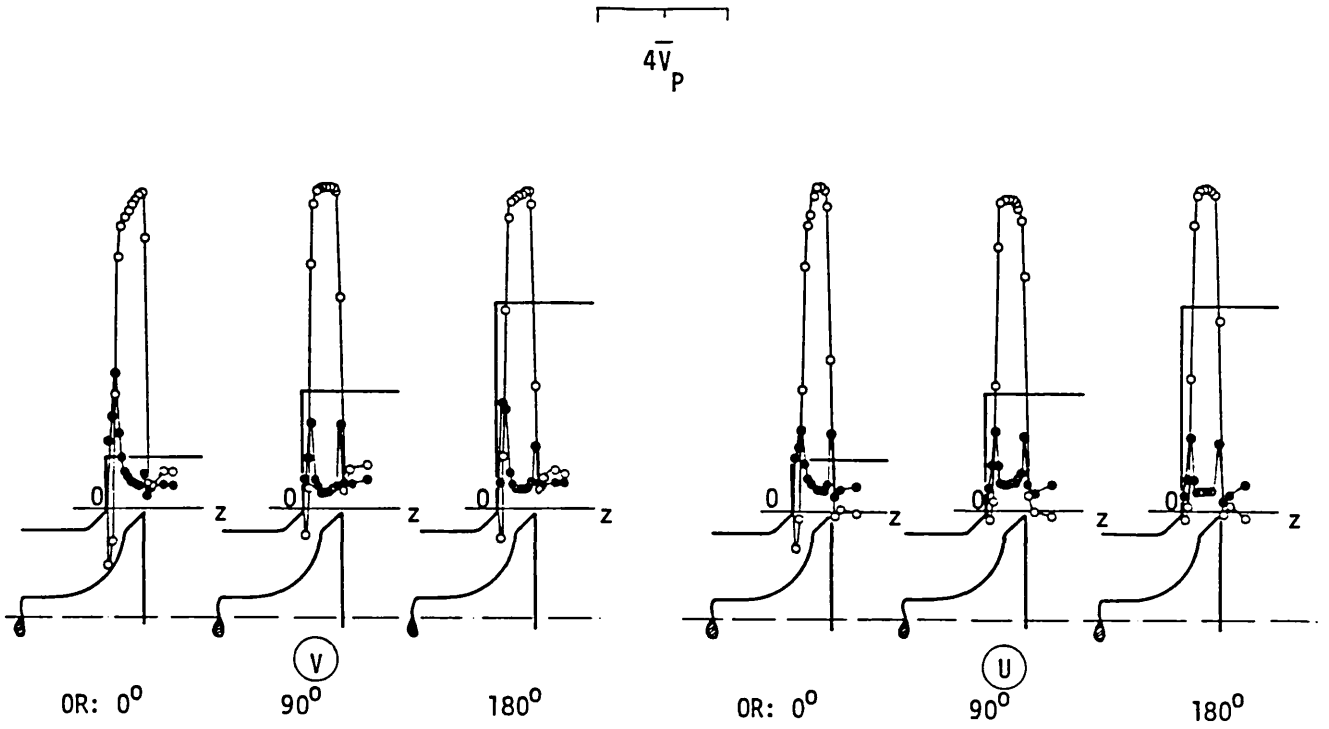

(c)

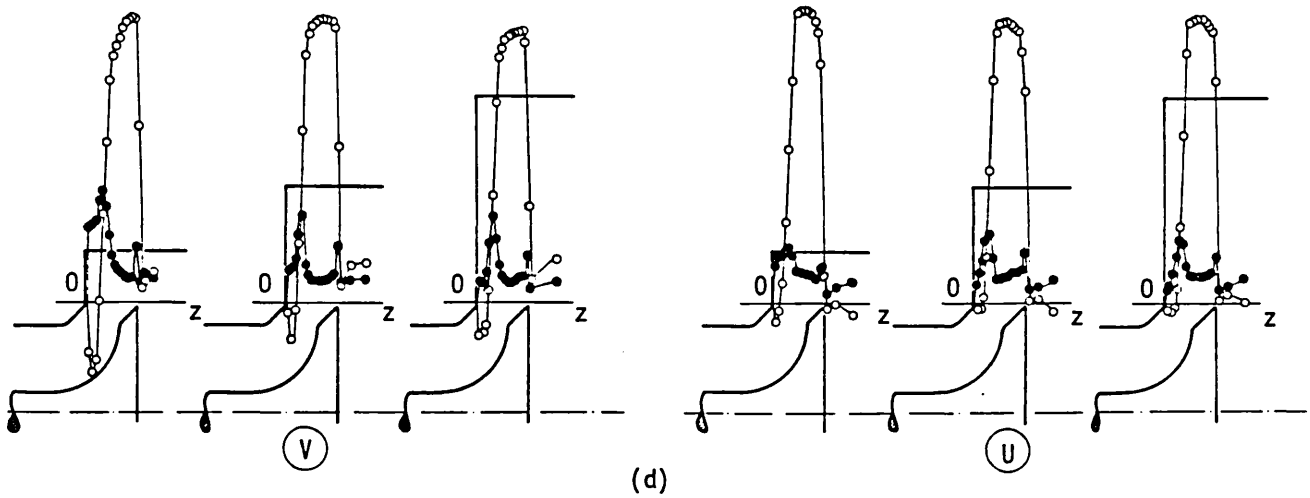

(d)

Fig. 2.17 Radial and axial velocity distribution at the exit of the off-centre valve, along the 0, 90 and 180° measurement planes. Steady flow. a) L = 2.15 mm, b) L = 4.25 mm, c) L = 6 mm, d) L = 8 mm

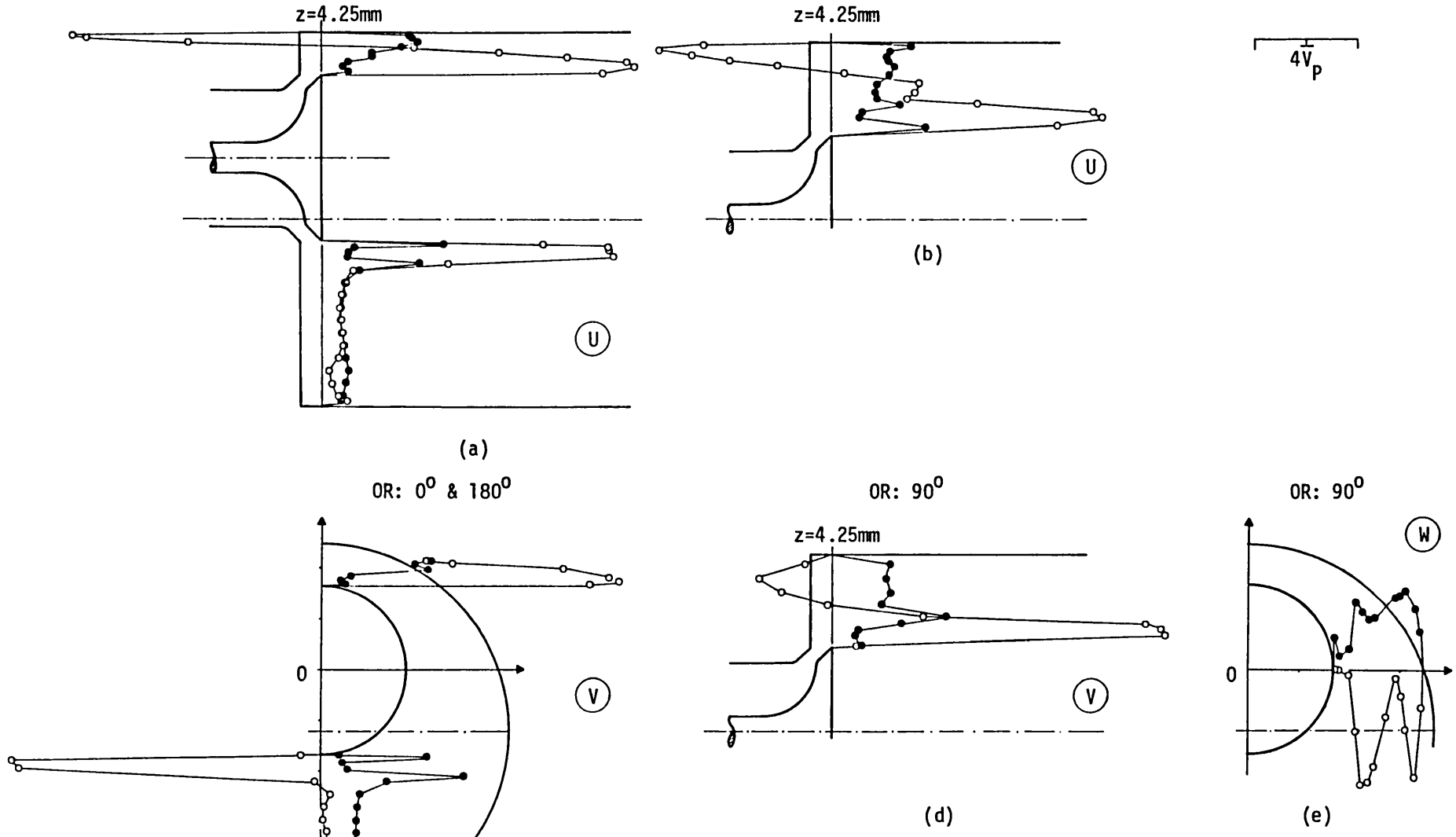

Fig. 2.18
(Cont'd)

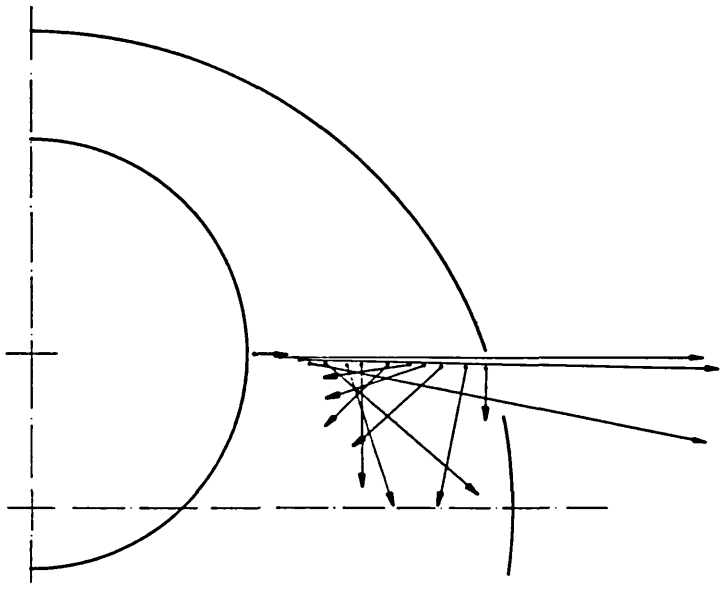

(f)

Fig. 2.18 Axial (a,b), radial (c,d) and tangential (e) velocity distribution at z = L = 4.25 mm. Vector addition of radial and tangential velocities along the 90^{o} measurement plane (f). Steady flow, off-centre valve

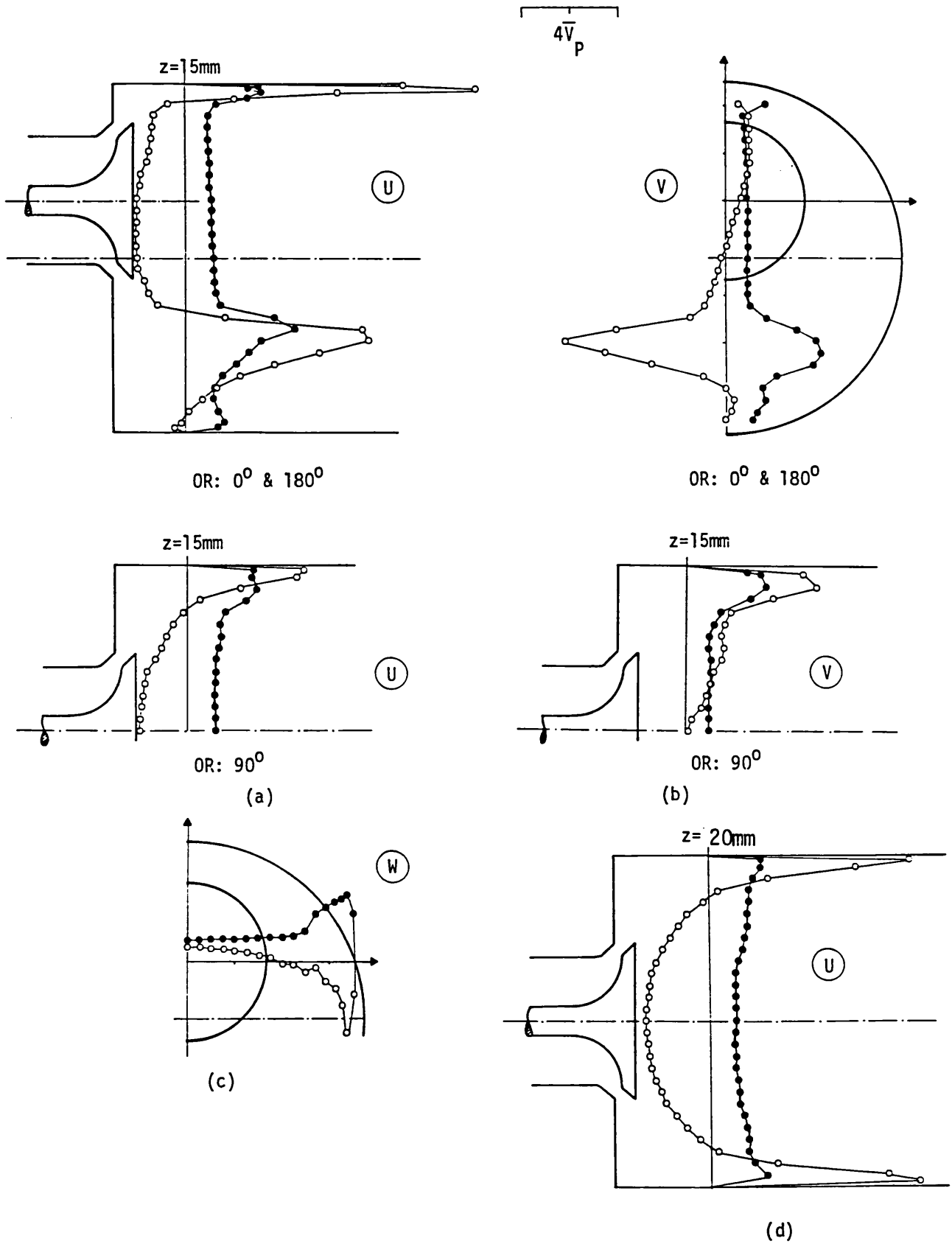

Fig. 2.19 Axial (a), radial (b) and tangential (c) velocity distribution at z = 15 mm. L = 4.25 mm, off-centre valve, steady flow. Symmetry test at z = 20 mm (d)

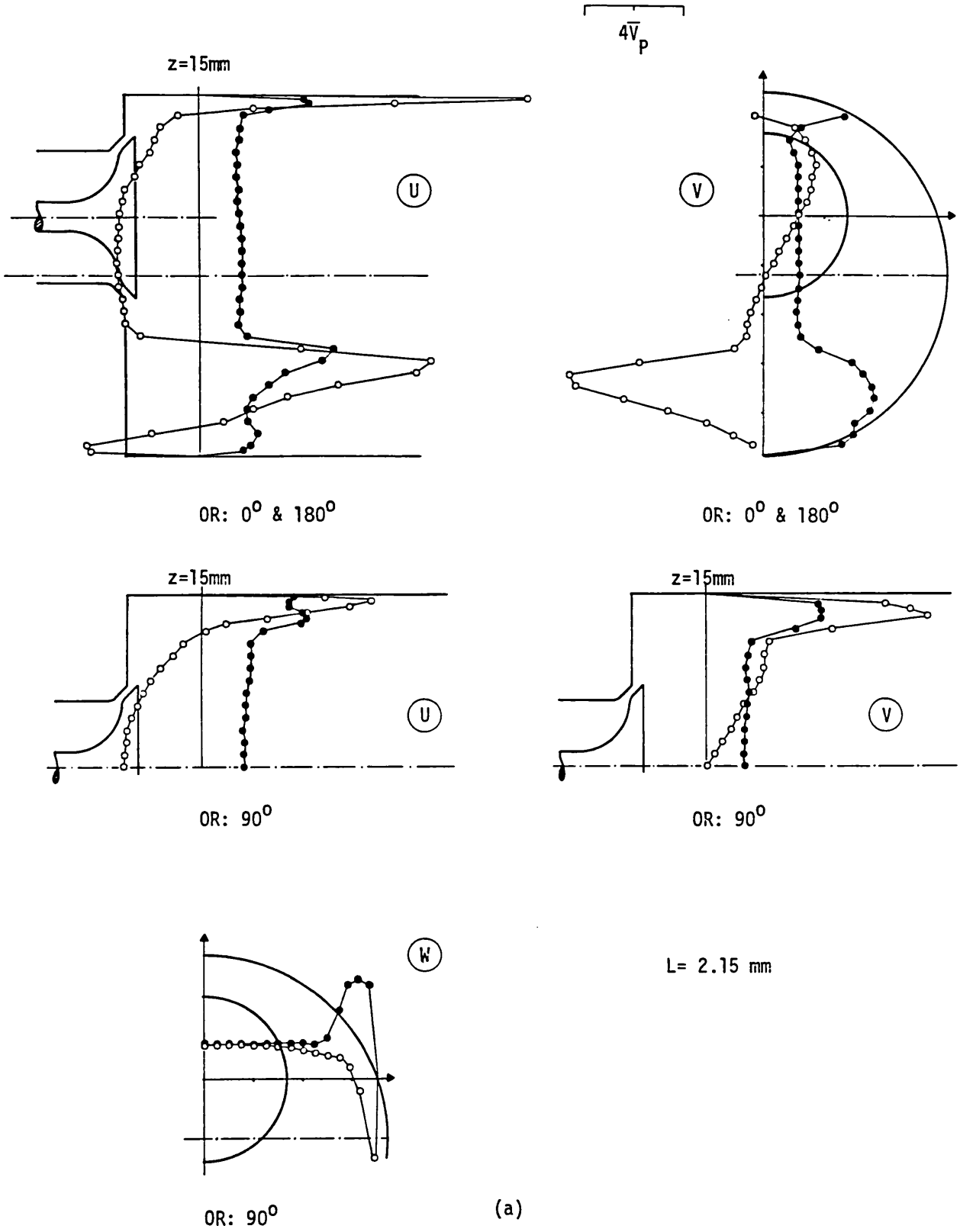

(a)

Fig. 2.20
(Cont'd)

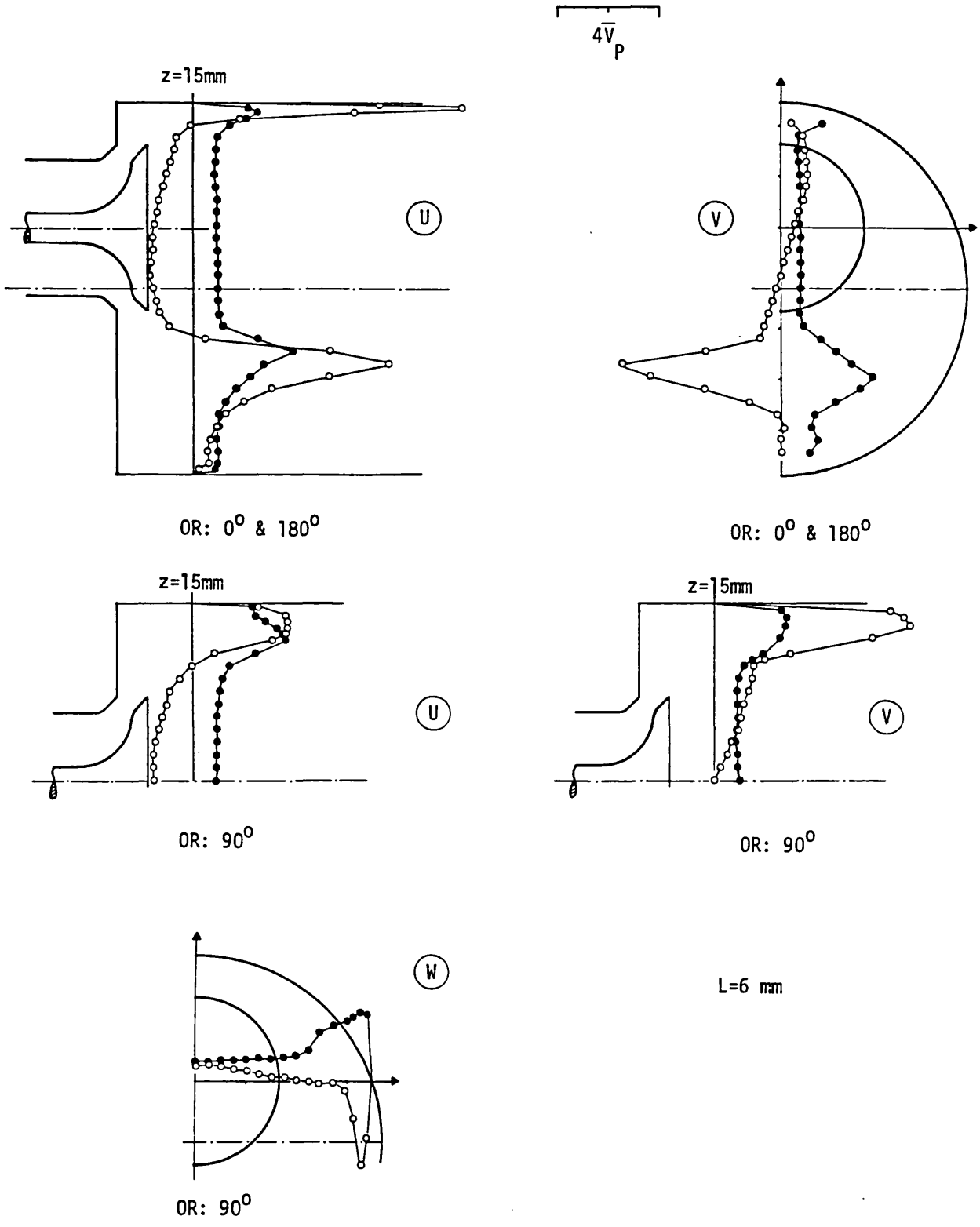

(b)

Fig. 2.20
(Cont'd)

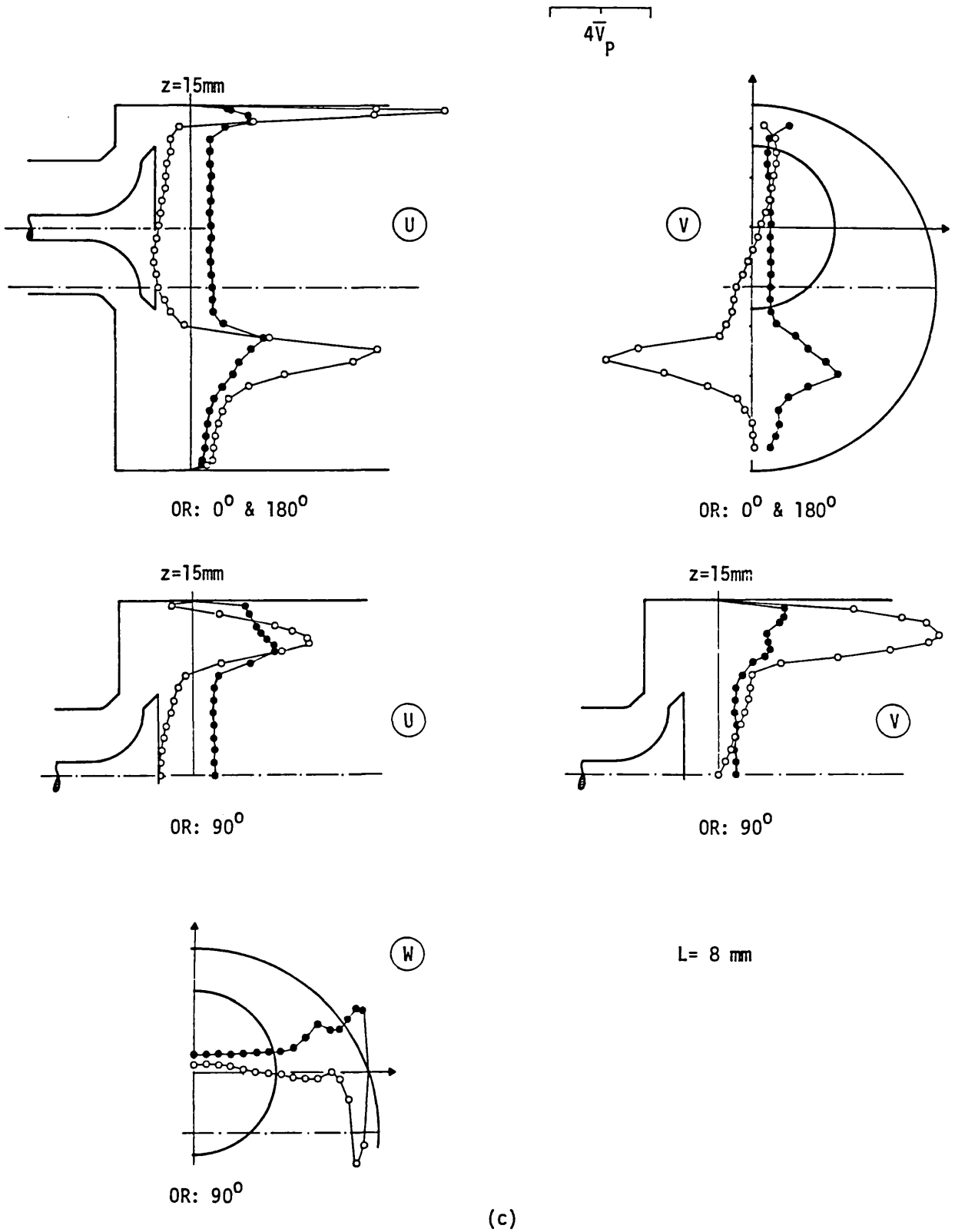

(c)

Fig. 2.20 Axial, radial and tangential velocity distribution at z = 15 mm along the three measurement planes. Steady flow. a) L= 2.15 mm, b) L = 6 mm, c) L = 8 mm

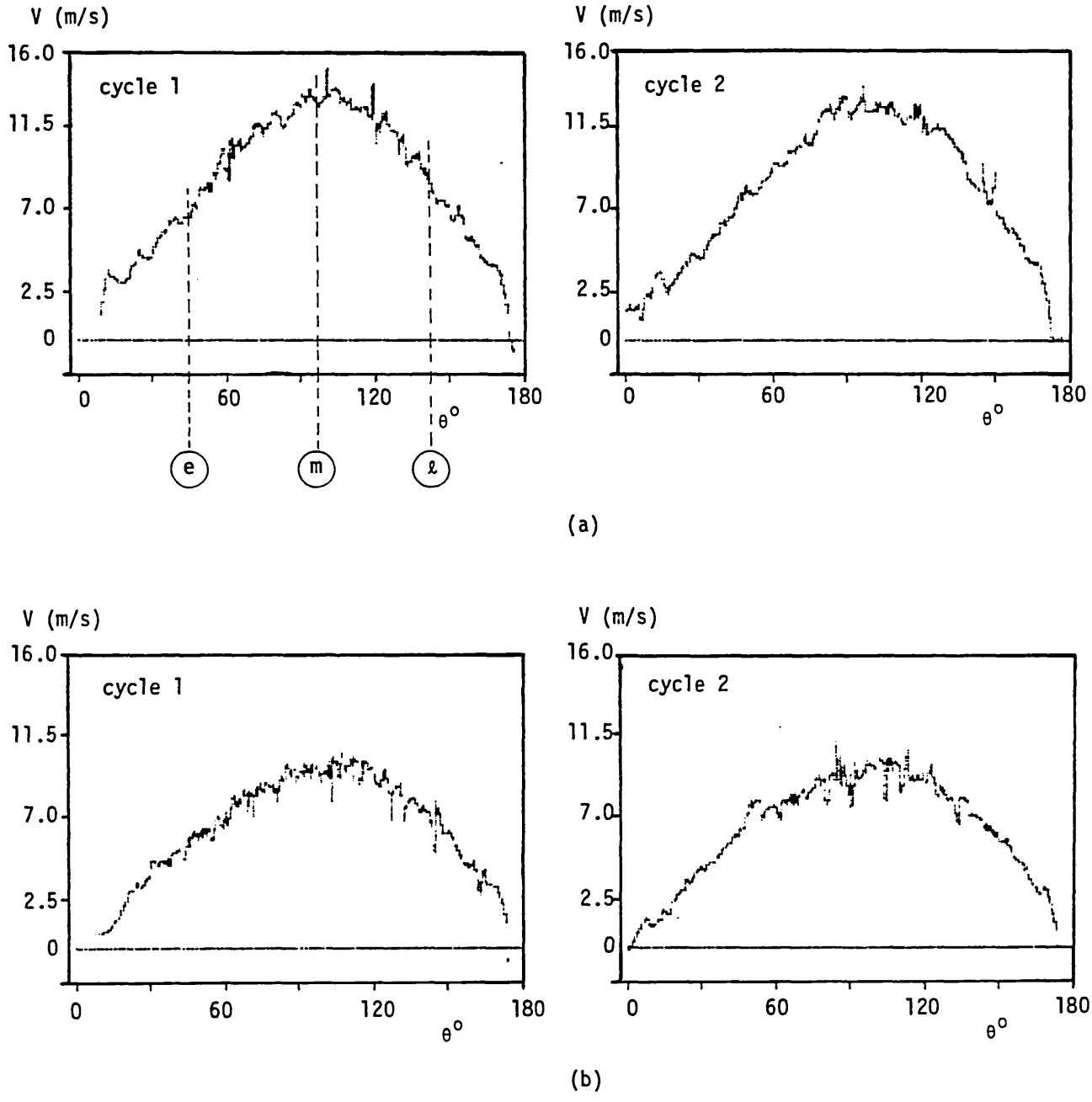

Fig. 2.21 Cycle-resolved radial velocity measurements at the exit of the stationary valve, at r = 17 mm. Unsteady flow. a) L = 4.25 mm, z = 2 mm, b) L = 6 mm, z = 4.5 mm

Notation: (e): Early induction, $\theta = 45^{o}$

(m): Mid-induction, $\theta = 96^{o}$

(ℓ): Late induction, $\theta = 145^{o}$

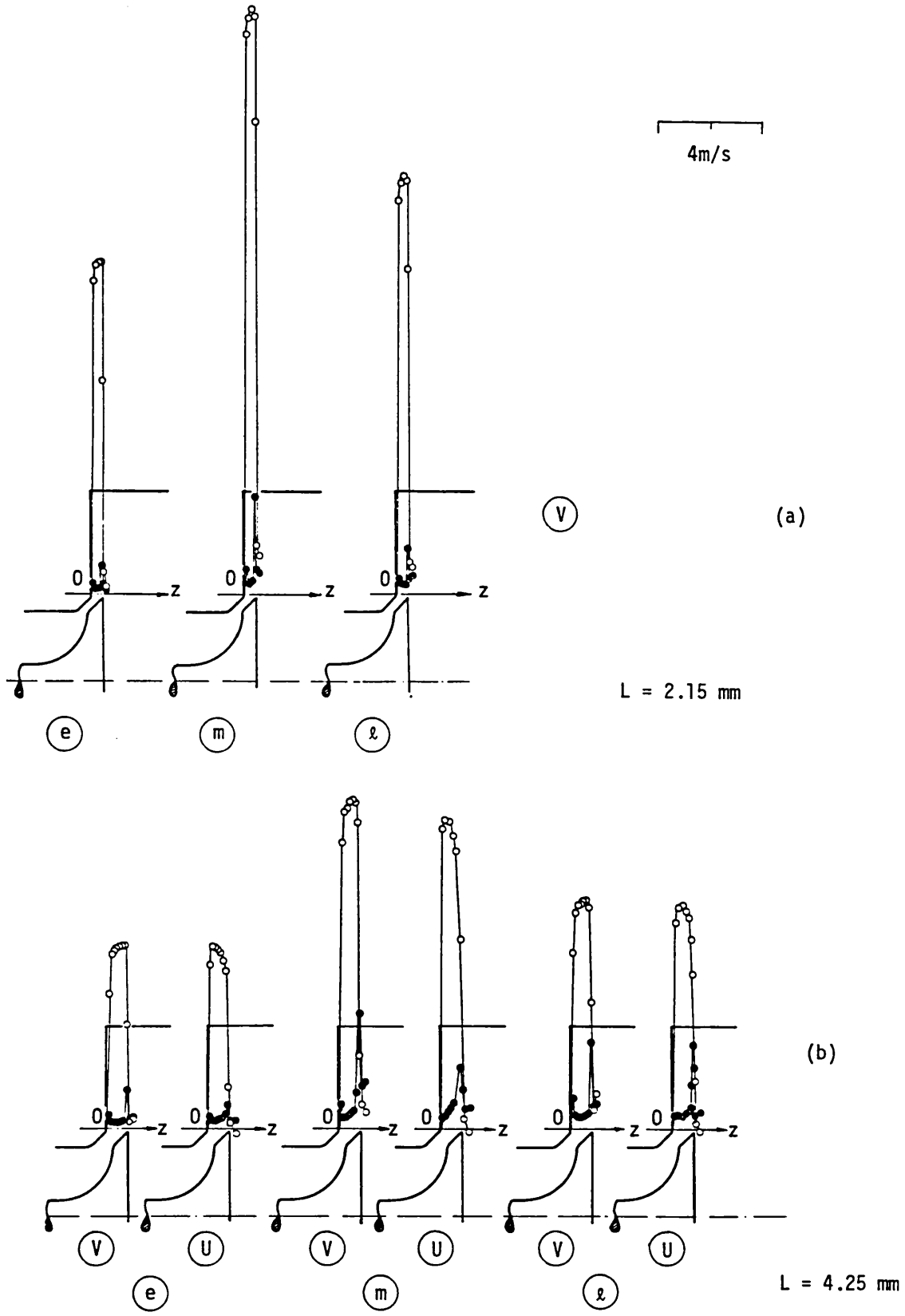

Fig. 2.22
(Cont'd)

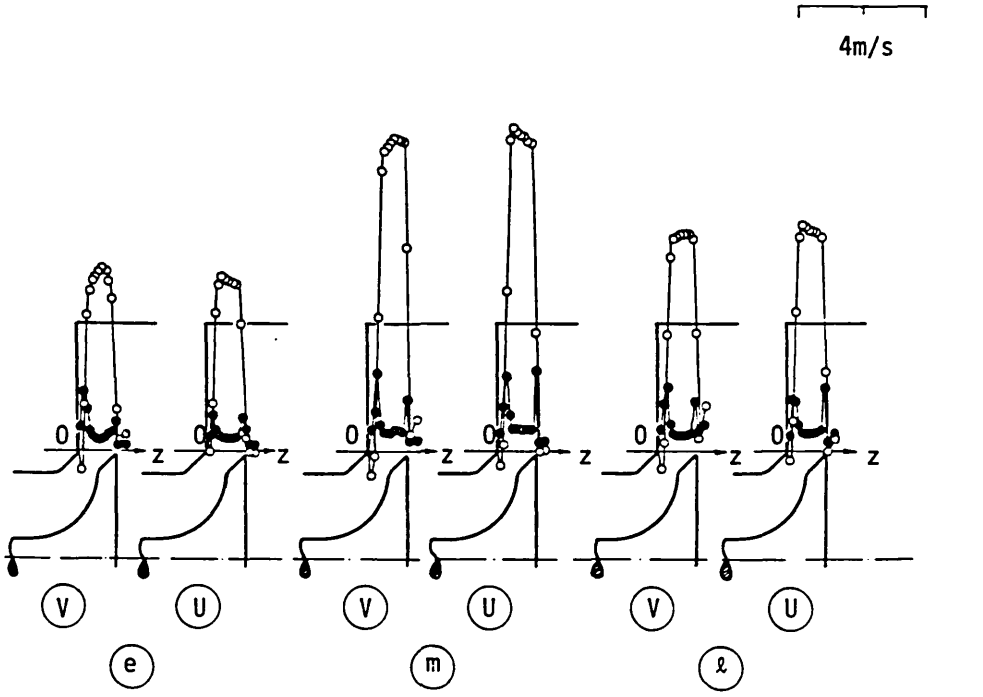

(c)

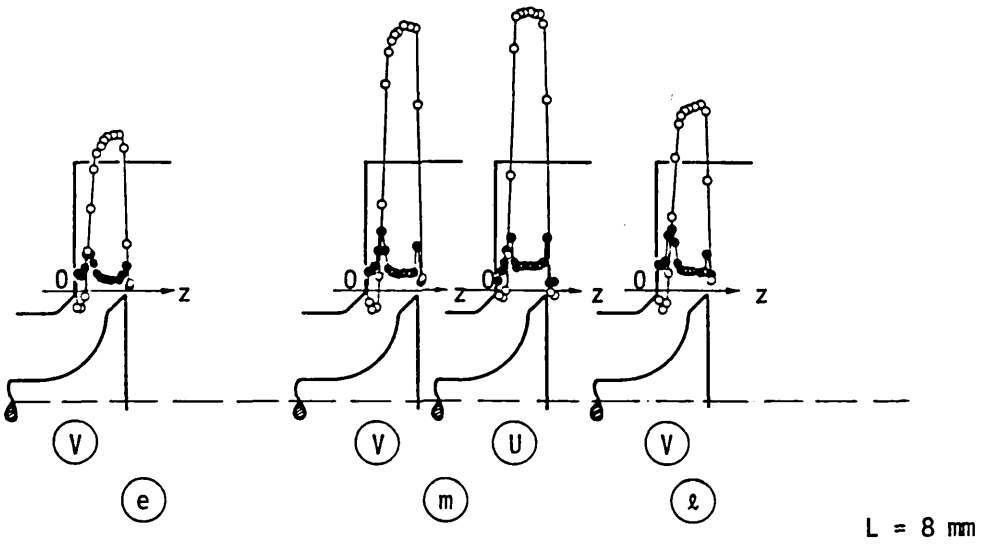

(d)

Fig. 2.22 Radial and axial velocity distribution at the valve exit. Axisymmetrically confined valve, unsteady flow. Early (e), Mid- (m) and Late (ℓ) induction.
a) L = 2.15 mm, b) L = 4.25 mm, c) L = 6 mm, d) L = 8 mm

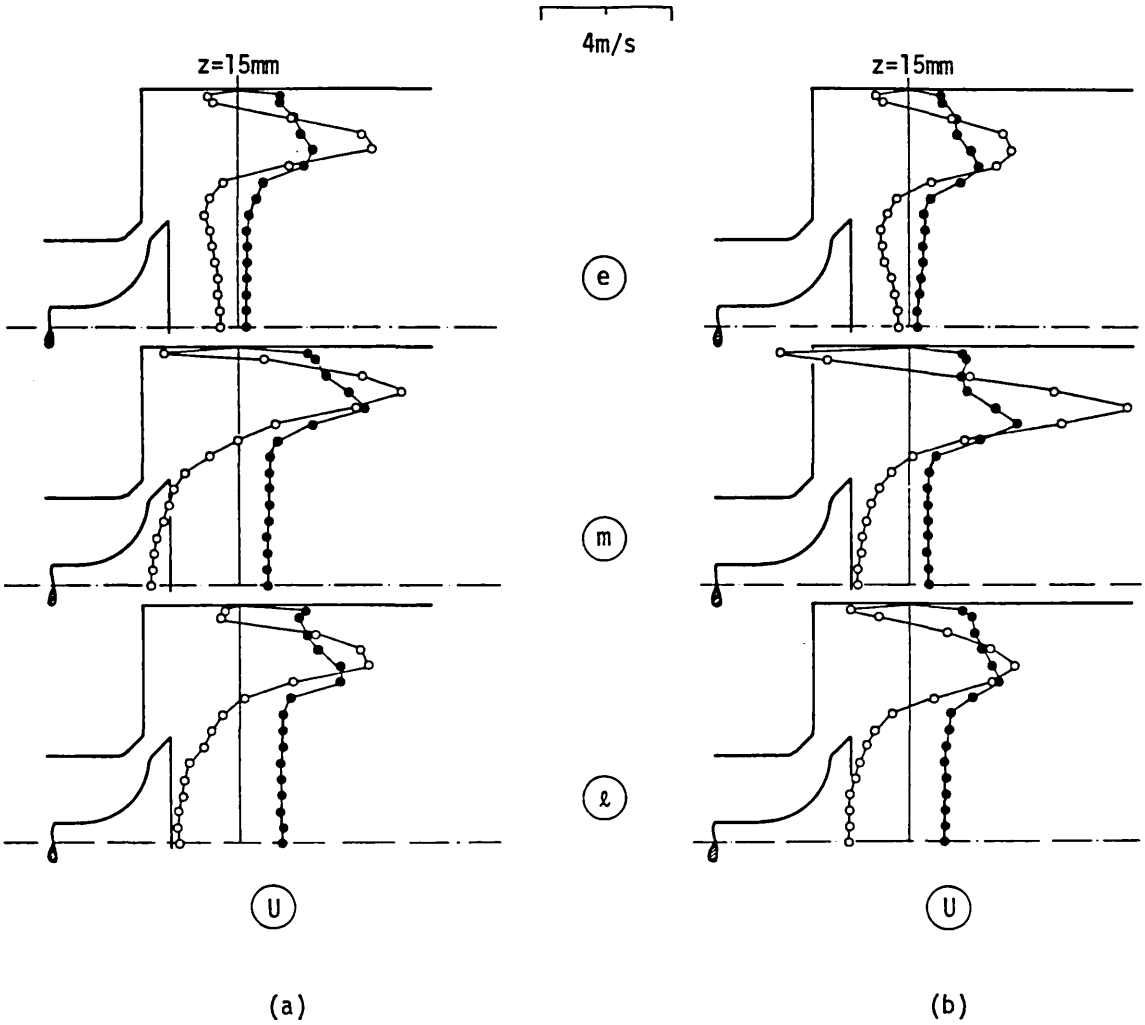

Fig. 2.23 Axial velocity distribution at z = 15 mm.
Axisymmetrically confined valve, unsteady flow;
early, mid- and late induction.
a) L = 4.25 mm, b) L = 6 mm

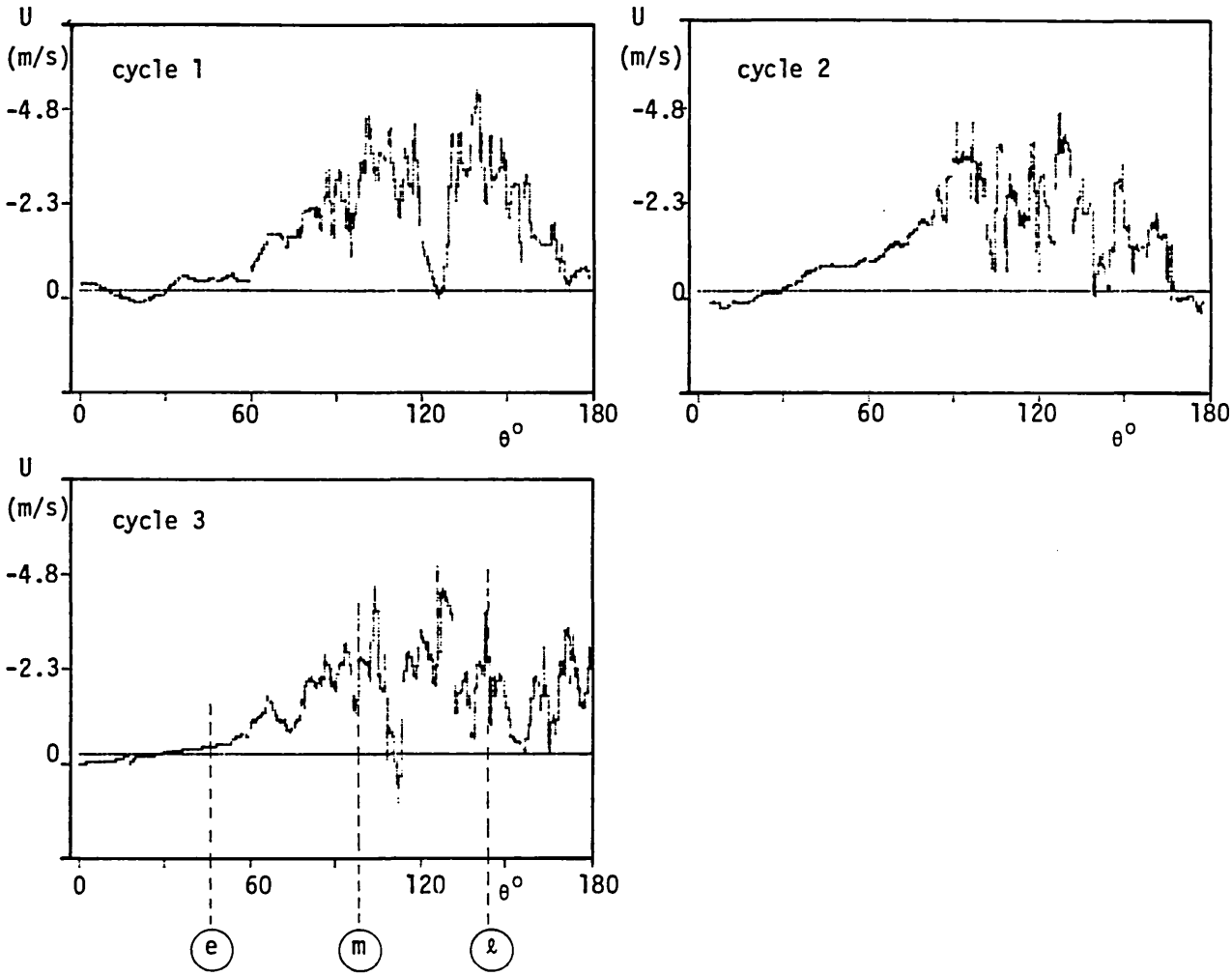

Fig. 2.24 Cycle-resolved axial velocity measurements at z = 15mm and r=0 (centre-line). Axisymmetrically confined valve, unsteady flow

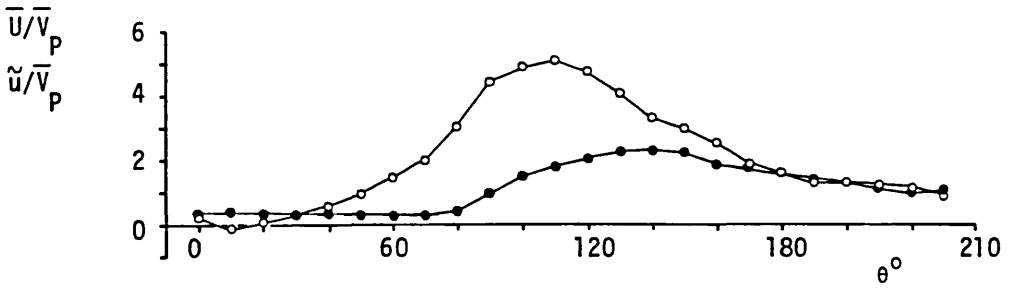

Fig. 2.25 Temporal ensemble-averaged axial velocity measurements at z = 15 mm and r = 0. Axisymmetrically confined valve, unsteady flow

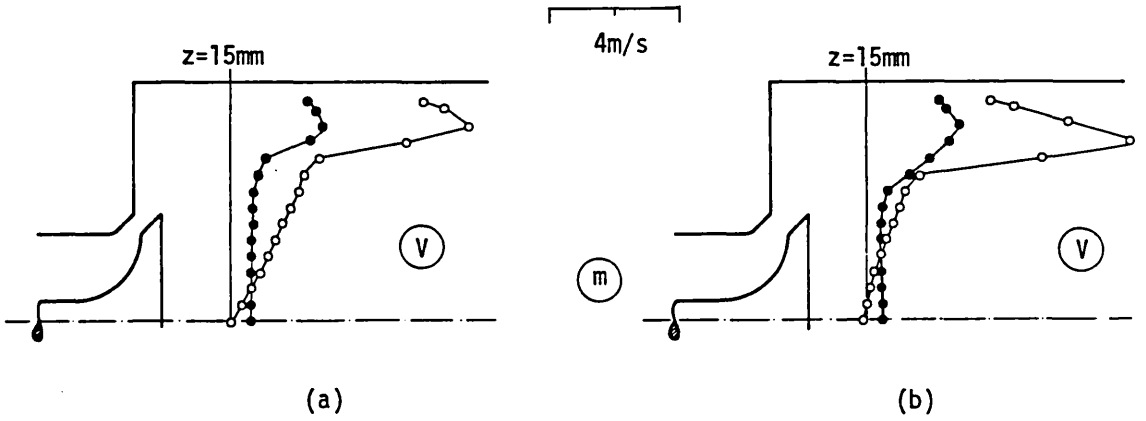

Fig. 2.26 Radial velocity distribution at z = 15 mm. Axisymmetrically confined valve, unsteady flow, mid-induction.
a) L = 4.25 mm, b) L = 6 mm

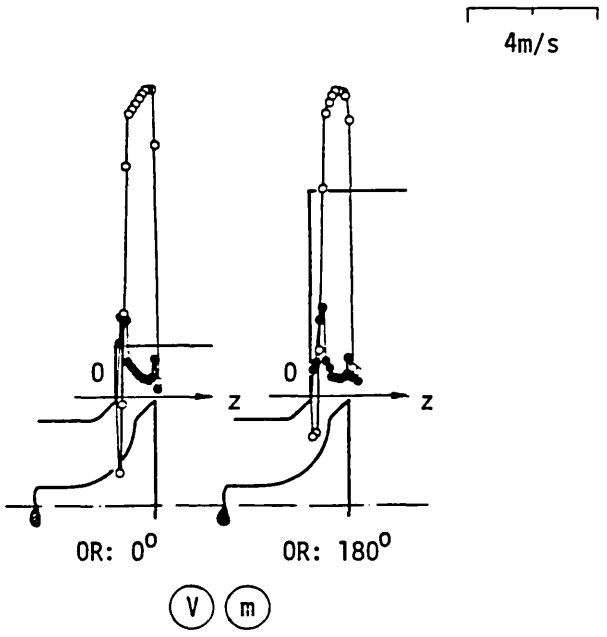

Fig. 2.27
Radial velocity distribution at the valve exit. Off-centre valve, unsteady flow, mid-induction, L = 6 mm, 0 and 180° measurement planes

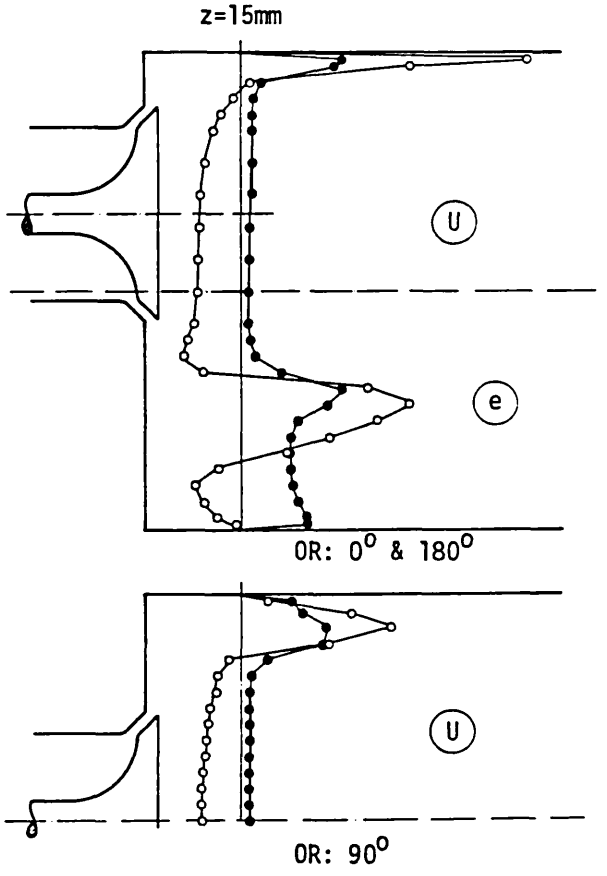

Fig. 2.28
Axial velocity distribution at z = 15 mm. Off-centre valve, unsteady flow, early induction, L = 2.15 mm

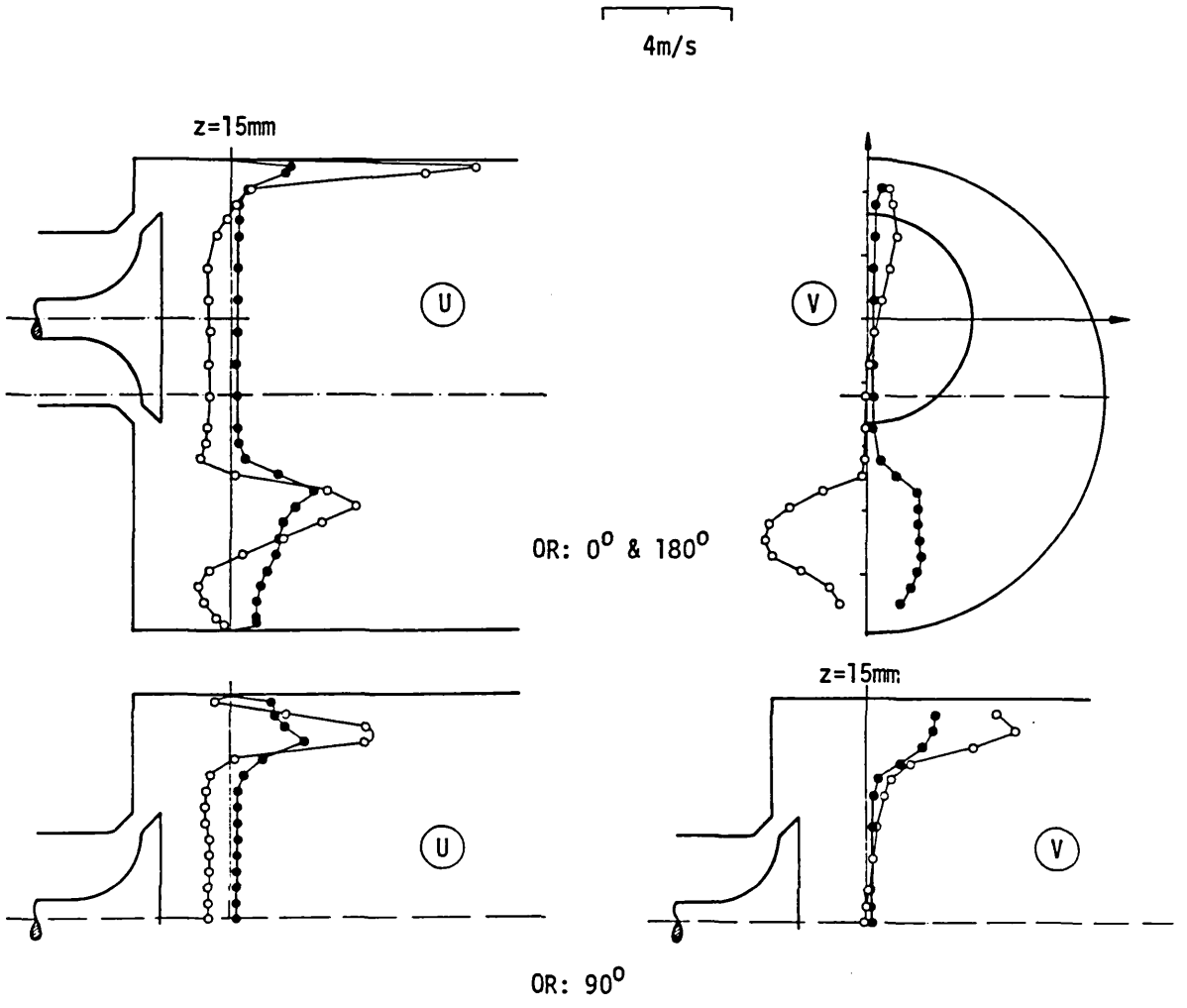

(e)

(a)

Fig. 2.29
(Cont'd)

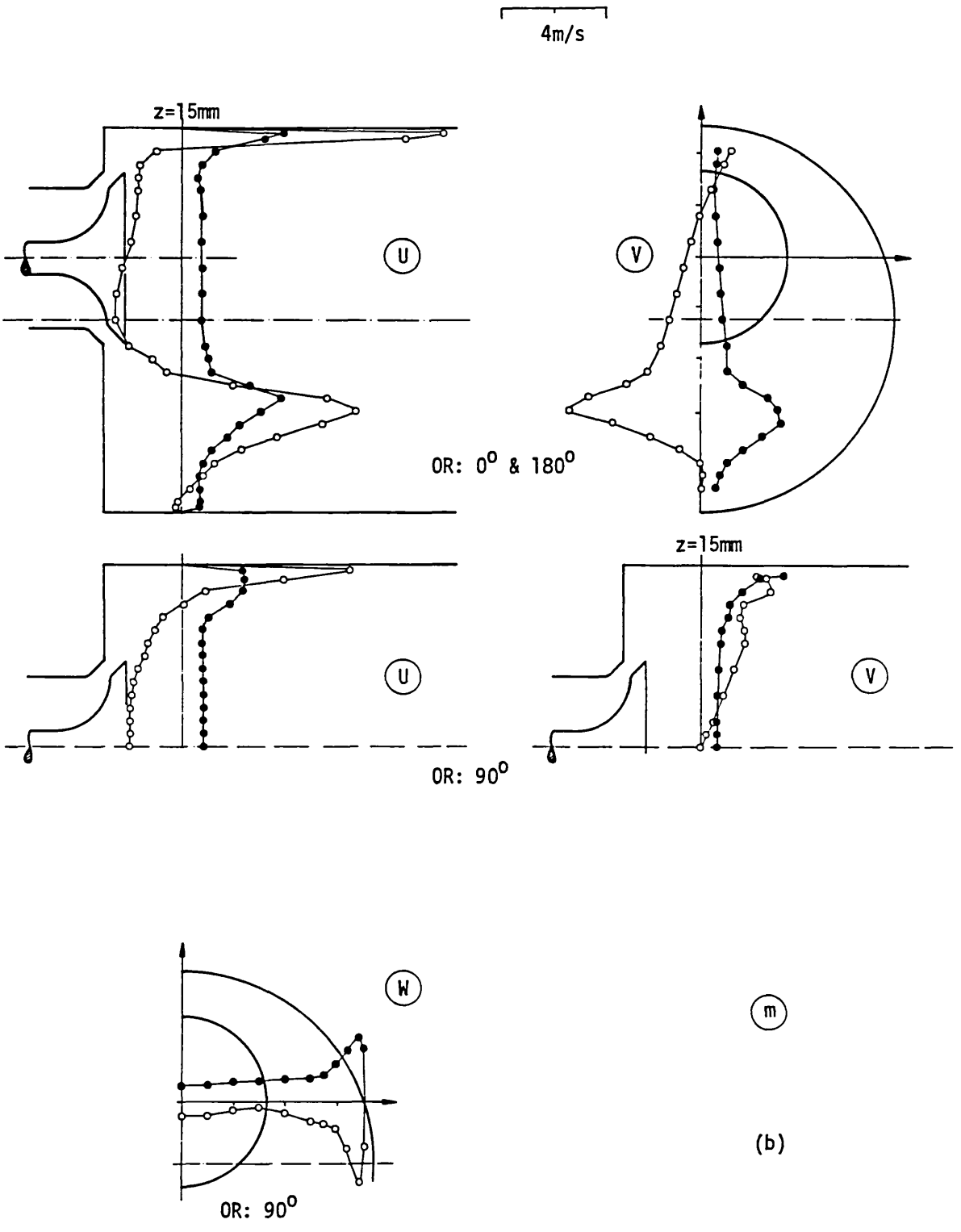

Fig. 2.29 Axial, radial and tangential velocity distribution at z = 15 mm. Off-centre valve, unsteady flow, L = 4.25 mm. a) Early induction, b) Mid-induction

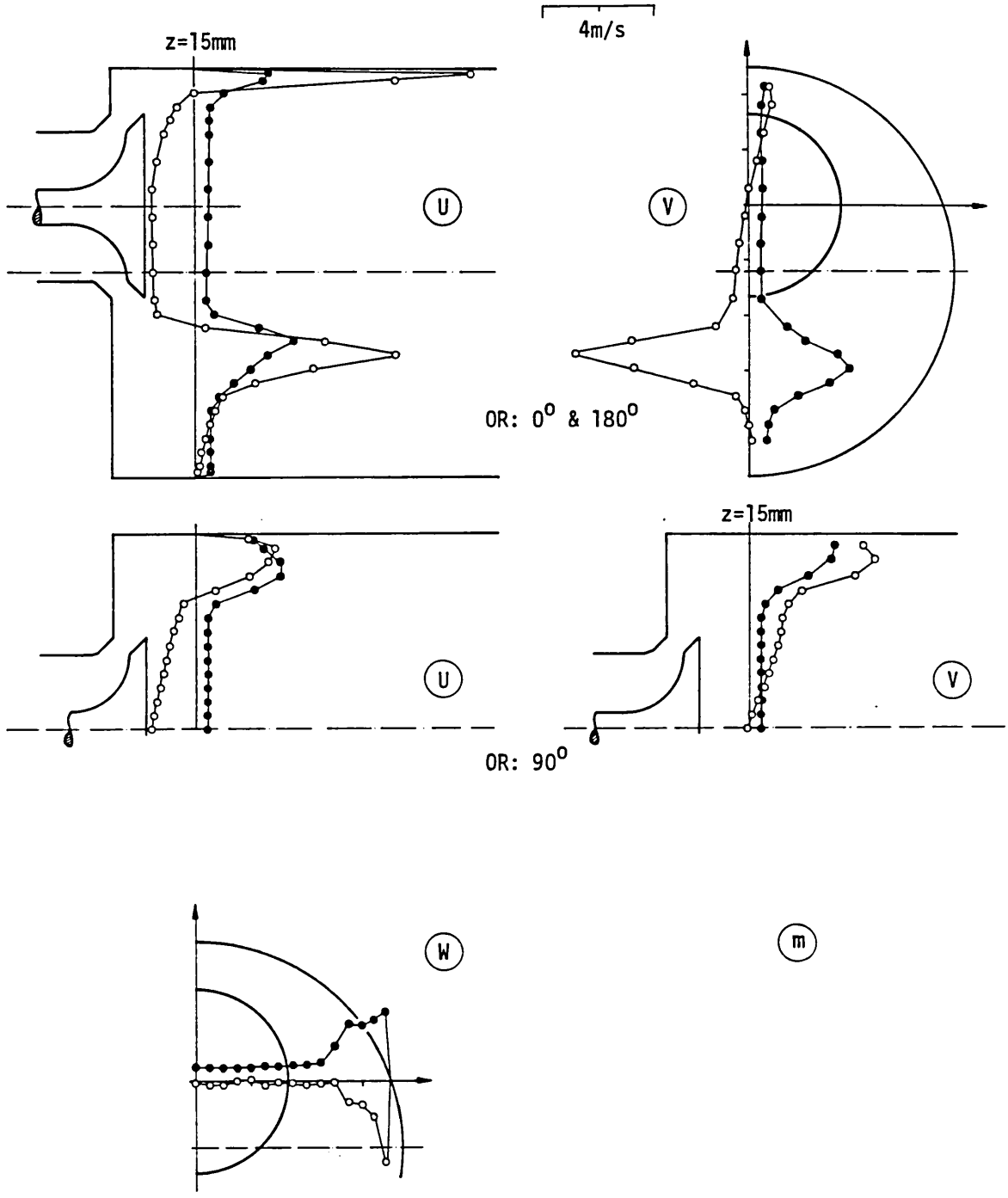

Fig. 2.30 Axial, radial and tangential velocity distribution at z = 15 mm. Off-centre valve, unsteady flow, mid-induction, L = 6 mm

CHAPTER 3

FLOW IN MODEL ENGINES

3.1 INTRODUCTION

This chapter describes an experimental investigation of the in-cylinder flowfield in a model engine motored at 200 rpm with various intake port and combustion chamber configurations.

The influence of valve and piston operation on the valve exit flow is investigated in axisymmetric and off-centre port/valve configurations identical to those examined under steady and unsteady flow conditions in the previous chapter. The development of the induction flowfield and its evolution during compression is also investigated for these port/valve configurations with flat and squish piston geometries. Finally, the effect of the induction-generated flow on the TDC mean and turbulent flowfield is examined for various intake port configurations generating substantially different flow structures during induction.

The main objective of these experiments is to examine the memory characteristics of the in-cylinder flowfield and to investigate the extent to which the TDC flowfield can be controlled by the details of the induction process. The second objective is the complete characterisation of simple intake port configurations under operating conditions and the comparison of their behaviour with that under steady flow conditions. The final objective is the detailed description of the in-cylinder flowfield in axisymmetric and three-dimensional engine geometries to provide a database and assist the development of multi-dimensional prediction methods.

The following two sections describe the flow configurations and experimental systems used in this study. The results obtained in the model engine with simple intake port configurations are presented in section 3.4, followed by sections 3.5 and 3.6 describing the in-cylinder flow development with roll- and swirl-producing intake ports respectively. A summary of the most important findings is given in section 3.7.

3.2 FLOW CONFIGURATIONS

The measurements of the in-cylinder flowfield were obtained in a model engine consisting of a crank mechanism driving a piston inside a cylinder at 200 rpm. The characteristics of the crank mechanism were identical to those used for the unsteady flow experiments described in the previous chapter and are summarised in Table 3.1. The piston of the model engine was made of duraluminium with an extension piece attached to it, allowing the variation of the compression ratio and combustion chamber geometry. Three graphite-reinforced and one PTFE compression rings were used to ensure good sealing and minimum lubrication requirements of the reciprocating piston. The liner of the piston/cylinder assembly was followed by a transparent cylinder made of cast acrylic (perspex) with a wall thickness of 12.7 mm which allowed full optical access in the cylinder space for forward-scatter LDA velocity measurements. The flat cylinder head was made of duraluminium and incorporated a single valve for both intake and exhaust which was operated by a double-cam and rocker mechanism in a four stroke mode. The modular construction of the model engine allowed various combinations of intake port and piston crown geometry to be investigated. These engine configurations are described below and are classified according to their induction system geometry.

a) Plain port configuration

This intake port consisted of an axisymmetric contraction leading to a short cylindrical section and was identical to that used for the steady and unsteady flow experiments presented in Chapter 2. The valve used had a 45^{o} seat angle with rounded corners at both sealing faces, (Valve type II); a diagram of this engine configuration is shown in Figure 3.1. The measurements were obtained for two positions of the intake port/valve assembly on the flat cylinder head: in the first it was located on the cylinder axis and in the second it was offset by 12 mm as shown in Figure 3.2. Two types of piston were used: the first was flat and the second incorporated a transparent cylindrical off-centre squish-bowl with its axis coinciding with the offset valve axis, (Fig. 3.2), both resulting in a volumetric compression ratio of 7.7.

In total four flow configurations were examined as follows:

i) Flat piston with axisymmetrically located stationary valve.

ii) Flat piston with axisymmetrically located and normally operating valve.

iii) Flat piston with normally operating valve, offset by 12 mm from the cylinder axis.

iv) Cylindrical bowl-in-piston and coaxial operating valve, both offset by 12 mm from the cylinder axis.

b) Central directed port configuration

This intake port/valve assembly was identical to the previous configuration but incorporated a 180^{o} shroud on the valve, blocking half of its exit area throughout the lift range, (Fig. 3.3). The valve was centrally located with respect to the cylinder axis and generated a three-dimensional flowfield in the chamber with an axial plane of symmetry bisecting the shroud and, consequently, did not produce any net flux of angular momentum (swirl) in the cylinder. A flat piston was used with this intake port configuration with a compression ratio of 6.7.

c) Swirl producing port configurations

These intake ports consisted of an axisymmetric contraction as the previous configurations. Swirl was produced upstream of the intake valve by means of swirl vanes located near the throat of the axisymmetric contraction, as shown in Figure 3.4. Two types of swirl vanes were used: the first had an angle of 30^{o} with respect to the cylinder axis and the second had a 60^{o} angle giving higher induction swirl level. The valve used with this port had a 60^{o} seat angle with respect to the cylinder head and the whole induction system could be positioned either on the cylinder axis or offset by 8 mm. This valve seat angle and port eccentricity was chosen in order to allow direct comparisons between the present results and those of Arcoumanis et al (1983), obtained with a similar port configuration.

Two piston geometries were again used: the first was flat and the second incorporated an axisymmetric re-entrant squish-bowl, both giving a volumetric compression ratio of 6.7. The following flow configurations were examined:

i) Flat piston with centrally located valve and 30^{o} swirl vanes.

ii) Flat piston with 60^{o} swirl vanes and both, off-centre and centrally located valve.

iii) Re-entrant bowl piston with 60^{o} swirl vanes and both, off-centre and centrally located valve.

The operating characteristics of the model engine and the geometric details of the configurations described above are summarised in Table 3.1.

3.3 MEASUREMENT SYSTEM AND PRECISION

3.3.1 In-cylinder pressure measurements

The in-cylinder pressure was measured by means of a calibrated piezo-electric pressure transducer (Kistler Type 6121) mounted on the engine cylinder. The electric charge yielded by the pressure transducer was converted to an electrical signal by a charge amplifier (Kistler Type 5007) and was monitored through an oscilloscope. The main sweep of the oscilloscope was externally triggered by a pulse from the gating circuit which was connected to an optical shaft encoder (Digitech DR 1034 A5) mounted on the half-speed shaft of the engine. The gating circuit activated the sweep of the oscilloscope at a preset crank angle window with an angular resolution of 0.72^{o}. The instantaneous output voltage of the charge amplifier was measured on the vertical scale of the oscilloscope display and was converted to pressure. The drift of the charge amplifier was minimised by allowing sufficient warm-up time and with appropriate choice of integration time-constant of the system; the zero-pressure voltage output was monitored immediately before and after each measurement.

The accuracy of the in-cylinder pressure measurements is estimated to be better than 3% of the maximum in-cylinder pressure, limited by the reading accuracy on the oscilloscope display and possible non-linearities of the system.

TABLE 3.1

Characteristics of the model engine

Cylinder diameter, D_c, mm	75.8
Piston diameter, D_p, mm	74.8
Stroke, S, mm	94.0
Connecting rod length, ℓ, mm	363.5
Intake valve opens, IVO, deg. BTDC	10
closes, IVC, deg. ABDC	30
Exhaust valve opens, EVO, deg. BBDC	30
closes, EVC, deg. ATDC	10
Maximum lift, L_{max}, mm	9
Engine speed, n, r.p.m.	200
Mean piston speed, $\bar{V}_p$, ms^{-1}	0.627

a) Plain port configuration

Intake/exhaust valve: Diameter,	D_v, mm	33
Seat angle,	ψ, deg.	45
Eccentricity,	e, mm	0 and 12
Flat piston: Clearance at TDC,	c, mm	14
Off-centre bowl: Eccentricity,	e, mm	12
Diameter,	d_b, mm	46
Depth,	h_b, mm	36
Bumping clearance,	b, mm	0.5
Compression ratio, CR		7.7:1

Cont'd.

Table 3.1 (cont'd)

b) Central directed port configuration

Intake/exhaust valve:	Diameter, D_v, mm	33
	Seat angle, ψ, deg.	45
	Shroud opening, deg.	180
Flat piston:	Clearance at TDC, c, mm	16.5
Compression ratio, CR		6.7:1

c) Swirl producing port configurations

Intake/exhaust valve:	Diameter, D_v, mm	34
	Seat angle, ψ, deg.	60
	Eccentricity, e , mm	0 and 8
Swirl vanes:	Vane angle, deg.	30 and 60
Flat piston	Clearance at TDC, c, mm	16.5
Axisymmetric re-entrant bowl:	Entry diameter, d_e, mm	23
	Bowl diameter, d_b, mm	47
	Bowl depth, h_b, mm	40
	Bumping clearance, b, mm	0.6
Compression ratio, CR		6.7:1

3.3.2 Velocity field measurements

Three velocity components were measured with laser Doppler anemometry in the transparent cylinder of the model engine. Particular effort was made to characterise the induction flowfield, especially in the close vicinity of the intake valve. The laser anemometer used was operated in the dual-beam forward-scatter mode and was identical to that described in section 2.3.2 consisting of a 5 mW He-Ne laser and a multiple track rotating diffraction grating. The main variable was the beam-intersection angle which was adjusted according to the flow and optical access requirements by changing the imaging lens and the beam separation. The optical characteristics of a typical system used in this study are shown in Table 3.2 together with those of a special configuration used to measure the axial velocity component at the valve exit, as close as 1 mm to the cylinder head. The in-cylinder flow was again seeded by 2 μm diameter silicone-oil droplets introduced to the flow at the upstream end of the intake port.

The velocity measurements in the non-axisymmetric engine configurations were obtained along planes passing through the valve axis which are indicated in Figures 3.2 and 3.3 as 0^{o}, 45^{o}, 90^{o} and 180^{o} planes. In some cases the 90^{o} plane was offset with respect to the cylinder axis and this, together with the cylinder wall thickness (12.7 mm), resulted in significant refraction of the laser beams even for the axial velocity measurements as illustrated in Figure A4 of Appendix 2.4. For this reason all measurements on the 90^{o} plane were obtained with the piston and cylinder head rotated with respect to the axis of the LDA system, so that a horizontal traverse of the optical system resulted in a traverse of the refracted beams along the required path. Thus, refraction corrections were required only for the tangential and radial velocity components and were limited to velocity magnitude and measurement position on the plane under investigation. This method was particularly useful for measurements inside the off-centre squish-bowl where off-axis light collection was also used to reduce the interference of the refracted and reflected beams with the forward scattered light.

The data processing system was identical to the one described in section 2.3.2 for the unsteady flow measurements. The shaft encoder, however, was mounted on the half-speed shaft of the engine in order to

TABLE 3.2

Optical characteristics of the laser Doppler anemometer

Laser: Wavelength, nm		632.8
Power, mW		5
Lenses: L_1, focal length, mm		100
L_2		300
L_3		300
Diffraction grating:		
Number of line pairs, (N_ℓ)	16384	4096*
Frequency of rotation, (f_r), Hz	variable	0 - 215
Frequency shift (1st order beams), (f_s), MHz	0 - 7.04	0 - 1.76
Beam separation, (s), mm	63	17.8
Beam intersection half angle, ($\phi/2$), deg.	5.99	1.70
Measurement volume dimensions ($1/e^2$ intensity)		
diameter, (b_x), μm	100	100
length, (b_y), μm	953	3390
Number of stationary fringes, (N_f)	32	10
Frequency to velocity conversion factor, (λ^*), ms^{-1}/MHz	3.032	10.67

(*) Third track of the diffraction grating; this configuration was used only for the axial velocity measurements at the exit of the intake valve.

distinguish the four engine strokes. This resulted in a lower resolution of 0.72^{o} of crangk angle, rather than 0.36^{o}, in the present measurements. The window ensemble-averaged velocity measurements, however, were again obtained with crank angle windows of 1.44^{o} during induction and up to 3.6^{o} during compression. A number of cycle-resolved velocity measurements were also obtained with the fast counting system described in section 2.3.2. The quality of the forward-scatter Doppler signal and the high seeding rate allowed a data rate of approximately two signals per degree of crank angle.

According to the error analysis of section 2.3.3 the average uncertainty of the velocity measurements during induction is expected to be 4 and 8% for the mean and rms velocity measurements with maximum errors of 10 and 15% respectively in regions of steep velocity gradients and high turbulence intensity. The corresponding uncertainty of the measurements during compression is expected to be lower, around 3 and 5% for the mean and r.m.s. velocities, mainly stemming from statistical uncertainties related to the sample size.

3.4 RESULTS: Plain port configuration

3.4.1 Pressure measurements

The lift diagram of the "intake valve" of the model engine was measured by a dial gauge micrometer under static conditions and is shown in Figure 3.5 together with the piston speed from IVO to IVC. In the same figure the valve lift "curtain" area ($A_L = \pi.D_v.L$) is shown against crank angle and is bounded upwards by the port area ($A_P = \frac{\pi}{4}(D_P^2 - d_S^2)$). Using the discharge coefficient, C_L, derived in section 2.4.1 for the instantaneous piston speed, (see Figure 2.12), the effective valve flow area ($A_E = C_L.A_L$) has been calculated and is also presented in Figure 3.5. These data would be necessary to calculate the peak cylinder pressure in an engine motored at high speeds. For the present low speed engine, however, it can be shown that the induction process is almost incompressible and that the air mass trapped in the cylinder is almost independent of the discharge characteristics of the valve.

The in-cylinder pressure history is presented in Figure 3.6 in terms of absolute pressure, p_θ, against crank angle and shows that the peak absolute pressure inside the cylinder was 9.5 bar. The same results are plotted in Figure 3.7a in logarithmic scales normalised by the peak absolute pressure and the corresponding clearance volume at TDC of compression. The slope of these curves yields the magnitude of the polytropic process exponent, n, of the equation

$$\frac{p_{TDC}}{p_\theta} = \left[\frac{V_\theta}{V_{TDC}}\right]^n$$

The curves of Figure 3.7a indicate that the compression process is nearly isothermal ($n \simeq 1.1$) and the expansion process has a polytropic exponent closer to adiabatic ($n \simeq 1.2$). It must be noted here that the calculated swept volume V_θ takes into account the intake valve closure point and the piston crevice volume (2% of V_{TDC}); although the nominal volumetric ratio of the engine is 7.7 the actual compression ratio (V_{IVC}/V_{TDC}) is only 6.6. Figure 3.7b shows similar results obtained in the model engine operating with a lower nominal compression ratio of 6.7. In this case both compression and expansion processes are closer to adiabatic as indicated by the slopes of the corresponding curves. This should be attributed to the relatively lower heat losses in the low compression ratio engine due to the lower temperatures encountered during the compression stroke. An interesting feature in both cases is the abrupt change of pressure curve slope during expansion at around $\theta = 400^o$. This phenomenon may be attributed to the condensation of air moisture at this instant which is visually manifested by the formation of a cloud in the cylinder volume during early expansion.

The accurate calculation of the cylinder pressure is important for the theoretical prediction methods since it determines, together with the cylinder temperature, the density of the air charge throughout the engine cycle. This is usually accomplished by simulating the heat losses from the cylinder by use of wall functions and with several assumptions with respect to the cylinder wall temperature. These methods, however, cannot represent air leakages through the piston rings and the non-uniform temperature of the various parts of the piston/cylinder assembly.

The present results are expected to provide useful guidance for the correct choice of the corresponding model variables.

3.4.2 Velocity field measurements

The results of the in-cylinder velocity measurements are presented and discussed in the following paragraphs of this section. Sub-section 3.4.2.1 describes the induction flowfield at the exit and downstream of a stationary intake valve in an axisymmetric port/cylinder configuration. These results are compared with those obtained with a normally operating valve configuration (sub-section 3.4.2.2) and with those of the steady and unsteady flow experiments presented in the previous chapter and conclude the investigation related to the validity of the quasi-steady assumption for the intake valve flowfield. Sub-sections 3.4.2.3 and 3.4.2.4 present similar results in non-axisymmetric engine geometries with flat and squish pistons respectively. The development of the in-cylinder flow throughout induction and compression is also studied and the effect of flow asymmetry and piston configuration on the flowfield at TDC of compression is investigated.

The results of the velocity measurements are presented in all cases normalised with the mean piston speed, $\overline{V}_p = 0.627$ ms^{-1}, defined as

$$\overline{V}_p = \frac{S.\omega_e}{\pi}$$

3.4.2.1 Axisymmetric stationary valve

The model engine with the flat piston configuration was used with the valve located on the cylinder axis and held open throughout the engine cycle. Measurements of axial and radial velocity components were obtained at the exit plane and downstream of the valve at crank angles θ = 30, 48

and 68 degrees and for valve lifts L = 4.25, 6 and 8 mm respectively. These crank angles were chosen to correspond to the valve lifts of the normal engine operating conditions as shown in the valve lift diagram of Figure 3.5.

The radial and axial velocity measurements obtained at the valve exit plane (r = 17 mm) are shown in Figure 3.8. The axial velocity component was measured with small intersection angle of the laser beams and the corresponding turbulence intensity values may have been overestimated by velocity gradient broadening due to the increased length of the measuring volume (Table 3.2). No axial velocity measurements could be obtained closer than 1 mm to the cylinder head due to limited optical access in this region. Comparison of the relative magnitudes of radial and axial velocities indicates that the flow issues from the valve passage at almost the same angle as the valve seat, varying slightly (45 ± 2^{o}) with valve lift. The radial velocity measurements clearly show the presence of two flow regimes throughout the valve lift range, characterised by the flow separation from the valve seat for lifts greater than 6 mm. Turbulence intensity increases towards mid-induction as a result of longer time available for turbulence transport from the shear layers to the core of the annular jet. Comparison with the results obtained under steady flow conditions (Fig. 2.14), which are shown again for clarity in Figure 3.9, confirms the similarity in the mean flow pattern. The velocity magnitudes are different due to the different mass flow rates but the mean velocity distribution, flow angle and length of the recirculation regions near the valve seat are almost identical for the three valve lifts. Turbulence intensity is higher for the unsteady flow case at $\theta = 68^{o}$, probably due to the flow deceleration at this crank angle. For this flow configuration it can be stated that the presence of the flat piston operating downstream of the stationary valve did not influence the velocity distribution at its exit; the valve flow characteristics are represented well by steady flow tests performed with the appropriate Reynolds number.

The in-cylinder axial and radial velocity distributions are shown in Figure 3.10 for the same valve lifts and crank angles as the valve exit results discussed above. For valve lift L = 4.25 mm and crank angle $\theta = 30^{o}$ the flow issues from the valve at about 45^{o} to the cylinder axis, as discussed earlier, but immediately deviates towards the cylinder axis

as indicated by the relative magnitudes of axial and radial velocity components at z = 4.25 mm (Fig. 3.10a). Further downstream, at z = 15 mm (Fig. 3.10b), a complex vortical pattern is present. The incoming flow through the valve impinges on the piston face and splits into two, forming a corner vortex at the cylinder wall and a main vortex behind the valve. However, due to the simultaneous motion of the piston, part of the air charge near the centre-line began to follow the piston without knowledge of the developing wake of the valve. The result of this delay is the formation of a third vortex near the centre-line. Turbulence is generated at the shear layer around the valve and is gradually transported in the wake region, as indicated by the continuously decreasing values of turbulence intensity towards the cylinder axis. With valve lift L = 6 mm at $\theta = 48^{o}$ (Fig. 3.10c) the central vortex disappears. A main vortex behind the valve occupies most of the cylinder space and a corner vortex spans the cylinder wall periphery. The mean flow direction at the shear layer region at z = 15 mm deviates towards the cylinder axis and turbulence intensity is uniformly distributed inside the wake of the valve. Similarly at $\theta = 68^{o}$ with L = 8 mm the flow adjusts itself in the space available for the growth of the wake of the valve exhibiting characteristics similar to those with a valve lift L = 6 mm. The flow angle varies significantly with radial position at z = 15 mm reaching 45^{o} at the shear layer region.

Comparison of the in-cylinder flow results with the corresponding steady and unsteady flow measurements of Chapter 2 confirms that the presence of the piston significantly influences the growth of the in-cylinder vortices, as they scale with the piston axial position rather than the valve diameter. In the case of early induction, steady flow tests fail to predict even the gross features of the in-cylinder flowfield.

3.4.2.2 Axisymmetric operating valve

Measurements of two velocity components were obtained in the model engine with flat piston and axisymmetrically located and normally operating valve.

The distributions of radial and axial mean and rms velocities at the exit plane of the operating valve are shown in Figure 3.11 at crank angles θ = 30, 48 and 68^{o} with corresponding valve lifts L = 4.25, 6 and 8 mm. Comparison of these results with those obtained with the stationary valve (Fig. 3.8) and discussed in sub-section 3.4.2.1 indicates that the corresponding mean velocity and turbulence intensity distributions at the valve exit are almost identical in both configurations. The flow again exhibits two flow regimes over the lift range; it initially emerges as a plug type flow at 45^{o} to the cylinder axis and later separates from the valve seat deviating at the same time towards the cylinder axis until mid-intake (θ = 68^{o}) when it starts deviating towards the cylinder wall as a result of the pressure field downstream of the valve. From these results it can be concluded that for the engine speed of interest the valve operation does not influence the velocity field at its exit plane. Furthermore, comparing these results with those obtained under steady and unsteady flow conditions it can be concluded that with low speed and relatively large clearance at TDC, the flow unsteadiness, valve operation and piston confinement did not affect the valve flow characteristics. The flowfield in the valve exit under operating conditions could therefore be predicted with reasonable accuracy from steady flow tests.

Figure 3.12 shows the axial and radial velocity distribution in the cylinder space during the intake stroke and under normal operating conditions. At early intake (θ = 30^{o}, Fig. 3.12a) three counter-rotating vortices are present as in the stationary valve case with the central vortex occupying larger space, probably due to the opening valve history. Later in the stroke (θ = 48^{o}, Fig. 3.12b) the central vortex has disappeared leaving some evidence of its existence on the slightly decreased magnitudes of reverse velocities near the centre-line. Comparison of these results with those obtained with stationary valve and shown in Figure 3.10 reveals similarities in both mean velocity and turbulence intensity distributions. Radial velocities at the region of the shear layer at z = 15 mm are slightly higher for the operating valve case indicating a more oblique angle of the flow which may be traced back to the changes in the valve flow pattern associated with the varying valve lift. From these results it can be concluded that the in-cylinder flowfield seems to be unaffected of the opening valve history, at least during the first half of the intake stroke.

The similiarity of both valve and in-cylinder flow between stationary valve and normal engine flow configurations has useful practical implications. Accurate predictions of the intake flow field in a real engine can be made from measurements in a non-compressing engine configuration provided that they are obtained at crank angles and valve lifts corresponding to the normal operating conditions. Thus, practical difficulties imposed by the compression stroke (e.g. high pressure, thick cylinder walls etc.) can be avoided and the experimental procedure simplified.

The velocity distribution at TDC of compression is shown in Figure 3.13. The velocity field is characterised by a weak vortical pattern, indicated by the radial velocity measurements obtained at r = 25 mm and shown in Figure 3.13c. Turbulence appears to be homogeneous within 20% and near isotropic with intensity values around 0.45 $\overline{V}_p$. Similar turbulence intensity characteristics have been reported by Arcoumanis et al (1983) in axisymmetric model engine configurations with different valve seat-angle (60^o) and lower compression ratio (6.7), indicating that these operating characteristics do not influence significantly the turbulence field at TDC of compression.

3.4.2.3 Off-centre valve, Flat piston

The cylinder head of the model engine with the flat piston was modified to accommodate the intake port/valve assembly 12 mm off the cylinder axis. Measurements of axial and radial velocity components were obtained across three planes passing through the valve axis as indicated in Figure 3.2. The tangential velocity components were also measured across the 90^o plane. No velocity measurements were obtained in the vicinity of the operating valve as, in the light of the previous results, the velocity distribution at its exit was expected to be similar to that measured under steady and pulsating flow conditions presented is sub-sections 2.4.2.3 and 2.5.2.

The axial and radial velocity distribution at z = 15 mm and $\theta = 30^o$ (L = 4.25 mm) is shown in Figures 3.14a and b respectively, across the three measurement planes. As can be seen from the axial velocity profiles,

a complex vortical pattern is present in the cylinder space during early induction; it exhibits similar features to those observed with the axisymmetric valve configuration with two counter-rotating vortices behind the valve, both offset with respect to the valve and cylinder axes. The corner vortex is found only at the 90^{o} plane and does not span the whole cylinder periphery, while a fourth vortex is formed near the cylinder wall on the 180^{o} plane. The formation of the latter vortex can be attributed to the delayed response of the air charge at this far corner of the cylinder to the incoming flow with a similar mechanism to that described earlier for the formation of the central vortex. Turbulence intensity is not uniformly distributed inside the complex wake of the valve with lower values at the region between the valve and cylinder axes, as also found and discussed in the axisymmetric configuration.

At $\theta = 48^{o}$ (L = 6 mm, Fig. 3.15) the in-cylinder flow develops to form a main vortex behind the valve, again offset with respect to both the valve and cylinder axes. A secondary corner vortex is also formed spanning part of the wall periphery and varying in size and strength, being larger across the 180^{o} plane. As indicated by the radial velocity measurements at z = 15 mm the flow direction in the jet region across the 0^{o} plane is almost parallel to the cylinder wall and has a significant spread on the other planes. Turbulence intensity is now uniformly distributed inside the wake of the valve with maximum values in the annular jet regions. The mean and turbulent velocity distributions on the 90^{o} plane at both $\theta = 30^{o}$ and 48^{o} show, not surprisingly, similarities with the corresponding distributions in the axisymmetric case, (Figures 3.12a and b). The velocity distribution at $\theta = 68^{o}$ (L = 8 mm) is shown in Figure 3.16 and exhibits similar flow characteristics to that at $\theta = 48^{o}$. The annular jet region is now better defined along the 90^{o} and 180^{o} planes with flow angles varying with azimuthal position. Figure 3.17 shows the axial velocity distribution at z = 15 mm during late induction, ($\theta = 134^{o}$) with a corresponding valve lift of L = 6 mm (valve closing period). Comparison of these results to those obtained at early induction ($\theta = 48^{o}$), with the same valve lift, (6 mm) shows differences in velocity magnitudes and in vortex sizes and locations, although the piston speed at both crank angles is nearly the same. Further comparison with the corresponding steady flow measurements of Figure 2.20b indicates that the velocity distribution at $\theta = 134^{o}$ is better

simulated by the steady flow results than the distribution at early induction. This is because the instantaneous piston position at $\theta = 134^{o}$ is almost three times the valve diameter (z_p = 96 mm) allowing the vortex pattern to develop and scale with the valve and cylinder diameter as in the steady flow case.

The axial and radial velocity distributions during the compression stroke, at $\theta = 288^{o}$ and 360^{o} (TDC) are shown in Figures 3.18 and 3.19 respectively. The vortical structure created during intake has collapsed at $\theta = 288^{o}$ and the turbulence intensity significantly suppressed to values around 0.7 $\bar{V}_p$, uniformly distributed in all directions. At TDC of compression ($\theta = 360^{o}$, Fig. 3.19) turbulence intensity is reduced even more to values around 0.45 $\bar{V}_p$ as in the axisymmetric valve configuration. A weak flow structure is present in the clearance volume consisting of a counter-clockwise rolling vortex, evidenced by the radial velocity measurements of Figure 3.19b. This flow structure may be attributed to the intake flowfield where, as shown in Figures 3.15 and 3.16, the major radial velocity components near the cylinder head were directed downwards, (negative $\bar{V}$), thus inducing a weak counter-clockwise rolling mean flow structure.

The development and decay of the tangential mean flow pattern is shown in Figure 3.20 along the 90^{o} plane at z = 15 mm. A double vortex structure is present in this plane during early induction ($\theta = 30^{o}$ and 48^{o}, Figs. 3.20a, b) which reduces to a single vortex at mid- to late induction ($\theta = 68^{o}$ and 134^{o}, Figs. 3.20c, d). This tangential flow pattern is created by the impingement of the off-centre valve flow on the cylinder wall as shown with the steady flow results of Figure 2.18f. Comparison of these results with the steady flow measurements shows similar tangential flow patterns for the two configurations only during late induction ($\theta = 134^{o}$). The interaction of the developing vortex near the wall with the flow field near the centre-line is shown in Figures 3.20a to c where the strength and size of the central vortex are gradually decreased due to the increasing strength of the outer vortex. Soon after the inlet valve closure the tangential flow pattern had decayed considerably (Fig. 3.20e) and collapses entirely at TDC of compression (Fig. 3.20f). The observed decay of the tangential vortical pattern is mainly attributed to the continous exchange of momentum between the

component vortices as they grow during induction symmetrically around the 0^{o} and 180^{o} plane.

Overall it can be concluded that the complex vortical pattern generated during induction by the off-centre intake port decayed rapidly after inlet valve closure and resulted in a weak rolling flow structure at TDC of compression. The breakdown of the induction generated vortices resulted in a near uniform turbulence intensity distribution at inlet valve closure which decayed to values around 0.45 $\overline{V}_p$ at TDC of compression as in the axisymmetric valve configuration.

3.4.2.4 Off-centre valve, Piston-bowl

The piston of the model engine was modified to incorporate a cylindrical bowl located on the axis of the off-centre operating valve. Measurements of the three velocity components were obtained at the valve exit and cylinder space as well as inside the piston bowl. As can be deduced from the valve lift and piston position diagrams, shown in Figure 3.6, the valve was axisymmetrically confined by the off-centre piston-bowl during the early stages of the intake stroke.

The radial and axial velocity distributions at the valve exit are shown in Figures 3.21a and b across the 90^{o} and 180^{o} measurement planes respectively. These measurements have been obtained at crank angles $\theta = 30^{o}$, 48^{o} and 68^{o} corresponding to valve lifts L = 4.25, 6 and 8 mm respectively as with the flat piston configurations. The results obtained on the 90^{o} plane (Fig. 3.21a) indicate the presence of the two flow regimes identified in all previous cases with the flow detachment from the valve seat for lifts greater than 6 mm. The axial velocity distribution indicates a radial spread of the valve jet with the larger lifts and, when compared with the radial velocity component, shows a considerable variation of flow angle with valve lift. The results obtained on the 180^{o} plane, Figure 3.21b, are in contrast to those of the previous steady and unsteady flow configurations in that the flow at $\theta = 30^{o}$ (L = 4.25 mm) separates from the valve head and issues towards the cylinder wall at an angle of about 60^{o} with respect to the cylinder axis.

At $\theta = 48^{o}$ (L = 6 mm) the flow remains attached on both sealing faces of the valve and separates from the valve seat at $\theta = 68^{o}$ (L = 8 mm). Comparison with the results obtained under steady and pulsating flow conditions, (Fig. 2.17), shows that the close proximity of the piston to the valve exit, especially during early intake, strongly influences the valve flow pattern. Thus, in contrast to the observations made with the flat piston, the valve exit flowfield cannot be decoupled here from the in-cylinder flowfield and the steady flow tests cannot simulate the corresponding flow patterns.

The axial velocity distribution at z = 15 mm and $\theta = 30^{o}$, Figure 3.22, indicates that the non-uniform velocity distribution around the valve periphery induces a three-dimensional flow pattern inside the co-axial bowl consisting of a clockwise rolling vortex. The valve jet enters the piston bowl only on the 0^{o} plane and seems to deviate in the clearance space on the 180^{o} plane. A similar but stronger flow pattern is present inside the bowl at $\theta = 48^{o}$ and z = 30 mm (Fig. 3.23). The magnitudes of the axial velocities outside of the bowl are much larger than the radial ones on the 0^{o} and 90^{o} planes and suggest that the inlet flow still enters the piston-bowl at these regions but not near the 180^{o} plane where the inlet flow angle is almost 45^{o} and impinges on the piston face forming a double vortex in the clearance space, similar to that observed with the flat piston configuration (see Fig. 3.14). At $\theta = 68^{o}$ (L = 8 mm, Fig. 3.24) the flow pattern inside the piston bowl remains that of a rolling vortex with significantly lower reverse velocities at z = 45 mm. The axial and radial distribution in the cylinder space resembles that obtained with the flat piston configuration indicating the presence of a main vortex behind the valve and a single corner vortex spanning part of the cylinder periphery with varying strength and size. Turbulence intensity increases both in the valve wake and inside the piston bowl relative to that at early intake. The development of the tangential flow pattern at $\theta = 48^{o}$ and 68^{o}, Figures 3.23 and 3.24, does not present similar structure to that observed at early intake with the flat piston (Fig. 3.20) probably due to the larger space available for the flow development between the bottom of the piston bowl and the valve head.

The axial velocity distribution in the cylinder space and inside the bowl, measured during the compression stroke ($\theta = 288^{o}$, Fig. 3.25)

indicates a deceleration of the flow near the cylinder axis and uniform turbulence levels of about $0.7\,\overline{V}_p$ both outside and inside the bowl as with the flat piston configuration. The flow structure generated during intake has collapsed soon after inlet valve closure and turbulence is suppressed. At $\theta = 314^o$ (Fig. 3.26) a weak axial flow towards the piston-bowl is observed accompanied by a radial motion towards the bowl axis on the 90^o and 180^o planes. This signifies the onset of the squish which, being non-axisymmetric, results also in a tangential flow pattern near the piston face directed towards the smaller squish area part of the piston face, (Fig. 3.26c). The in-bowl flow pattern is that of a three-dimensional double vortex and turbulence levels are reduced to about $0.6\,\overline{V}_p$.

At TDC of compression the in-bowl axial flow pattern is transformed to a single rolling vortex on the 0^o and 180^o planes (Fig. 3.27a) and a double vortex on the symmetry plane (Fig. 3.27b) very similar to that measured in an axisymmetric valve/bowl configuration (Arcoumanis et al, 1983). Turbulence intensity is almost uniformly distributed with values $0.5 - 0.6\,\overline{V}_p$, with slightly lower magnitudes towards the bottom of the bowl. The rolling flow structure inside the bowl is also illustrated by the radial and tangential velocity measurements shown in Figure 3.28.

From the results discussed above it can be concluded that the intake valve flowfield was significantly affected by the piston face proximity. However, the resulting complex flow structure generated during the intake stroke collapsed soon after inlet valve closure to a nearly uniform flow which was then transformed due to the non-axisymmetric squish motion.

3.4.3 Summary

The velocity field measurements in a model engine operating at 200 rpm with an off-axis and an axisymmetrically located plain axisymmetric intake port revealed the following:

1. The velocity distribution at the exit plane of the intake valve was not influenced by the flow unsteadiness and valve operation at the

engine speed investigated. The presence of the operating piston had a negligible effect on the valve flowfield when the TDC clearance was relatively large (half valve diameter); the close proximity of the squish-piston to the valve exit, however, significantly influenced the velocity distribution at the valve exit during early induction. Thus steady flow tests could simulate the valve flow under operating conditions only in the case of the flat piston. The size of the vortices generated during early induction scaled with the instantaneous piston position so that the in-cylinder flowfield downstream of the valve could not be predicted by simple steady or unsteady flow simulations in open-ended cylinder configurations.

2. The exchange of momentum between the induction-generated vortices on the tangential plane in the off-centre valve configuration resulted in their decay by inlet valve closure. The stronger axial flow structures decayed gradually throughout induction and compression and resulted in a weak flow structure at TDC of compression with the flat piston. The break-down of the induction-generated flow structures resulted in a near uniform distribution of turbulence intensity at early compression with similar magnitudes for both intake valve and piston configurations.

3. The compression process with the flat piston resulted in an almost uniform and near isotropic turbulence distribution at TDC of compression with intensity values around $0.45\,\overline{V}_p$. The off-axis squish piston, however, resulted in a three-dimensional vortex pattern inside the piston-bowl at TDC of compression and increased turbulence intensity of $0.5 - 0.6\,\overline{V}_p$.

Considering these results with those obtained in similar model engine configurations with lower compression ratios and different valve seat angle and valve eccentricity, (Arcoumanis et al, 1982a, 1983, 1984a), it can be concluded that these parameters do not have a significant effect on the TDC flow field.

3.5 RESULTS: Central directed port configuration

The system of vortices generated during induction with the plain port configuration decayed soon after the closure of the intake valve and did not contribute significantly to turbulence production during the compression stroke. In an effort to investigate the possibility for an axial flow structure to persist during compression and its effect on turbulence production after the closure of the intake valve, a central directed port configuration with a shrouded valve was arranged. The objective was to create a single rolling vortex inside the cylinder during induction, which would survive after the closure of the intake valve.

The inlet flow has been studied in terms of valve discharge coefficient and velocity distribution at the valve exit under steady flow conditions. These results are presented in sub-section 3.5.1 and are followed by those obtained in the model engine which are presented in sub-section 3.5.2. The main findings are summarised in sub-section 3.5.3.

3.5.1 Inlet flow characteristics

The discharge coefficient of the shrouded valve was measured for a constant mass flowrate of 12 kg/h (corresponding to an engine speed of 200 rpm) according to the procedure outlined in sub-section 2.3.1. The results are presented in Figure 3.29 and show the discharge coefficient C_L based on both the true open area ($\pi . D_v L/2$) and the fictitious valve lift "curtain" area ($\pi . D_v . L$). This representation has been chosen to facilitate comparison of these results with those obtained with the unshrouded valve Type II, which are also presented in the same figure. Comparison of the two curves based on the "curtain" area indicates that the discharge coefficient of the shrouded valve is almost 50% lower than that of the unshrouded valve and would lead to a dramatic deterioration of the volumetric efficiency of a practical high speed engine; no significant effect, however, is expected in the low speed model engine. Close examination of the discharge coefficient curve of the shrouded valve suggests that there exist at least two flow regimes in the valve lift range, indicated by an abrupt change of slope at L = 5.5 mm. When the

C_L curve based on the true open area is compared with that of the unshrouded valve, it can be seen that the discharge coefficient of the former is significantly lower at low valve lifts, probably due to increased frictional losses at the edge of the shroud and the higher velocities through the valve passage. At higher lifts this becomes less apparent as the ratio of flow to wall area increases and the two curves approach each other.

The distribution of radial and axial velocity components at the exit from the shrouded valve was measured along three axial planes, (indicated as 0^o, 45^o and 90^o measurement planes in Figure 3.3), under steady flow conditions as described in sub-section 2.3.2. The results are shown in Figure 3.30 and 3.31 for valve lifts of 3 and 6 mm respectively. Comparison of the radial velocities along the 0^o measurement plane (symmetry plane) allows the two flow regimes suggested by the discharge coefficient measurements to be identified. The flow at L = 3 mm is attached on both sealing faces, while at L = 6 mm it detaches from the valve sealing face. The flow angle at L = 3 mm is about the same as the valve seat-angle (45^o), as can be deduced from the relative magnitudes of the radial and axial velocity components, and remains constant around the valve periphery, at least up to the 45^o measurement plane. At L = 6 mm the flow deviates appreciably from the seat angle and discharges at an angle of about 60^o with respect to the cylinder axis. When these results are compared with those obtained with the unshrouded valve (Fig. 2.14) show that the presence of the shroud forces the flow to discharge at an angle larger than that of the valve seat and results in flow separation from the valve head rather than the valve seat. Turbulence intensity at the valve gap is of similar magnitude to that in the unshrouded valve with the exception of the shear layer at the edge of the shroud.

3.5.2 In-cylinder flowfield

The axial and tangential velocity distribution was measured along the 0^o and 90^o measurement planes at an axial location z = 40 mm from the cylinder head during late induction ($\theta = 144^o$). The results obtained along the symmetry plane (0^o plane, Fig. 3.32a) clearly show the presence

of a strong rolling vortex in the axial direction with maximum velocities of 10 - 12 $\overline{V}_p$ near the cylinder wall. The axial flow pattern along the 90^o measurement plane is more complex with maximum forward velocities of 6 $\overline{V}_p$ near the cylinder wall which compensate for the return flow of the main rolling vortex along this measurement plane. Turbulence intensity is not uniformly distributed along the measurement planes and varies between 1 and 2 $\overline{V}_p$. These magnitudes are similar to those reported by Arcoumanis et al (1982b) for the same phase of induction and for various axisymmetric intake port configurations.

The velocity measurements obtained along the mid-plane of the clearance volume at TDC of compression ($\theta = 360^o$) are shown in Figure 3.33. The axial velocity distribution on the 0^o and 45^o measurement planes suggests that the rolling vortex generated during induction survived the induction and compression strokes and resulted in a similar, but weaker, flow structure at TDC of compression. The tangential flow pattern along the same plane is that of a double vortex with maximum velocities of 1 $\overline{V}_p$. The persistence of the induction-generated flow structure throughout compression casts doubt in the generality of previous statements about the flow memory in the axial direction. It appears that the early decay of the axial flow structure with simple intake port configurations was a result of the near axisymmetric development of the counter-rotating vortices behind the valve; the exchange of momentum between these pairs of vortices resulted in their decay by the closure of the intake valve. In the present configuration, angular momentum is induced by the directional port on the plane of symmetry and its decay is controlled mainly by the frictional losses on the cylinder boundaries. This is clearly demonstrated by the theoretical analysis of Gosman et al (1985) which indicates that the strength of the rolling vortex during late compression ($\theta = 320^o$) is still one third of that at $\theta = 144^o$ and it is only after this that an appreciable decay occurs near TDC.

The turbulence intensity distribution at TDC of compression is also shown in Figure 3.33. Turbulence is not uniformly distributed in the clearance volume and is generally non-isotropic with an intensity which varies between 1 and 1.3 $\overline{V}_p$ in the cylinder space, that is twice as large as that usually observed at TDC of compression in disc-type combustion chambers. Similar turbulence intensity magnitudes have been calculated

for this engine configuration by Gosman et al (1985) who found that the volume-averaged turbulence intensity was $0.8\overline{V}_p$. This was again higher than in all previous calculations in disc-type combustion chambers where turbulence intensities of $0.45 - 0.5\overline{V}_p$ were predicted and were considered to be the upper limit of turbulence intensity in such configurations (Hayder et al, 1984). This increase of turbulence levels cannot be attributed to high turbulence intensity during induction since, as shown above, the values at the valve passage and inside the cylinder are comparable to those of plain port configurations. A detailed analysis of turbulence energy balance (Gosman et al, 1985) indicated that, contrary to other unshrouded valve configurations, the total turbulence production during compression associated with the compression and shear stresses counterbalances dissipation and peaks near $\theta = 320^{o}$. The main contributor to turbulence production was found to be the Reynolds stresses stemming from the continuously increasing velocity gradients as the persisting rolling vortex was compressed. These shear forces eventually predominated and caused the final decay of the rolling vortex with consequent production of turbulence.

This mechanism of turbulence augmentation suggests that the TDC turbulence levels in disc-type combustion chambers can be increased through the induction flowfield. It should be remembered, however, that this was achieved at the expense of the discharge capacity of the induction system and any attempt to implement this method to practical engine configurations should seek an optimum balance between these contradictory requirements.

3.5.3 Summary

The velocity measurements in a model engine with a centrally located directed intake port revealed the following:

1. A complex multi-vortex structure was created during induction, the most important characteristic of which was a strong rolling motion on the axial plane of symmetry.

2. The induction-generated rolling vortex was sustained and amplified during compression, contrary to the near-axisymmetric axial flow structures generated by plain intake port configurations.

3. The turbulence intensity in the clearance volume of the disc-type combustion chamber at TDC of compression was found to be between 1 - 1.3 $\overline{V}_p$, nearly double that achieved in similar engine configurations with plain intake ports. The increase of TDC turbulence was associated with the straining of the long-lived axial flow structure during the compression stroke.

This study also demonstrated the advantages of combined experimental and theoretical investigations in gaining valuable insight into the in-cylinder flow processes.

3.6 RESULTS: Swirl producing port configurations

The evolution of the induction-generated flow structures on the axial and tangential planes of the cylinder of the model engine has been investigated in the previous two sections for several intake port configurations. A common feature of these intake ports was that they did not produce any net flux of angular momentum on the tangential plane of the cylinder and the resulting flow was symmetric around an axial plane. These features led to a rather short life of the tangential flow structures which decayed by the time the intake valve closed. It is known, however, that when swirl is imparted to the cylinder charge during induction, its angular momentum tends to be conserved and results in an organised swirl flow pattern at TDC of compression.

This section describes velocity field measurements obtained in the model engine for two idealised intake ports generating swirl by means of swirl vanes. The flow development throughout the engine cycle is studied in terms of velocity distribution inside the cylinder with two piston configurations and the results are presented in sub-section 3.6.1 with those related to the decay of angular momentum of the air charge in sub-section 3.6.2. These are followed by an investigation of the precession of the swirl centre presented in sub-section 3.6.3 and a summary in sub-section 3.6.4.

3.6.1 Velocity field measurements

The radial distributions of swirl velocity in the vicinity of the intake valve (z = 10 mm) at $\theta = 36^{o}$ and 90^{o} are shown in Figure 3.34 for the three axisymmetric configurations. With low swirl (30^{o} vanes, Fig. 3.34a) higher velocities occur nearer to the cylinder wall while with high swirl (60^{o} vanes, Fig. 3.34b) they occur nearer to the cylinder axis. An intermediate shape of swirl velocity distribution is obtained with the re-entrant bowl piston configuration (Fig. 3.34c). These differences in swirl velocity distribution may be explained by considering the conservation of angular momentum and the effect of the swirl-induced radial pressure gradient on the in-cylinder flow. In the low swirl case, the radial pressure gradient is balanced by the centrifugal force $\rho(W^2/r)$ and results in the usual flow pattern with higher swirl velocities near the cylinder wall. With increasing swirl the radial pressure gradient is not balanced by the centrifugal force alone and a radial motion towards the cylinder axis is initiated. This forces the swirl velocities at this region to increase in order to conserve the angular momentum on this plane. With the re-entrant bowl configuration, the smaller clearance between piston face and cylinder head makes the contribution of the viscous forces significant, as indicated by the magnitude of the shear stresses above the squish area of the piston, and opposes the distortion of the swirl velocity profile. An additional reason may be the effect of the outflow from the piston bowl in the wake of the valve which alters the pressure field at this region.

The distribution of swirl velocities at the end of induction ($\theta = 205^{o}$) is shown in Figure 3.35 for the three axisymmetric configurations. The intake port with 60^{o} swirl vanes gave a flatter distribution and nearly double magnitudes of swirl velocities than the 30^{o} vanes, with steep velocity gradients near the swirl centre which does not always coincide with the cylinder axis. The main differences between flat and re-entrant bowl piston are concentrated near the cylinder axis where, with the latter, mean velocity gradients are less steep and the offset of the swirl centre is smaller. The differences in the swirl velocity distribution at inlet valve closure reflect those observed during early induction and the axial stratification of the swirl velocities reflects the history of the induction process for each flow configuration. Turbulence intensity away

from the cylinder axis is generally lower in the high swirl case, and decreases towards the piston face. The turbulence intensity near the swirl centre, however, is in all cases higher and increases with velocity gradient steepness and swirl centre offset. This effect is less apparent in the case of the re-entrant bowl and has been also observed by Johnston et al (1979) and Witze (1980b) and was attributed to a "cyclic precession" of the swirl centre which broadens the ensemble-averaged turbulence measurements. A more detailed investigation of this aspect of the in-cylinder swirl flow is described in sub-section 3.6.3.

The swirl velocity distribution at TDC of compression is shown in Figure 3.36. It can be seen that mean velocities over the flat piston tend to solid body rotation with the 30^{o} swirl vanes but not with the 60^{o} vanes, which result in a flatter velocity distribution and steeper gradients near the swirl centre; the swirl characteristics observed during induction persist at TDC of compression. Turbulence intensity decays during compression for both induction swirl levels and is about 15% lower in the high swirl case, away from the cylinder axis where higher magnitudes are observed as at the end of induction. With the re-entrant bowl piston the interaction of swirl with squish results in a complex vortical pattern which is characterised by three counter-rotating toroidal vortices inside the bowl as indicated by the axial velocity measurements of Figure 3.37. The corresponding swirl velocity distribution (Fig. 3.36c) is influenced by the complexity of the axial flow pattern and is not uniform along the axis of the bowl. Turbulence is near homogeneous with average intensity of 1 to 1.5 $\overline{V}_p$, decreasing towards the bottom of the piston-bowl. Comparison of these results with those obtained with an identical piston-bowl configuration but lower swirl level (Arcoumanis et al, 1983) indicates that the increase of induction swirl resulted in a more complex vortical pattern inside the bowl but similar turbulence intensity. These findings support the suggestions of El Tahry (1982) and Gosman and Johns (1978), of unique flow structure inside the bowl for each induction swirl level and the similar turbulence intensity found in both cases confirms that squish is the main mechanism responsible for turbulence production.

3.6.2 Angular momentum

The swirl velocity measurements obtained at IVC and TDC, as well as at late exhaust ($\theta = 684^{o}$), have been processed according to the procedure outlined in Appendix 3.1 to yield the rotational speed ω and angular momentum Ω of the air charge at these phases of the engine stroke. The results obtained are shown in Table 3.3. The swirl ratios (SR) at TDC of compression (defined as the mean rotational speed of the air charge at TDC, normalised by the engine speed) obtained with the 30^{o} and 60^{o} swirl vanes and the flat piston were 1.9 and 5.6 respectively. The corresponding swirl ratio for the re-entrant bowl with the 60^{o} vanes was 11 as opposed to 5, reported for the same piston configuration with 30^{o} swirl vanes (Arcoumanis et al, 1983). The axial distribution of the rotational speed, ω, of the air charge at IVC and TDC is presented in Figure 3.38 and shows a dependence on the radial distribution of the local swirl velocities (Fig. 3.35). In the re-entrant bowl, however, it is clear that the lower parts of the air charge rotate faster than those near the bowl entry. The distribution of angular momentum, Ω, along the axis at IVC (Fig. 3.38) is less uniform with the 30^{o} than with the 60^{o} swirl vanes probably due to the smaller ratio of angular to axial momentum (swirl number, SN) during induction with the first configuration. In addition, the in-bowl angular momentum at IVC was found to be comparable to that at late exhaust ($\theta = 684^{o}$), indicating that the piston bowl does not contribute significantly in the induction process.

The loss of angular momentum from IVC to TDC of compression (Table 3.3) with the flat piston was found to be around 30% for both swirl ratios and the loss throughout the cycle larger for the lower swirl. It was expected that the higher induction swirl would lead to larger decay of angular momentum as a result of greater diffusivity (El Tahry, 1982). However, the increased frictional losses associated with the relatively higher velocities near the wall with the 30^{o} swirl vanes, balanced this effect and resulted in nearly opposite trends. The loss of angular momentum during compression with the re-entrant bowl and high swirl was 47% and 40% with the low swirl ratio (extrapolated from data of Arcoumanis et al, 1983). The larger decay rate observed with this piston configuration is partly due to increased frictional losses stemming from the higher swirl velocities and surface to volume ratio in the squish chamber and

partly to increased diffusion resulting from the higher turbulence levels towards the end of compression. The angular momentum conversion efficiency, η, of the re-entrant bowl, as defined in Appendix 3.1, was found to be 68% for the high swirl ratio. This is in agreement with the conversion efficiencies of 75 and 70% calculated by Arcoumanis et al (1983) and Brandl et al (1979) for their geometries respectively. Existing data of angular momentum decay from BDC of induction, rather than IVC, to TDC of compression (Tanabe et al, 1978) do not show differences between flat and squish-bowl pistons, which all result to angular momentum losses of about 45% for various swirl ratios. Numerical predictions reported by Gosman and Johns (1978) and Davis and Kent (1979) show 50% loss of angular momentum from BDC of induction to TDC of compression with cylindrical bowl pistons and lower swirl ratios. The calculations of El Tahry (1982) in axisymmetric configurations similar to the model engine showed a greater effect of swirl ratio on the loss of angular momentum which varied from 10 to 40% and 25 to 60% for flat and re-entrant bowl piston geometries respectively. These results are not in agreement with the present findings indicating possible deficiencies of the turbulence models used in the numerical studies.

Finally, the decay of angular momentum from IVC to late exhaust ($\theta = 684^{o}$) with the high swirl ratio was found to be 50 and 77% for the flat and re-entrant bowl pistons respectively. This difference is reflected in the angular momentum at IVC (Table 3.3) which is lower by 8% with the piston bowl and supports the argument of Davis and Kent (1979), that the induction swirl builds up from the residual swirl level existing at the inlet valve opening (IVO).

3.6.3 Precession of the swirl centre

The measurements of the radial distribution of swirl velocity at IVC and TDC of compression, shown in Figures 3.35 and 3.36, indicated that the axisymmetric geometry of the model engine did not give rise to an axisymmetric swirl flowfield. The swirl centre was offset from the cylinder axis, particularly for the high swirl ratio configuration, and

TABLE 3.3

Angular momentum decay and mean rotational speed of the cylinder charge

		IVC (θ = 205°)		TDC (θ = 360°)		EXH (θ = 684°)	
Piston geometry	Vanes angle	$\overline{\Omega}$	$\overline{\omega}$	$\Delta\overline{\Omega}/\overline{\Omega}$	$\overline{\omega}$	$\Delta\overline{\Omega}/\overline{\Omega}$	$\overline{\omega}$
Flat	30°	1.2	3.0	-30%	1.9	-58%	1.1
Flat	60°	2.6	8.4	-28%	5.6	-49%	2.0
Re-entrant	30°(*)	1.0	2.5	-40%	5.0	-	-
Re-entrant	60°	2.4	6.9	-47%	11.0	-77%	3.2

(*)Extrapolated from data of Arcoumanis et al (1983)

this displacement was associated with high r.m.s. velocities which were significantly reduced with the re-entrant bowl piston configuration. The origin of these flow asymmetries is considered in this sub-section together with the implications for the ensemble-averaged r.m.s. velocities.

The swirl velocity distribution along a cylinder diameter at z = 20 mm and θ = 205° (IVC) is shown in Figure 3.39a for the axisymmetric configuration with 60° swirl vanes and flat piston. These results were obtained with two LDA configurations and show the effect of the velocity gradient broadening on the rms velocity measurements near the swirl centre. The swirl velocity distribution is not axisymmetric with the swirl centre being approximately 5 mm offset from the cylinder axis and the corresponding r.m.s. velocity 100% higher than elsewhere in this plane. Ensemble-averaged measurements were obtained on the cylinder axis at the same axial plane as a function of crank angle (Fig. 3.40a) and at θ = 205° along the cylinder axis (Fig. 3.40b) and show that the swirl centre position changes with both crank angle and axial location. This indicates that the swirl centre performs a helical motion which, in average, is in phase with the piston motion and results in a non-axisymmetric mean flow pattern. It is worth noting that the swirl velocity distribution is axisymmetric at a crank angle θ = 288° (Fig. 3.42) where the temporal velocity profile of Figure 3.40a suggests that the swirl centre coincides with the cylinder axis.

Similar measurements were performed with the re-entrant bowl piston configuration and, as shown in Figure 3.39b, the swirl velocity distribution at z = 20 mm and θ = 205° is axisymmetric and the r.m.s. velocities,

free of velocity gradient broadening, are near uniform with maximum values almost half of those measured with the flat piston. The swirl velocity variation with crank angle at z = 20 mm (Fig. 3.41a) and the scanning of the cylinder axis at IVC (Fig. 3.41b) indicate that the re-entrant bowl piston has almost eliminated the helical motion of the swirl centre and the associated high r.m.s. velocities in this region have been reduced by up to 40%.

The cycle-resolved velocity measurements obtained at a point on the cylinder axis at z = 20 mm for a number of consecutive cycles (Fig. 3.43) indicate similar trends in terms of the helical motion of the swirl centre as the temporal ensemble-averaged measurements of Figures 3.40a and 3.41a. It can also be seen that the instantaneous velocity trace with the flat piston has a large amplitude, low frequency component which is not repeatable from one cycle to the next and results in a broadening of the ensemble-averaged r.m.s. velocity measurements. Whether this flow characteristic should be considered as cyclic variation of the mean velocity or low frequency turbulence is a matter of definition; it is certain, however, that if a spark was ignited at this location in a firing engine this phenomenon would have resulted in undesirable cyclic variations of the combustion process. The corresponding instantaneous velocity traces with the re-entrant bowl piston (Fig. 3.43b) do not indicate the presence of low frequency oscillations until the onset of squish ($\theta = 270^{o}$) which results in steep swirl velocity gradients with associated high turbulence intensity and low frequency oscillations.

In order to clarify the relationship between the reduction of the helical motion of the swirl centre and the presence of the axisymmetric piston-bowl a non-axisymmetric geometry was examined with the same intake port located 8 mm off the cylinder axis. Figure 3.44 shows the swirl velocity results obtained at z = 20 mm and $\theta = 205^{o}$ across two perpendicular diameters with the flat and re-entrant bowl pistons and the off-axis port configuration. Again, the velocity gradients near the swirl centre are steeper and the corresponding r.m.s. velocities higher with the flat piston than with the re-entrant bowl piston and persist up to TDC of compression (Fig. 3.45). The corresponding temporal ensemble-averaged (Fig. 3.46) and cycle-resolved (Fig. 3.47) measurements again indicate that the helical motion of the swirl centre is reduced with the re-entrant bowl piston. It is evident that the coincidence of the re-

entrant bowl and induction swirl axes is not the reason for the reduction of the helical motion of the swirl centre and of the associated broadening of the r.m.s. velocity measurements.

The helical motion of the swirl centre is not a unique phenomenon in engine or unsteady flows. It has also been observed in steady swirling flows (for example Chanaud, 1965) and is usually termed "precession" of the swirl centre. It is particularly apparent in swirling flows behind axisymmetric bluff bodies, as the measurements of Founti (1983) suggest. In reciprocating engines this phenomenon has been attributed to the off-axis position of the intake valve (Johnston et al, 1979) but the present results confirm its existence even in axisymmetric configurations. It appears that the precession of the swirl centre in the present flow originates from the interaction of the swirling valve jet during early induction with the developing wake behind the valve. This induces a low frequency flow oscillation which is manifested as a helical motion of the swirl centre. The close proximity of the piston face to the intake valve with the re-entrant bowl configuration restricts this interaction, as the results of Figure 3.34c suggest, and almost eliminates the oscillation of the swirling flow. The magnitude of the ensemble-averaged r.m.s. velocities depends on the amplitude of this oscillation as well as the steepness of the local swirl velocity gradient. These measurements are believed to properly characterise the turbulence field of the in-cylinder isothermal flow, by including the contribution of all frequency components as they would in a stationary flow.

3.6.4 Summary

The velocity field measurements obtained in the model engine with two swirl-producing ports and flat and re-entrant bowl piston configurations revealed the following:

1. The swirl velocity distribution during induction was determined by the swirl level and the geometric characteristics of the piston/cylinder assembly. The main features of the initial swirl velocity distribution were retained throughout the intake and compression strokes.

2. High induction swirl levels resulted in lower turbulence intensities at TDC of compression with the flat piston and more complex vortex pattern inside the re-entrant piston bowl than the low swirl. The turbulence production in the squish chamber was controlled mainly by squish which resulted in turbulence intensities of 1 - 1.5 $\overline{V}_p$ at TDC of compression.

3. The decay of swirl momentum from inlet valve closure to TDC of compression was shown to depend on initial swirl level and velocity distribution and was about 30% and 45% for the flat and re-entrant bowl piston respectively. The in-cylinder angular momentum at inlet valve closure depended on the residual swirl before inlet valve opening.

4. The swirl centre performed a weak helical motion whose development was a function of the clearance volume at TDC. This helical motion and the associated high r.m.s. velocities near the swirl centre were significantly reduced with the re-entrant bowl piston configuration.

3.7 CONCLUSIONS

This chapter presented detailed velocity field measurements obtained during the induction and compression strokes in a model engine motored at 200 rpm with various intake port and combustion chamber geometries. The main findings of this investigation can be summarised as follows:

1. The flow at the exit of the intake valve responded quickly enough to the changes of flow rate and flow area, under these operating conditions, so that it could be considered as quasi-steady. The interaction of the valve jet with the downstream flow, however, restricted the usefulness of steady flow tests for the valve flow simulation to engine configurations with relatively large clearance volume at TDC.

2. The in-cylinder flow during induction was determined by the intake port/valve configuration and the combustion chamber geometry. The latter parameter together with the transient nature of the flow did

not allow its simulation by steady flow configurations, particularly at early induction. The development of the in-cylinder vortex pattern during induction was controlled by the relative size and strength of the component vortices and determined the flow structure at the end of the intake stroke. The multi-vortex structure produced by plain axisymmetric ports decayed by the end of induction through the exchange of momentum between the counter-rotating vortices. However, flow structures with a dominant vortex on either the axial or tangential plane, produced by specific induction systems, were sustained by conserving the angular momentum of the main vortex throughout the intake stroke.

3. The in-cylinder flow structure at intake valve closure and the combustion chamber geometry determined the evolution of the flow during compression. In the case of a disc-type combustion chamber and in the absence of significant mean flow at IVC, the compression process was nearly one-dimensional and resulted in a near zero mean flow at TDC of compression with little memory of the intake flow. Turbulence, produced by the compression stresses, was counterbalanced by dissipation which resulted in a net decay and a near homogeneous and isotropic turbulence field at TDC of compression with turbulence intensity around 0.45 $\overline{V}_p$. When a strong rolling vortex was present on the axial plane of the cylinder at IVC, its decay during compression was accompanied by turbulence production through the shear stresses associated with the deformation of the axial velocity gradients. In this case turbulence dissipation was counterbalanced by production and resulted in turbulence intensity of about 1 $\overline{V}_p$ at TDC of compression.

The decay of a swirl flow pattern on the tangential plane was associated with the wall frictional losses and depended on swirl level and swirl velocity distribution. Turbulence again decayed during compression and its intensity at TDC of compression decreased with increasing swirl level to values lower than 0.45 $\overline{V}_p$. The flowfield at TDC of compression in a squish-type combustion chamber was determined by the piston bowl geometry. In the absence of induction swirl a toroidal vortex was formed inside the bowl and turbulence was generated by the shear stresses produced by the squish flow near its entry. When swirl was present the in-bowl flow pattern was affected by the bowl geometry as well as the swirl level while turbulence intensity was again determined by the squish flow.

4. The flow generated in the cylinder by the swirl-producing intake ports was characterised by a low frequency oscillation of the swirl velocities near the swirl centre which was manifested as a helical motion of the swirl centre. This flow characteristic was associated with the interaction of the valve jet with the wake of the valve and was significantly reduced in the case of a squish piston with small bumping clearance at TDC of induction.

The above results were obtained in a low speed model engine with idealised port and combustion chamber geometries. Although these data are useful for the assessment of relevant multidimensional prediction methods, questions may arise with respect to their relevance to practical engine configurations and realistic engine speeds. For this reason the present investigation was extended to study the in-cylinder flow development in two modified production engines. The results of these studies are presented in the following chapters.

APPENDIX 3.1

Calculation of angular momentum and rotational speed of the cylinder charge

The non-dimensional rotational speed, ω, of the charge and its angular momentum, Ω, are calculated by integration of the swirl velocity profiles performed by piecewise quadratic approximation and with the assumption of axisymmetric distribution of angular momentum with respect to the centre of rotation of the air charge, as follows:

Rotational speed of air charge at a cylinder cross-section:

$$\omega = \frac{1}{\omega_e} \cdot \frac{1}{R} \cdot \int_0^R \frac{\overline{W}}{r} \, dr$$

Mean in-cylinder rotational speed of air charge:

$$\overline{\omega} = \frac{1}{\omega_e} \cdot \frac{1}{Rz_p} \cdot \int_0^{z_p} \int_0^R \frac{\overline{W}}{r} \, dr.dz$$

The swirl ratio (SR) of an engine configuration is defined as the mean rotational speed of the charge at TDC of compression:

$$SR = \left[\overline{\omega}\right]_{TDC}$$

Angular momentum of air charge at a cylinder cross-section:

$$\Omega = \frac{1}{R_c^2.\omega_e} \left\{ \frac{2}{R^2} \int_0^R r^2.\overline{W}.dr \right\}$$

Mean in-cylinder angular momentum of air charge:

$$\overline{\Omega} = \frac{1}{R_c^2.\omega_e} \left\{ \frac{2}{z_p.R^2} \int_0^{z_p} \int_0^R r^2\overline{W}.dr.dz \right\}$$

The swirl number (SN) is defined as the ratio of the angular to axial momentum fluxes at a cylinder cross-section:

$$SN = \frac{1}{R_c} \cdot \frac{\int_0^R r^2 . \overline{U} . \overline{W} . dr}{\int_0^R r . \overline{U}^2 . dr}$$

The angular momentum conversion efficiency of a chamber geometry A with respect to a chamber geometry B is defined as:

$$\eta = \left[\frac{\overline{\Omega}_A}{\overline{\Omega}_B}\right]_{TDC}$$

where geometry B is here considered to be the disc-type combustion chamber.

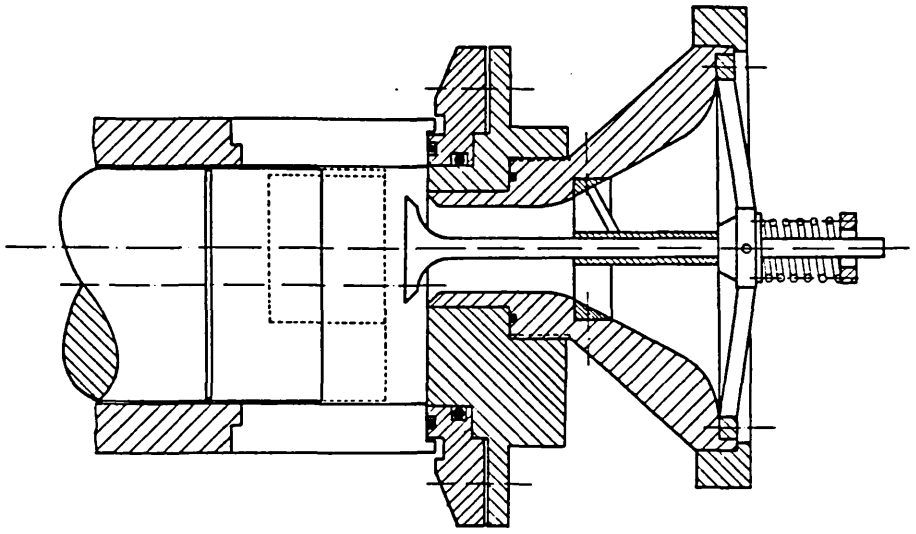

Fig. 3.1 Diagram of the piston-cylinder assembly; plain port configuration

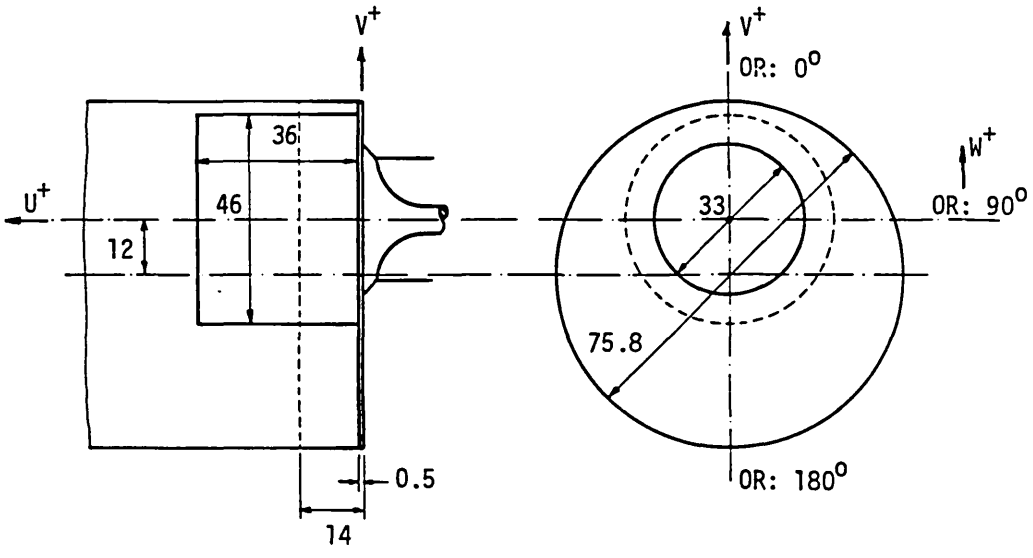

Fig. 3.2 Off-centre valve and bowl geometry; measurement planes and sign conventions

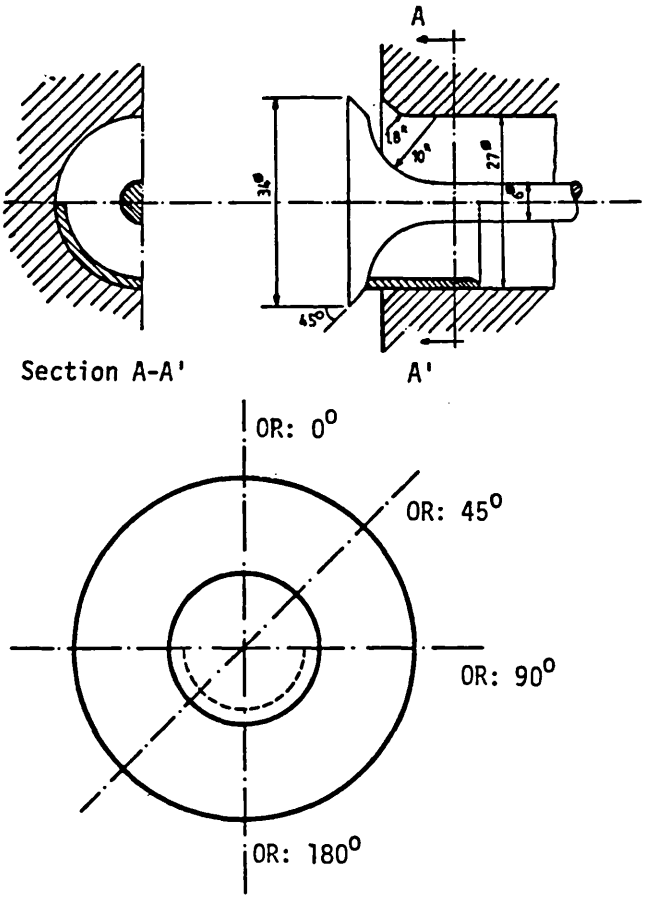

Fig. 3.3 Central directed port configuration, (shrouded valve)

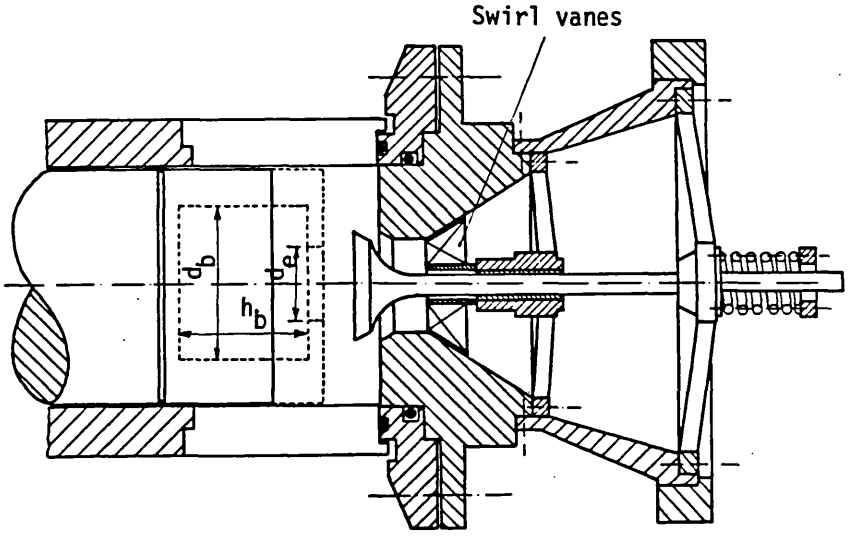

Fig. 3.4 Diagram of the piston-cylinder assembly with the swirl-producing intake port configuration

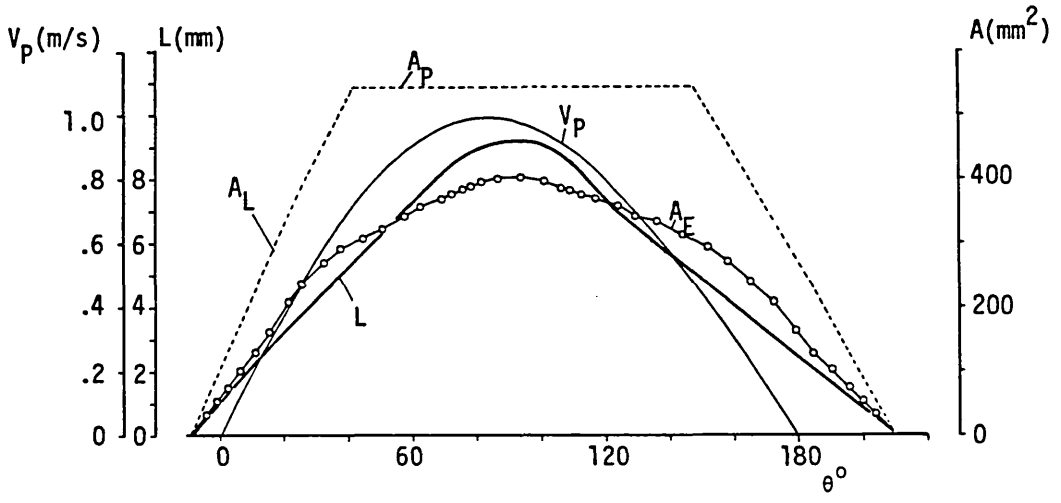

Fig. 3.5 Valve lift diagram indicating the variation of A_L, A_E, V_P

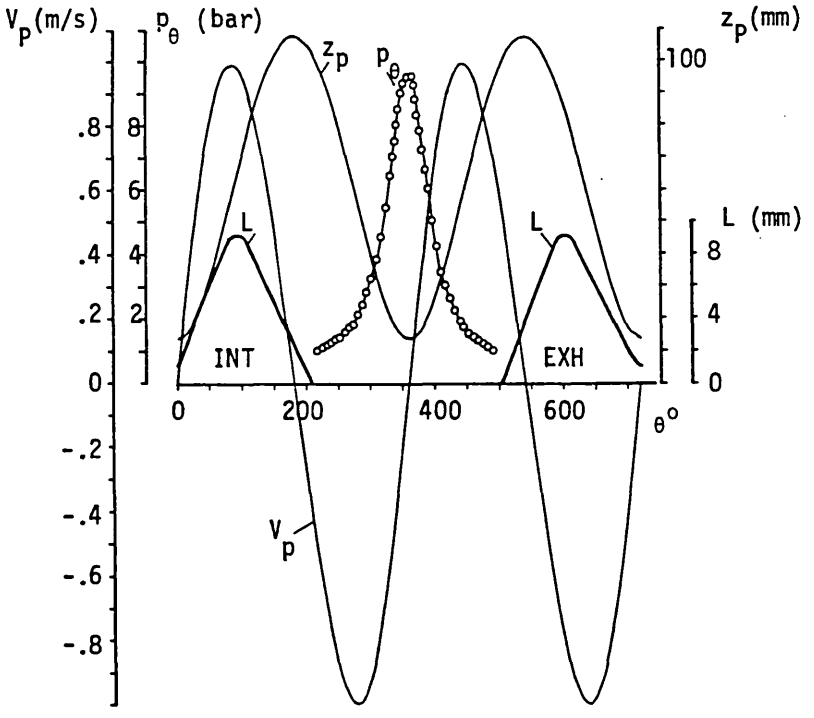

Fig. 3.6 Piston velocity, position, valve lift and in-cylinder absolute pressure diagrams, (CR = 7.7)

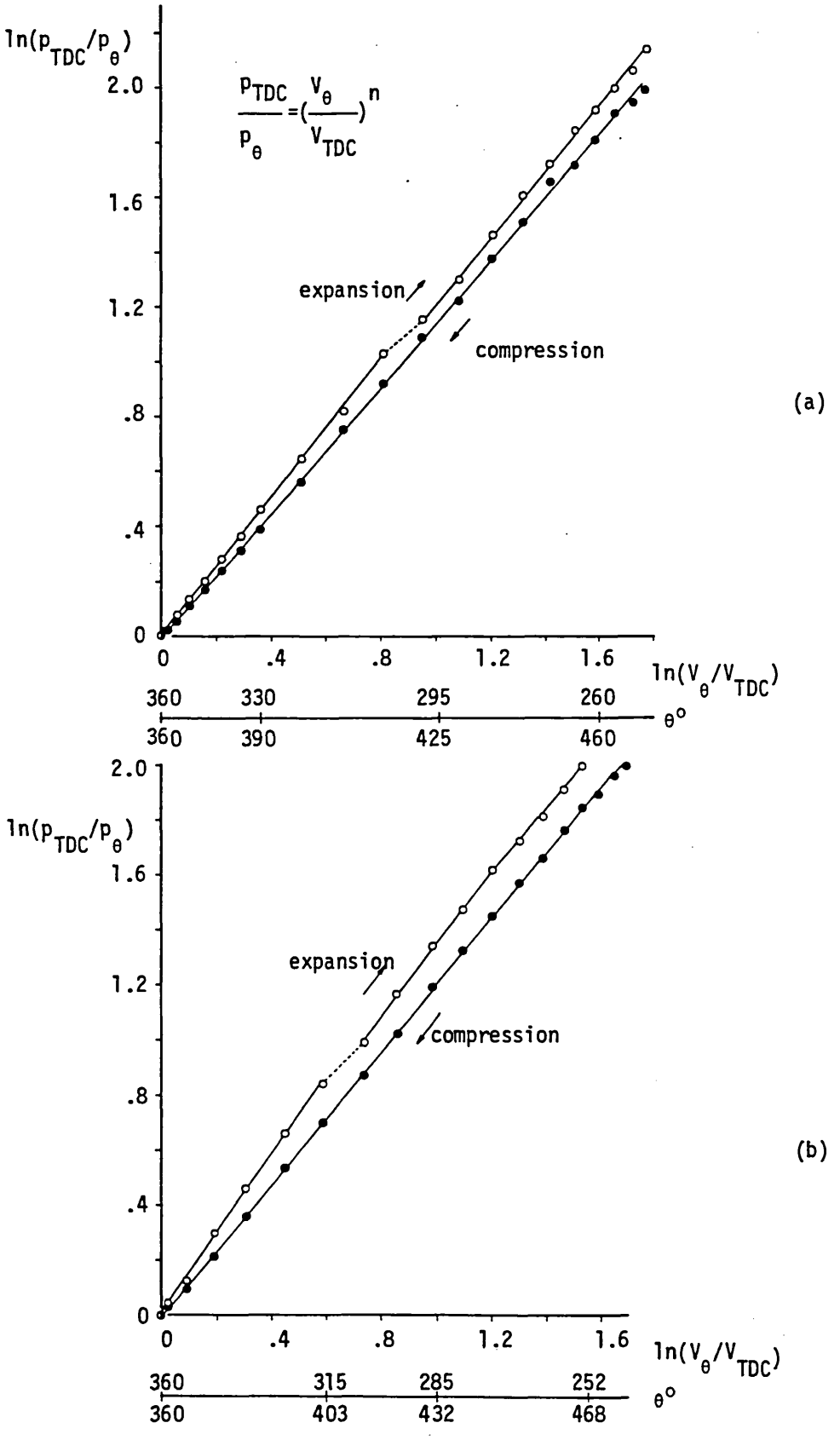

Fig. 3.7 Cylinder pressure diagrams in logarithmic scales.
a) CR = 7.7, b) CR = 6.7

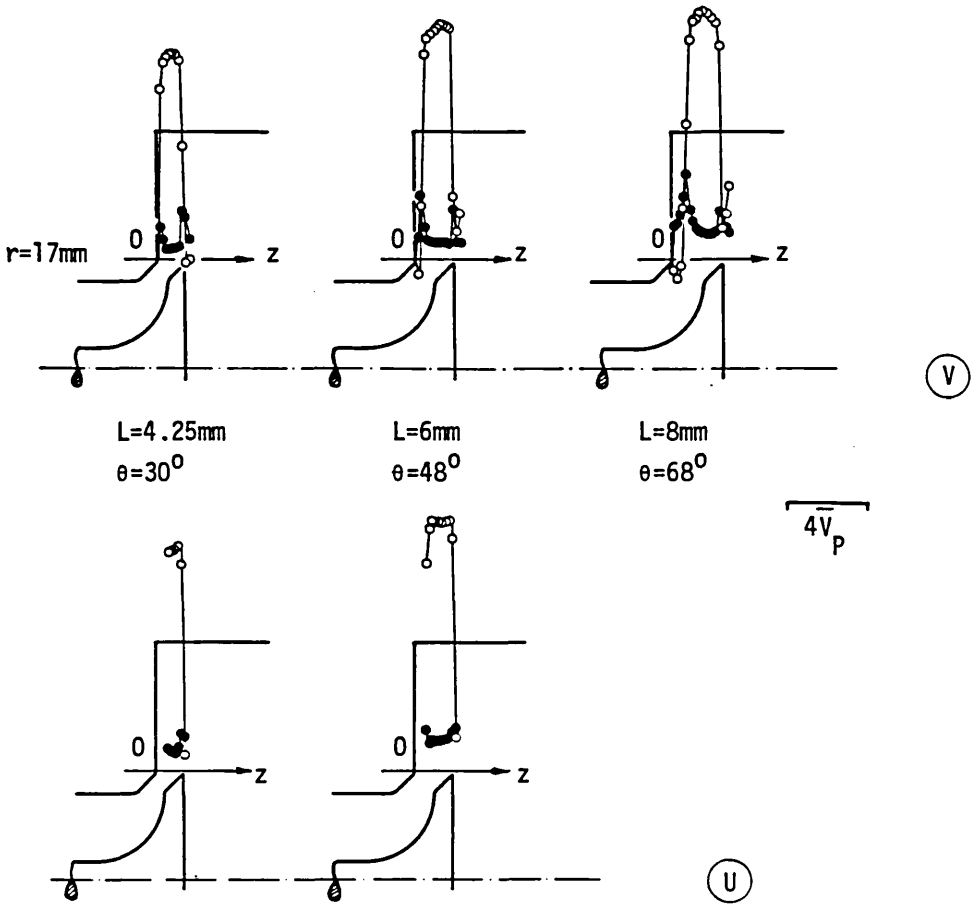

Fig. 3.8 Radial and axial velocity distribution at the valve exit. Stationary axisymmetric valve

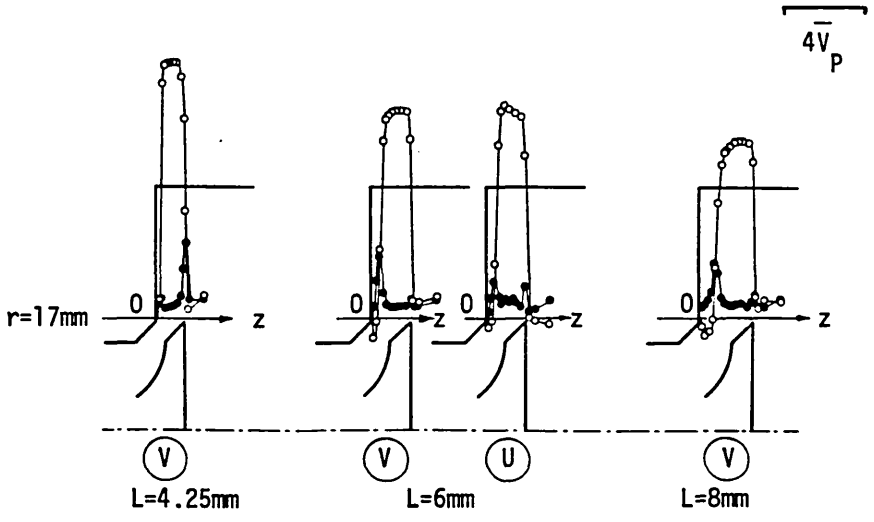

Fig. 3.9 Radial and axial velocity distribution at the valve exit. Steady flow, axisymmetric valve

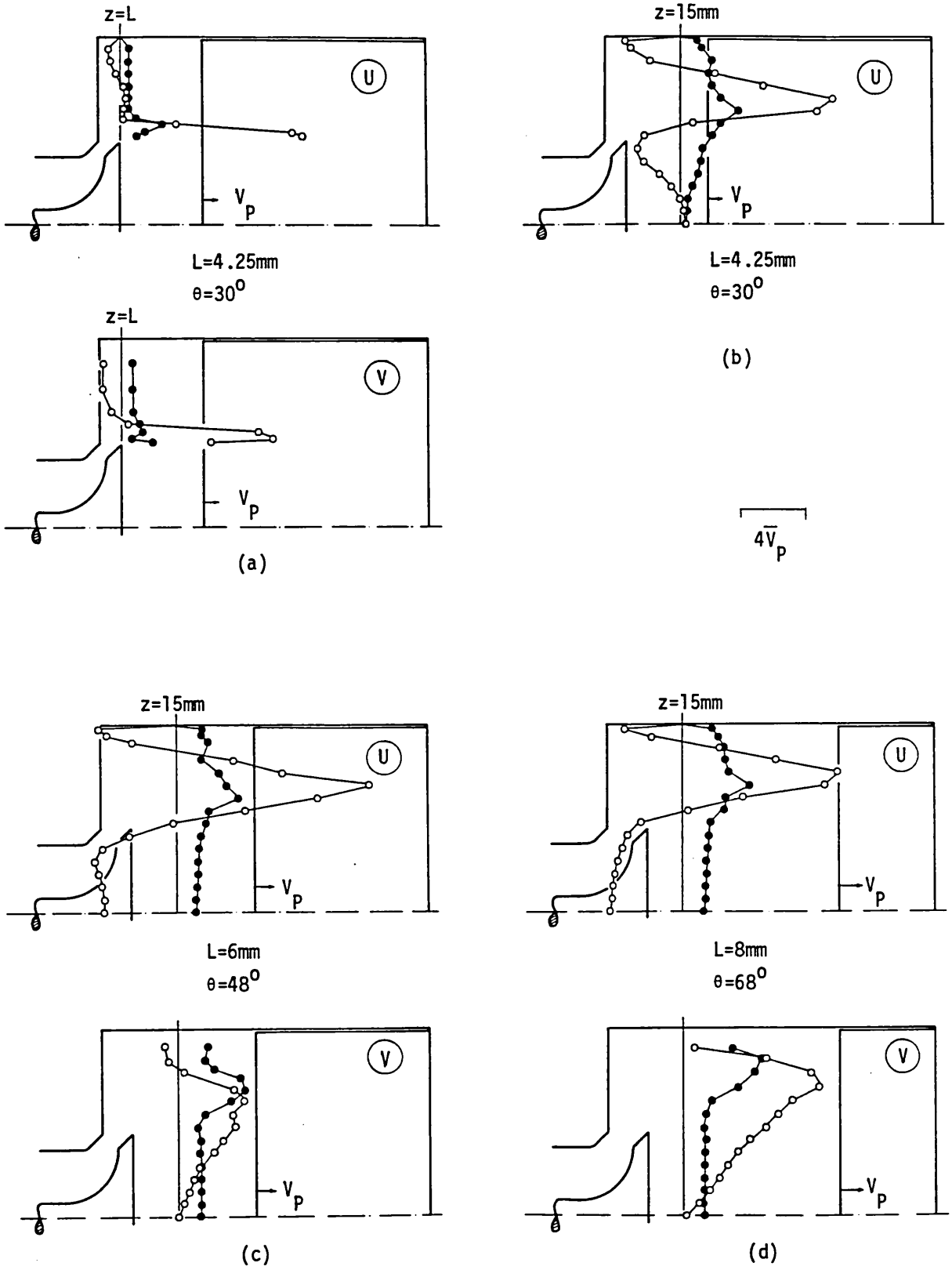

Fig. 3.10 Axial and radial velocity distribution at z = L and z = 15 mm. L = 4.25, 6, 8 mm and θ = 30, 48 and 68° respectively. Axisymmetric stationary valve

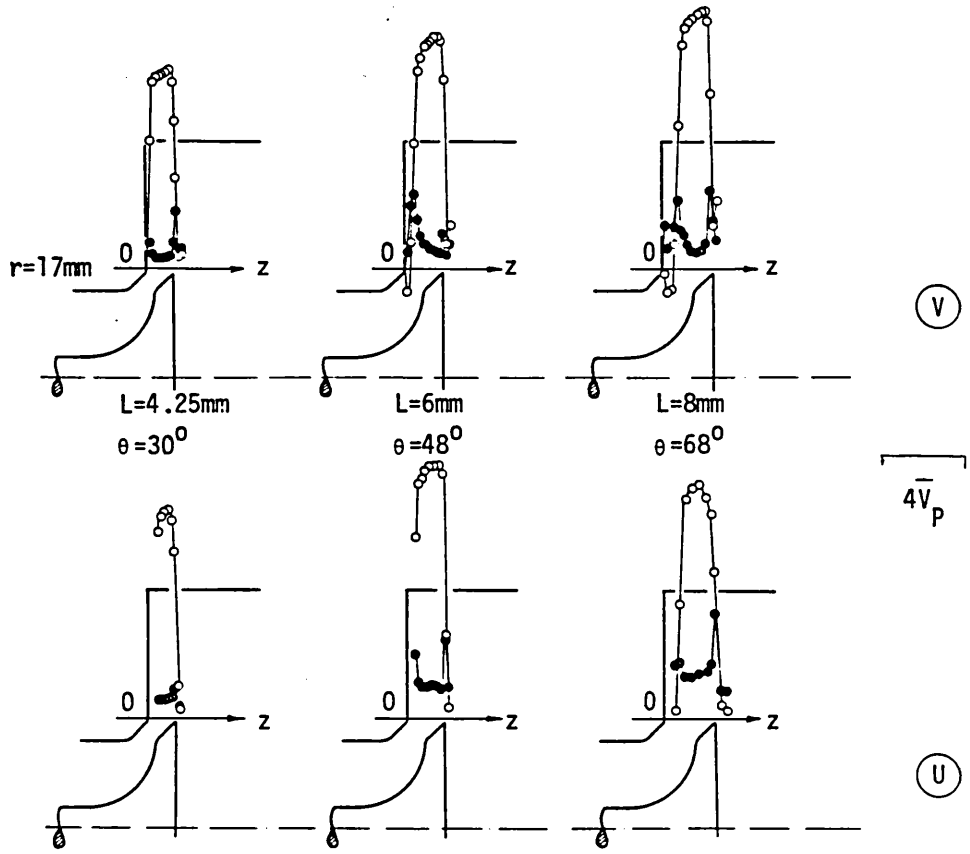

Fig. 3.11 Radial and axial velocity distribution at the exit of the operating axisymmetric valve. Flat piston

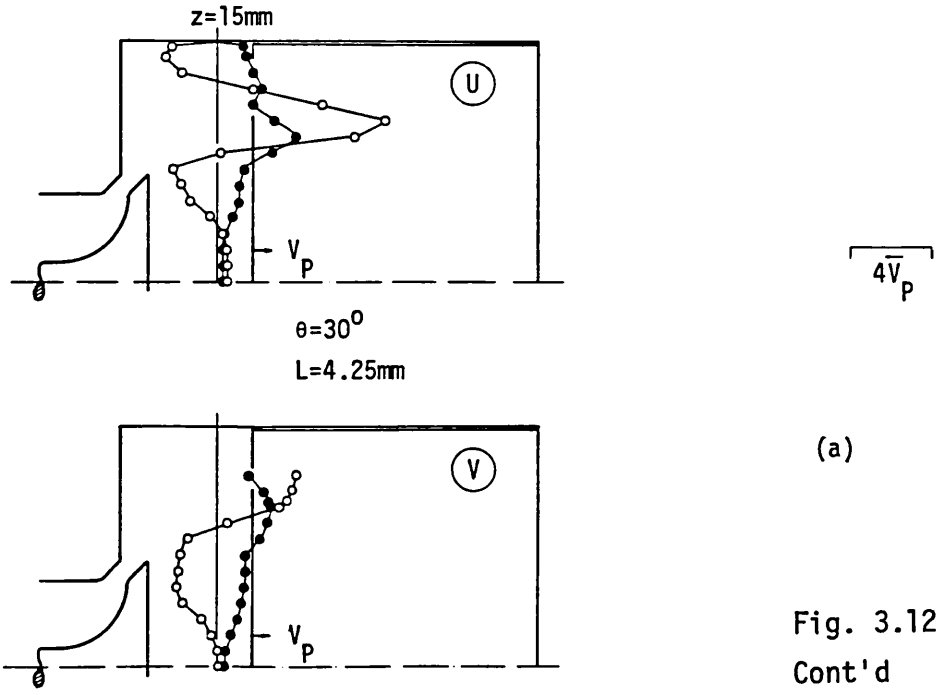

Fig. 3.12 Cont'd

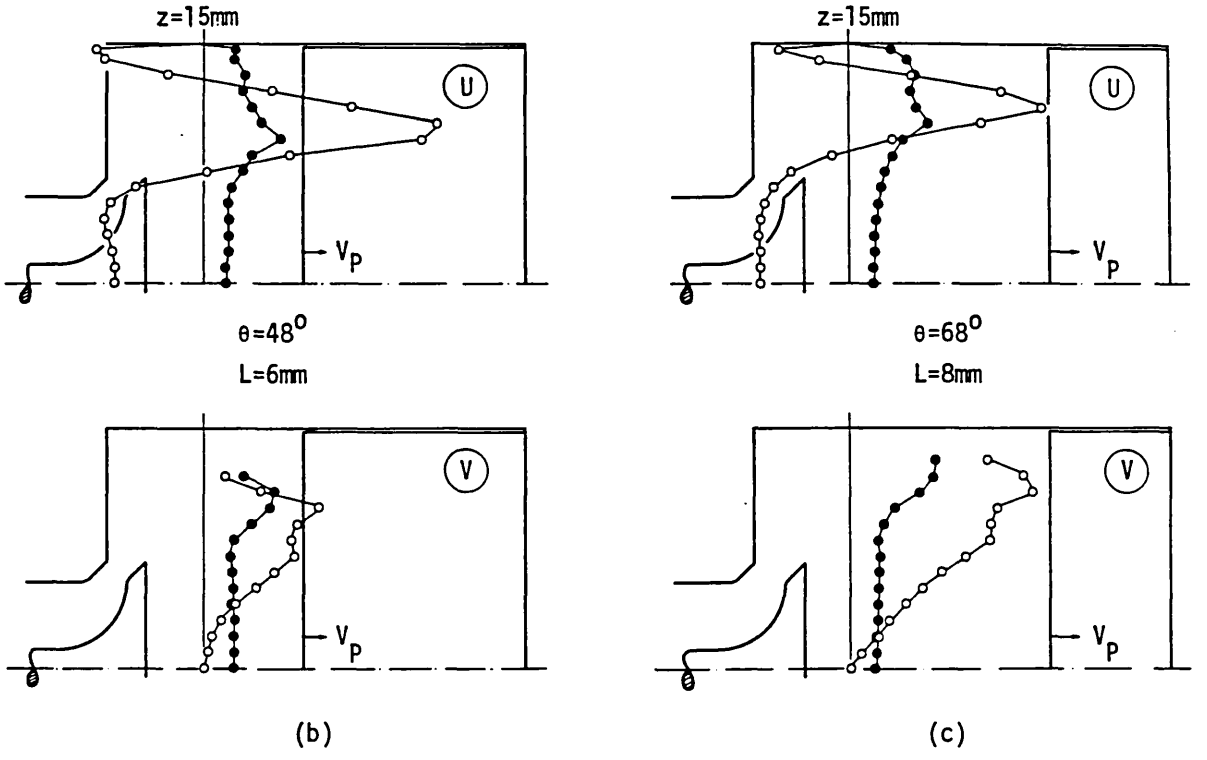

Fig. 3.12 Axial and radial velocity distribution at z = 15 mm. Axisymmetric operating valve. Flat piston.
a) $\theta = 30^{o}$, L = 4.25 mm, b) $\theta = 48^{o}$, L = 6 mm,
c) $\theta = 68^{o}$, L = 8 mm

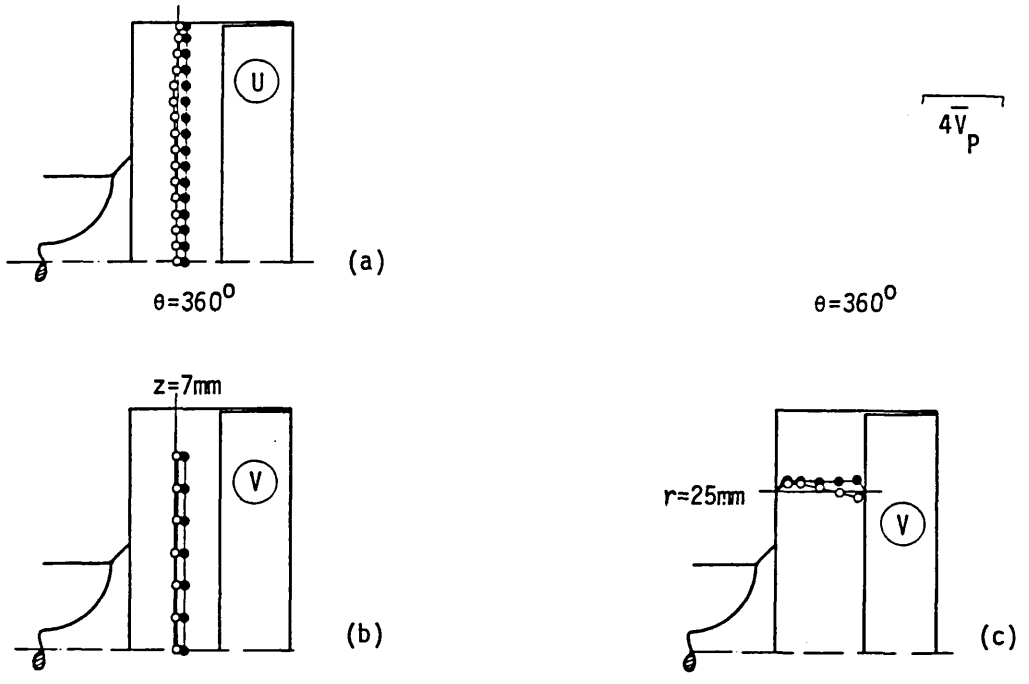

Fig. 3.13 Axial (a) and radial (b,c) velocity distribution at $\theta = 360^{o}$ (TDC). Axisymmetric valve, flat piston

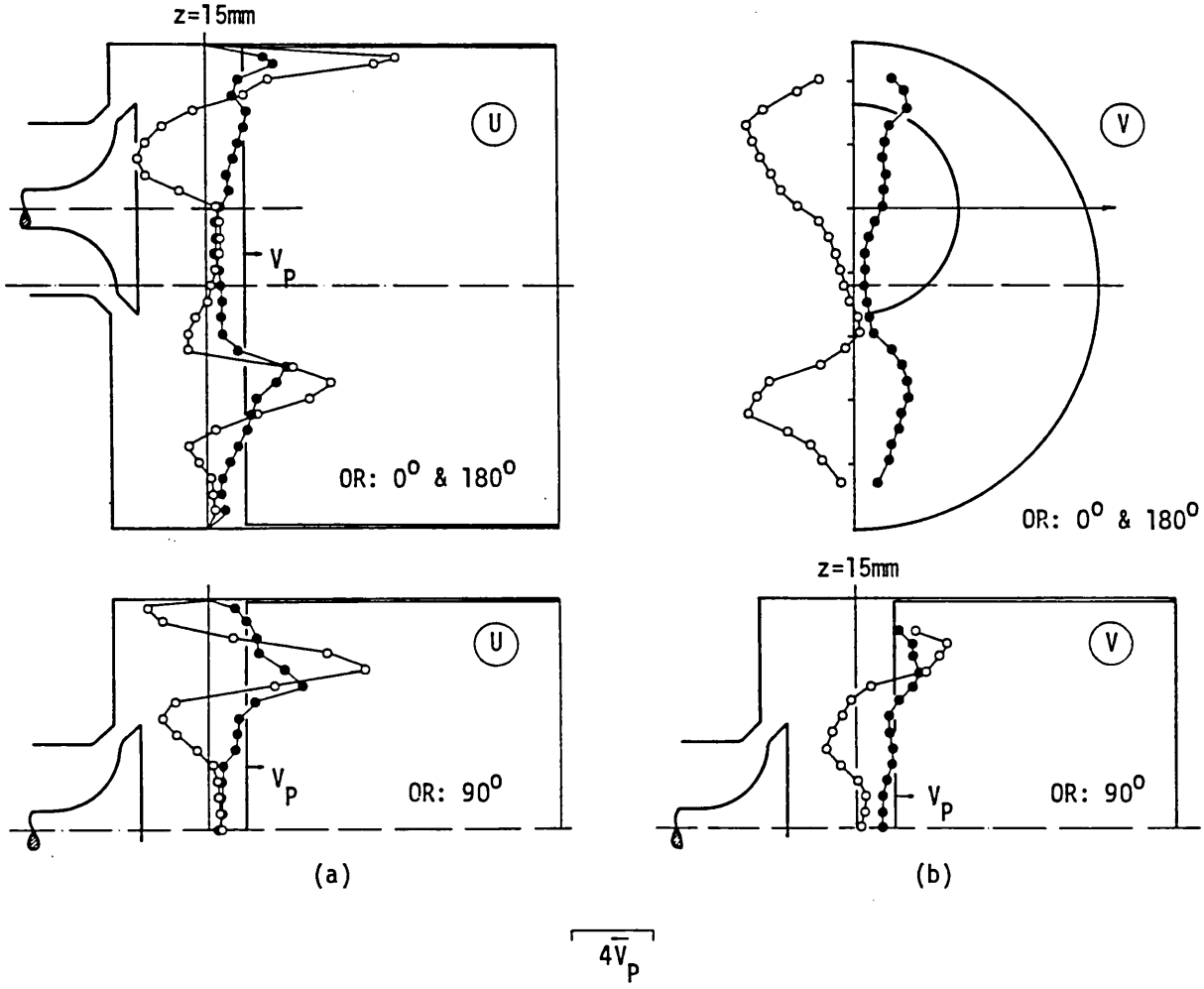

Fig. 3.14 Axial (a) and radial (b) velocity distribution at z = 15 mm, along the 0, 90 and 180° measurement planes. θ = 30° (L = 4.25 mm), off-centre valve, flat piston

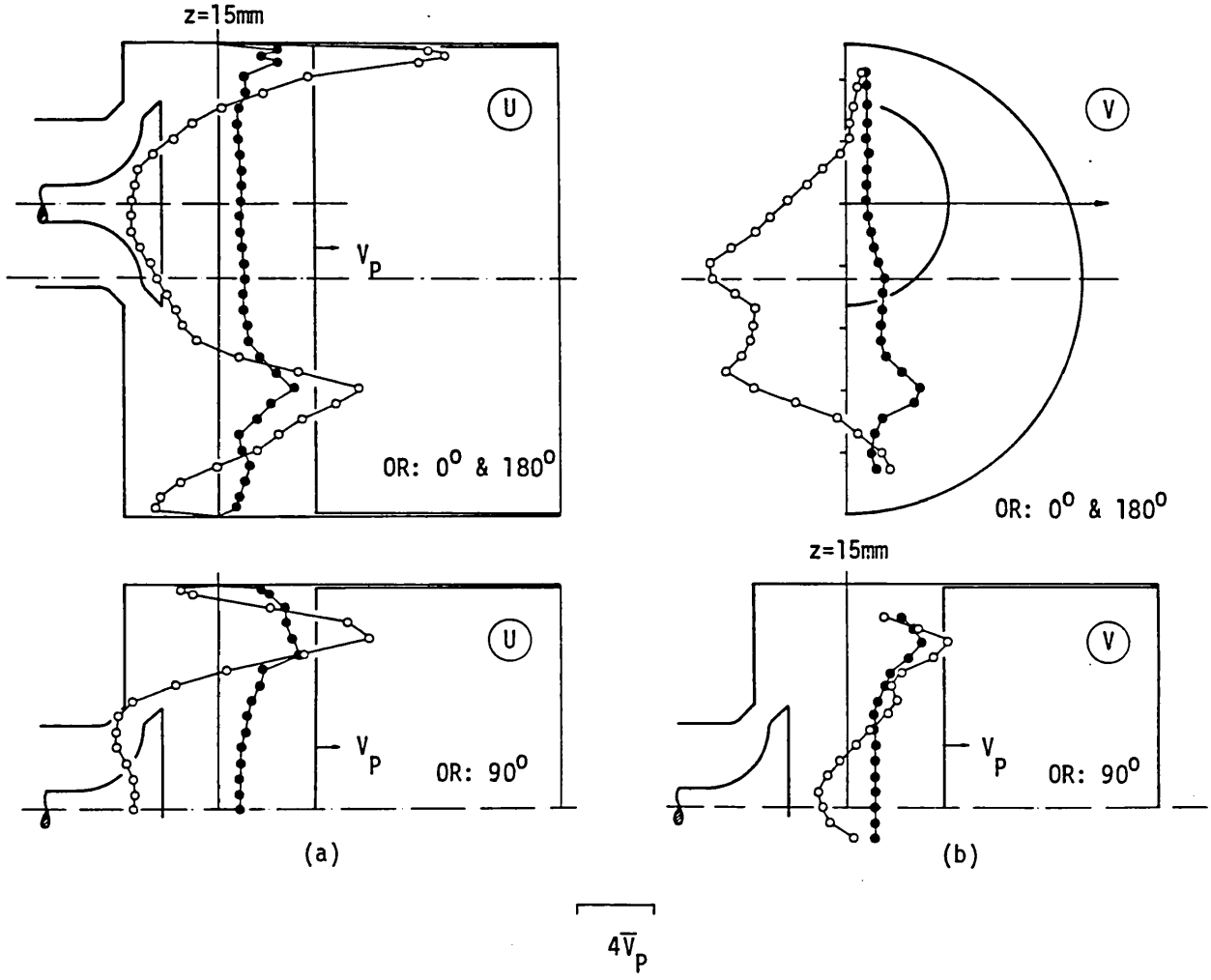

Fig. 3.15 Axial (a) and radial (b) velocity distribution at z = 15 mm, along the 0, 90 and 180° measurement planes. $\theta = 48^{o}$ (L = 6 mm), off-centre valve, flat piston

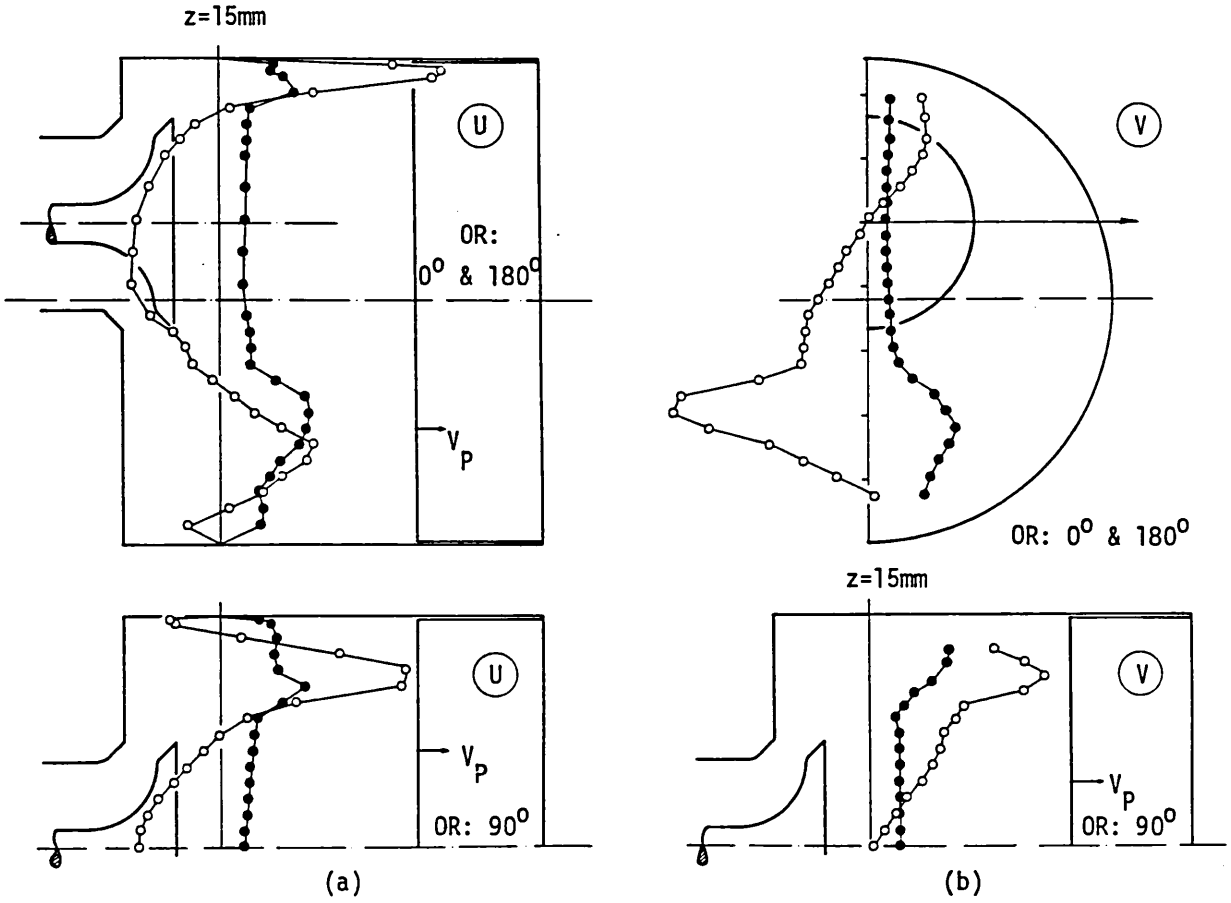

Fig. 3.16 Axial (a) and radial (b) velocity distribution at z=15mm along the 0, 90 and 180° planes. θ=68° (L=8mm), off-centre valve, flat piston

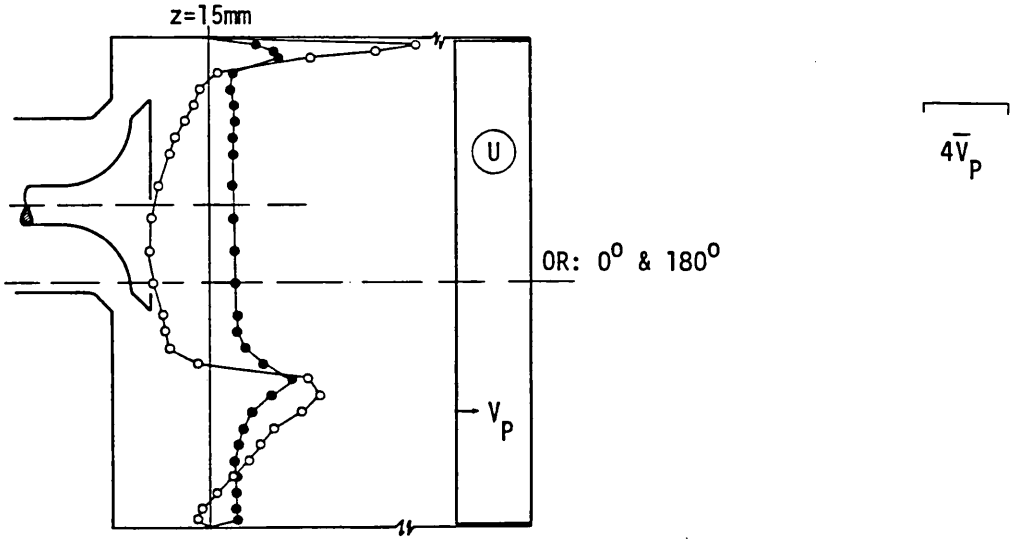

Fig. 3.17 Axial velocity distribution at z=15mm along the 0 and 180° measurement planes. θ=134° (L=6mm), off-centre valve, flat piston (z_p= 96 mm, not to scale)

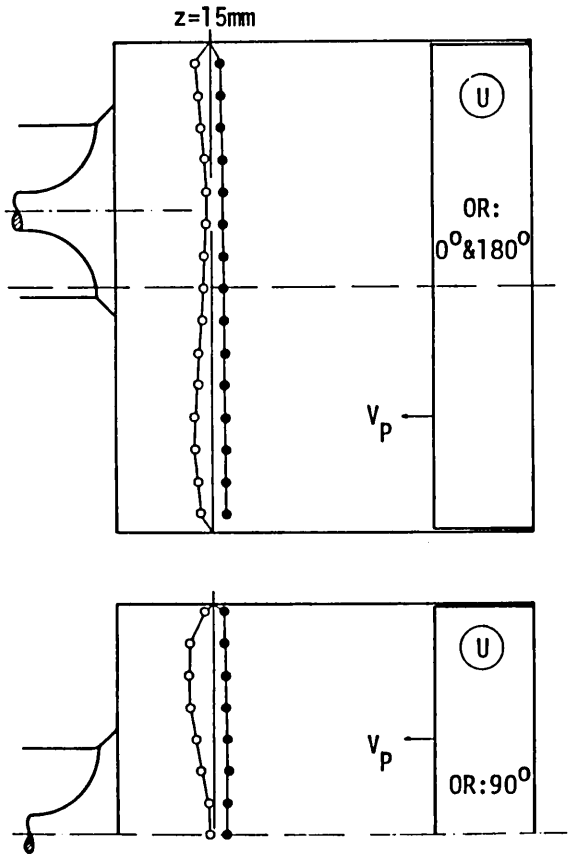

Fig. 3.18 Axial velocity distribution at z=15mm along the 0, 90 and 180° measurement planes. θ=288°, off-centre valve, flat piston

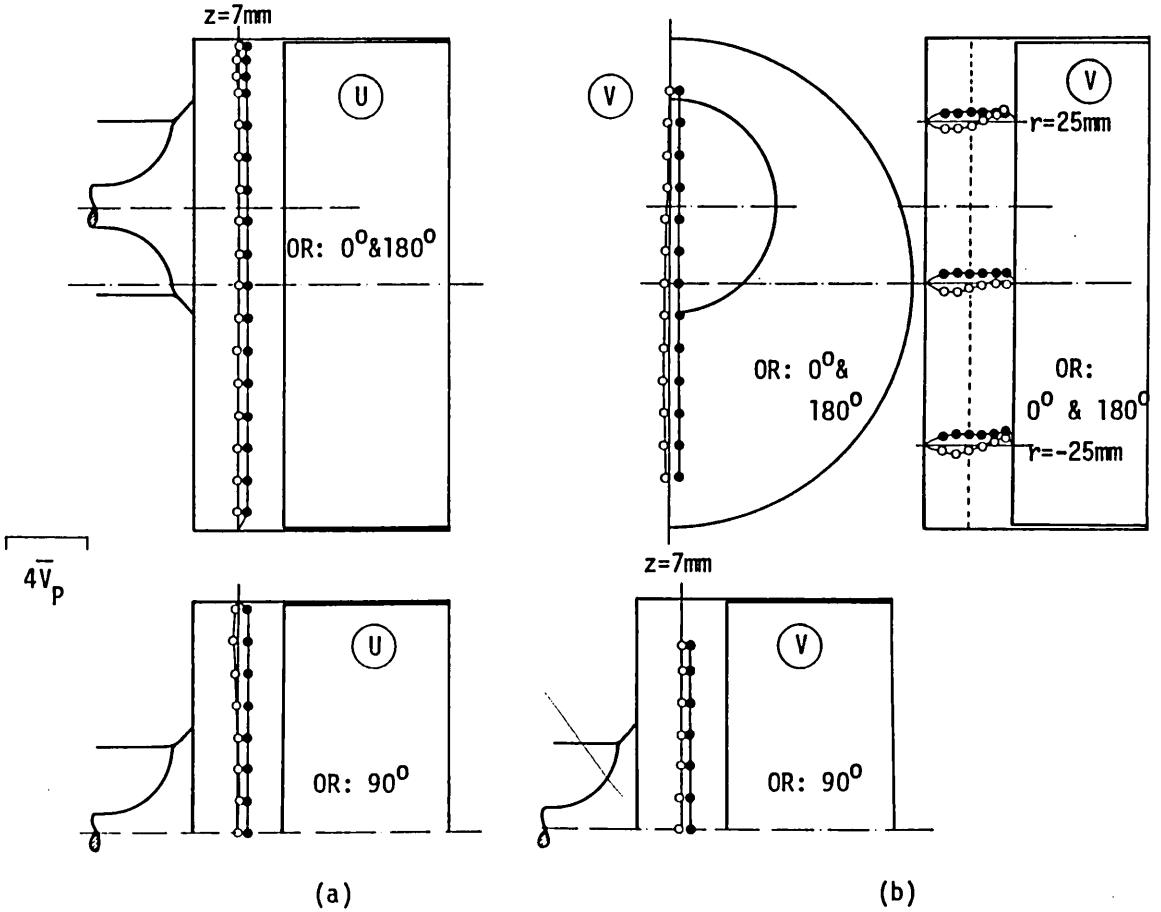

Fig. 3.19 Axial (a) and radial (b) velocity distribution at θ=360° (TDC). Off-centre valve, flat piston

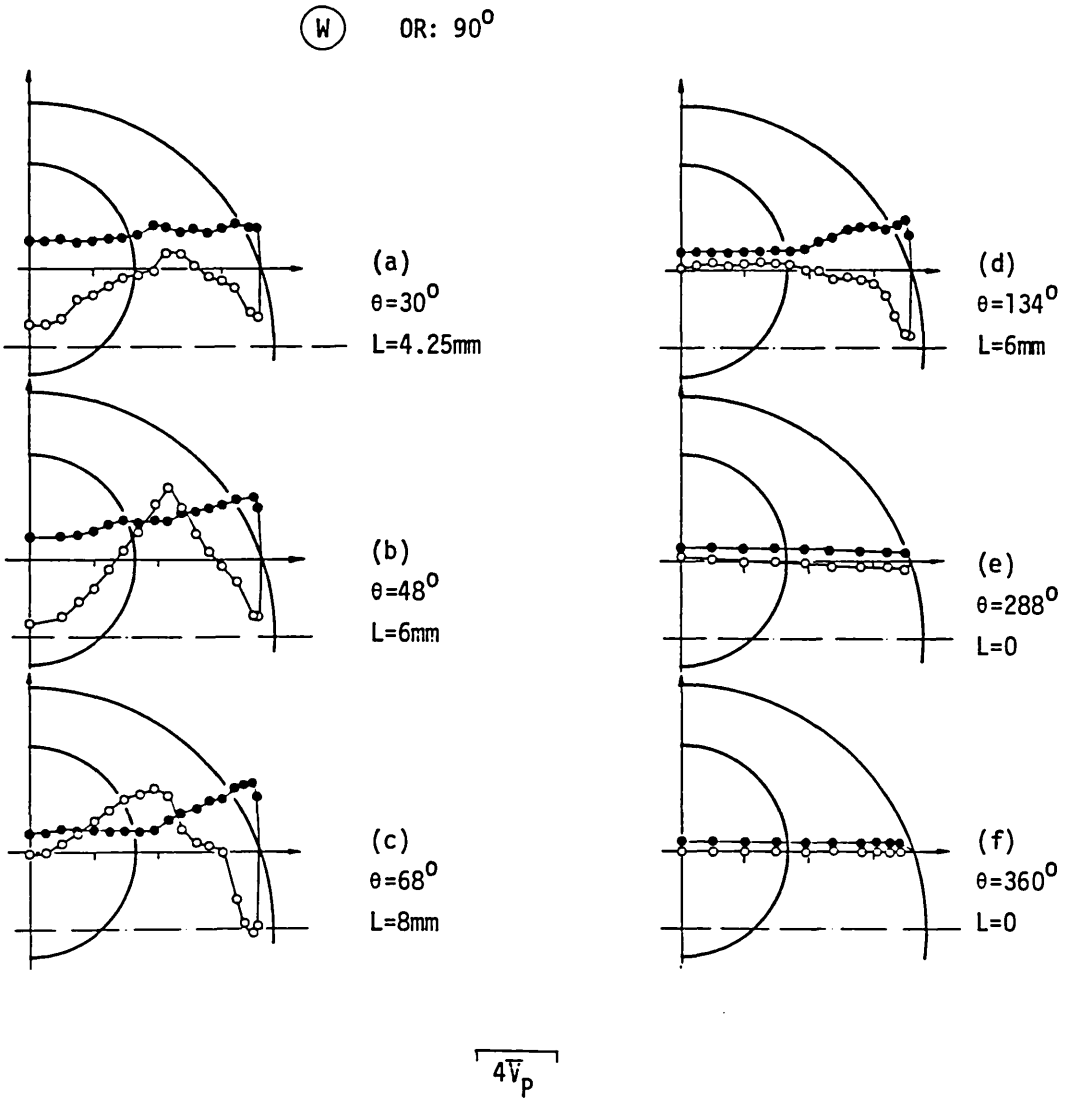

Fig. 3.20 Development and decay of the tangential velocity component at z = 15 mm (except at θ = 360° where z = 7 mm) along the 90° measurement plane. Off-centre valve, flat piston

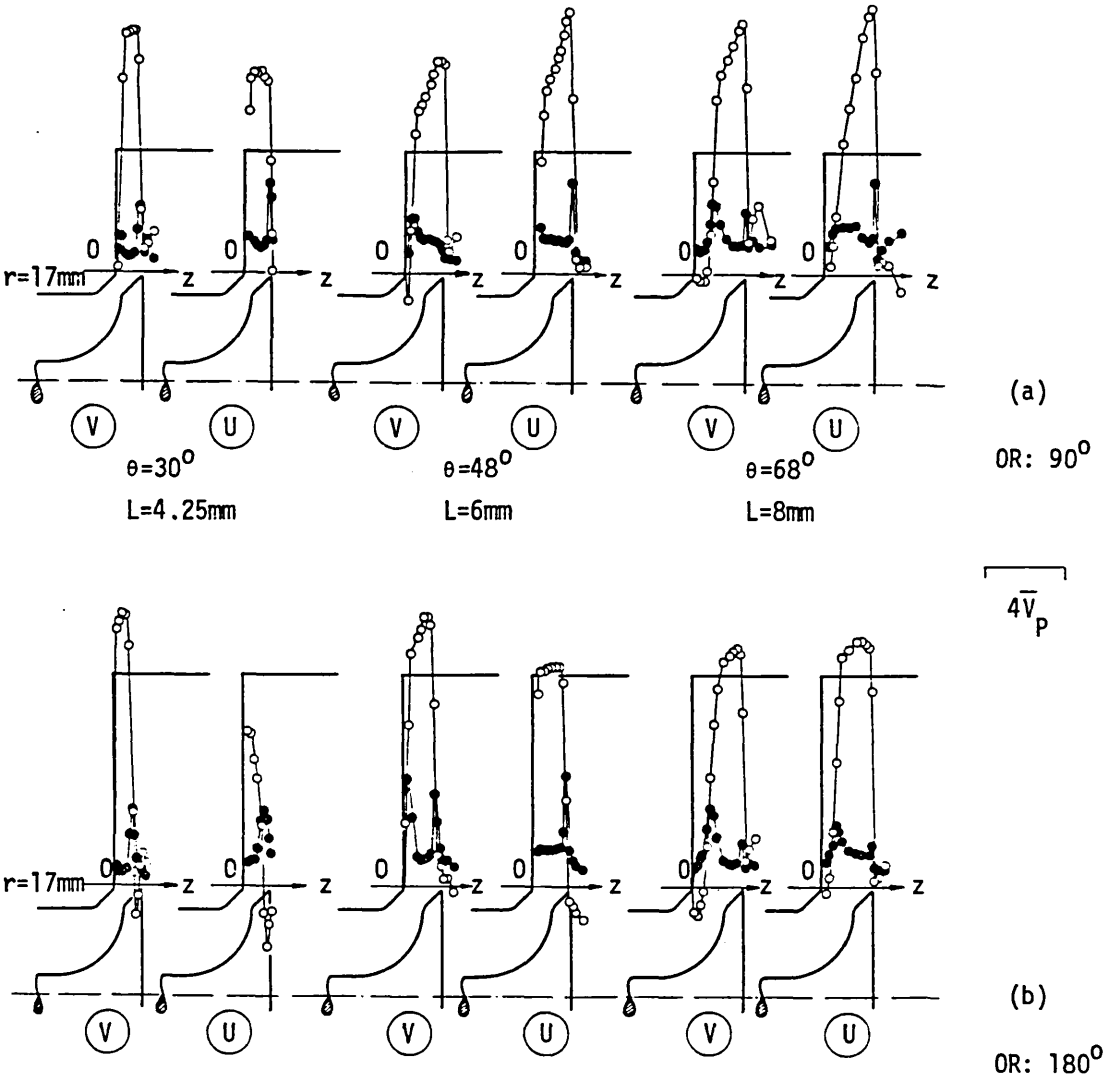

Fig. 3.21 Radial and axial velocity distribution at the exit of the operating off-centre valve with the co-axial piston bowl along the a) 90^{o} and b) 180^{o} measurement planes

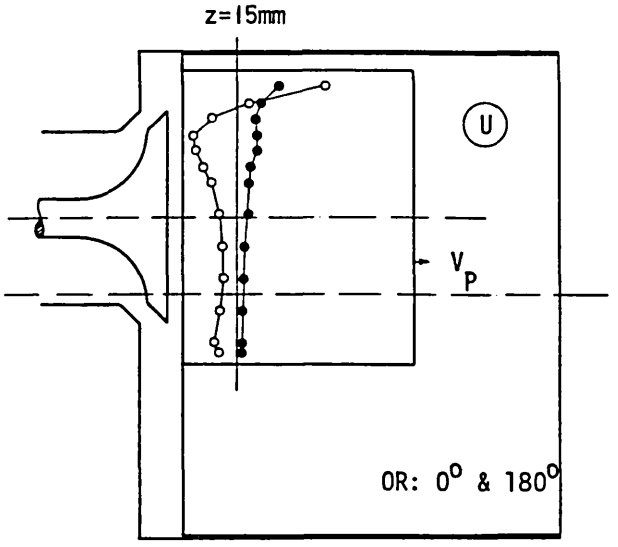

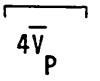

Fig. 3.22
Axial velocity distribution inside the piston-bowl. $\theta = 30^{o}$ (L = 4.25 mm), z = 15 mm, 0 and 180^{o} measurement planes

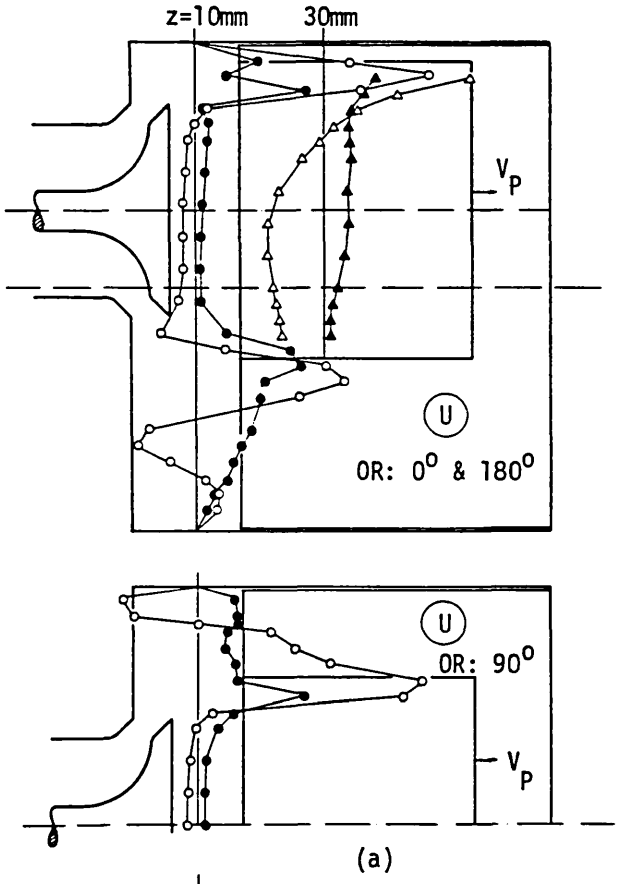

(a)

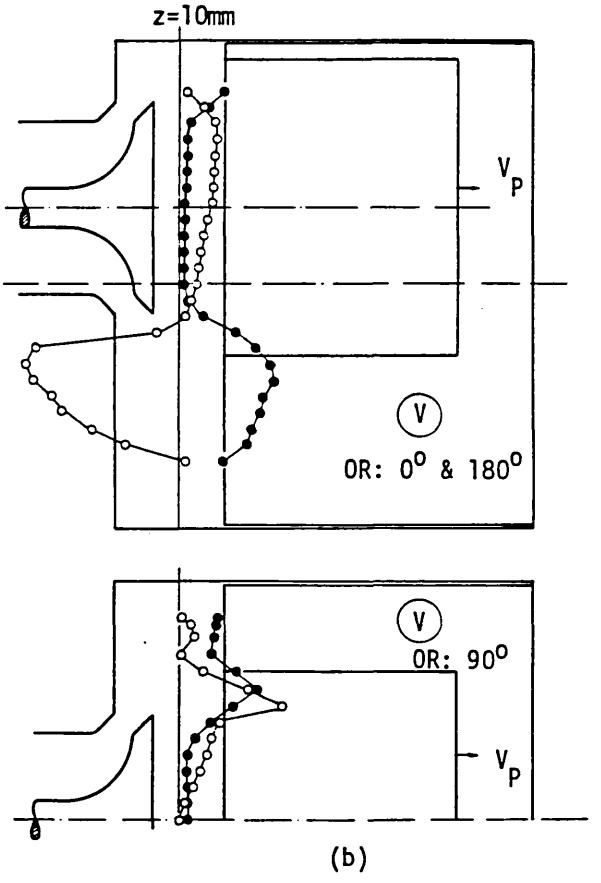

(b)

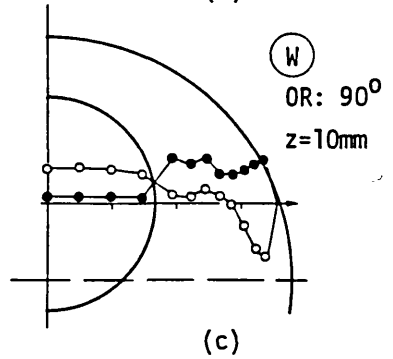

(c)

Fig. 3.23
Axial (a), radial (b) and tangential (c) velocity distribution at z = 15 mm along the 0, 90 and 180^{o} measurement planes. $\theta = 48^{o}$ (L = 6 mm), off-centre valve and piston bowl

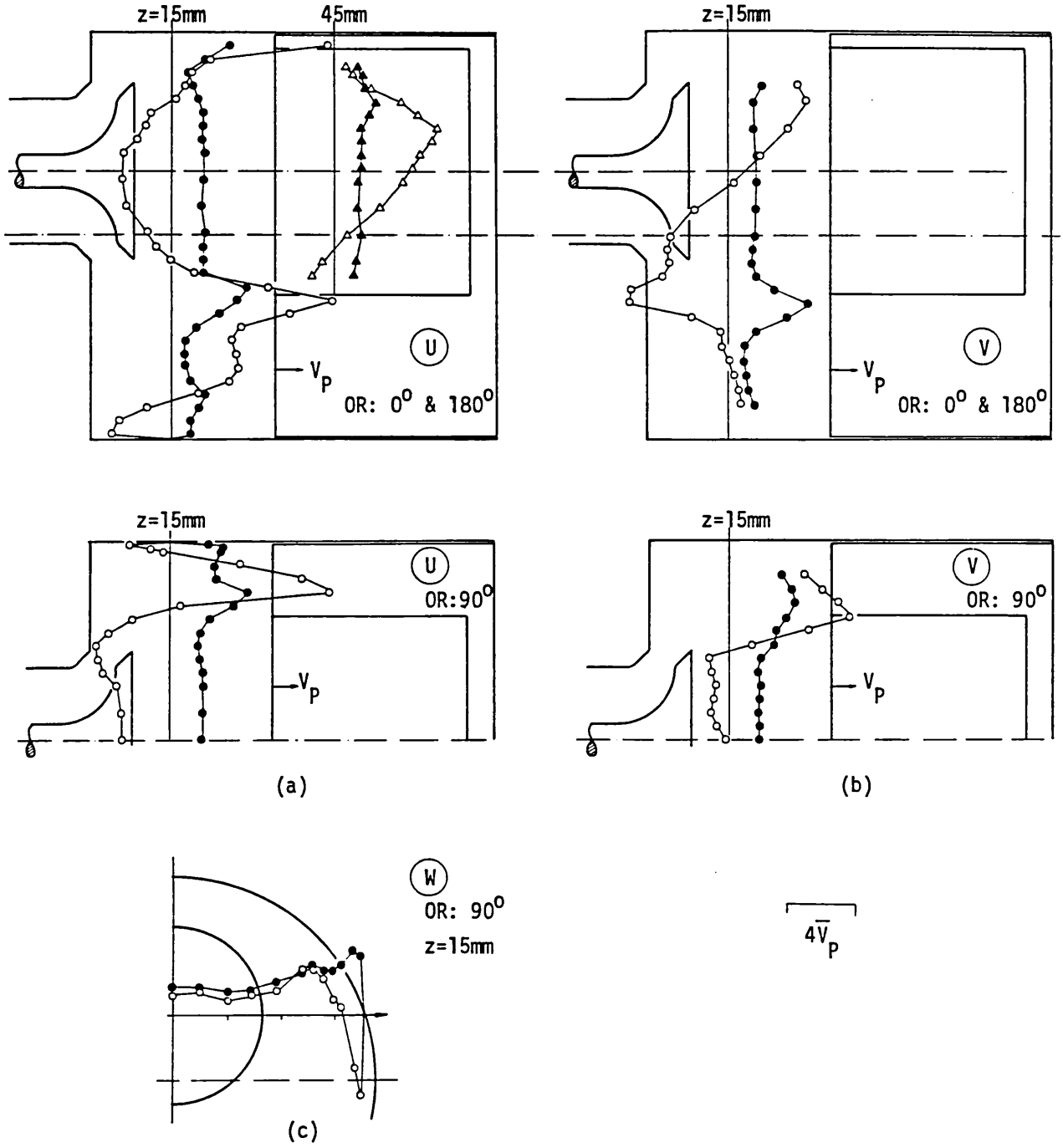

Fig. 3.24 Axial (a), radial (b) and tangential (c) velocity distribution at z = 15 mm along the 0, 90 and 180° measurement planes. θ = 68° (L = 8 mm), off-centre valve and piston-bowl

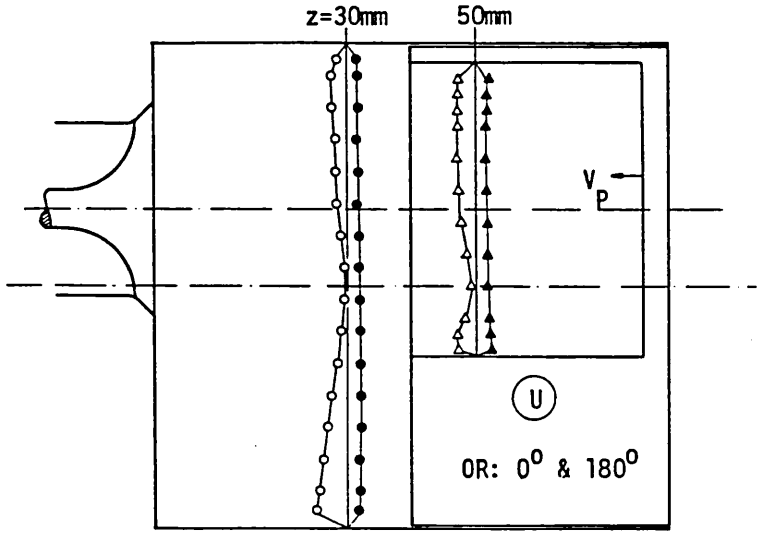

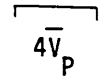

Fig. 3.25
Axial velocity distribution at z=30 and 50 mm along the 0 and 180° measurement planes. θ=288° off-centre valve and piston-bowl

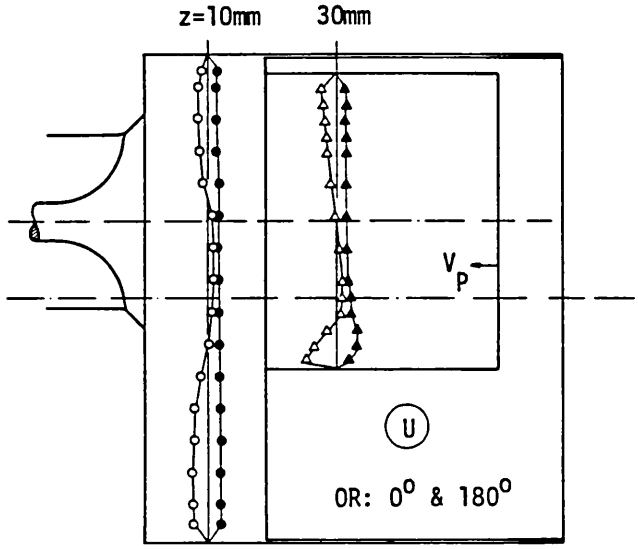

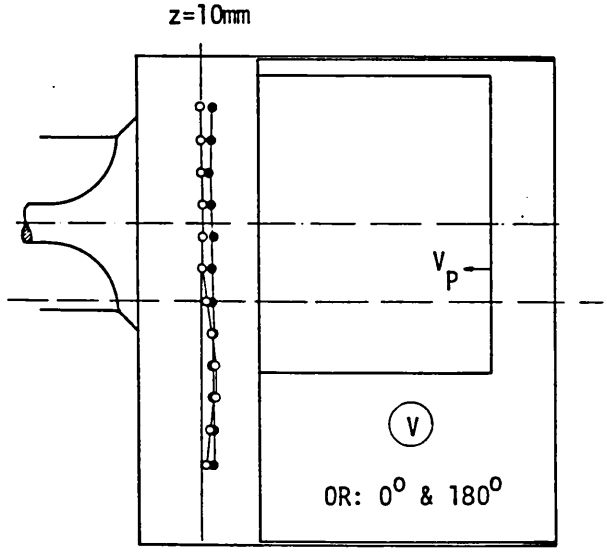

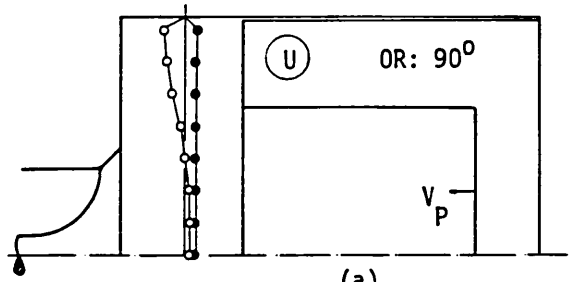

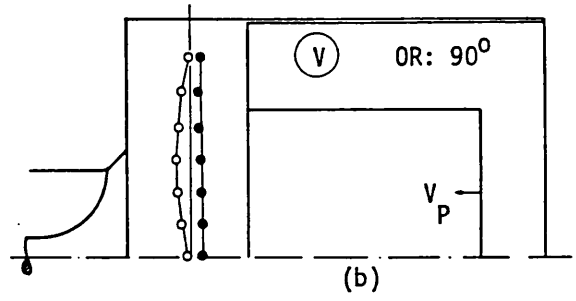

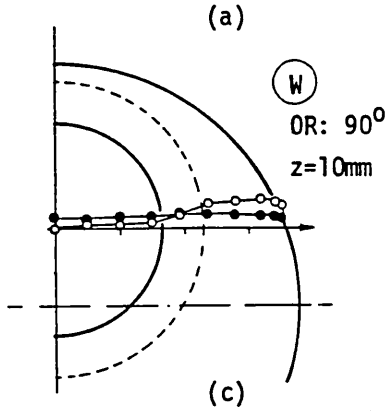

Fig. 3.26
Axial (a), radial (b) and tangential (c) velocity distribution at z=10mm along the 0, 90 and 180° measurement planes. θ=314°, off-centre valve and piston-bowl

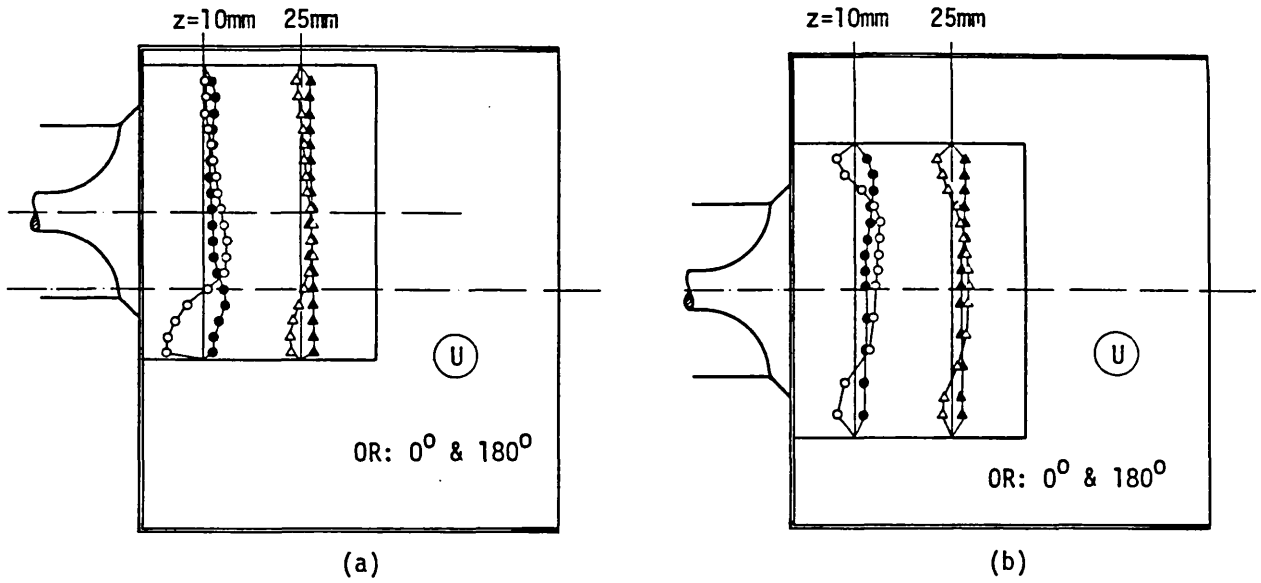

Fig. 3.27 Axial velocity distribution at z = 10 and 25 mm along the a) 0 and 180^{o} and b) 90^{o} measurement planes. $\theta = 360^{o}$ (TDC), off-centre valve and piston bowl

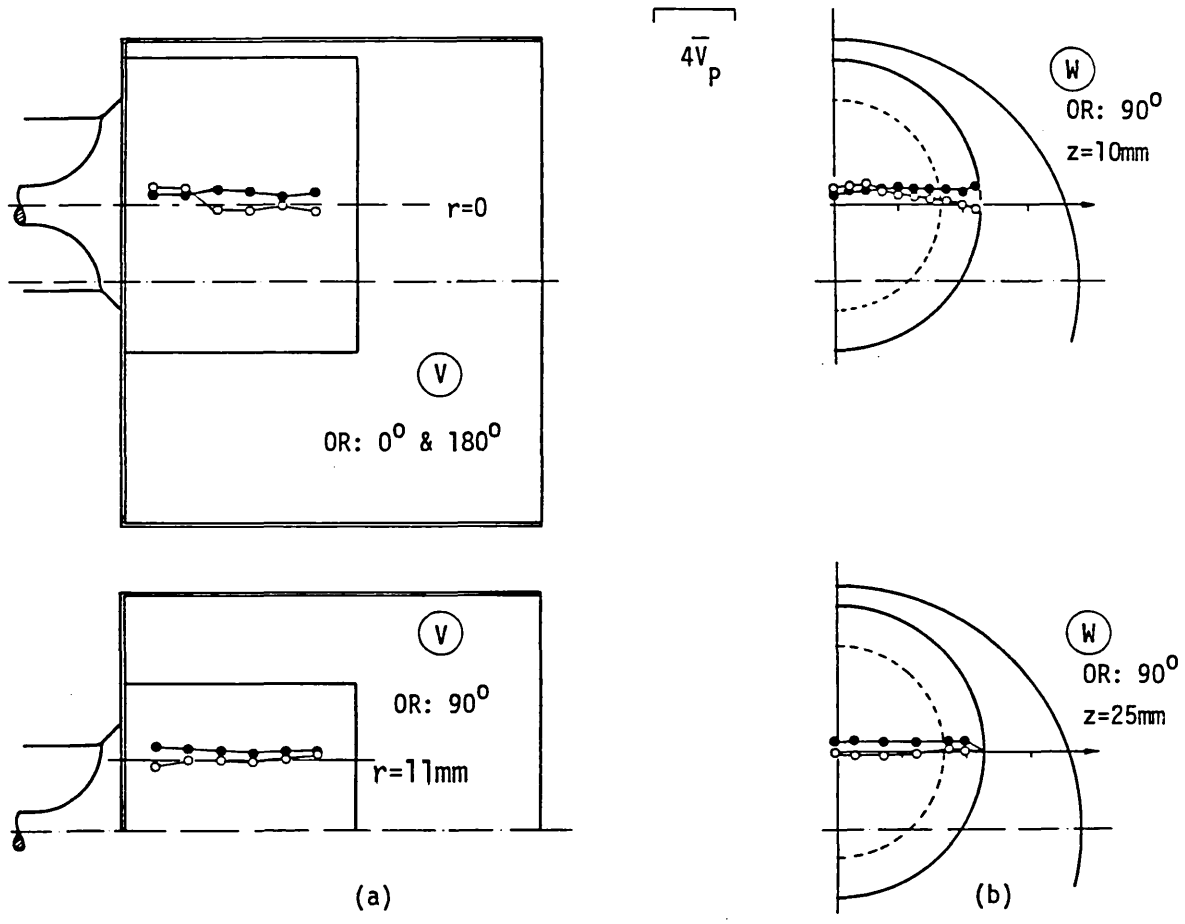

Fig 3.28 Radial (a) and tangential (b) velocity distribution inside the piston-bowl at $\theta = 360^{o}$

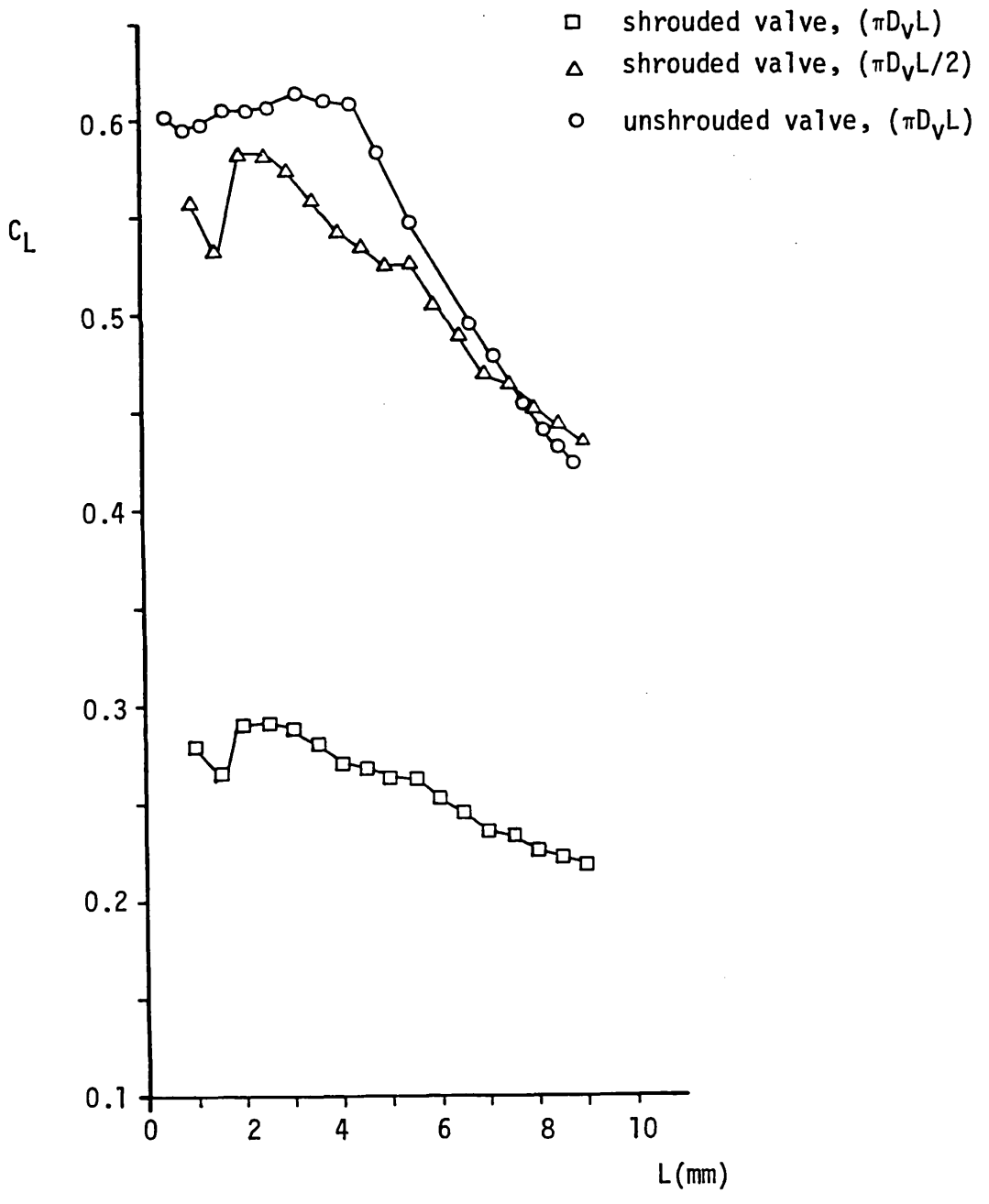

Fig. 3.29 Discharge coefficient, C_L , of the shrouded and unshrouded valves

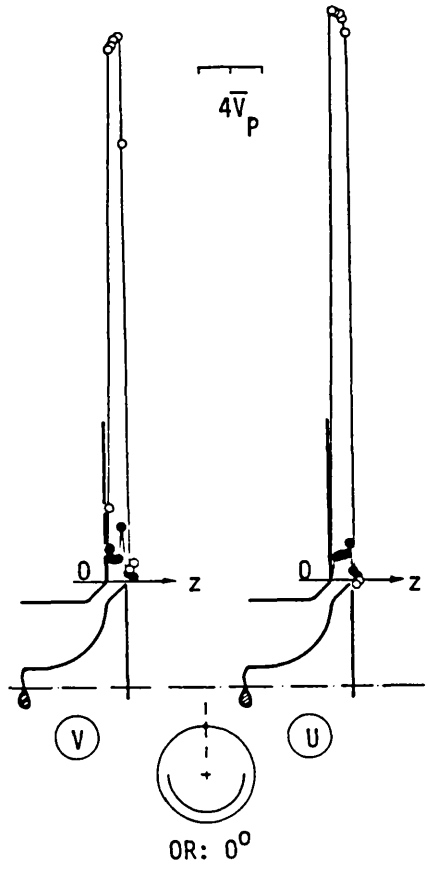

(a)

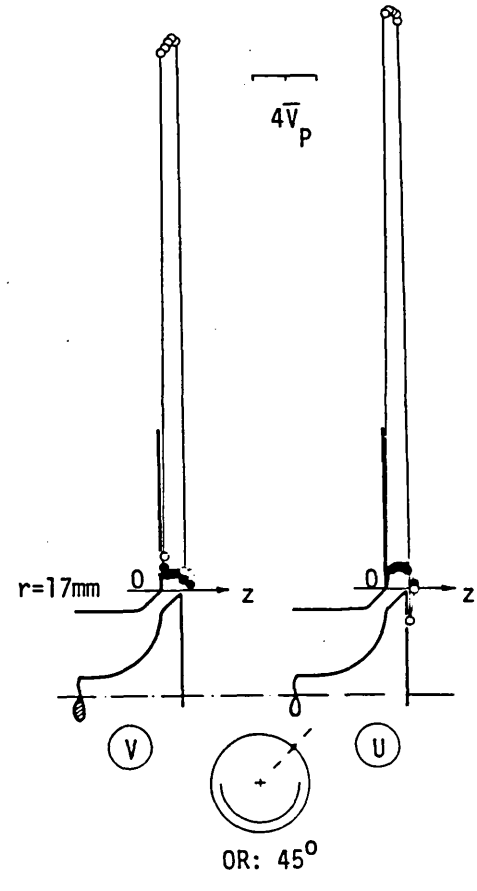

(b)

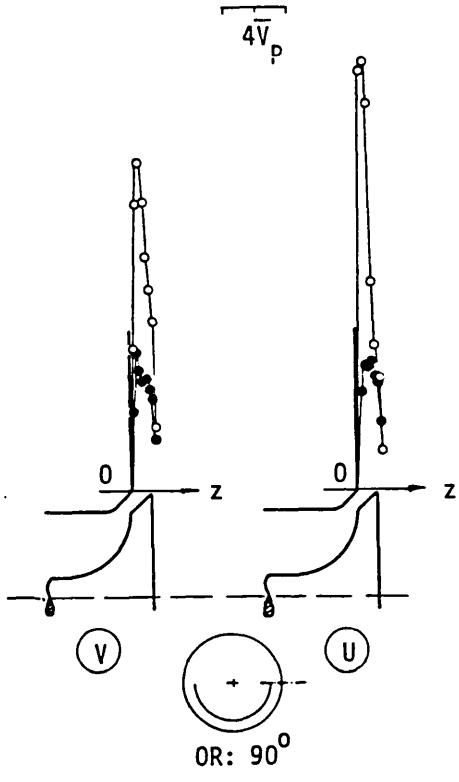

(c)

Fig. 3.30
Radial and axial velocity distribution at the exit of the shrouded valve along the a) 0^o, b) 45^o and c) 90^o measurement planes. Steady flow, L = 3 mm

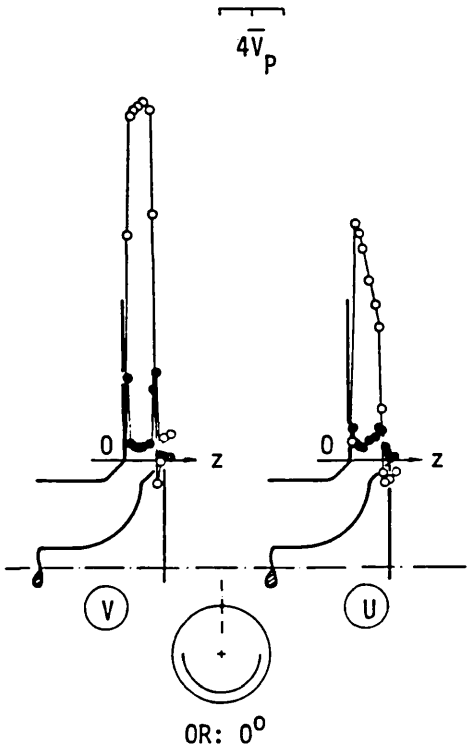

(a)

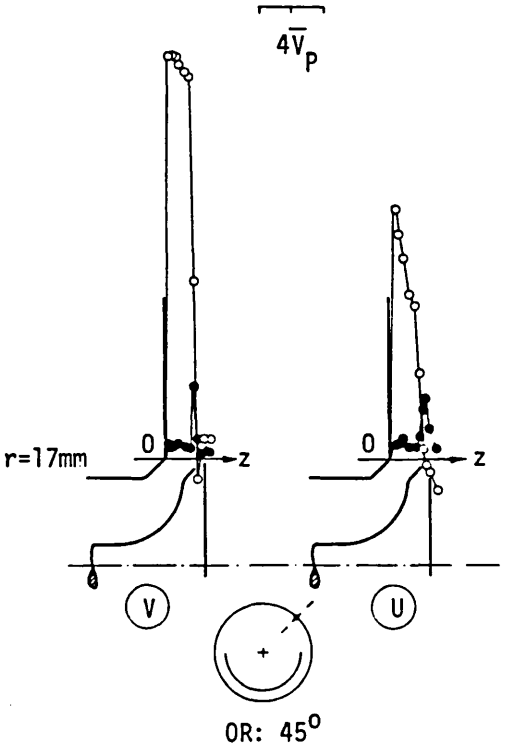

(b)

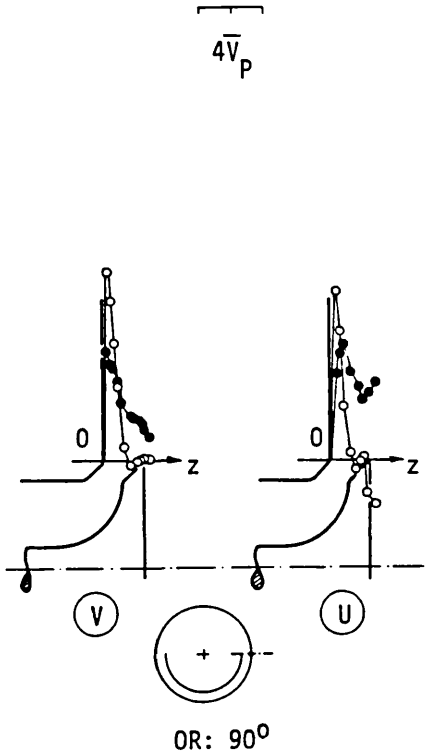

(c)

Fig. 3.31
Radial and axial velocity distribution at the exit of the shrouded valve along the a) 0^o, b) 45^o and c) 90^o measurement planes.
Steady flow, L = 6 mm

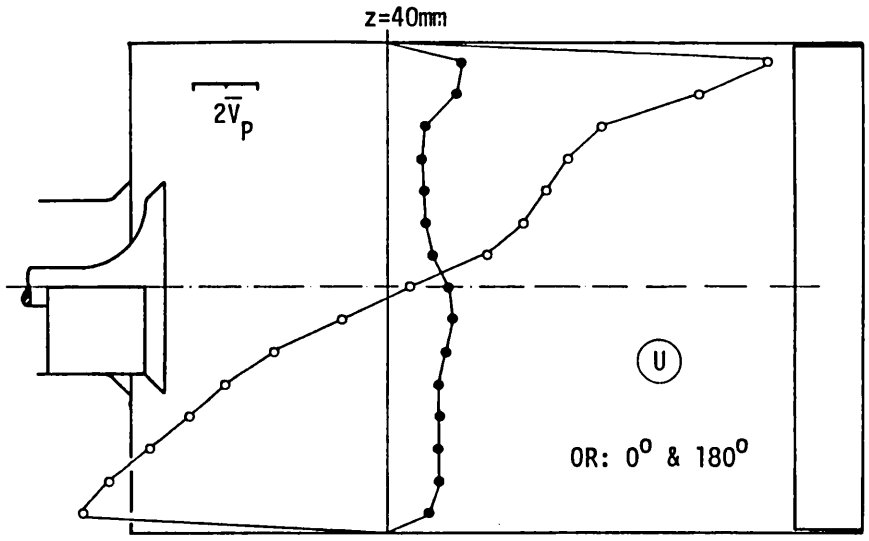

(a)

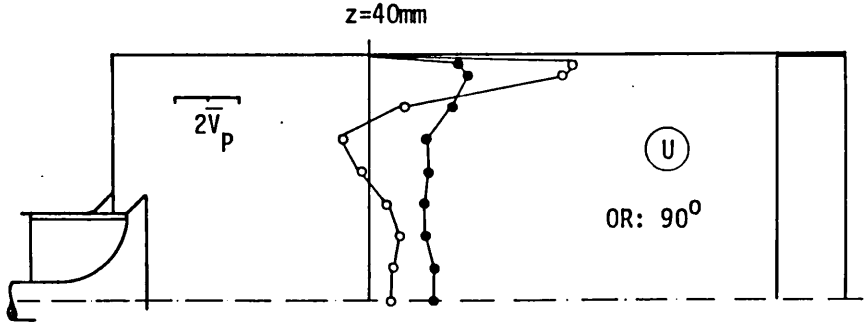

(b)

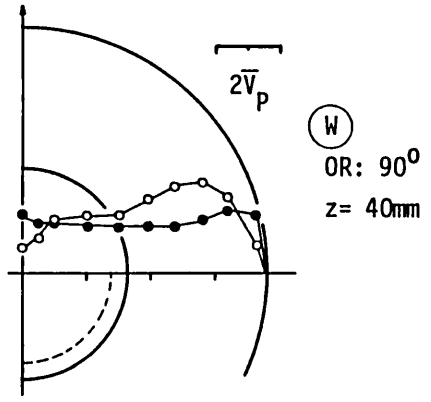

(c)

Fig 3.32
Axial (a,b) and tangential (c) velocity distribution at z = 40 mm along the 0, 90 and 180° measurement planes. θ = 144° (L = 5.3 mm), central directed port (shrouded valve), flat piston

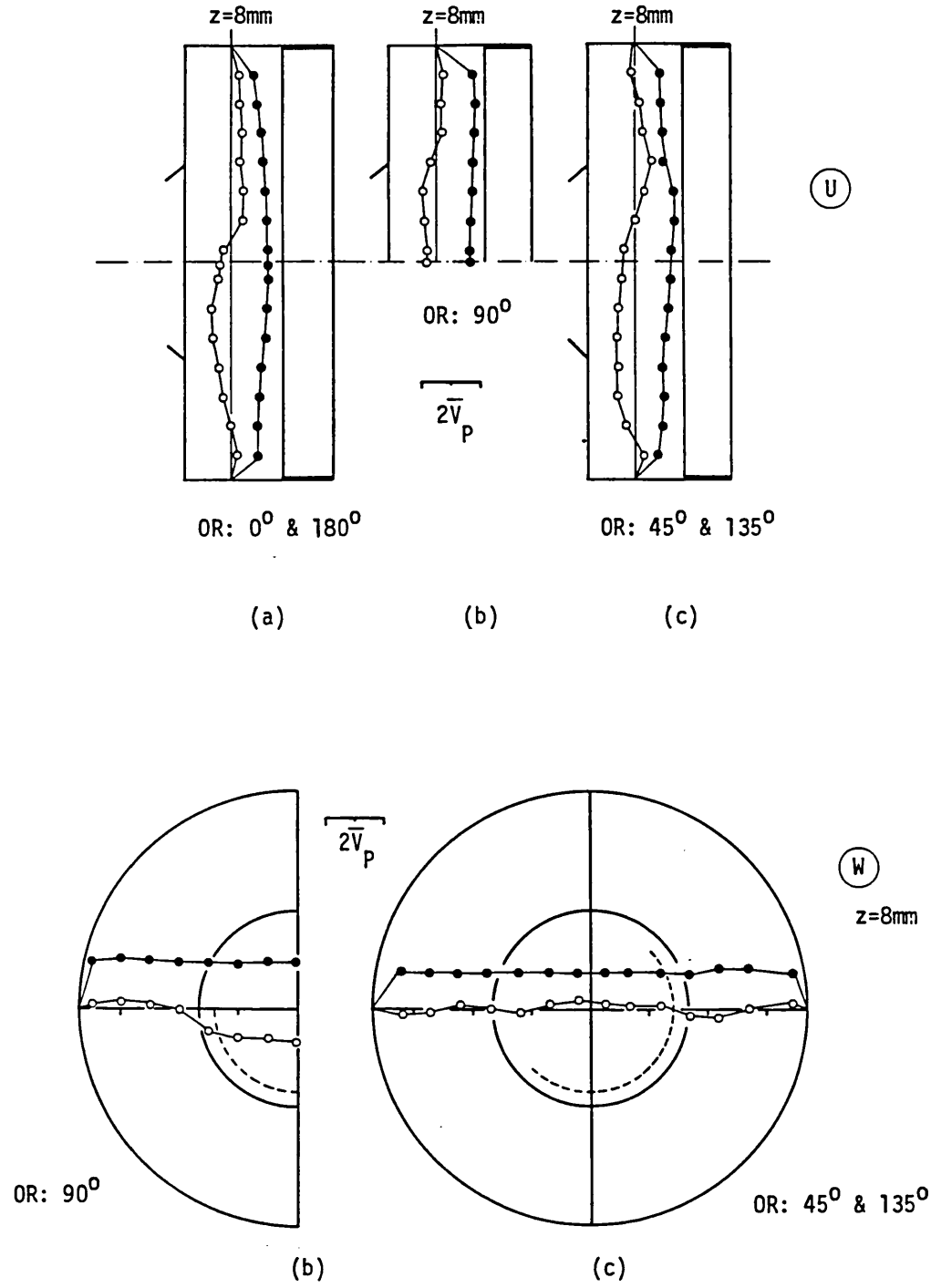

Fig. 3.33 Axial and tangential velocity distribution at z = 8 mm and $\theta = 360^{o}$ (TDC). Central directed port (shrouded valve), flat piston. a) 0 and 180^{o} , b) 90^{o} , c) 45 and 135^{o} measurement planes

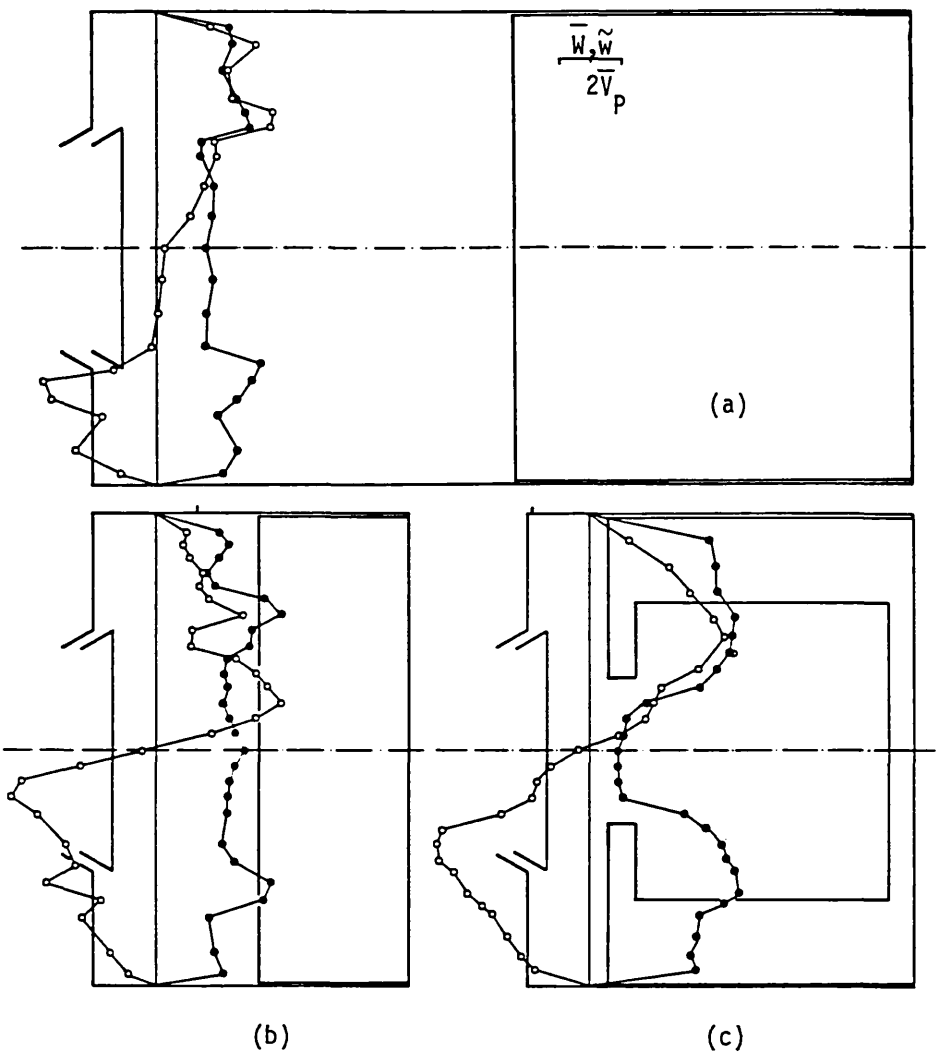

Fig. 3.34 Swirl velocity distribution at z = 10 mm. Swirl-producing intake ports. a) Flat piston, 30^{o} swirl vanes, $\theta = 90^{o}$, b) Flat piston, 60^{o} swirl vanes, $\theta = 36^{o}$, c) Re-entrant bowl piston, 60^{o} swirl vanes, $\theta = 36^{o}$

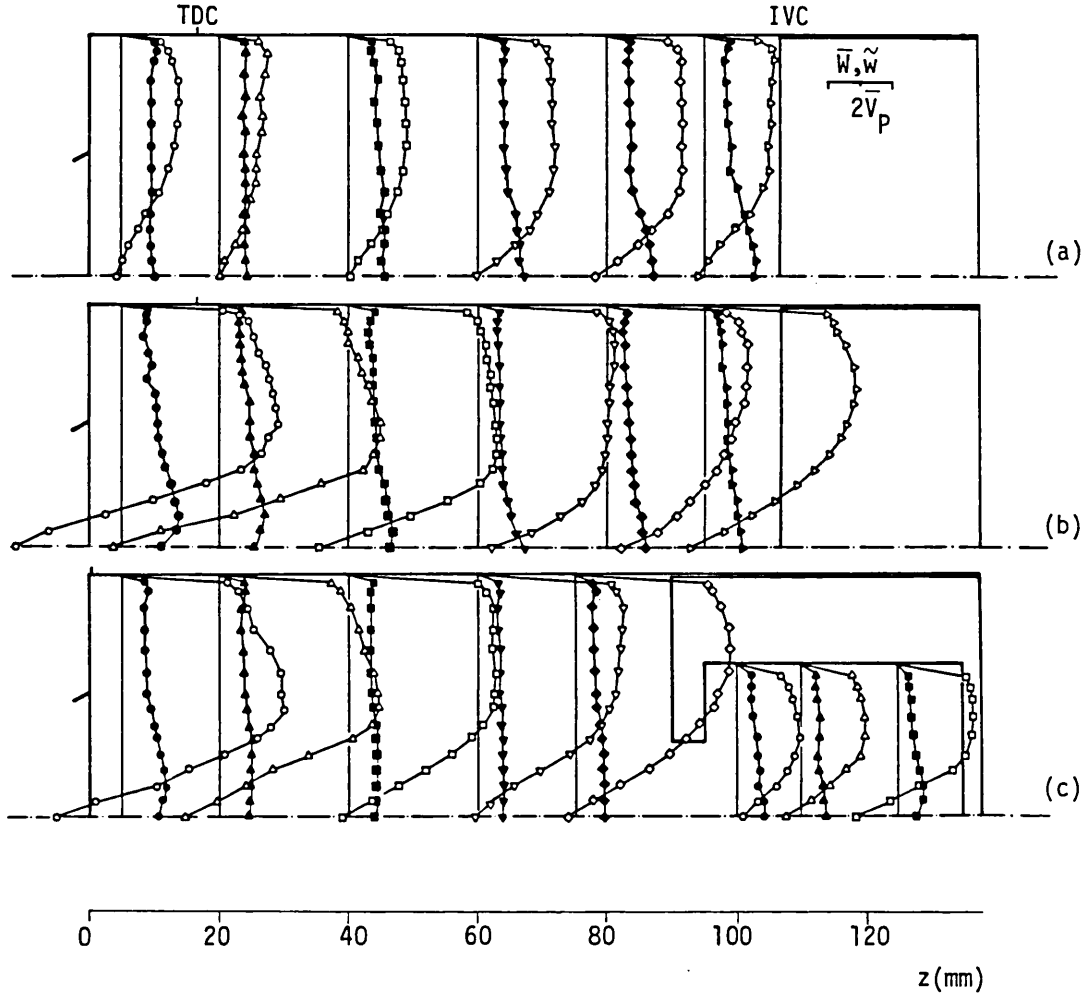

Fig. 3.35 Swirl velocity distribution at $\theta = 205^{o}$ (IVC). a) Flat piston, 30^{o} swirl vanes, b) Flat piston, 60^{o} swirl vanes, c) Re-entrant bowl piston, 60^{o} swirl vanes

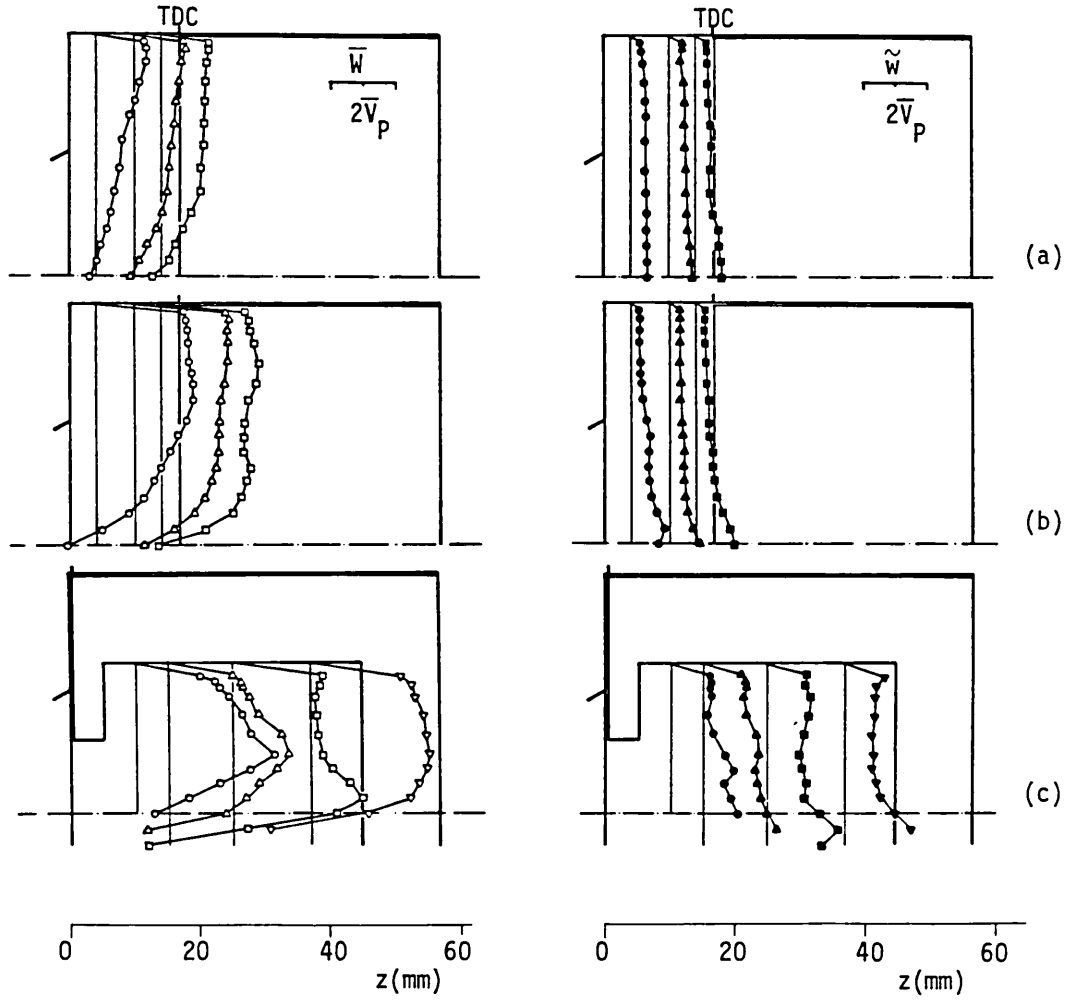

Fig. 3.36 Swirl velocity distribution at $\theta = 360^{o}$ (TDC). a) Flat piston, 30^{o} swirl vanes, b) Flat piston, 60^{o} swirl vanes, c) Re-entrant bowl piston, 60^{o} swirl vanes

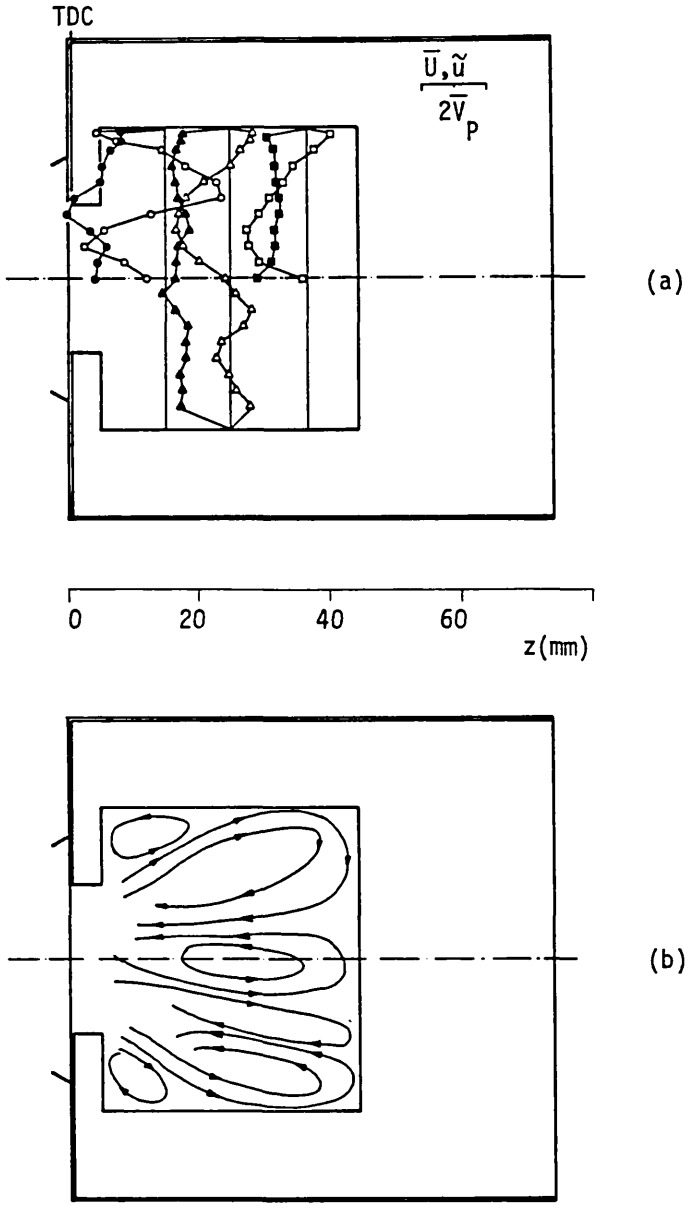

Fig. 3.37 Axial velocity distribution (a) and mean flow pattern (b) at $\theta = 360^{o}$ (TDC). 60^{o} swirl vanes, re-entrant bowl piston

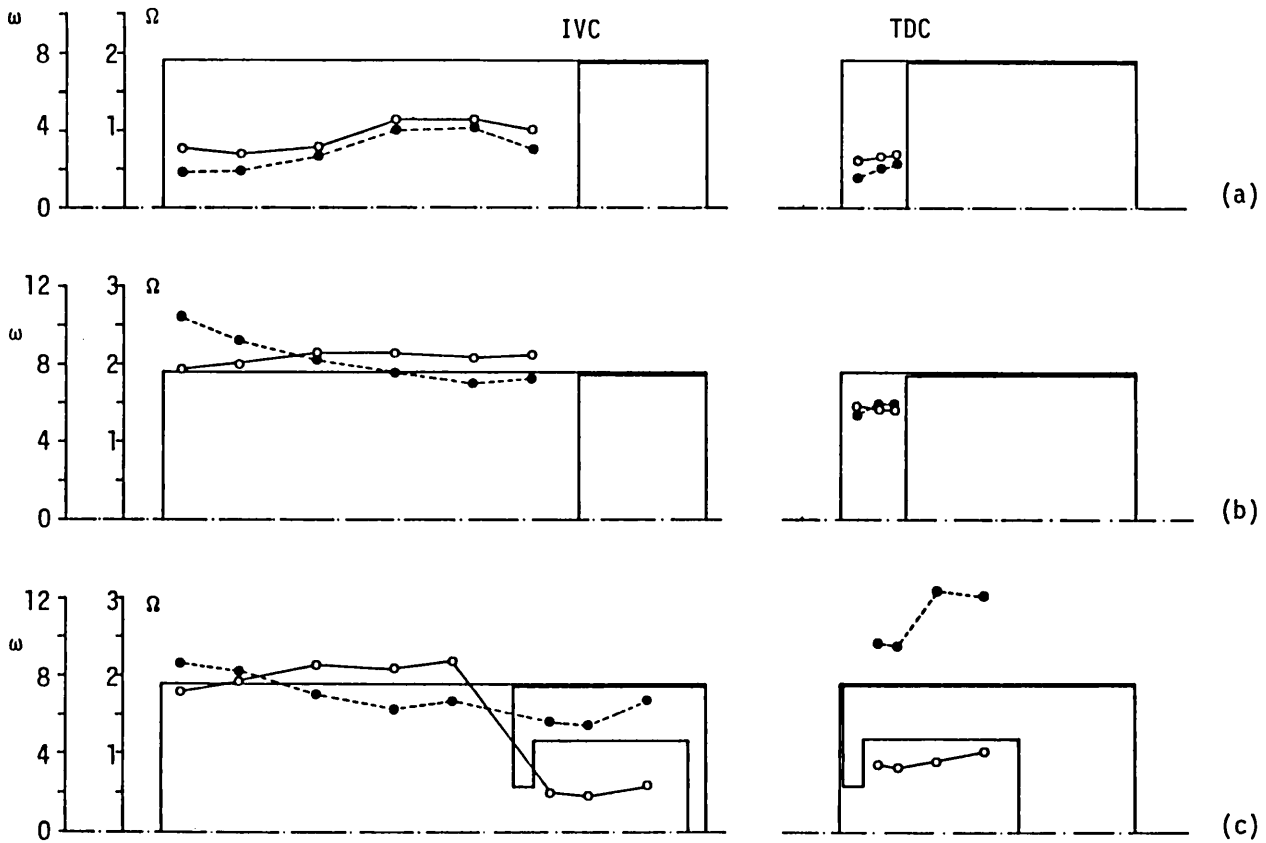

Fig. 3.38 Angular momentum (o) and rotational speed (●) axial distribution at $\theta=205^{o}$ (IVC) and $\theta=360^{o}$ (TDC). a) Flat piston, 30^{o} swirl vanes, b) Flat piston, 60^{o} swirl vanes, c) Re-entrant bowl piston, 60^{o} swirl vanes

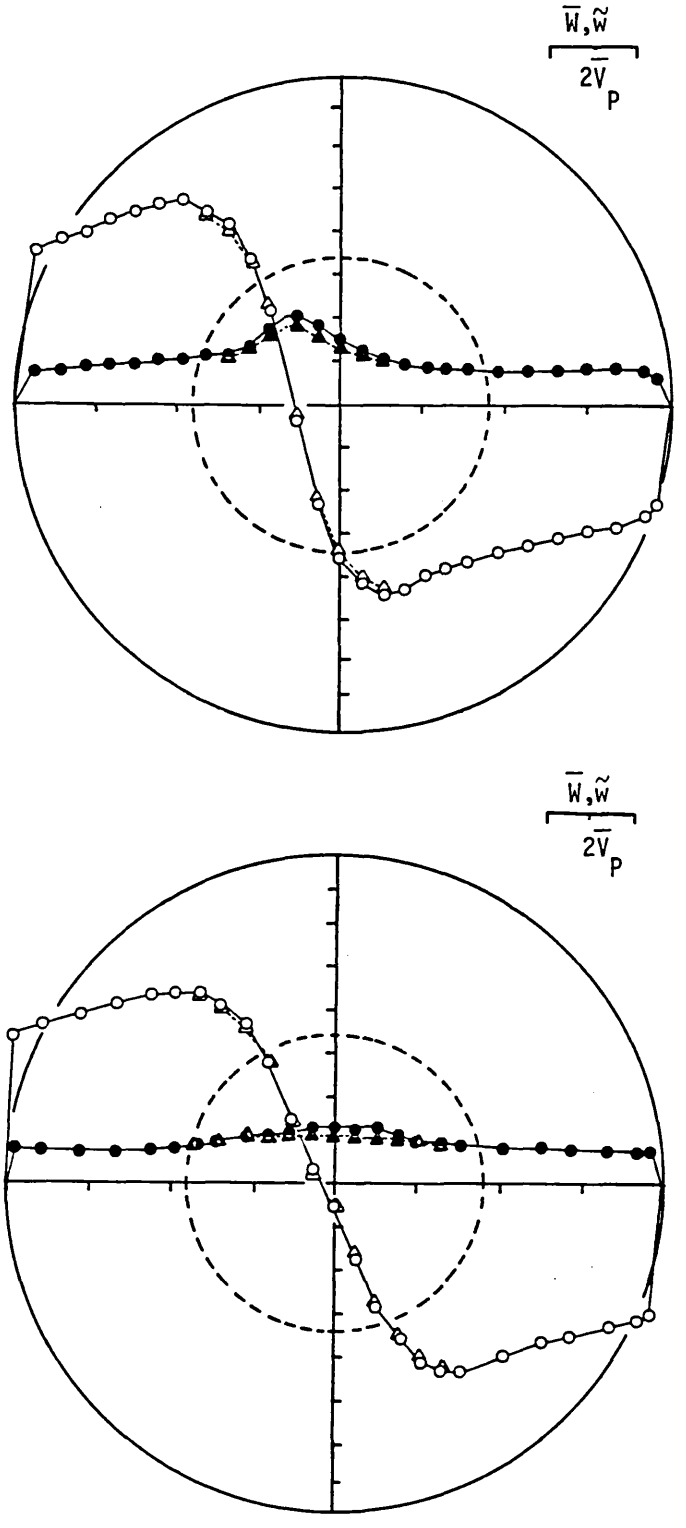

Fig. 3.39 Swirl velocity distribution at z = 20 mm. a) Flat piston, b) Re-entrant bowl piston. $\theta = 205^{o}$ (IVC), 60^{o} swirl vanes. (o, ●) : Length of measurement volume b_y= 600 μm (Δ, ▲) : Length of measurement volume b_y= 110 μm

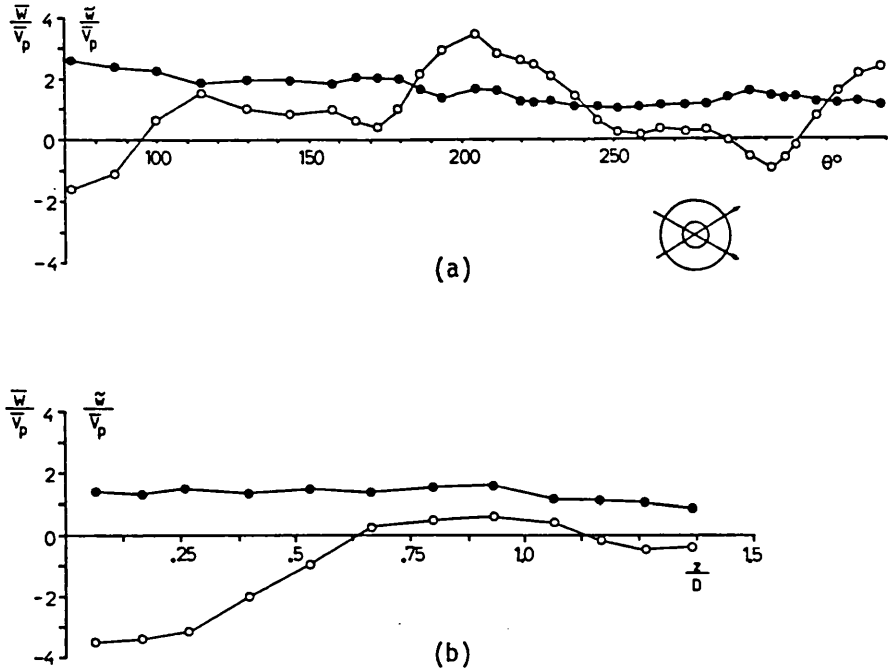

Fig. 3.40 Ensemble-averaged swirl velocities. Flat piston, 60° swirl vanes. a)Temporal profile at z=20mm, r=0. b) Cylinder axis scanning at θ=205° (IVC)

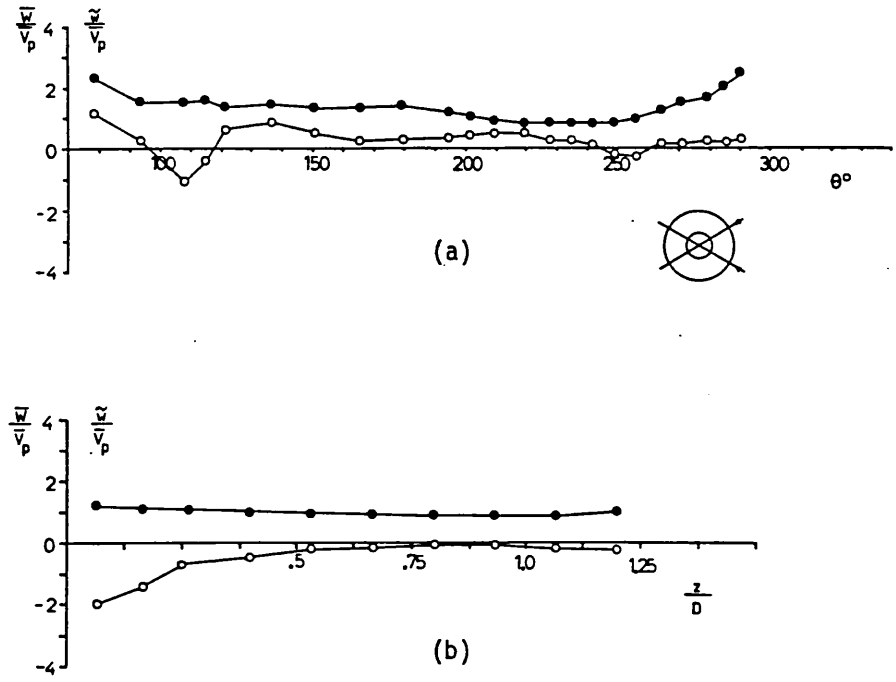

Fig. 3.41 Ensemble-averaged swirl velocities. Re-entrant bowl piston, 60° swirl vanes. a) Temporal profile at z=20mm, r=0. b) Cylinder axis scanning at θ=205°

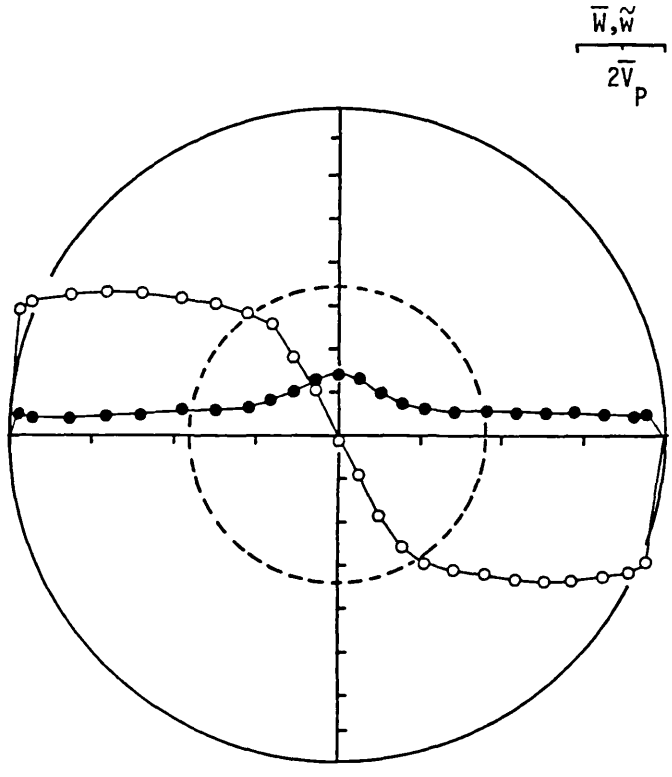

Fig. 3.42 Swirl velocity distribution at z = 20 mm.
Flat piston, 60^o swirl vanes, $\theta = 288^o$

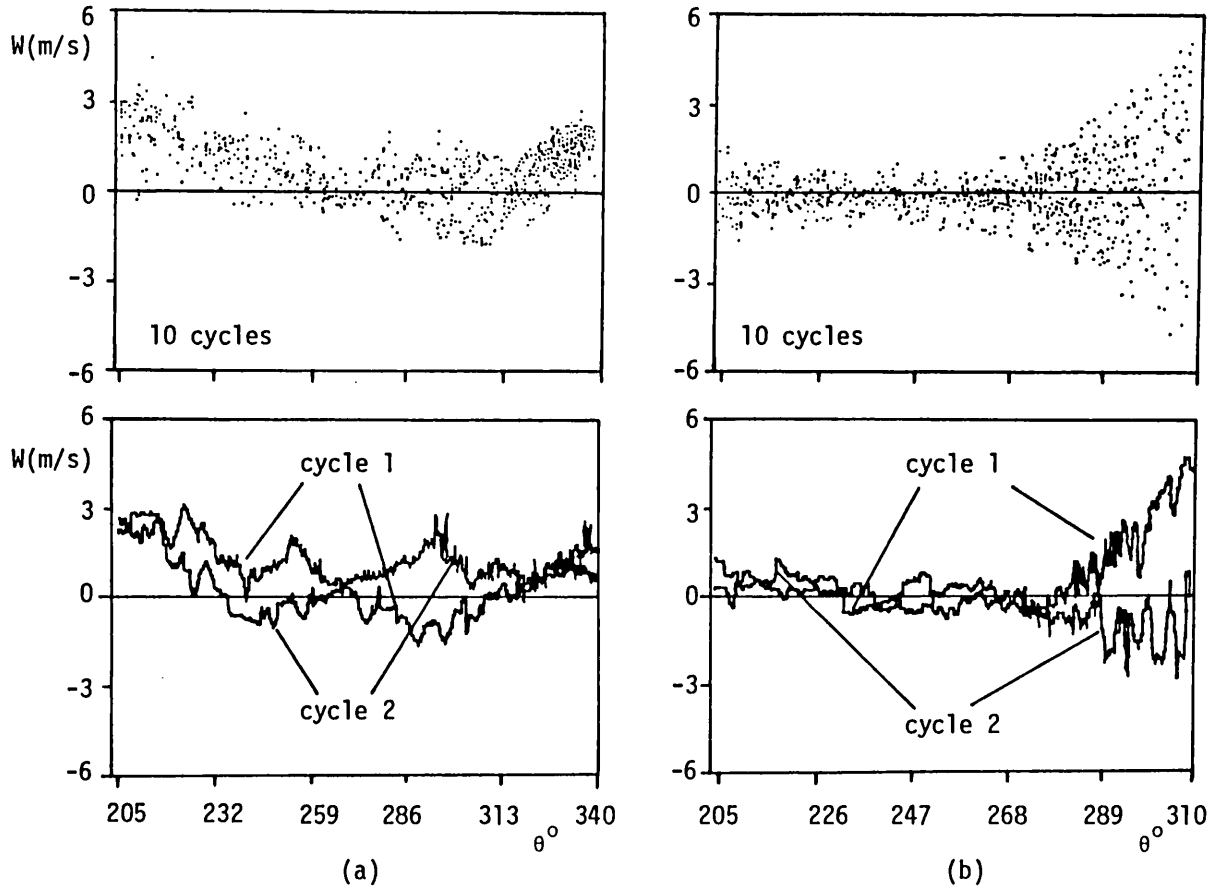

Fig. 3.43 Cycle-resolved instantaneous swirl velocity at z = 20 mm and r = 0 with 60^{o} swirl vanes. a) Flat piston, b) Re-entrant bowl piston

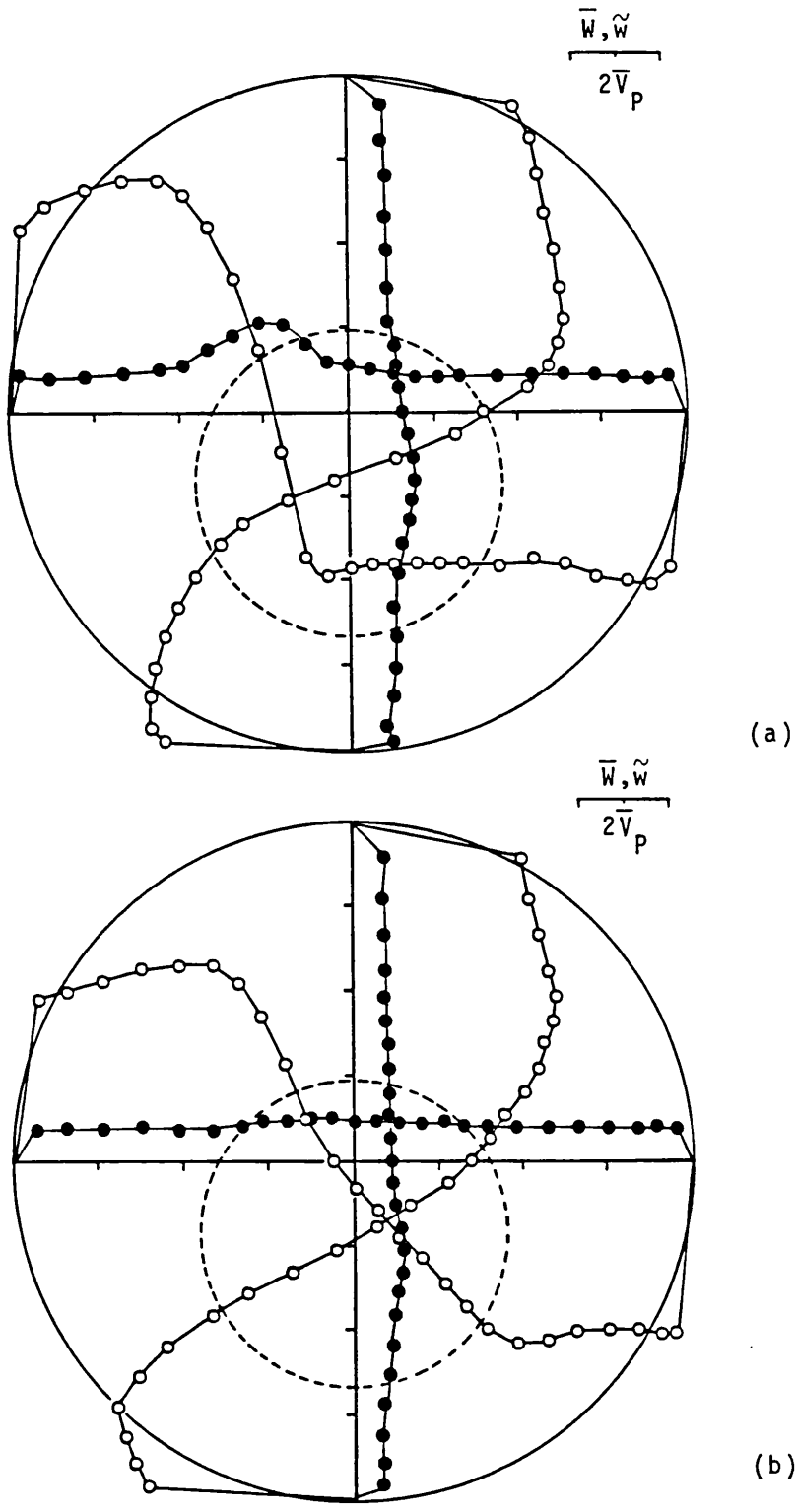

Fig. 3.44 Swirl velocity distribution at z = 20 mm and $\theta = 205^{o}$ (IVC). Off-centre valve, 60^{o} swirl vanes. a) Flat piston, b) Re-entrant bowl piston

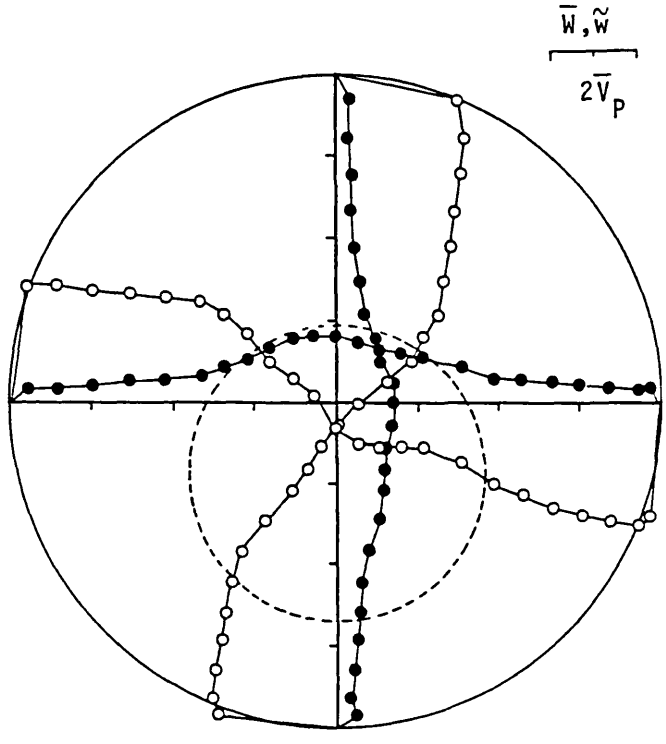

Fig. 3.45 Swirl velocity distribution at z = 10 mm. Flat piston, 60^o swirl vanes, $\theta = 360^o$ (TDC), off-centre valve

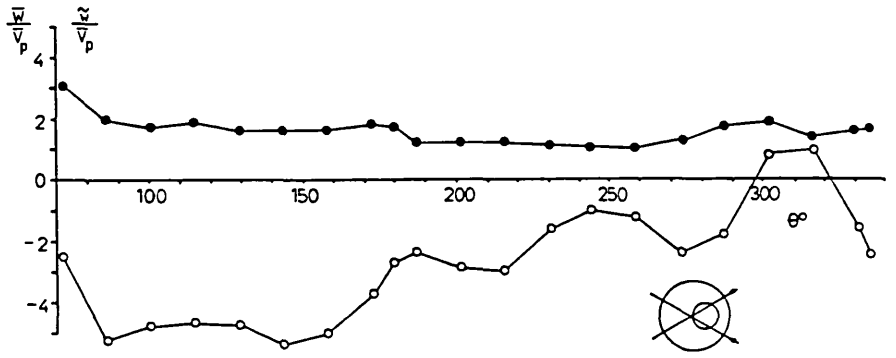

(a)

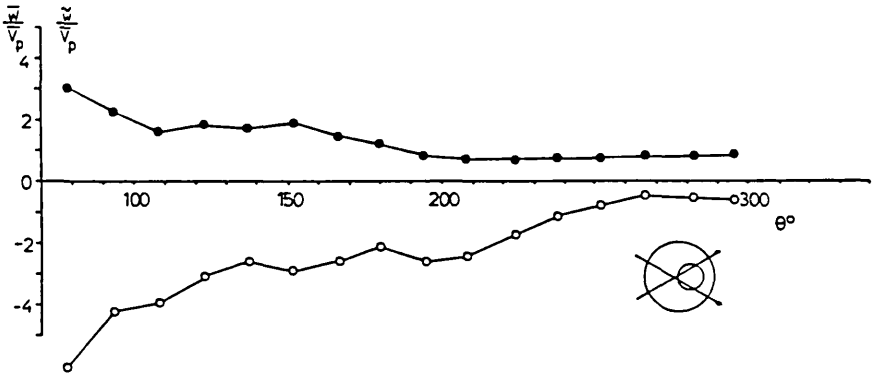

(b)

Fig. 3.46 Ensemble-averaged swirl velocity temporal profiles at z = 20 mm, r = 0. Off-centre valve, 60^{o} swirl vanes. a) Flat piston, b) Re-entrant bowl piston

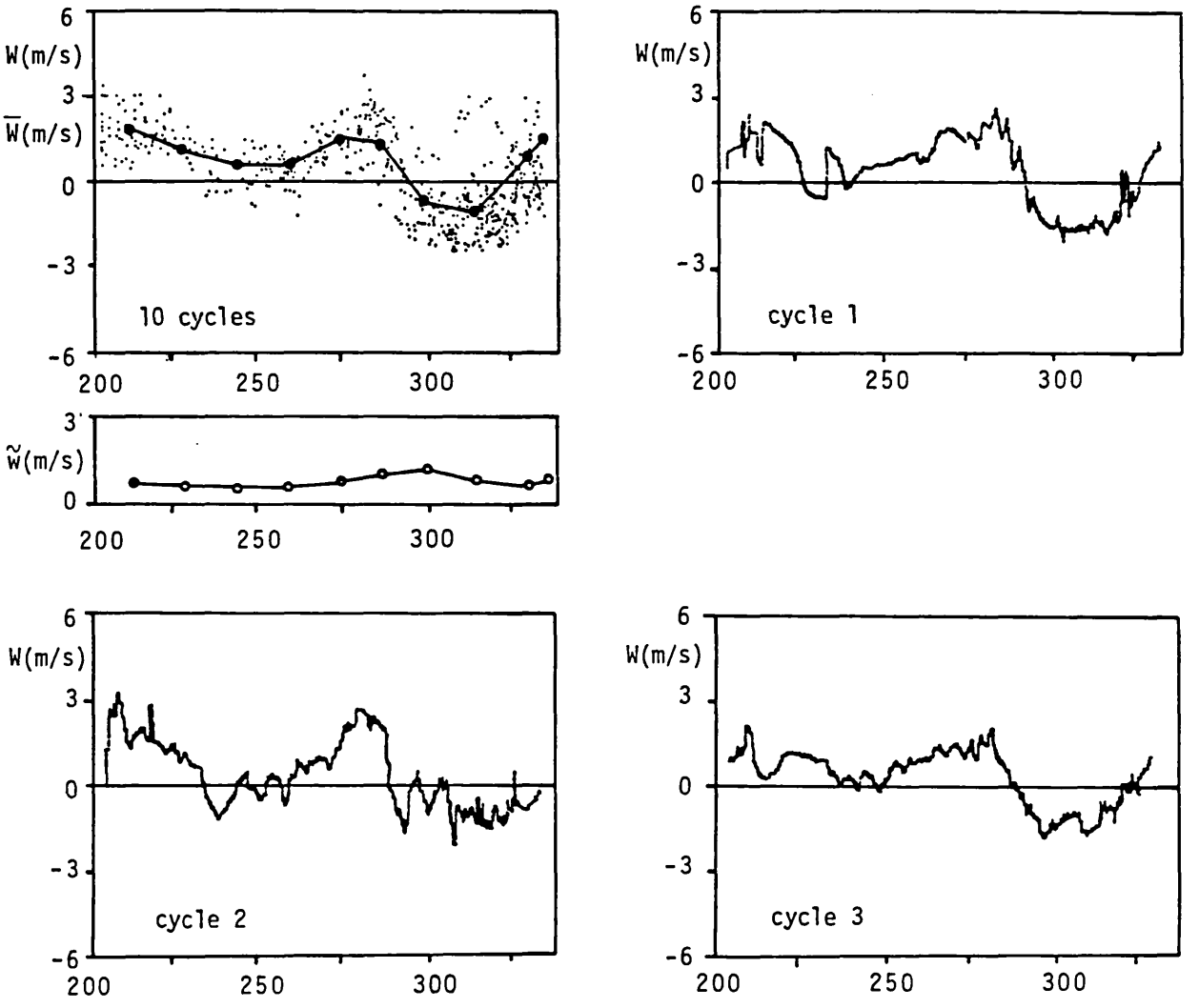

Fig. 3.47 Cycle-resolved instantaneous and ensemble-averaged swirl velocities at z = 20 mm, r = 0. Off-centre valve, 60^{o} swirl vanes

CHAPTER 4

FLOW IN A HIGH SPEED ENGINE

4.1 INTRODUCTION

The previous chapter described a detailed investigation of the development of the in-cylinder flowfield in a motored model engine with a variety of intake port and combustion chamber geometries. Common features of these engine configurations were the use of a single valve for both intake and exhaust and the low engine speed. Available information on in-cylinder flows suggests that there is a linear relationship between TDC turbulence and engine speed but, as discussed in sub-section 1.2.5.2 of the introduction, this conclusion is based on few data obtained in poorly documented engine configurations. For this reason, and considering the non-linearity of the induction process (sub-section 1.2.5.1), further investigation of the effect of engine speed on the in-cylinder flowfield was considered to be necessary.

This chapter describes detailed velocity measurements obtained in a modified production engine motored in the speed range of 300 - 2000 rpm. The induction system and combustion chamber geometries are similar to those of the off-centre plain port configuration of the model engine described in sub-section 3.4.2.3 of the previous chapter. The flow configuration and the measurement system are described in the following two sections. The in-cylinder flow development is described and compared with that of the model engine in sub-section 4.4.1 and is followed by a description of a detailed investigation of the effect of engine speed on TDC turbulence in sub-section 4.4.2. The conclusions of this study are summarised in section 4.5.

4.2 FLOW CONFIGURATION

A twin-cylinder horizontally opposed piston Citroen 2CV M28 gasoline engine was modified to provide full optical access in one of its cylinders for forward-scatter laser Doppler anemometry measurements (Fig. 4.1).

This engine was chosen for its inherent dynamic balance and simplicity which allowed modifications to be made with minimum effort. One of the engine liners was extended by 60 mm with a transparent cast acrylic (perspex) cylinder of 73.5 mm internal diameter and 13 mm wall thickness. The original piston was also extended by a cylindrical block and the original hemispherical cylinder head was replaced by the purpose-built flat head shown in Figure 4.2. The nominal volumetric compression ratio of the modified cylinder with the disc-type combustion chamber was 7.4. The intake port consisted of a smooth axisymmetric contraction leading to a short cylindrical section forming an idealised cylindrical port. The intake valve had a 45^{o} seat angle with rounded edges on both the valve head and valve seat (Valve type II, section 2.2) and was positioned 12 mm off the cylinder axis. All details of the downstream end of the intake port and its position on the cylinder head were identical to those of the off-centre plain port configuration described in section 3.2 of the previous chapter. The exhaust valve was similar to the intake valve and the exhaust port had a simple right angle diffusing bend shape. The two valves were operated through a pushrod-rocker mechanism by the original camshaft of the engine. The lubrication system of the engine remained unaltered and only one additional compression ring was incorporated to the original piston to minimise oil leakage to the combustion chamber. The operational characteristics of the modified engine are summarised in Table 4.1.

The modified Citroen engine was motored by a 5.6 kW thyristor-controlled DC motor through a toothed belt geared up with a ratio of 1:1.25. The engine/motor assembly was rigidly mounted on a 900 kg concrete block which was floor mounted through a vibration damping pad. The engine could be motored at speeds up to 2600 rpm with a speed stability better than 0.5% and with minimal vibrations. The rate of oil contamination of the transparent cylinder was very satisfactory for engine speeds below 2000 rpm but increased at higher speeds.

TABLE 4.1

Characteristics of the modified Citroen engine

Cylinder diameter, D_c, mm		73.5
Piston diameter, D_p, mm		72.2
Stroke, S, mm		70.0
Connecting rod length, ℓ, mm		130.0
Clearance at TDC, c, mm		10.9
Compression ratio		7.4
Intake valve:	Diameter, D_v, mm	33.0
:	Seat angle, ψ, deg.	45
:	Eccentricity, e, mm	12.0
:	Opens, IVO, deg. BTDC	14
:	Closes, IVC, deg. ABDC	80
:	Maximum lift, L_{max}, mm	8.9
Exhaust valve:	Diameter, D_v, mm	28.0
:	Seat angle, ψ, deg.	45
:	Eccentricity, e, mm	21.0
:	Opens, EVO, deg. BBDC	65
:	Closes, EVC, deg. ATDC	36
:	Maximum lift, L_{max}, mm	8.5
Engine speed, n, rpm (variable)		300 - 2000

4.3 MEASUREMENT SYSTEM

4.3.1 Velocity measurements

The in-cylinder velocity measurements were obtained with a laser Doppler anemometer operating in the dual-beam forward-scatter mode, similar to that used in the model engine investigation and described in section 2.3.2. The main differences were the smaller beam intersection angle used here to obtain axial velocity measurements along the whole diameter of the clearance volume at TDC, and the collecting optics which consisted of a DISA 55X34 optical module and an RCA4526 photomultiplier tube positioned at an angle of about 30^{o} to the laser axis. The off-axis light collection was chosen to avoid saturation of the photomultiplier from the reflections of the laser beams from the moving parts of the engine, as well as to reduce the effective size of the measuring volume and improve the signal-to-noise ratio. The LDA optics were mounted on a traversing mechanism which was independently based and vibration isolated from the engine block. The details of the LDA optical system are given in Table 4.2 and on Figure 4.3.

The flow was seeded with silicone-oil droplets as in the model engine. In this case, however, the blast atomiser used discharged continuously into a closed circuit system which recirculated the exhaust air to the intake port through a 0.1 m^3 chamber. This chamber was equipped with a high efficiency particle filter (Racal, Class P3, DIN 3181) which equilibrated the chamber pressure with the atmospheric and, at the same time, prohibited the silicone-oil droplets from leaving the system. The large size of the chamber (~ 350 times the piston swept volume) also damped the pressure fluctuations and allowed for cooling of the exhaust air.

The Doppler signal from the photomultipler was amplified and band-pass filtered in the range 0.5 to 20 MHz by a Harwell 95/2153 - 1/6 amplifier and subsequently high-pass filtered by a variable filter (Krohn-hite model 3200). The conditioned signal was passed to a purpose-built 4ns resolution Doppler frequency counter interfaced to an Apple IIe microcomputer used for remote programming of the counter as well as for data acquisition and processing. The frequency counter, which is described in detail by Heitor et al (1984), validated the Doppler signals in the amplitude (Doppler envelope recognition) and frequency domains

TABLE 4.2

Optical characteristics of the laser Doppler anemometer

Laser:	Wavelength, nm	632.8
	Power, mW	5
	Beam diameter at $1/e^2$ intensity, mm	0.8
Lenses:	L_1, focal length, mm	100
	L_2	200
	L_3	300
Diffraction grating:		
	Number of line pairs, (N_ℓ)	16384
	Frequency of rotation, (f_r) Hz	0 - 200
	Frequency shift (1st order beams), (f_s), MHz	0 - 6.55
Beam separation, (s), mm		42
Beam intersection half angle, ($\phi/2$), deg.		3.85
Measurement volume dimensions ($1/e^2$ intensity)		
	diameter, (b_x), μm	150
	length, (b_y), μm	2220
Number of stationary fringes, (N_f)		32
Frequency to velocity conversion factor,		
	(λ^*), ms^{-1}/MHz	4.712
Light collection angle, deg.		30
Magnification of collecting optics, (M)		0.67
Pinhole diameter, (d_{Ph}), mm		0.1
Effective diameter of measurement volume, μm		150
Effective length of measurement volume, μm		900

(5/8 or 10/16 cycles comparison) and allowed for gated measurements through an "external request" input. This measuring system was preferred to the fixed-gate or 10 ns resolution counters used for the ensemble-averaged and cycle-resolved measurements in the model engine, due to its higher speed (40 μs cycle time) and better resolution and validation capabilities. The latter feature was essential since the signal quality was lower than that in the model engine, due mainly to oil-contamination of the transparent cylinder.

An optical shaft encoder provided 2000 pulses per revolution (HP HEDS-6010B09) and was mounted on the camshaft of the engine with its pulse train processed by an electronic circuit to give a variable gating pulse which enabled the microcomputer to validate measurements within the preset crank angle windows. These data were subsequently ensemble-averaged to provide mean and r.m.s. velocity values, while a facility for monitoring the probability density distribution of the measured frequencies was also available. This allowed further digital filtering or rejection of a sample and increased the confidence of the velocity measurements.

4.3.2 Measurement uncertainty

The error sources in the velocity measurements in the high speed engine are similar to those discussed for the model engine in sub-sections 2.3.3 and 3.3.2. A brief analysis of the measurement errors is given below with particular emphasis on the frequency response of the seeding particles in the high speed engine and the accuracy of the frequency counter.

The experiments of Lancaster (1976) showed that 80% of the turbulent energy of the TDC flowfield in a disc-type combustion chamber engine motored at 1500 rpm is contained in the frequency spectrum below 1 kHz. The velocity fidelity of the silicone-oil droplets with diameters of 1 - 3 μm is known to be very good at even higher frequencies (see sub-section 2.3.3) and therefore the seeding material is not expected to introduce errors in the TDC turbulence measurements in the speed range investigated.

The measurement accuracy of the 4 ns resolution frequency counter, in the range of frequencies encountered, was approximately 0.2% and led to a maximum systematic error of 0.008 MHz, equivalent to 0.038 ms^{-1}.

The "fringe bias" was rendered insignificant by using adequate frequency shift and measuring over 8 only cycles of the Doppler signal, while the good signal quality of the forward-scatter LDA and the validation circuitry of the counter minimised the possibility of erroneous frequency measurements. The possibility of measurement broadenings due to velocity gradients and finite measurement window was also minimised by the effective reduction of the measurement volume by the off-axis light collection (see Table 4.2) and the small measurement crank angle window of 3.6^{o} used. The resolution of the shaft encoder was 0.36^{o} and the engine speed and frequency shift were stable within 0.5% and 0.3% r.m.s. respectively. The main uncertainty in the estimation of the r.m.s. of the turbulent fluctuations is introduced by the finite sample size (1200) and is expected to be accurate within 3% with a confidence level of 95%; the corresponding uncertainty of the mean velocity measurements is typically 2.5% for the measurements obtained at IVC and increases towards TDC of compression due to the simultaneous increase of the relative turbulence intensity, as the mean velocities tend to zero. The day-to-day repeatability of the r.m.s. and mean velocity measurements at TDC of compression was better than 4% and 10% respectively.

The velocity measurements have been corrected for refraction effects as described in Appendix 2.4 and the positioning uncertainty was similar to that in the model engine experiments. The overall maximum error in the r.m.s. velocity measurements is expected to be less than 5%, since all the measurements reported here were obtained in flow regions without severe velocity gradients in space or in time and with relatively low turbulence intensity. The error in the mean velocity measurements is around 4%, increasing as the velocity magnitudes decrease. These errors, however, are not expected to influence the conclusions of this investigation.

4.4 RESULTS AND DISCUSSION

In the first part of this section the development of the in-cylinder flowfield from BDC of induction to TDC of compression is described for the modified engine operating at 1000 rpm and is compared with that of the low speed model engine with the off-centre plain intake port described in sub-section 3.4.2.3. In the second part a detailed investigation of the effect of engine speed on the TDC flowfield is presented for a speed range of 300 to 2000 rpm.

4.4.1 Flow development

The distributions of the axial mean and r.m.s. velocity components on the plane defined by the axes of the valves are presented in Figures 4.4a and b for $\theta = 180^{o}$ (BDC of induction) and $\theta = 267^{o}$ respectively. The BDC flowfield is characterised by a weak vortex occupying most of the cylinder space, indicative of the persistence of the induction generated flow structure at this point of the cycle. The distribution of turbulence intensity along the measurement plane is not uniform with maxima of around $2\overline{V}_p$ at the exhaust valve side of the cylinder. This is attributed to the higher production of turbulence at this side of the valve jet during induction, as shown in Figures 3.14 - 3.17 for the model engine, which starts being redistributed by the end of the intake stroke. Shortly after the inlet valve closure, at $\theta = 267^{o}$ (Fig. 4.4b), turbulence has decayed considerably and has been redistributed along the cylinder diameter with maximum values around $1.1\ \overline{V}_p$ near the cylinder axis. The mean flow is not uniform and exhibits axial velocities 50% higher than the instantaneous piston speed near the exhaust valve side of the cylinder. Detailed scanning of the measurement plane did not reveal any flow reversals in the cylinder space at this point of the engine cycle. The axial velocity measurements at TDC of compression, in the mid-plane of the clearance volume and along two diameters perpendicular to each other, are shown in Figures 4.5a and b and do not show strong axial flow structures. The distribution of the axial r.m.s. velocities is not uniform with magnitudes decreasing from $0.65\ \overline{V}_p$ near the cylinder axis to $0.4\ \overline{V}_p$ near the wall. The measurements of tangential and radial

velocity components, Figures 4.5c and d, do not suggest flow structures, while the magnitude and distribution of the corresponding r.m.s. velocites are nearly identical to those in the axial direction. These results indicate that the TDC turbulence is near isotropic but deviates from homogeneity by up to 35%.

Similar measurements to those of Figure 4.5a were obtained with the lower speed of 300 rpm and are shown in Figure 4.6; in this case the turbulence intensity decreases only by 25%, from 0.55 $\overline{V}_p$ near the cylinder axis to 0.4 $\overline{V}_p$ near the cylinder wall. Comparison of the results at 300 and 1000 rpm indicates that the non-homogeneity of the TDC turbulence field increases with engine speed, as also suggested by the calculations of Ahmadi-Befrui (1985b). The results for the 300 rpm are shown here in order to allow a better comparison between the TDC flowfield in the present engine configuration with that in the 200 rpm model engine. It should be noted that the two engines have comparable mean piston speeds at 300 and 200 rpm, ($\overline{V}_p$ = 0.7 and 0.627 ms^{-1} respectively) due to their different strokes (70 vs 94 mm). The measurements of the axial mean and r.m.s. velocities obtained in the 200 rpm model engine along the same plane in the clearance volume (Fig. 3.19a of Chapter 3) are also shown, superimposed on the 300 rpm results of Figure 4.6. The scale of this diagram has been enlarged to emphasise possible differences, but mean velocity distributions are the same in both cases with even better similarity of the turbulence intensity distributions. It should be stressed that the two engine configurations differed significantly in bore-to-stroke ratio (1.05 vs 0.8), valve timing (IVC = 210 vs 260^o) and by the presence or not of an exhaust valve. The common features of the two engines were the geometry and location of the intake port, the geometry of the combustion chamber and the compression ratio (7.7 vs 7.4) and consequently these parameters are likely to be the main factors affecting the flowfield characteristics at TDC of compression. In addition, the results of this comparison justify the model engine investigation as a good approximation of a realistic engine.

4.4.2 Speed investigation

The effect of engine speed on the in-cylinder flowfield at TDC of compression was investigated in the speed range 300 to 2000 rpm by measuring the axial mean and r.m.s. velocity components along a diameter in the middle of the clearance volume and on the plane defined by the valve axes. The results are presented in Figure 4.7 and are normalised by the associated mean piston speeds. The mean velocity distribution does not change with increasing engine speed, remaining between -0.05 $\overline{V}_p$ and + 0.15 $\overline{V}_p$ over the larger part of the cylinder with an exception near the wall at the side of the intake valve. The lack of clear trend in mean velocity variation with engine speed combined with the measurement uncertainty in the mean velocities due to the high relative turbulence intensity does not allow any firm conclusion to be drawn. The turbulence intensity data, however, exhibit variations which are larger than the measurement uncertainty and indicate a greater than linear dependence on engine speed. This trend of the ensemble-averaged r.m.s. velocities might be attributed to an increase of the "cyclic variations" as defined by Liou et al (1984) but their data show that the so-defined ensemble-averaged cyclic variations of the mean velocity, when normalised with the mean piston speed, decrease with increasing rpm. This observation, together with the expected accuracy of the rms velocity measurements, confirms that the trends of the window ensemble-averaged measurements represent adequately the actual variations of TDC turbulence with engine speed.

Overall the non-homogeneity of turbulence increases with engine speed, particularly in the low speed range of 300 - 1000 rpm. Turbulence intensity exhibits maxima of 0.55 to 0.7 $\overline{V}_p$ near the cylinder axis for 300 and 2000 rpm respectively, decreasing by up to 35% towards the cylinder wall. This non-uniformity is clearly shown by the different slopes of the curves of Figure 4.8 which represent the variation of the r.m.s. of the turbulent velocity fluctuations as a function of engine speed at five locations on the measurement plane. This figure also illustrates the inadequacy of measurements obtained at one only point of the clearance volume for the characterisation of TDC turbulence even in the simplest combustion chamber configurations.

In order to establish the relationship between TDC turbulence and engine speed in a more comprehensive way, the data of Figure 4.7 have

been processed to yield the average turbulence intensity on the mid-plane of the clearance volume at TDC of compression, defined as:

$$\sqrt{\overline{u^2}}_{aver} = 4\left[\sum_{i=0}^{N} \tilde{u}_i (r_{i+1}^2 - r_i^2)\right]/D^2$$

where N is the number of data points and $\tilde{u}_i$ the mean value of the rms velocities at equal distances from the cylinder axis along the measurement diameter. With the assumption of isotropy, which has been already established at 200 and 1000 rpm, and of uniform axial distribution of turbulence intensity in the clearance volume, this quantity can be regarded as a measure of the volume-averaged turbulence intensity, (Gosman et al, 1985), and allows the quantification of the turbulence level at TDC of compression with a single parameter. The variation of this quantity with engine speed is shown in Figure 4.9 and clearly indicates a greater than linear increase of TDC turbulence with engine speed. Two characteristics of this curve should be emphasised: the extrapolation of the curve towards lower engine speeds passes through the origin of the axes, which does not seem to be the case for some of the previous data shown in Figure 1.3 of Chapter 1, and its non-linearity decreases for engine speeds greater than 1500 rpm. The latter feature is attributed to a decrease of volumetric efficiency at higher speeds which results in a small reduction of the TDC turbulence (Lancaster, 1976) and counter-balances the increase due to the engine speed (Ahmadi-Befrui, 1985a). The data of Figure 4.9 are also compared with a line representing an ideal linear increase of TDC turbulence with engine speed for $(\sqrt{\overline{u^2}}_{aver}/\overline{V}_p) = 0.5$, which has been claimed to be the upper limit for the TDC turbulence in a disc-type combustion chamber, (Hayder et al, 1984, Liou et al, 1984). The measured data deviate by up to 16% from this line at 2000 rpm and the actual value of the ratio $\sqrt{\overline{u^2}}_{aver}/\overline{V}_p$ is shown to increase from 0.47 to 0.59. The results of a computational study of the effect of engine speed on TDC turbulence (Ahmadi-Befrui, 1985b) are also plotted in Figure 4.9 and, when compared with the experimental data, indicate a similar non-linearity but lower values of $\sqrt{\overline{u^2}}$ which could be attributed to the higher compression ratio as well as the deficiencies of the turbulence model used in this theoretical study. In this work the non-linear increase of TDC turbulence with engine speed was attributed to the relatively stronger flow structures

present at early compression with increasing engine speed which in turn decreased the rate of decay of turbulence during compression and resulted in a relative increase of turbulence intensity at TDC of compression.

The maximum velocities encountered in the intake port of the engine are around 70 ms^{-1} during early induction at the maximum speed of 2000 rpm. This velocity magnitude may have introduced some compressibility effects which may lead to a non-linear scaling of the induction flowfield with engine speed. Since the TDC turbulence in the present engine configuration is primarily determined by the induction-generated flowfield, it is expected that these non-linearities will be reflected on the TDC turbulence. For this reason the trends of the results presented here should not be extrapolated to higher engine speeds; a detailed investigation of the correlation between the velocity field at the exit of the intake valve and the TDC turbulence should be undertaken to clarify this aspect of the in-cylinder flows.

Other parameters such as induction swirl and compression squish are also expected to influence the behaviour of the TDC turbulence since they affect the mechanisms responsible for its generation and decay throughout the engine cycle. The present results are not expected to be valid in these flow configurations and an extension of this study to include the effect of this parameters on the scaling of the TDC turbulence is necessary.

4.5 CONCLUSIONS

The detailed velocity measurements obtained in a modified production engine with a disc-type combustion chamber operating in the speed range of 300 to 2000 rpm with a compression ratio of 7.4 and in the absence of induction swirl revealed the following:

1. The induction-generated flow structures decayed soon after the closure of the intake valve resulting in a near-zero mean flow pattern at TDC of compression which was not influenced by engine speed.

2. Turbulence at TDC of compression was nearly isotropic but not homogeneous at all engine speeds. Turbulence intensity exhibited variations along the mid-plane of the TDC clearance volume which increased from 20 to 35% with engine speed. The magnitude and spatial distribution of turbulence intensity was shown to be determined mainly by the intake port and combustion chamber geometry.

3. The TDC average turbulence intensity increased more than linearly with engine speed, particularly in the range of 300 to 1250 rpm, and its ratio with the associated mean piston speed varied from 0.47 at 300 rpm to 0.59 at 2000 rpm.

The results justified the use of the model engine as a good approximation of a realistic engine configuration and demonstrated that measurements, obtained at a few points in the clearance volume, are not sufficient to characterise the TDC turbulence even in a simple combustion chamber geometry. These conclusions should not be extrapolated to higher engine speeds or other engine geometries with induction swirl or compression squish. A similar detailed study should be carried out with these configurations and, ideally, should be accompanied by a relevant theoretical investigation.

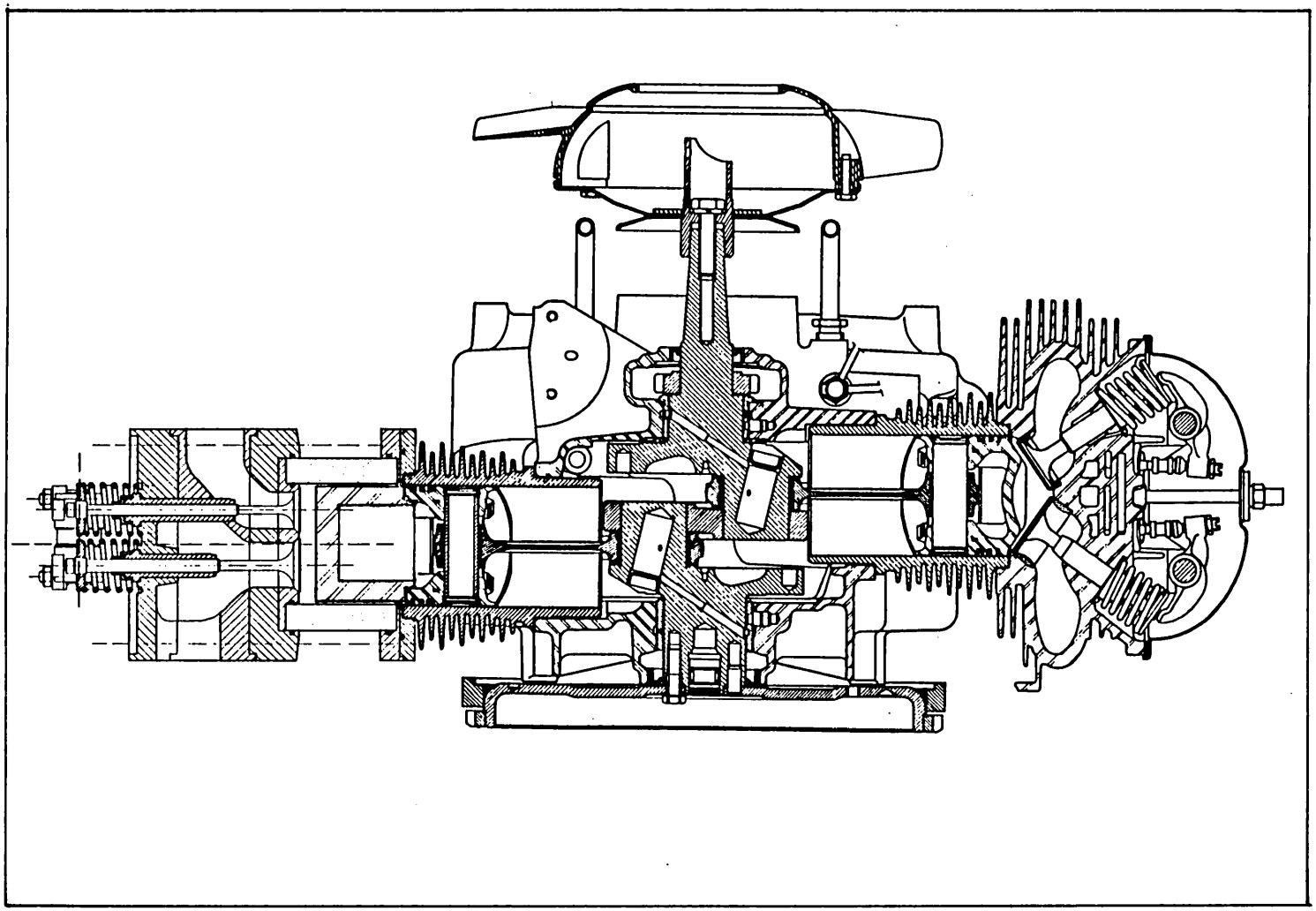

Fig. 4.1 Diagram of the modified Citroen engine

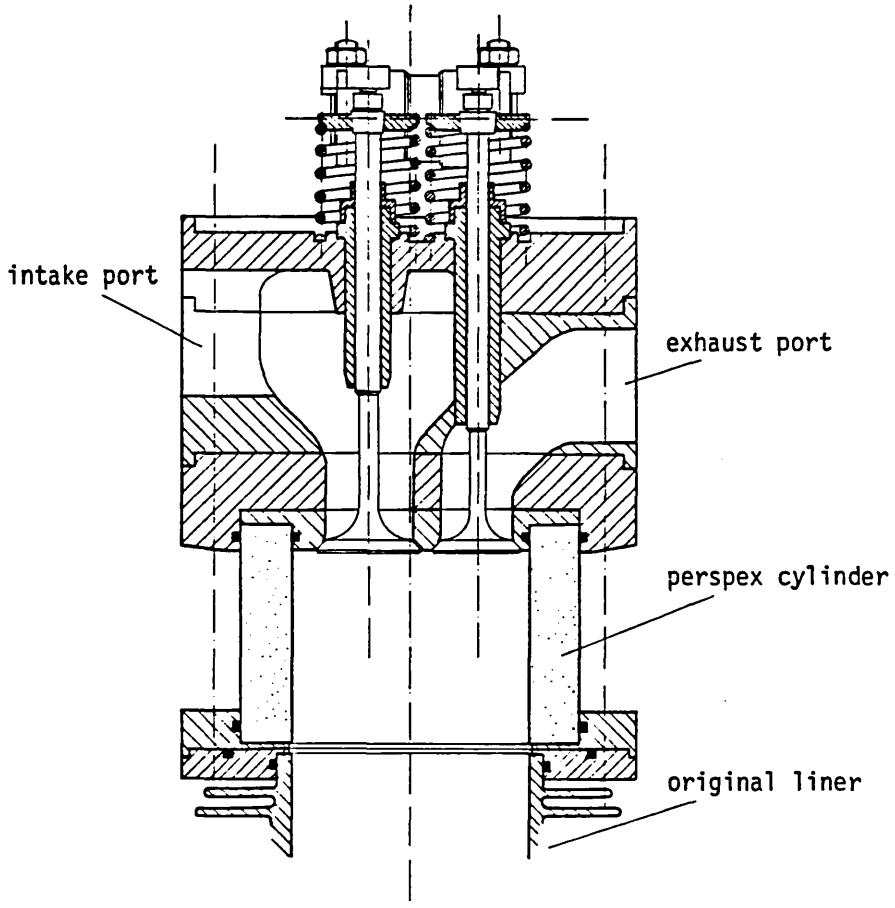

Fig. 4.2 Geometry of the cylinder head; optical access to the cylinder

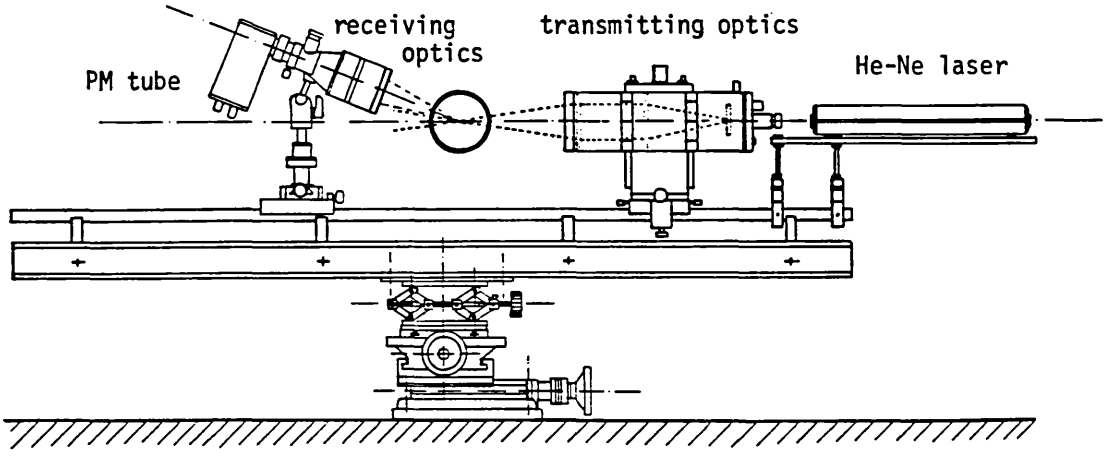

Fig. 4.3 Diagram of the LDA system and traversing mechanism

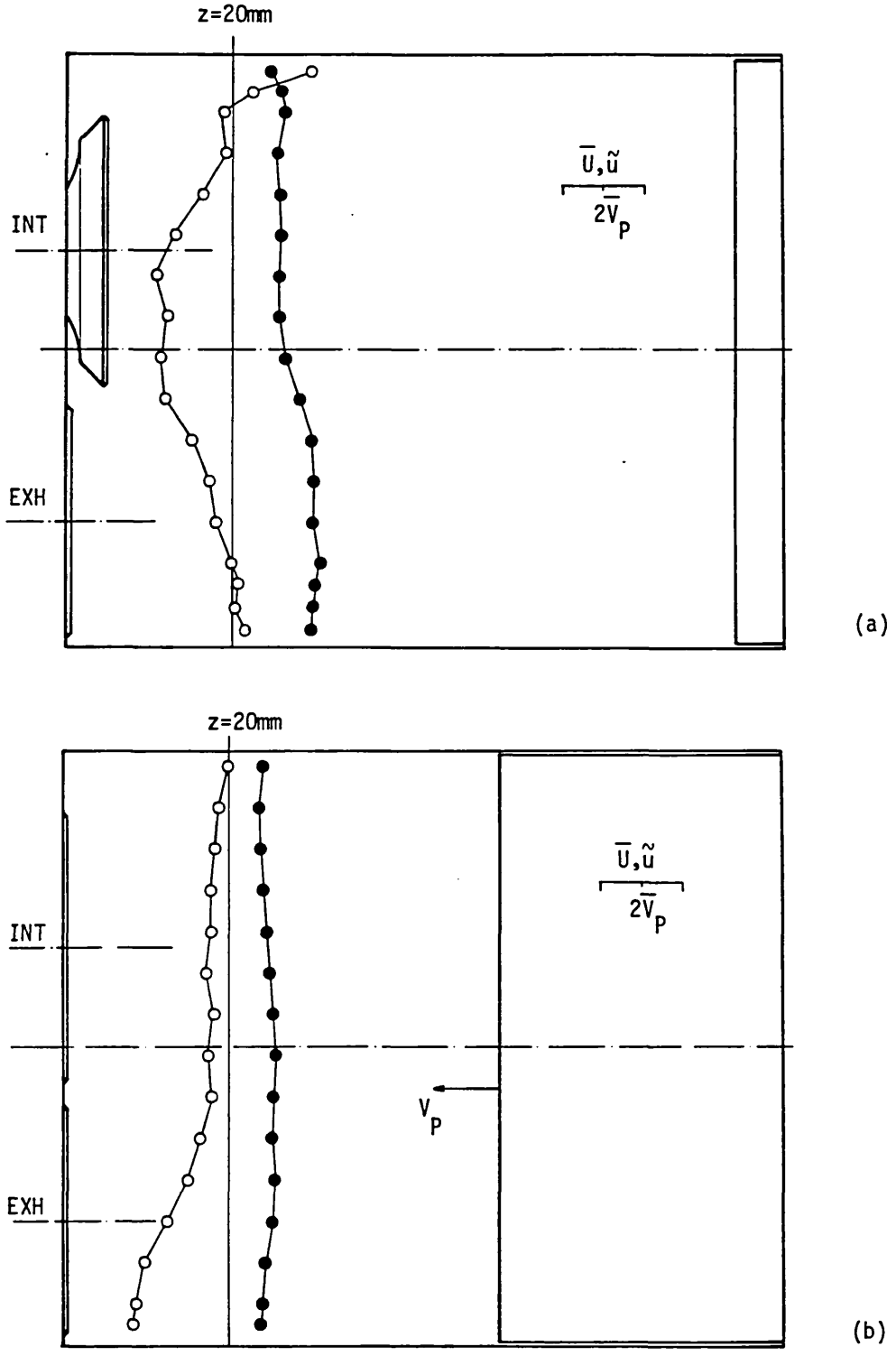

Fig. 4.4 Axial velocity distribution at z = 20 mm, n = 1000 rpm.
a) $\theta = 180^{o}$ (BDC) b) $\theta = 267^{o}$

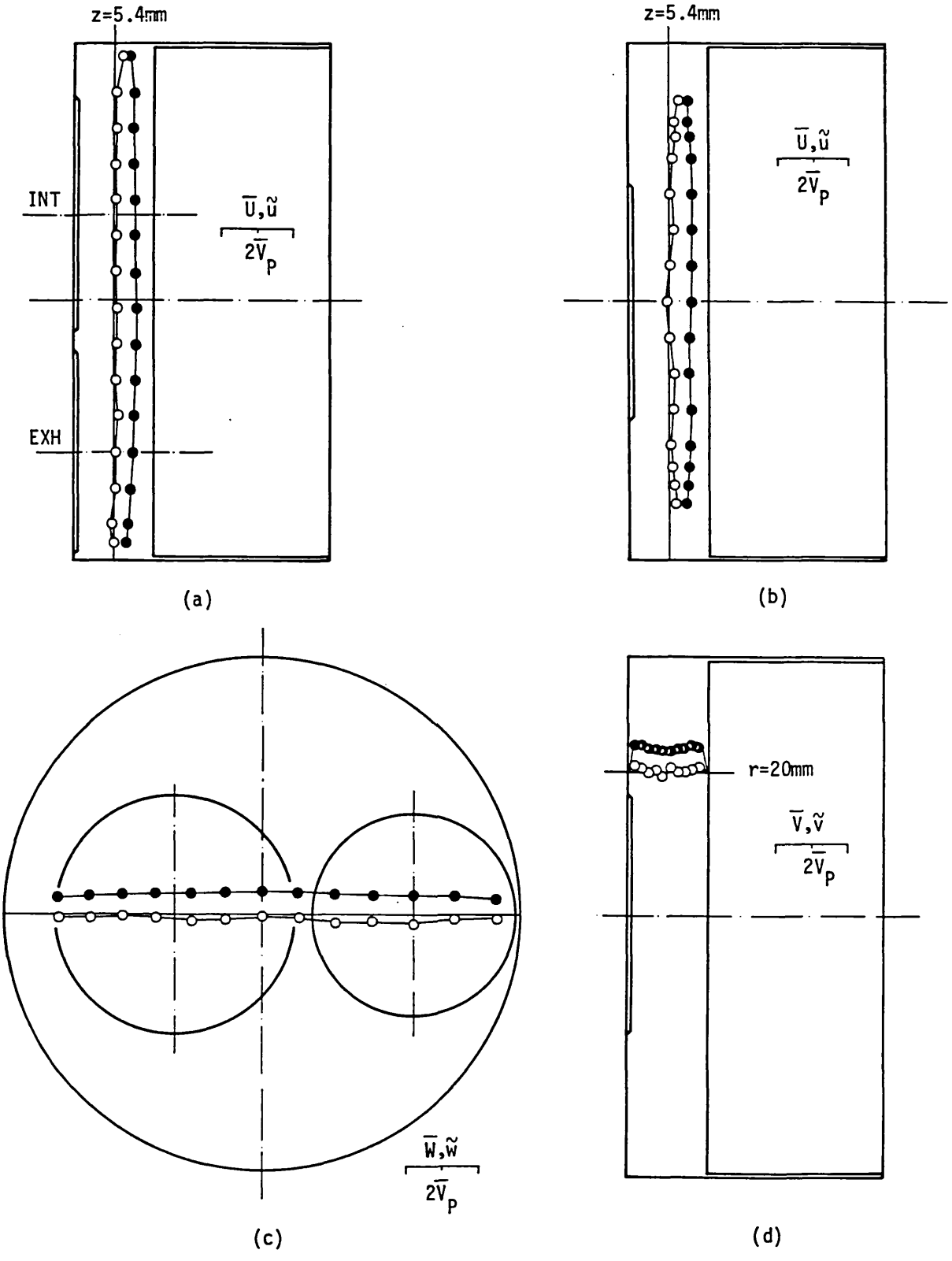

Fig. 4.5 Axial (a,b), tangential (c) and radial (d) velocity distribution in the clearance volume at $\theta = 360^{o}$ (TDC), n = 1000 rpm

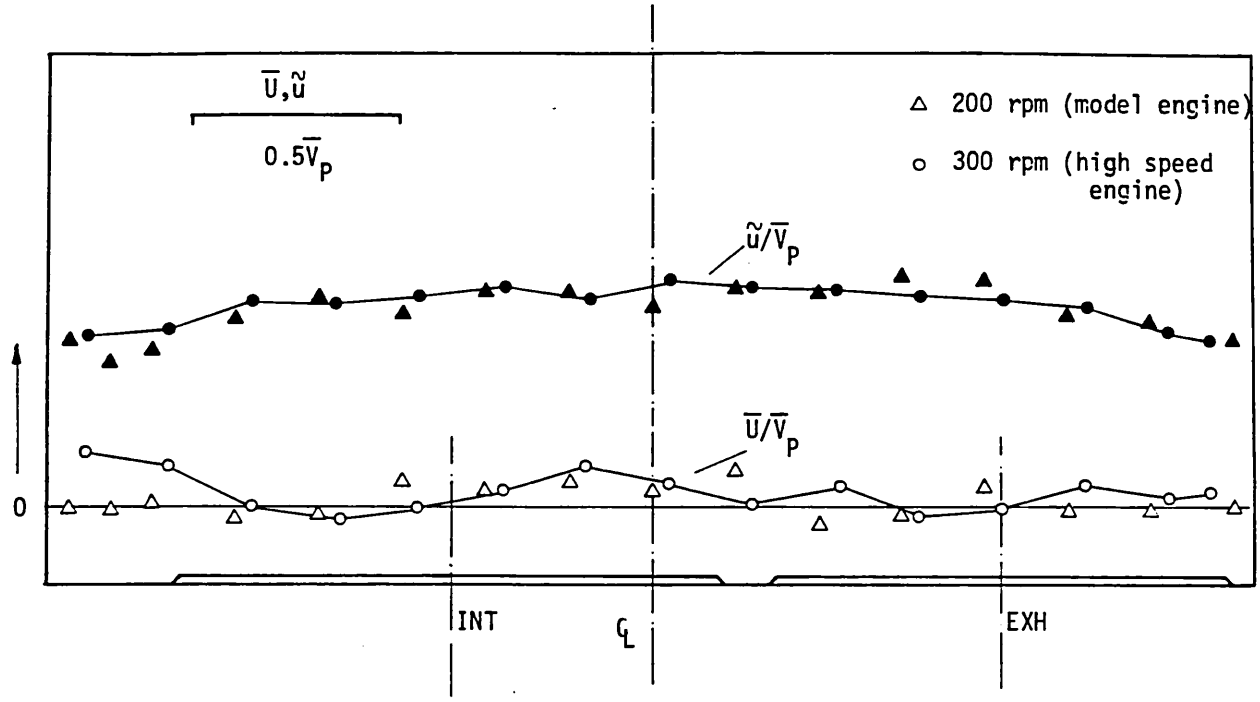

Fig. 4.6 Axial mean and rms velocity distribution at z = 5.4 mm and θ = 360° (TDC). (△,▲) Model engine, n = 200 rpm (see Fig. 3.19a) (○,●) High speed engine, n = 300 rpm

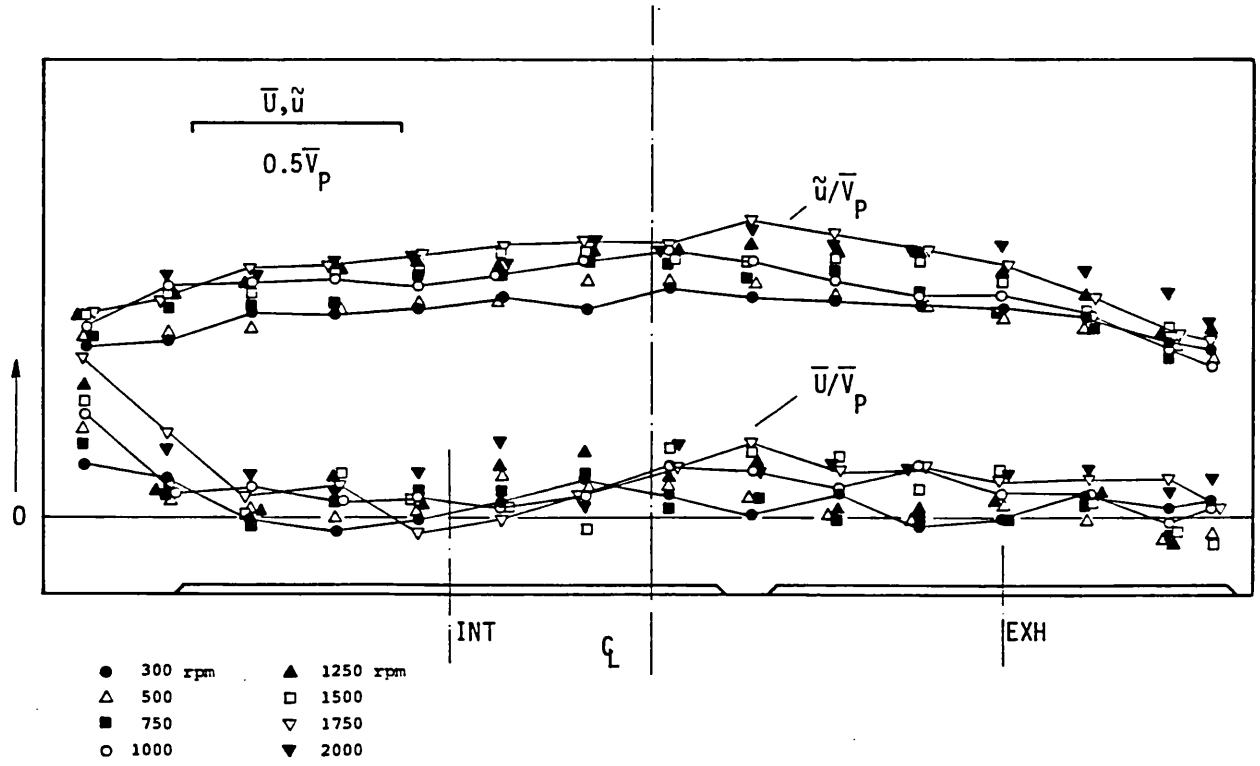

Fig. 4.7 Axial mean and rms velocity distribution at z = 5.4 mm and θ = 360° (TDC), for various engine speeds (n = 300 - 2000 rpm)

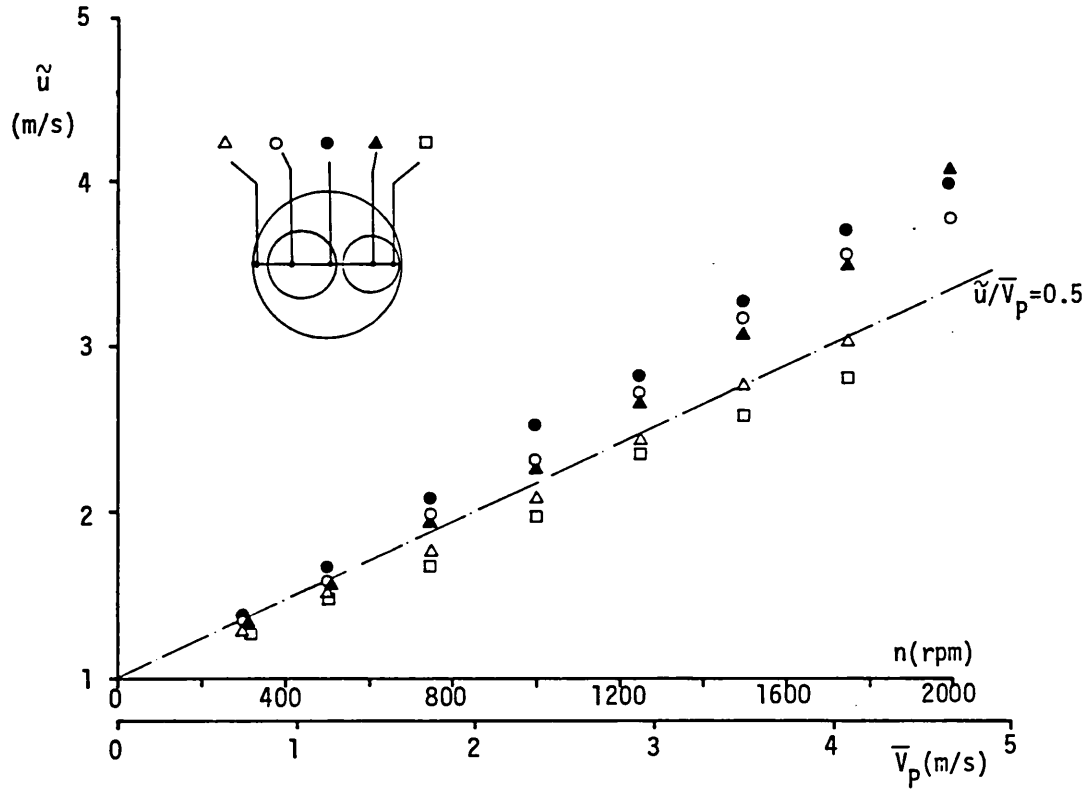

Fig. 4.8 Variation of the axial rms velocity component with engine speed at $\theta = 360^{o}$ (TDC) and at various locations of the mid-plane ($z = 5.4$ mm) of the clearance volume

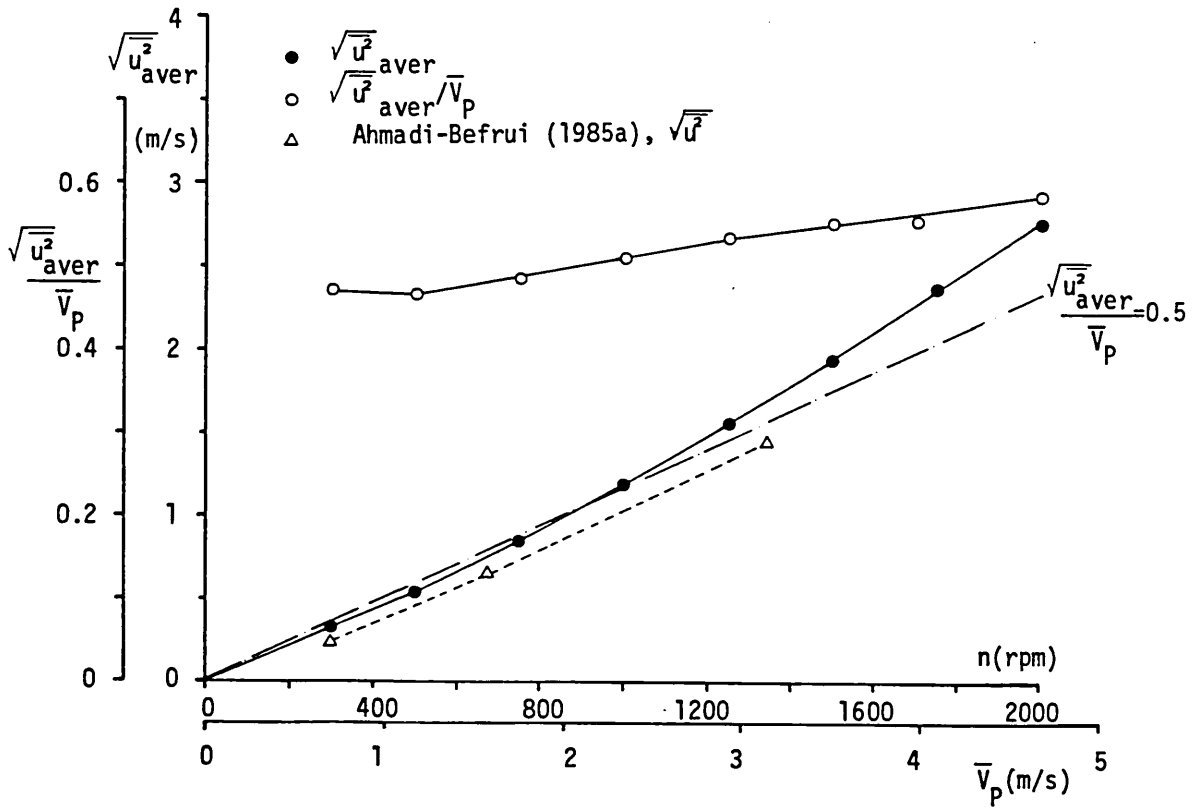

Fig. 4.9 Variation of the average turbulence intensity at TDC of compression with engine speed

CHAPTER 5

FLOW IN A PRODUCTION ENGINE

5.1 INTRODUCTION

The model and modified production engine configurations of the previous chapters had the common feature of simplified, and often idealised, intake port/valve geometries. These allowed control of the induction-generated flowfield and, consequently, enabled a detailed investigation of the influence of individual parameters on the in-cylinder flow. The induction systems of modern production engines, however, are more complicated and, although their advantages in terms of engine performance are well established, the details of the inlet flow that they produce are unknown.

This chapter describes an investigation of the in-cylinder flowfield generated by a helical intake port of a modern high speed direct injection (HSDI) Diesel engine. The focus is the induction-generated flow, both at the valve exit and inside the cylinder, as well as the flow during compression in a disc-type combustion chamber. The main objective of the investigation is to examine the differences and similarities of the in-cylinder flow development in simplified and production engines and to assess the extent to which the conclusions drawn by the previous investigations can be extrapolated in real engine configurations. The second objective is the detailed characterisation of the helical intake port and the provision of experimental data for the assessment of the ability of multidimensional prediction codes to cope with practical engine geometries. The achievement of these objectives, however, sets as a prerequisite the development of an experimental system, capable of providing the information required.

The flow configurations are described in section 5.2, and are followed by a brief description of the measurement systems in section 5.3. The results of this study are presented in section 5.4 and a summary of the main findings is given in section 5.5.

5.2 FLOW CONFIGURATIONS

The flow characteristics of the helical intake port of a Ford 2.5L HSDI Diesel engine (see Bird, 1985) were studied in terms of discharge coefficient and flowfield at the exit of the intake valve under steady flow conditions. Velocity measurements were also obtained at the valve exit and inside the cylinder of an engine incorporating this intake port and motored at 916 rpm. This engine speed was chosen as a good compromise between measurement difficulty and realistic operating conditions as suggested by the results of the previous chapter. The steady flow rig used is described in sub-section 5.2.1 followed by a description of the engine flow configuration in sub-section 5.2.2.

5.2.1 Steady flow

The Ford 2.5L cylinder head(*) was mounted on a blow-down-type steady flow rig, shown schematically in Figure 5.1, and was fitted with a transparent perspex cylinder of 94 mm internal diameter, 3 mm wall thickness and 250 mm length. The flow rig was connected to a compressed air supply which delivered a maximum air mass flow rate of 130 kg/h. The air flow was controlled by a series of pressure and flow regulators and measured by a standard B.S. orifice meter, as described in sub-section 2.3.1 of Chapter 2. A small part of the air flow (~ 0.5%) was bypassed to a blast atomiser which provided silicone-oil droplets used as seeding material for the LDA measurements. The main air flow and the seeded air were subsequently introduced into a stagnation chamber of 5.5 dm^3 volume which incorporated a disc-shaped baffle at its entry and a round-to-rectangular transition piece at its exit. This piece acted as an intake manifold and was connected at its downstream end with the intake port entry of the cylinder head, while its upstream end protruded into the stagnation chamber to create a stagnation region near its base. The total air pressure was measured at this region by means of a Betz micromanometer, together with the air

(*) Since the Ford 2.5L is a four-cylinder engine the original cylinder head was cut and part of it, corresponding to one cylinder, was used for this study.

temperature, in order to define the stagnation conditions upstream of the intake port. The helical port is shown schematically in Figure 5.2 and was of the steep ramp type while the intake valve had a 30^{o} seat angle and a nominal diameter of 42 mm (Fig. 5.3). The location of the intake valve in the cylinder head is also shown in Figure 5.3 together with the three planes along which the LDA velocity measurements were obtained (0^{o}, 90^{o} and 180^{o} planes). The valve lift was set by a micrometer screw with an accuracy of ±0.01 mm. The flow through the intake port/valve assembly discharged into the open-ended transparent cylinder at a rate of 101 kg/h which corresponded to an engine speed of 916 rpm. The cylinder head and the stagnation chamber could be rotated around the cylinder axis to allow the LDA measurements to be obtained along the three measurement planes shown in Figure 5.3.

5.2.2 Engine flow

The method used to provide full optical access to the engine cylinder for forward-scatter LDA measurements was similar to that used in the high speed engine of section 4.2. A single cylinder Petter PJ1 Diesel engine was used as the basic engine block; the original cylinder head was removed and the liner was extended by 70 mm with a transparent perspex cylinder of 93.7 mm internal diameter and 13 mm wall thickness, as shown in Figure 5.4. The Ford cylinder head, together with the attached stagnation chamber, was mounted on the extended cylinder and the intake and exhaust valves were operated through pushrods by the original camshaft of the Petter engine. The original piston was also extended to form a disc-type combustion chamber with a nominal compression ratio of 8. Again, the lubrication system remained unaltered and the engine was motored by a 3 kW thyristor-controlled DC motor through a toothed belt with a gear ratio of 2:1. The engine/motor assembly was rigidly fixed on an 800 kg concrete block and was mounted on the floor through a vibration damping pad. The modified engine could be motored at speeds up to 1000 rpm, limited by the rated speed of the DC motor and the torque requirements of the engine. The speed stability was better than ±0.5% at 916 rpm, and the system operated with negligible vibrations and satisfactory rate of oil contamination of the transparent

cylinder. The detailed operational characteristics of the modified engine are summarised in Table 5.1.

TABLE 5.1

Characteristics of the modified Diesel engine

Cylinder diameter, D_c, mm		93.7
Piston diameter, D_p, mm		92.5
Stroke, S, mm		110.0
Connecting rod length, ℓ, mm		231.9
Clearance at TDC, c, mm		15.85
Compression ratio		8
Intake valve:	Diameter, D_v, mm	42.0
	Seat angle, ψ, deg.	30
	Opens, IVO, deg. BTDC	4.5
	Closes, IVC, deg. ABDC	35.5
	Maximum lift, L_{max}, mm	11.0
Exhaust valve:	Diameter, D_v, mm	36.5
	Opens, EVO, deg. BBDC	35.5
	Closes, EVC, deg. ATDC	4.5
Engine speed, n, rpm		916

5.3 MEASUREMENT SYSTEMS

5.3.1 Discharge coefficient measurements

The discharge coefficient of the intake port/valve assembly was measured under steady flow conditions for a range of valve lifts and pressure drops across the valve, as well as for a constant mass flow rate corresponding to the mean piston speed at 916 rpm. The total pressure upstream of the port was taken to be equal to the stagnation pressure inside the stagnation chamber (Fig. 5.1) and the static pressure downstream of the valve was assumed to be atmospheric. The discharge coefficient, C_L, was calculated according to the procedure outlined in Appendix 2.2 of Chapter 2 and was defined in terms of the valve lift "curtain" area, $A_L = \pi D_V L$.

5.3.2 Velocity measurements

Three mean velocity components and the corresponding normal stresses were measured at the exit plane of the intake valve and inside the cylinder under steady and normal operating conditions, by laser Doppler anemometry. Preliminary tests conducted under steady flow conditions revealed that the spectrum of the Doppler frequencies in some locations of the cylinder had a bandwidth of up to 20 MHz. This precluded the use of the previously employed LDA optical configurations as they provided a maximum frequency shift of 7 MHz which was not sufficient to separate the pedestal and Doppler frequency spectra. Additionally, the measurements of the swirl velocity component at the valve exit required the use of an LDA system operating in the back-scatter mode, since the forward scattered light was blocked by the body of the valve. For these reasons three different LDA optical configurations were used for this investigation; they are described in the following paragraphs and their detailed characteristics are given in Table 5.2.

- High frequency shift, forward-scatter anemometer (I)

The light transmitting arrangement of the anemometer (DISA 55X) is shown in Figure 5.5 and consisted of a beam splitter, an acousto-optic modulator (Bragg-cell) which shifted the frequency of one of the two laser beams by 40 MHz relative to the other, and a plano-convex imaging lens. This system employed a 5 mW He-Ne laser and the forward scattered light from the measurement volume was collected by a bi-convex lens with 150 mm focal length and focused on the cathode of an EMI 9817 B photomultiplier tube. This optical configuration was used for the measurement of the axial and radial velocity components at the valve exit and the swirl velocity component downstream of the valve under steady flow conditions.

- High frequency shift, back-scatter anemometer (II)

This system consisted of the same light transmitting optics (DISA 55X) shown in Figure 5.5 and a high power (1.4 W) Argon-ion laser operating in the blue line. The back-scattered light was collected by the imaging lens of the optical unit, deflected by an inclined mirror and focused on the pinhole of an RCA 4256 photomuliplier through a DISA 55X34 optical module. This arrangement was used for the swirl velocity component measurements at the exit of the intake valve. In several cases, and due to limited optical access, a second mirror was located outside the optical unit to deflect both the incident beams and the back-scattered light, thus allowing an easier access into the valve gap. The only limitation of this system was its inability to measure the swirl velocity component near the valve seat where the reflection of the incident light overshadowed the Doppler signal.

- Medium frequency shift, forward-scatter anemometer (III)

High frequency shift was undesirable in some cases, particularly during the compression stroke in the motored engine, where there were difficulties associated with the filtering and amplification of the high frequency signals and the relatively large measurement error occuring in the velocity measurements when the Doppler frequency was small compared to the magnitude of the frequency shift, (see sub-section 5.3.4). For these reasons a new optical arrangement was developed which employed a rotating diffraction grating, as described in sub-section 2.3.2 of Chapter 2, but made use of the second order diffracted beams. The

advantage of this configuration was that, for a given rotational speed of the grating, the frequency shift was double that of the first order diffracted beams, (see Appendix 2.3), and continuously variable in the range of 0-14 MHz. The disadvantage of the system was the relatively high laser power required since the second order beams contained only a small fraction (~ 10%) of the incident power (Oldengarm et al, 1976). An Argon-ion laser was used operating in the green line and providing a power of 400 mW. The laser power at the measurement volume was approximately 40 mW, and was sufficient for forward-scatter LDA measurements. The light collecting optics consisted of a bi-convex lens of 150 mm focal length and an EMI 9814 B photomultiplier tube. This system was used for the in-cylinder velocity measurements in the motored engine while the valve exit velocities, under operating conditions, were measured with the Bragg-cell optical system operating in the forward-scatter mode and the 400 mW Argon-ion laser.

Several combinations of the systems described above were used in order to satisfy the specific measurement requirements at each point of the in-cylinder flow. Table 5.2 describes only the three basic optical systems.

Seeding of the flow was again by silicone-oil droplets in both the steady and engine flow configurations. In the latter, the exhaust air was again recirculated to the intake port through a 0.1 m^3 chamber as described for the high speed engine in sub-section 4.3.1 of the previous chapter.

The signal from the photomultiplier was amplified with an HP 461 A wide-band amplifier and high-pass filtered by a passive filter. The same frequency counting and processing system was used for the steady and engine flow measurements as for the model engine investigation, (see sub-section 2.3.2). In this case, however, the frequency counter (HP 5360 A) was operated mainly in the "fixed number of cycles", rather than "fixed gate time", mode. This mode of operation required 32 Doppler cycles to be counted in order to validate a measurement and significantly increased the range and accuracy of the frequency measurements. An additional feature of the system used for the steady flow measurements was the simultaneous evaluation of the Doppler frequency spectrum of the unconditioned signal by an HP 8553 B spectrum analyser. This provided

TABLE 5.2

Optical characteristics of the laser Doppler anemometers

		(I)	(II)	(III)
Laser:	Wavelength, λ, nm	632.8	488	514.5
	Power, mW	5	1400	400
	Beam diameter ($1/e^2$ intensity), mm	0.8	1.35	1.5
Lenses:	L_1, focal length, mm	-	-	100
	L_2	-	-	200
	L_3	300	300	300
Frequency shift, (f_s), MHz		40	40	0 - 14
Beam separation, (s), mm		60	60	66.2
Beam intersection half angle, ($\phi/2$), deg.		5.73	5.80	6.30
Measurement volume dimensions ($1/e^2$ intensity)				
	diameter, (b_x), μm	304	139	66
	length, (b_y), μm	3026	1388	597
Number of stationary fringes, (N_f)		96	57	28
Frequency to velocity conversion factor, (λ^*), ms^{-1}/MHz		3.169	2.414	2.343
Magnification of collecting optics, (M)		2.5	0.67	2.5
Pinhole diameter, (d_{Ph}), mm		0.5	0.1	0.5

useful information on the Doppler spectrum bandwidth for proper signal conditioning; it also enabled the validation and digital filtering of the counter measurements through comparison of the probability density distribution of the measured frequencies with the Doppler spectrum.

5.3.3 Turbulence spectra

Some velocity measurements, obtained in the valve gap under steady flow conditions, exhibited bimodal probability distributions which usually suggest the presence of flow instabilities. A hot-wire anemometer and a frequency analyser were employed to provide the turbulence spectrum at these locations and to investigate the nature of these instabilities. A straight hot-wire probe (DISA 55P11) was held with a robust probe support at 60^{o} to the cylinder axis and was translated by a micropositioning device in the valve exit plane. Simultaneous LDA and hot-wire measurements did not reveal any detectable effect of the probe on the valve flowfield. The hot-wire probe was connected to a DISA 55M CTA bridge whose output was fed to a digital FFT analyser (Spectral Dynamics SD340). For convenience, the output of the CTA bridge was not linearised and the spectra obtained are not quantitatively representative of the turbulent energy spectra.

5.3.4 Measurement uncertainty

The air flow rate in the steady flow rig was kept constant with maximum long term variations of 0.5%. This uncertainty combined with the errors in the flow rate and pressure drop measurements, discussed in sub-section 2.3.1 of Chapter 2, resulted in an overall uncertainty in the discharge coefficient measurements of 3%.

The error sources and their contribution to the uncertainty of the velocity measurements are the same as for the steady and high speed engine flow configurations of the previous chapters. The use of high frequency shift in parts of this study, however, is expected to result

in larger uncertainties in the Doppler frequency measurements. The frequency shift provided by the Bragg-cell (40 MHz) was constant within ±0.1%. For a typical signal of 50 MHz the systematic error of the 1 ns resolution frequency counter was 0.08 MHz which, when the frequency shift is subtracted, gives an error of 0.8% in the Doppler frequency measurement; this error increases as the measured velocity (Doppler frequency) decreases. Taking this into account and considering the error analysis of the previously described measurement systems the overall average uncertainty in the steady flow mean and r.m.s. velocity measurements is expected to be 4 and 6% respectively, increasing to 6 and 12% in regions of high relative turbulence intensity and steep velocity gradients. The use of lower and variable frequency shift for the engine measurements, together with the small crank angle window used (3.6^{o}), resulted in lower average uncertainties of 3 and 5% for the ensemble-averaged mean and r.m.s. velocities respectively with corresponding maximum uncertainties of 5 and 10% associated with the measurements obtained during induction and in regions of high turbulence intensity.

5.4 RESULTS AND DISCUSSION

This section presents the results of this study and is divided in four parts. Sub-section 5.4.1 is concerned with the discharge coefficient measurements and is followed by the valve flow investigation under steady flow conditions presented in sub-section 5.4.2. A discussion of the turbulence spectra obtained at the valve exit is made in sub-section 5.4.3 and the results of the engine flow configuration are presented in sub-section 5.4.4.

5.4.1 Discharge coefficient measurements

The discharge coefficient, C_L, of the intake port/valve assembly is presented in Figure 5.6 as a function of valve lift for six different pressure drops across the valve in the range of 50 - 300 mmWg. The discharge coefficient decreases monotonically with valve lift reaching

values 50% lower than its maximum at full lift (L = 12 mm). The effect of pressure drop across the valve on the C_L values is more pronounced in the low lift range and low pressure drops and they tend to increase with increasing pressure drop. Similar observations were made in the idealised plain axisymmetric port/valve configuration (sub-section 2.4.1) and are attributed to the relatively large contribution of the viscous effects to the pressure losses at small lifts and low mass flow rates. An interesting, but practically less important, aspect of the discharge coefficient variation with valve lift is its markedly higher values (~ 0.76) at valve lifts less than 2 mm. Close examination of the port exit geometry (Fig. 5.3) reveals that over this lift range the flow discharges through the valve recess in the cylinder head which forms a convergent-divergent type of passage, favouring pressure recovery and resulting in higher values of the discharge coefficient. At higher lifts, the absence of discontinuities in the C_L curve suggests that, contrary to the behaviour of the idealised port geometry, the flow pattern at the exit of the helical port does not change abruptly with varying valve lift. Additionally, the discharge coefficient values measured with the idealised geometries (valves I and II) at the high lift range ($L/D > 0.15$) were up to 20% higher than those of the present configuration, suggesting that the pressure losses in the helical port are rather significant.

The variation of discharge coefficient with valve lift for a constant mass flow rate (101 kg/h), rather than constant pressure drop, is also shown in Figure 5.6. This flow curve lies between the 100 and 150 mmWg pressure drop curves for lifts greater than 4mm but deviates from all curves at lower valve lifts, as also observed and discussed in sub-section 2.4.1 for the idealised port geometry (see Figures 2.9 and 2.12). This observation, together with the findings of the earlier relevant investigation, prompted the decision to perform the steady flow velocity measurements at this constant mass flow rate, which corresponds to the mean piston speed of the engine at 916 rpm, and with valve lifts greater than 4 mm.

5.4.2 Valve exit velocity measurements

The velocity measurements at the exit of the intake valve under steady flow conditions are presented in terms of individual velocity component distribution at the valve gap and, where possible, in terms of velocity vectors for valve lifts L = 4, 7, 10 and 12 mm. Similar measurements obtained in the motored engine are presented in sub-section 5.4.4 together with the in-cylinder flow results.

Figure 5.7 shows the mean and r.m.s. of the radial velocity component at the three orientations around the valve periphery (0^o, 90^o and 180^o) for a valve lift of 4 mm. The mean velocities reach maximum values of 16.5 $\overline{V}_p$ at the 180^o plane compared to 13 $\overline{V}_p$ at the 0^o measurement plane. The non-uniformity of the velocity distribution around the valve gap is a result of the non-axisymmetric geometry of the intake port while the small difference in the velocity magnitudes indicates that, for this valve lift, the directional characteristics of this helical port are not very strong. The measured turbulence intensity is also non-uniformly distributed around the valve with levels of 5 $\overline{V}_p$ at the 0^o plane decreasing to 1-2 $\overline{V}_p$ at the 180^o plane. The unusually high turbulence intensity at the 0^o plane, compared to that measured at the exit of the plain axisymmetric port (sub-section 2.4.2.3, Fig. 2.17), prompted a more detailed investigation of the flow at this region which is presented in sub-section 5.4.3.

Both radial and swirl velocity components have been measured for a valve lift of 7 mm and are shown in Figure 5.8a and b respectively. The mean radial velocities are again non-uniformly distributed around the valve with magnitudes varying between 7 and 11 $\overline{V}_p$ with the maximum at the 90^o plane. Similarly the swirl velocity distribution varies between 5.5 and 8.5 $\overline{V}_p$ with minimum values at the 90^o plane. Turbulence intensity is similar in both radial and tangential directions and generally lower than that with the 4 mm valve lift, ranging between 1.5 and 3 $\overline{V}_p$. The vector addition of the radial and swirl velocities (Fig. 5.8c) indicates that the flow angle at the valve exit, with respect to the valve radius, does not change significantly with axial location along the valve gap but varies between 25 and 45^o around the valve periphery. Contrary to the idealised valve configuration the flow at the valve exit does not separate from either the valve seat or the valve head, as also suggested by the discharge coefficient measurements.

All three velocity components were measured with a valve lift of 10 mm. The magnitude of the radial velocity component (Fig. 5.9a) increases from 5.5 $\bar{V}_p$ at the 0^o plane to 10 $\bar{V}_p$ at the 180^o measurement plane, indicating that as the valve lift increased the directional characteristics of the port became more evident. Turbulence intensity decreases towards the 180^o plane in all three directions while the swirl velocity magnitudes and distribution (Fig. 5.9c) are similar to those observed with the 7 mm valve lift. This is because swirl is generated upstream of the valve and is not influenced by the valve lift. The resultant velocity vectors from the addition of the axial and radial velocity components in the 0^o and 180^o planes are presented in Figure 5.10a and show a variation of flow angle with respect to the valve axis between 50 and 60^o, suggesting that the flow at this lift follows roughly the angle of the valve seat. The vector addition of the radial and swirl velocities (Fig. 5.10b) shows similar variation of flow angle around the valve periphery as with the 7 mm valve lift and, again, little variation across the valve gap. Finally, the addition of axial and swirl velocity components (Fig. 5.10c) allows the determination of the angle of the helix formed by the flow at the valve exit. This is found to be around 50^o and indicates that the swirl number at this location is greater than unity.

Similar measurements were obtained for a valve lift of 12 mm and are shown in Figure 5.11. The radial velocity distribution (Fig. 5.11a) does not indicate any flow separation in the valve gap while turbulence intensity shows similar trends as with the lower lifts and, again, a peak value of 5 $\bar{V}_p$ near the valve seat on the 90^o measurement plane. This is consistent with all previous measurements at the same location with smaller valve lifts and its origin will be examined in the following sub-section. The vector addition of the axial and radial velocities along the 0^o plane (Fig. 5.12a) shows that the flow emerges from the valve gap at an angle which is smaller than the valve seat angle, as also observed with the idealised port for the large lifts. Comparison of the velocity vectors on the plane normal to the valve axis (Fig. 5.12b) with those presented for the smaller lifts shows only small differences in the flow angle with respect to the valve radius. This indicates that, contrary to the flow in the axial plane, the swirl flow pattern does not change significantly with increasing valve lift. Similar conclusions appear to be valid for

the angle of the valve flow on the tangential to the valve plane (Fig. 5.12c) which is again found to be around 55^{o} with respect to the valve axis.

The results show that the flow pattern at the exit of the helical intake port is more complicated than that at the exit of the idealised ports examined in Chapter 2, and indicate that the geometry of the intake port is important for the shaping of the flow as it enters the cylinder. The effect of these details of the intake flow on the flow-field at TDC of compression is likely to be small and this aspect of the in-cylinder flow development is examined in sub-section 5.4.4.

5.4.3 Turbulence spectra

The unusually high r.m.s. velocities measured at the port exit near the cylinder head (see Figs. 5.9a and 5.11a) suggested that a closer examination of the flow at these locations was necessary. Analysis of the LDA measurements obtained in the valve gap often indicated the presence of bimodal probability density distribution of the radial velocity component near the cylinder head. This is illustrated in Figure 5.13 which shows the probability density distribution of the radial velocity component at four locations in the valve gap for a valve lift of 10 mm along the 90^{o} measurement plane. At z = 1 mm there is a nearly symmetrical bimodal distribution, centered around ~40 MHz (zero velocity), and as the measurement point moves away from the cylinder head (z = 1.5 mm), the bimodal distribution becomes less symmetric and gradually (z = 2 and 5 mm) returns to a single mode with Gaussian characteristics. The velocity probability distribution at z = 1 mm shows that the flow pattern at this location is bi-stable with the radial velocity component either positive or negative suggesting a tendency for separation from the valve seat. Similar trends were observed at the same axial locations and for the larger valve lift of 12 mm and provide the explanation for the high r.m.s. velocities measured in this region.

The turbulence spectra were obtained by hot-wire anemometry at the same locations in the valve gap and for valve lifts L = 10 and 12 mm, Figures 5.14 and 5.15a respectively. In both cases a dominant frequency

of ~800 Hz is present and confirms the existence of flow instability in the valve flow. Furthermore this frequency scales linearly with the mass flow rate as shown by the turbulence spectra obtained for 75, 50 and 33% of the original flow rate, (Figs. 5.15b-d), indicating some form of periodic vortex shedding at these locations of the valve gap. A simple analysis for a Strouhal number value $S=(f_t \ell/V)=0.21$ yields a characteristic length $\ell \simeq 5$ mm and suggests that the most likely cause of this vortex shedding is the formation of vortices in the recess of the cylinder head around the valve seat (see Fig. 5.3) which are released with a periodicity corresponding to the dominant frequencies observed.

5.4.4 Engine flow

The flow at the exit plane of the intake valve under engine operating conditions (916 rpm) has been measured at crank angles $\theta = 29^o$ and 47^o which corresponded to instantaneous valve lifts of 4 and 7 mm respectively. The distribution of the radial velocity component along the 0^o measurement plane at these valve lifts is shown in Figures 5.16b and d and is compared with the corresponding results of the steady flow tests which are shown again in Figures 5.16a and c. The mean velocity distributions are similar in both cases, particularly for the lower lift. In addition, when the maximum mean velocities at the exit of the operating valve are scaled with the instantaneous, rather than mean, piston speed at the corresponding crank angles they agree with the steady flow results within 2 and 5% for the low and higher lift respectively. This is a good indication that the steady flow tests adequately simulate the flow at the exit of the operating valve as also demonstrated for the low speed model engine of sub-section 3.4.2.2. The magnitude of turbulence intensity in the gap of the operating valve, when scaled with the instantaneous piston speed, is lower than that in the steady flow configuration. Similar trends were observed with the model engine and were attributed to the developing nature of the valve flow during early induction. Finally, the high r.m.s. velocities measured near the cylinder head under steady flow conditions are not present in the case of the operating valve which indicates that the flow instabilities, detected at the valve gap under steady flow conditions, were eliminated by the valve operation.

The axial and swirl velocity distributions in the cylinder space have been measured at $\theta = 72^{o}$, which corresponds to a valve lift of 10 mm, and are shown in Figure 5.17. The flow pattern in the axial plane, parallel to the 90^{o} measurement plane, consists of a system of ring and toroidal vortices. At an axial location of z = 30 mm, the mean velocities peak at the far-valve side of the cylinder contrary to the model engine configuration which had a smaller valve eccentricity and resulted in opposite trends. The small forward (positive) velocities measured around the cylinder axis are attributed to the low pressure field generated during early induction and were also observed with the model engine configuration at crank angle $\theta = 30^{o}$ (see Fig. 3.14a). The presence of swirl in this configuration, however, enhances this effect and sustains the central vortex longer during induction. The swirl velocity distribution at the same location (Fig. 5.17b) exhibits characteristics of a double vortex pattern as also found in the model engine (Arcoumanis et al, 1984a) and the main swirl flow deviates significantly from solid body rotation. The r.m.s. velocity distribution exhibits maxima near the swirl centre, similar to those observed in the model engine configuration and attributed to the precession of the swirl centre (sub-section 3.6.3).

Later in the induction stroke, at $\theta = 166^{o}$ which corresponds to a 7 mm valve lift at the closing period of the valve, the swirl flow at z = 47 mm has returned to a single vortex pattern as shown in Figure 5.18. Similar swirl velocity measurements obtained at the same axial location and with the same valve lift but under steady flow conditions are shown in Figure 5.19. Comparison of these results with those of Figure 5.18 reveals differences which can be attributed to the integrated effect of the developing swirl throughout induction. This interpretation is supported by the similarity of the mean swirl velocity distribution under steady flow conditions with that measured at early intake ($\theta = 72^{o}$, Fig. 5.17b), although both valve lift and measurement location were different.

The double and single swirl vortex patterns at $\theta = 72^{o}$ and $\theta = 166^{o}$ respectively, have been also observed under steady flow conditions at a distance of one cylinder diameter from the cylinder head (Coghe et al, 1985) and were associated with correspondingly low and high valve lifts. In the engine, the transition from a double to single vortex swirl pattern is attributed to the variation of valve lift and, more important-

ly, to the evolution of the in-cylinder swirl flow towards a dynamically stable and persisting flow structure.

The distribution of the swirl velocity component near the cylinder head at IVC ($\theta = 220^{o}$) is shown in Figure 5.20a. It exhibits uniform velocities near the cylinder wall and forced vortex characteristics near the swirl centre, which now is located at the intake valve side of the cylinder providing further evidence of its motion during the engine cycle. Comparison of these results with those of Figure 5.20b obtained at the same crank angle but closer to the piston face, reveals an axial stratification of the swirl velocity distribution, as also observed in the model engine investigation. Near the cylinder head the swirl velocity profile shows signs of memory from the induction-generated flowfield, contrary to that at z = 50 mm where signs of flow evolution towards solid body rotation are clearly evident. Turbulence intensity follows the trends of the mean swirl velocity distribution exhibiting higher values (~ 0.9 $\overline{V}_p$) near the cylinder head and lower (0.7 $\overline{V}_p$) further downstream. The axial velocity distribution at IVC has also been measured at the same axial locations (z = 15 and 50 mm) and is shown in Figure 5.20c. The intake-generated axial flow pattern has decayed considerably and only a weak vortex is present, rotating in the opposite direction of that of the main vortex during induction. Similar flow structure has been observed in the model engine configuration with vane-induced swirl (Arcoumanis et al, 1982b) and is attributed to the swirl-induced in-cylinder pressure gradients (Gosman, 1983). Turbulence intensity has decayed to less than 50% of that measured at $\theta = 72^{o}$ and is nearly uniform in the cylinder space with tendencies towards isotropy. These results are in good agreement with those obtained with the model engine and idealised intake ports, justifying the simplifications made in these investigations.

Finally, the flow at TDC of compression has been measured along the mid-plane of the clearance volume and the results are shown in Figure 5.21. The use of a disc-type combustion chamber, instead of the piston-bowl configuration of the original production engine, allows conclusions about the flow development during compression in the absence of flowfield transformation due to squish effects. The swirl velocity distribution shown in Figure 5.21a is similar to that measured at the middle of the cylinder space at IVC, exhibiting solid body characteristics but with lower maximum velocities, indicative of the wall frictional losses during

compression. Turbulence intensity has decayed to an average of 0.4 $\bar{V}_p$ and is almost uniformly distributed and nearly isotropic, with somewhat higher values near the swirl centre in both, tangential and axial directions. Integration of the swirl velocity profile according to the procedure outlined in Appendix 3.1 showed that the swirl ratio (SR) at TDC of compression was 4.5. This confirms that the induction swirl level generated by the swirl vanes in the model engine configuration was realistic (see Table 3.3). The axial velocity measurements (Fig. 5.21c) do not suggest the presence of any significant flow structure on the axial plane of the clearance volume. The temporal variation of the mean and r.m.s. of the axial velocity component at a point in the clearance volume (r = 20 mm, z = 8 mm) during the compression stroke is shown in Figure 5.22 and is in close agreement with similar measurements in the model engine configuration reported by Arcoumanis et al (1982b). In both cases the r.m.s. velocities remained almost constant around 0.6 - 0.5 $\bar{V}_p$ until $\theta = 340^o$ and then suddenly decreased to 0.3 - 0.4 $\bar{V}_p$ towards and after TDC of compression.

The above results, and particularly the magnitude and distribution of turbulence intensity during compression, are in good agreement with the corresponding results of the model engine investigation, (see for example Figures 3.36a and 3.42). The only differences are in the precession of the swirl centre which is less evident with this engine configuration. This is attributed to the different swirl-producing port and the smaller interaction of the valve jet with the wake of the valve, due to the directional characteristics of the helical port. In general, although the characteristics of the induction-generated flowfield in the model and the production engine were not quantitatively comparable, the resulting flowfield during the compression stroke was very similar in both configurations. Therefore, it can be argued that the main conclusions drawn from the model engine investigation with respect to the decay of the induction-generated flowfield and its evolution during compression can be extrapolated, with confidence, to practical engine configurations.

5.5 CONCLUSIONS

The investigation of the flow generated by a helical intake port inside the cylinder of a modified production engine motored at 916 rpm revealed the following:

1. The flow at the exit of the helical port, studied under steady flow conditions, was non-uniform around the valve periphery and more complicated than in the previously examined simplified ports. No flow separation has been observed from the sealing faces of the intake valve and the swirl velocity distribution at its exit was not significantly influenced by valve lift, contrary to the axial velocities and the directional characteristics of the port.

2. The flow at the exit of the helical port under engine operating conditions appeared to be adequately simulated by the corresponding steady flow tests, contrary to the in-cylinder swirl flow. The axial flow pattern generated during induction consisted of a system of ring and toroidal vortices and the swirl flow exhibited double-vortex characteristics.

3. The intake flowfield decayed considerably by the time the intake valve closed and resulted in an axially stratified single-vortex swirl flow pattern which also influenced the axial velocity distribution. Turbulence was isotropic and near uniform and its intensity decreased during compression from $\sim 0.8\ \overline{V}_p$ to $0.3 - 0.4\ \overline{V}_p$ at TDC of compression.

4. Despite the differences between the induction-generated flows of the production and model engine configurations, the flow during compression was essentially the same in both cases, particularly with respect to the distribution and decay of turbulence. These similarities justified the previous model engine investigations and allowed their results to be extrapolated in practical engine configurations.

Finally, the detailed characterisation of the flow at the exit of the helical intake port and the velocity measurements of the in-cylinder flowfield are expected to provide adequate boundary conditions and validation data for the assessment of the ability of relevant multi-dimensional prediction codes to simulate practical engine configurations.

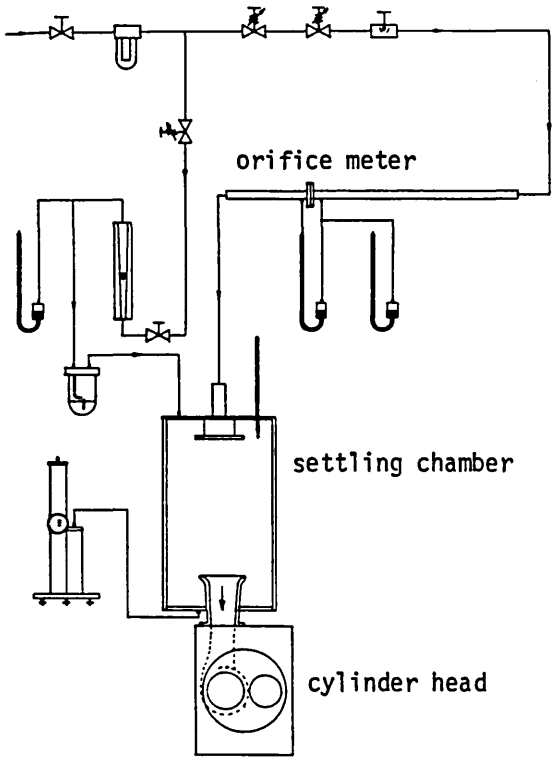

Fig. 5.1
Schematic diagram of the steady flow rig

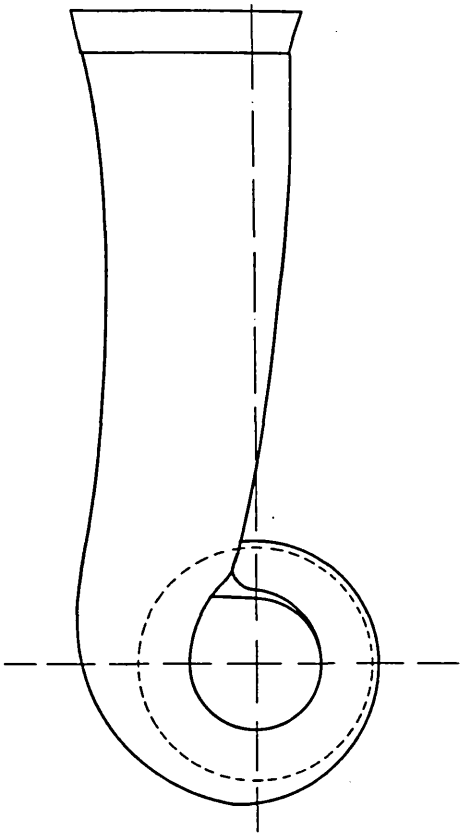

Fig. 5.2
Diagram of the helical intake port

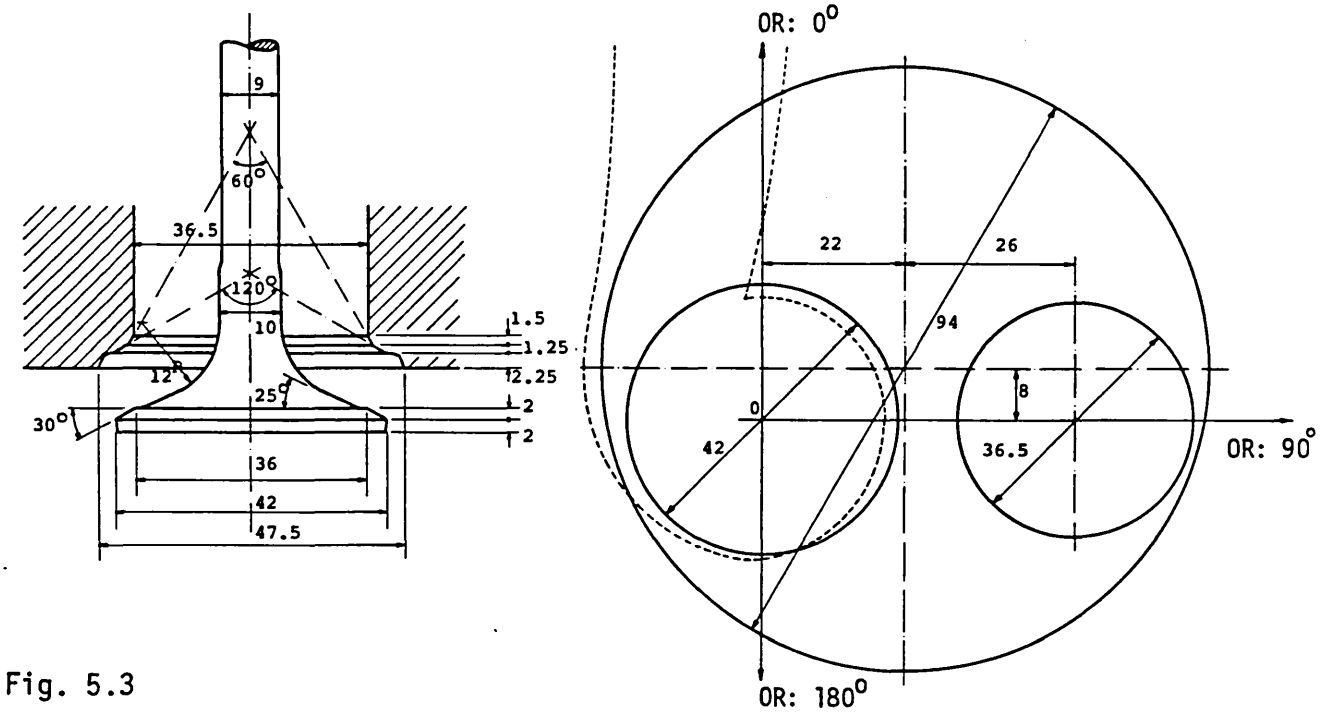

Fig. 5.3
Intake valve and cylinder head geometry. Definition of measurement planes

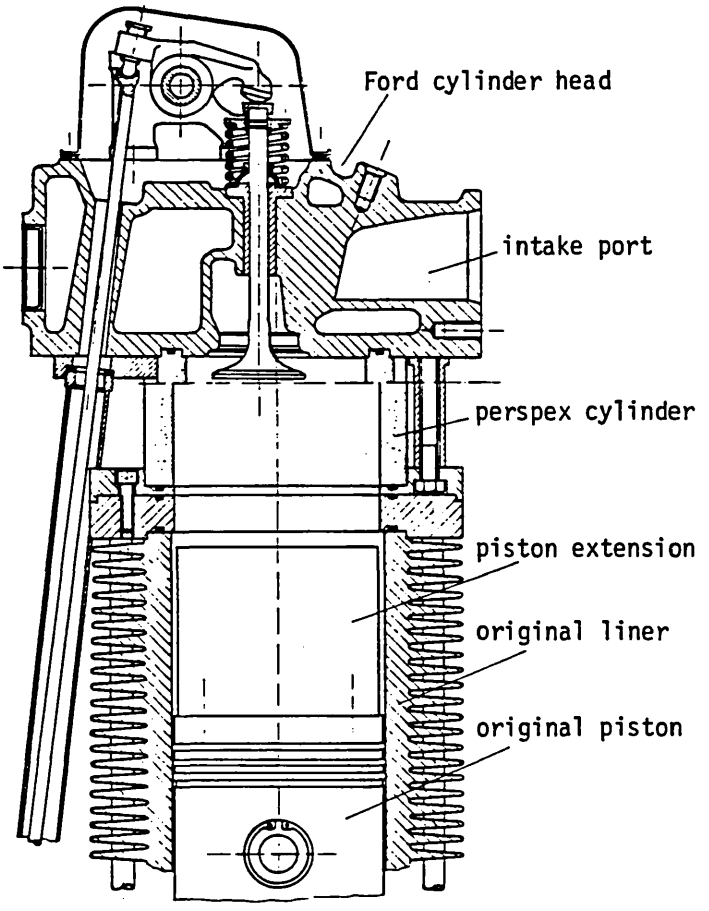

Fig. 5.4 Diagram of the modified Diesel engine with the Ford 2.5 L cylinder head; optical access to the cylinder

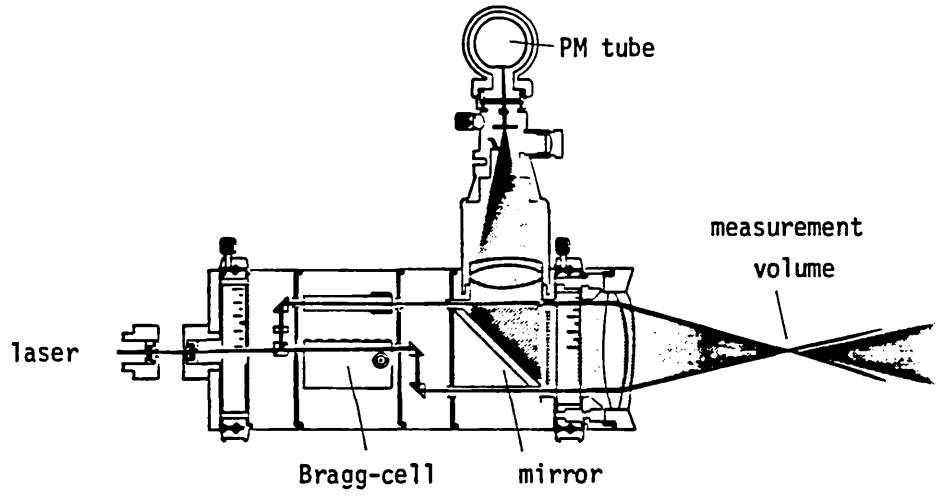

Fig. 5.5 Schematic of the Bragg-cell Lda optics

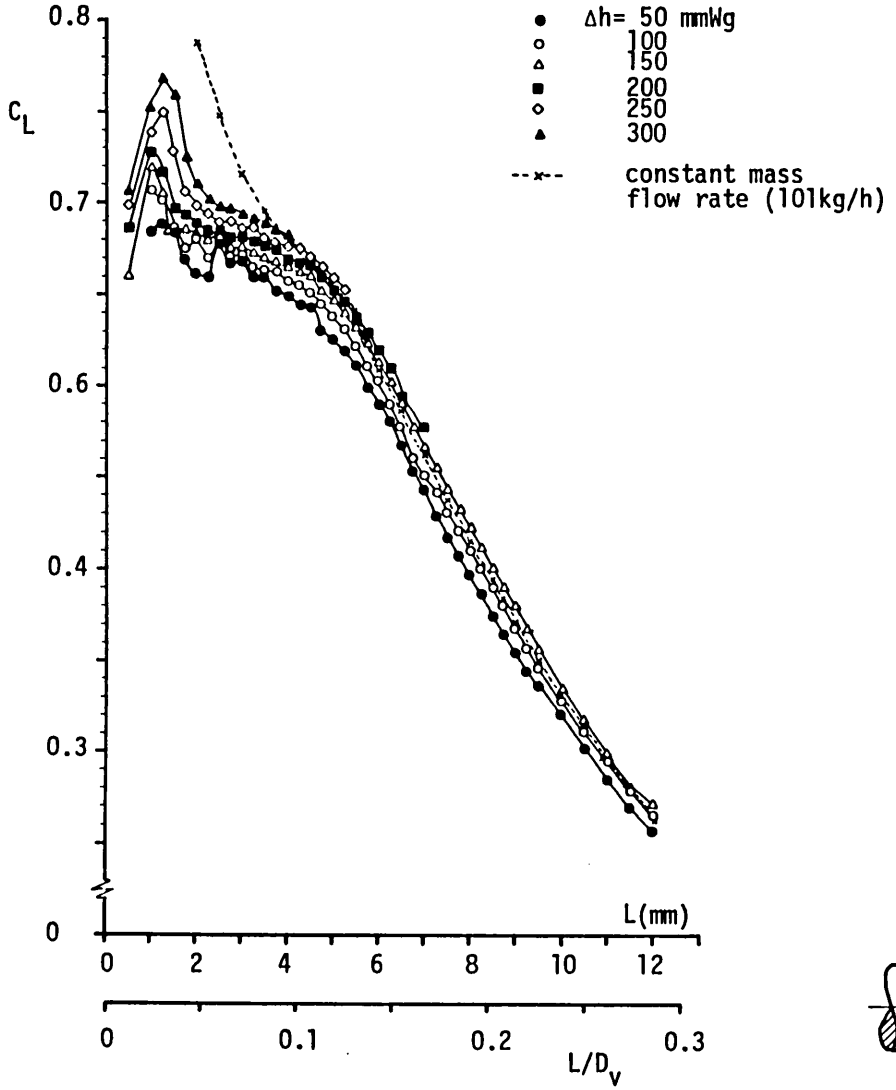

Fig. 5.6 Discharge coefficient of the intake valve

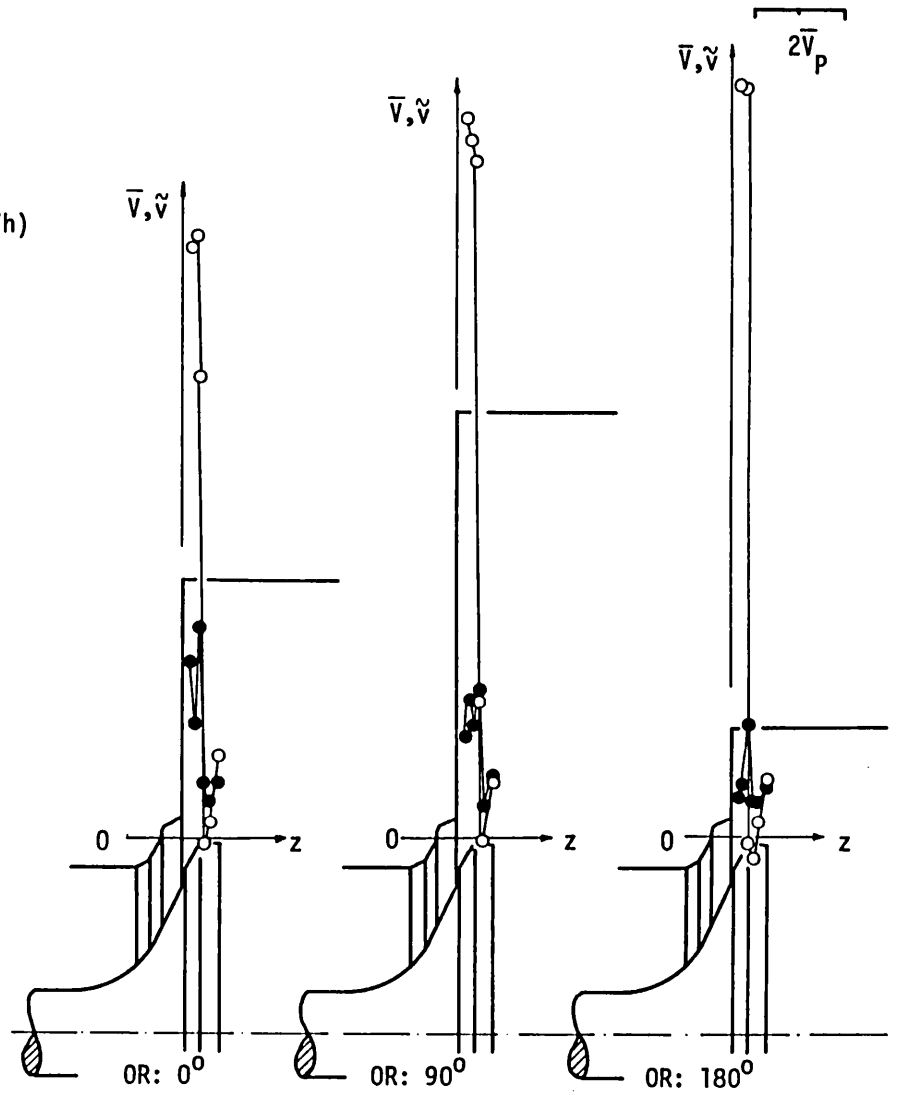

Fig. 5.7 Radial velocity distribution at the valve exit, along the 0, 90 and 180° measurement planes. L = 4 mm, steady flow

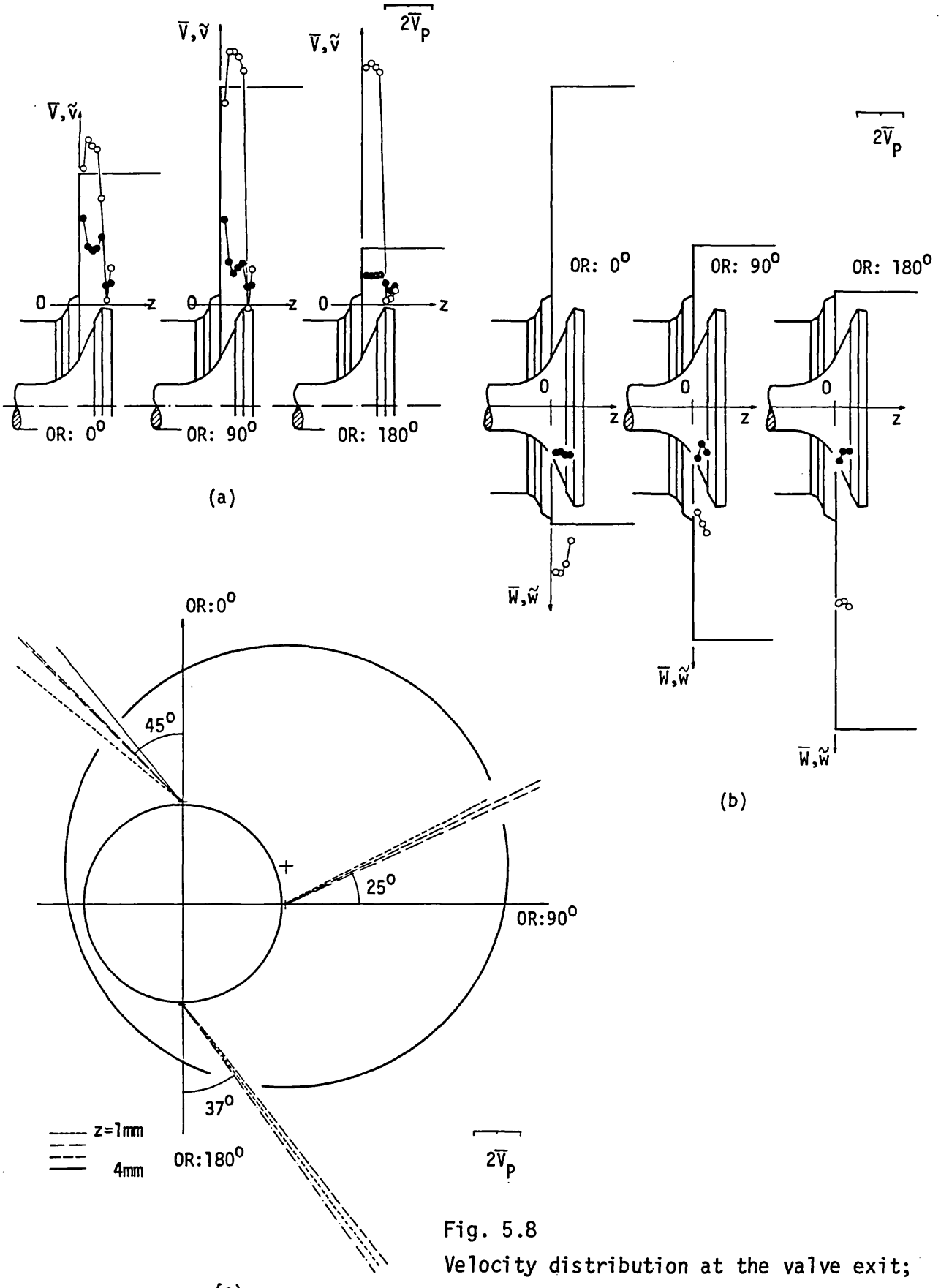

Fig. 5.8
Velocity distribution at the valve exit; L = 7 mm, steady flow. a) radial velocities, b) Swirl velocities, c) Vector addition of the radial and swirl velocity components

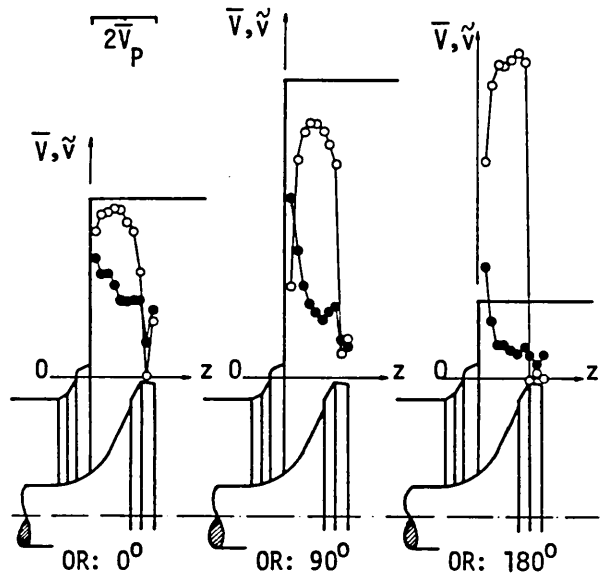

(a)

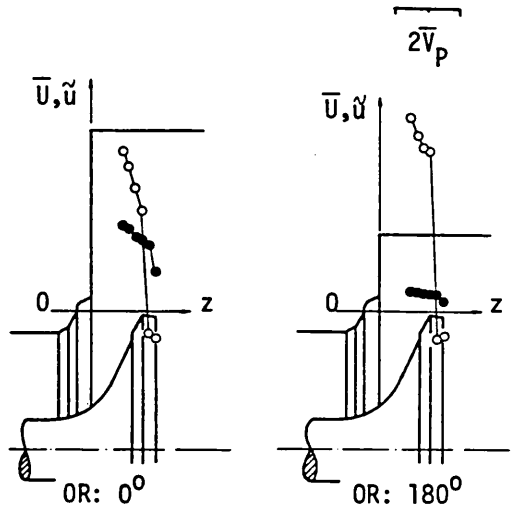

(b)

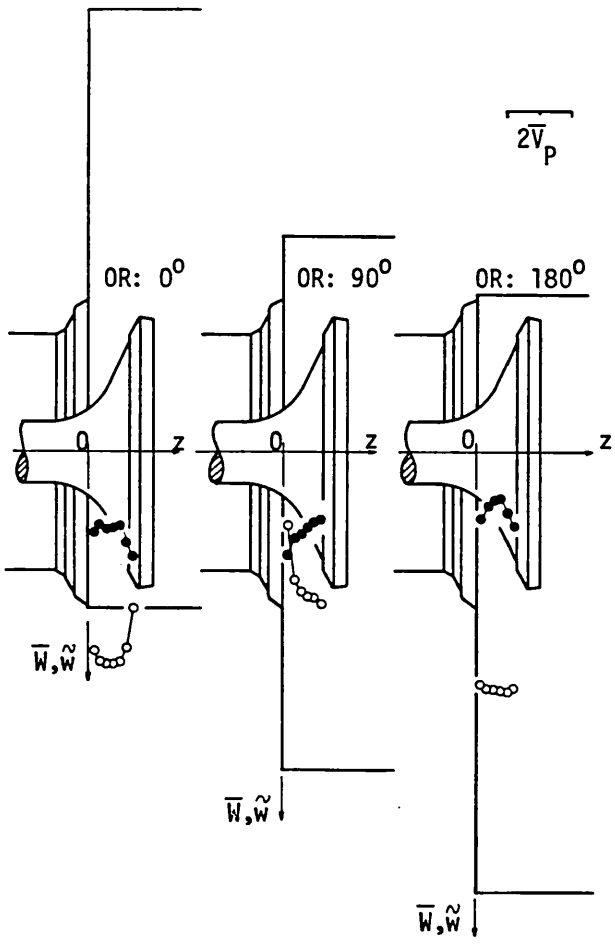

(c)

Fig. 5.9
Radial (a), axial (b) and swirl (c) velocity distribution at the valve exit along the 0, 90 and 180° measurement planes.
L = 10 mm, steady flow

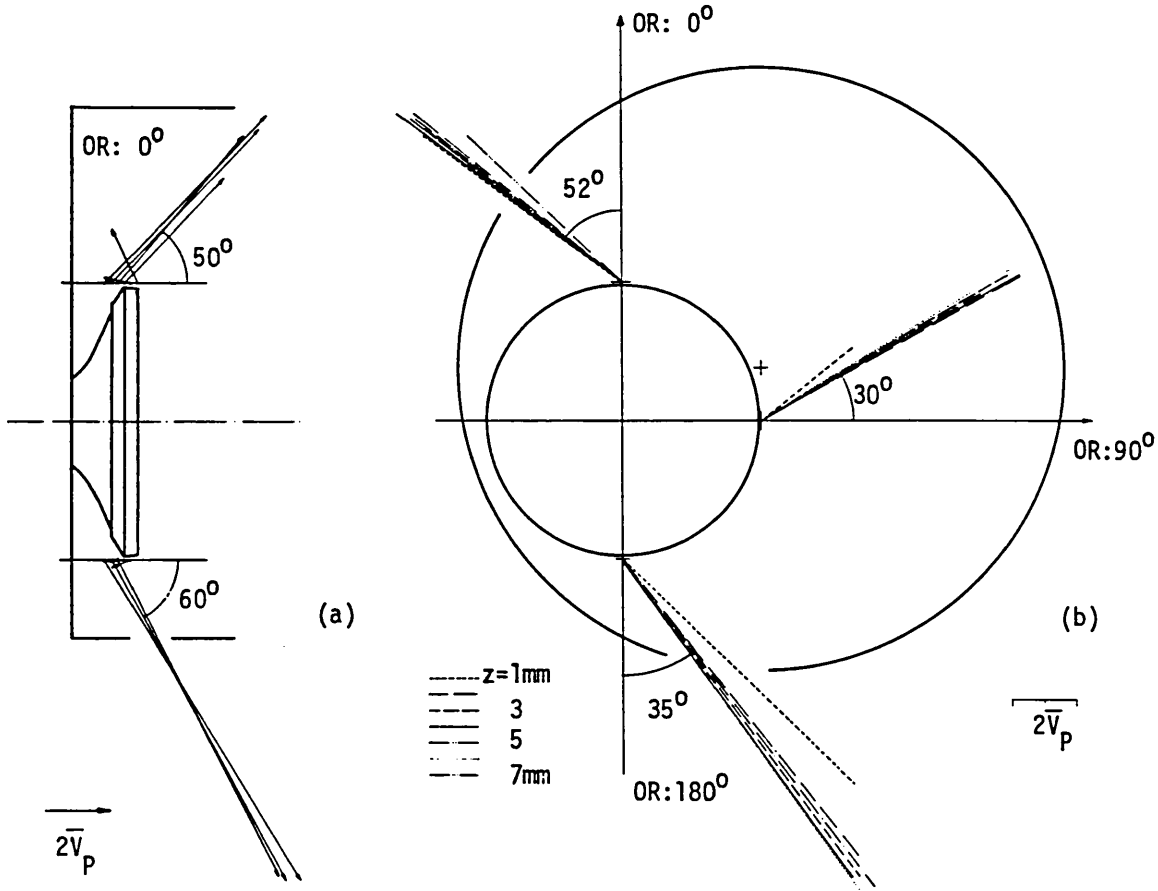

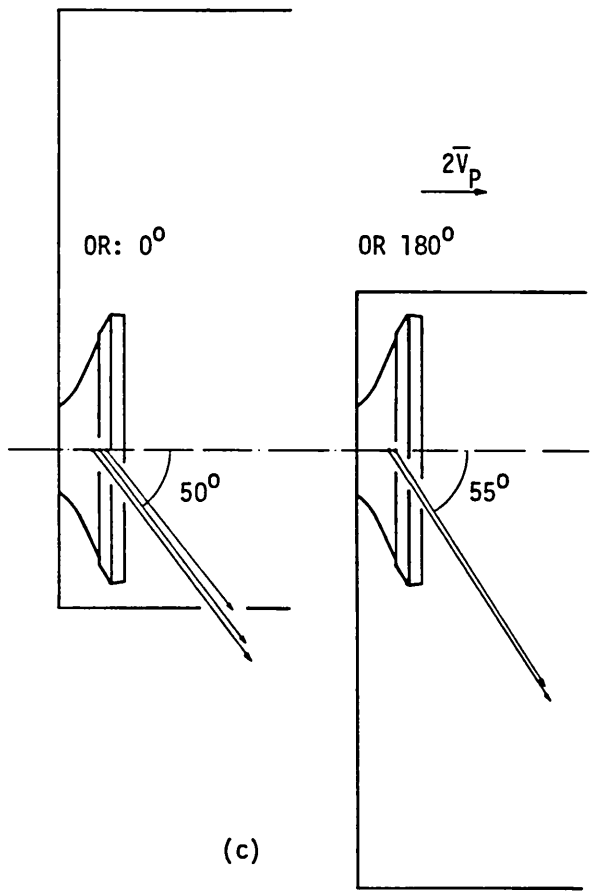

Fig. 5.10
Vector addition of the a) axial and radial, b) radial and swirl, c) axial and swirl velocity components at the valve exit. L = 10 mm, steady flow

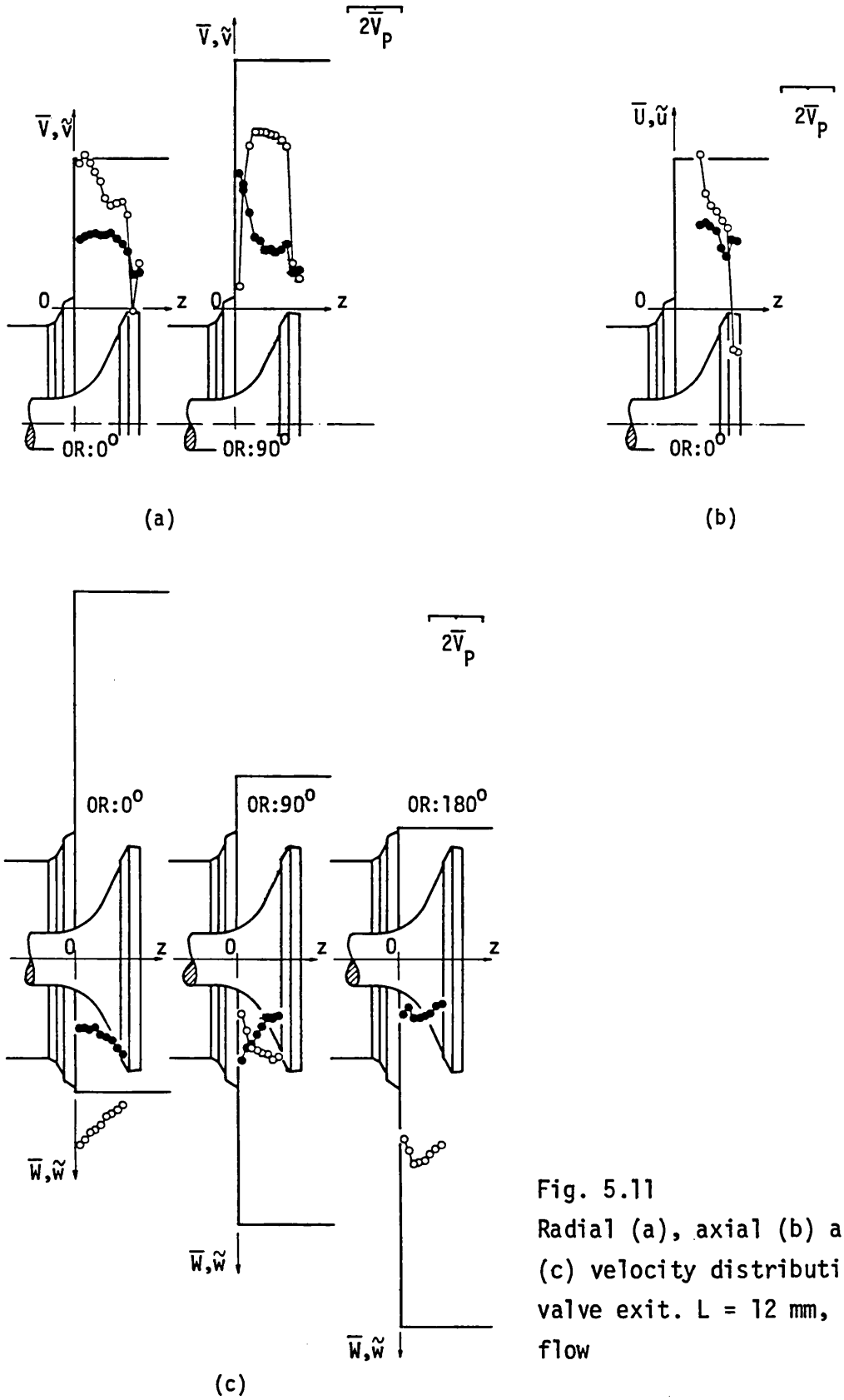

Fig. 5.11
Radial (a), axial (b) and swirl (c) velocity distribution at the valve exit. L = 12 mm, steady flow

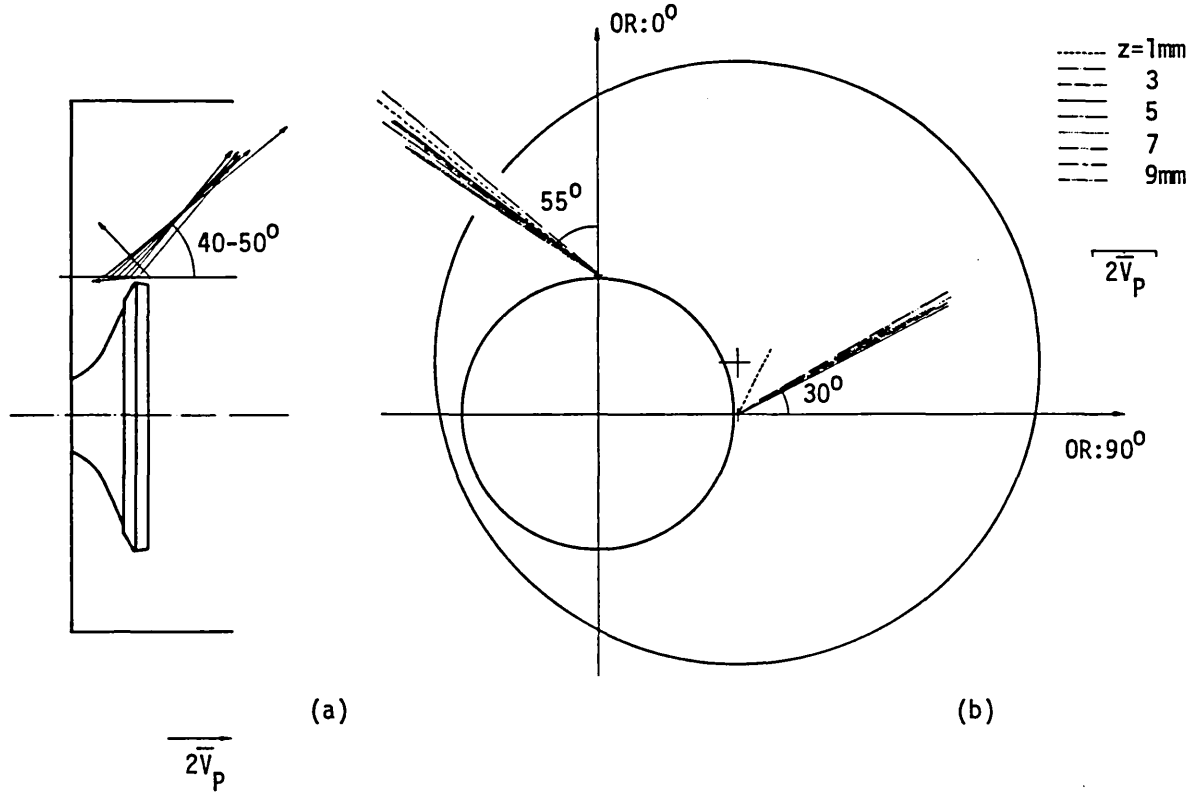

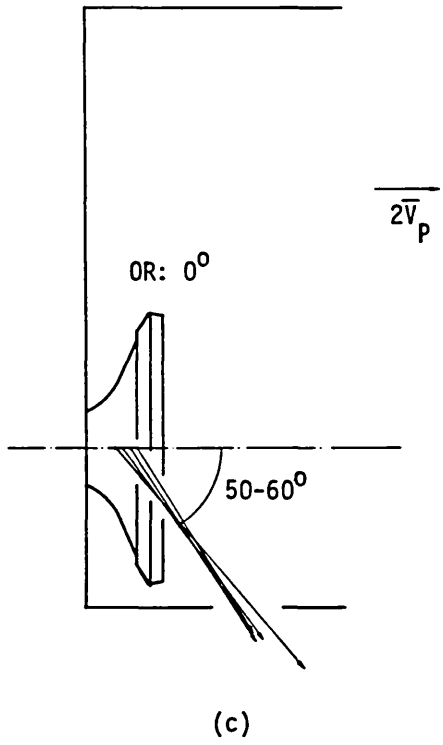

Fig. 5.12
Vector addition of the a) axial and radial b) radial and swirl c) axial and swirl velocity components at the valve exit.
L = 12 mm, steady flow

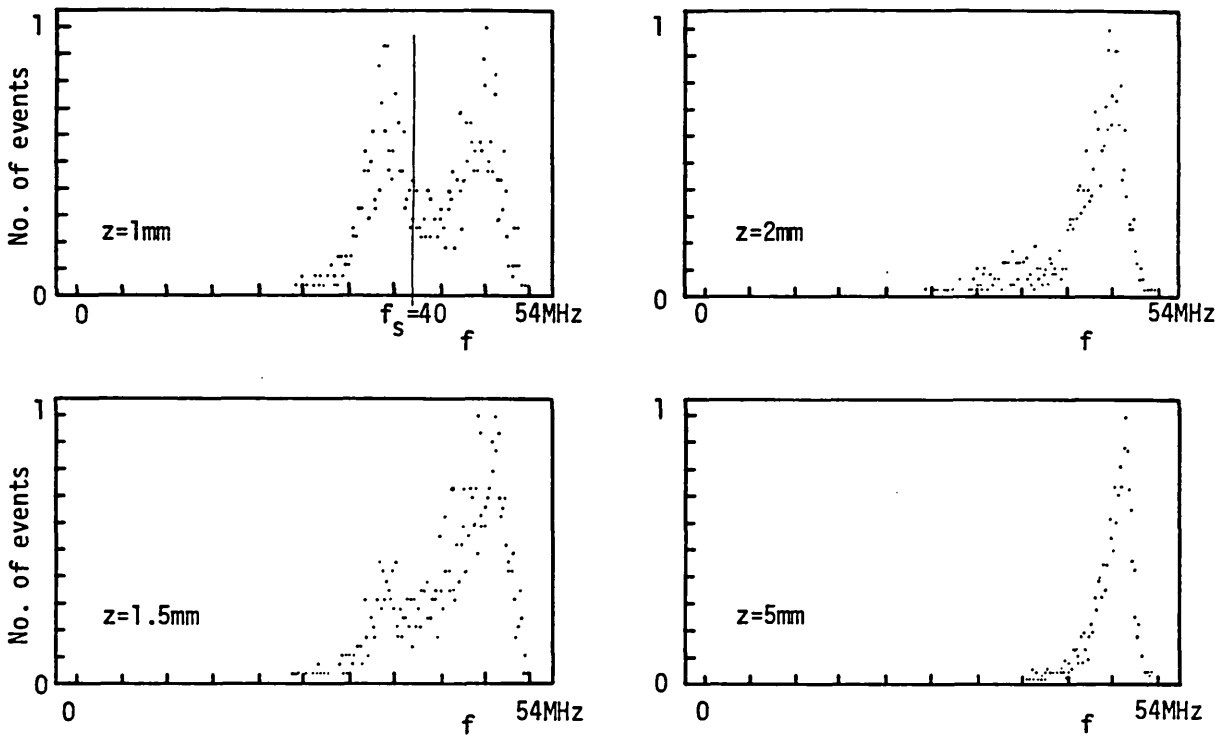

Fig. 5.13 Probability density distribution of the radial velocity at four locations of the valve exit plane. L = 10 mm, 90^{o} measurement plane, steady flow

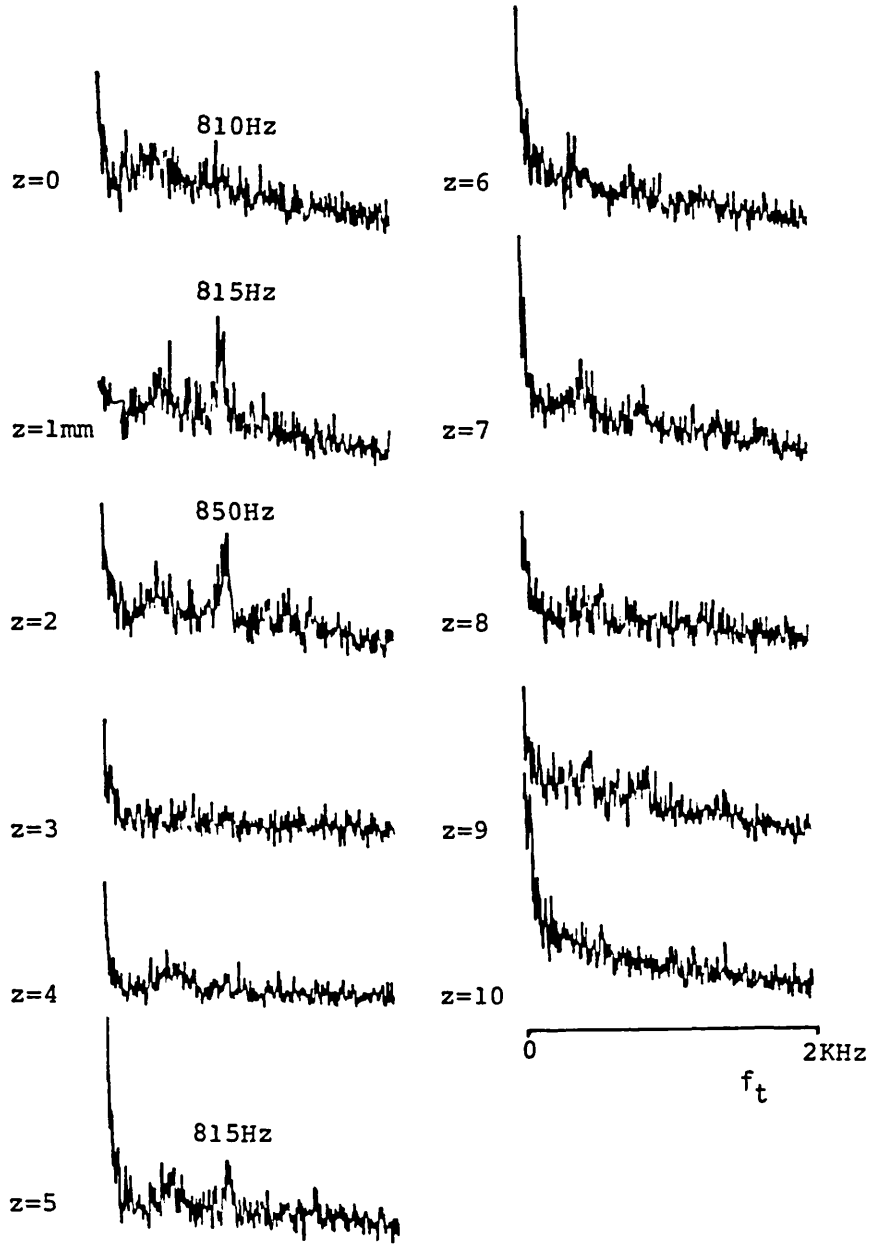

Fig.5.14 Turbulence spectra at the valve exit plane.
L = 10 mm, 90^{o} measurement plane, steady flow

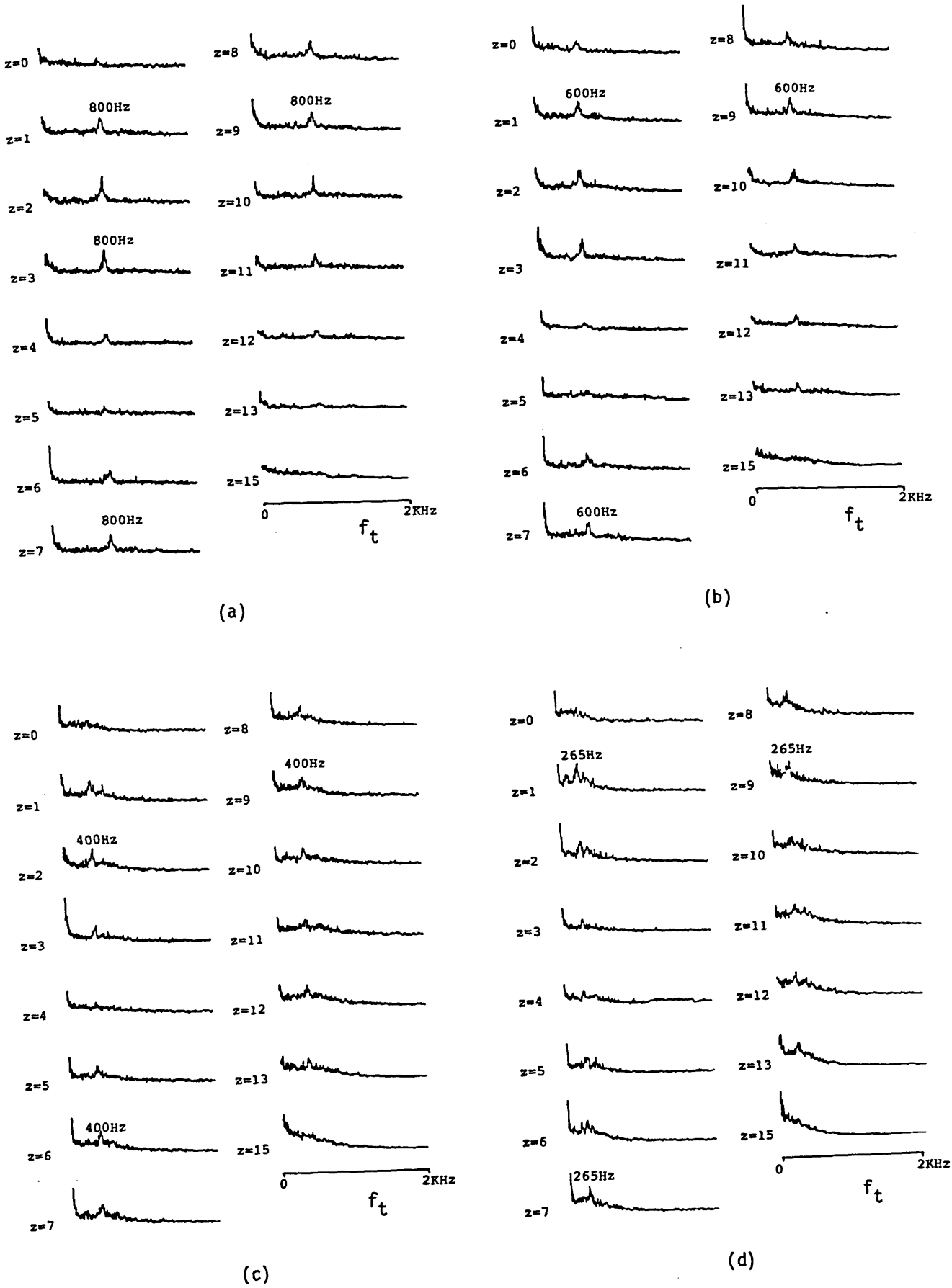

Fig. 5.15 Turbulence spectra at the valve exit plane. L = 12 mm, 90° measurement plane, steady flow. a) $\dot{m}$ = 100 kg/h, b) $\dot{m}$ = 75 kg/h, c) $\dot{m}$ = 50 kg/h, d) $\dot{m}$ = 33 kg/h

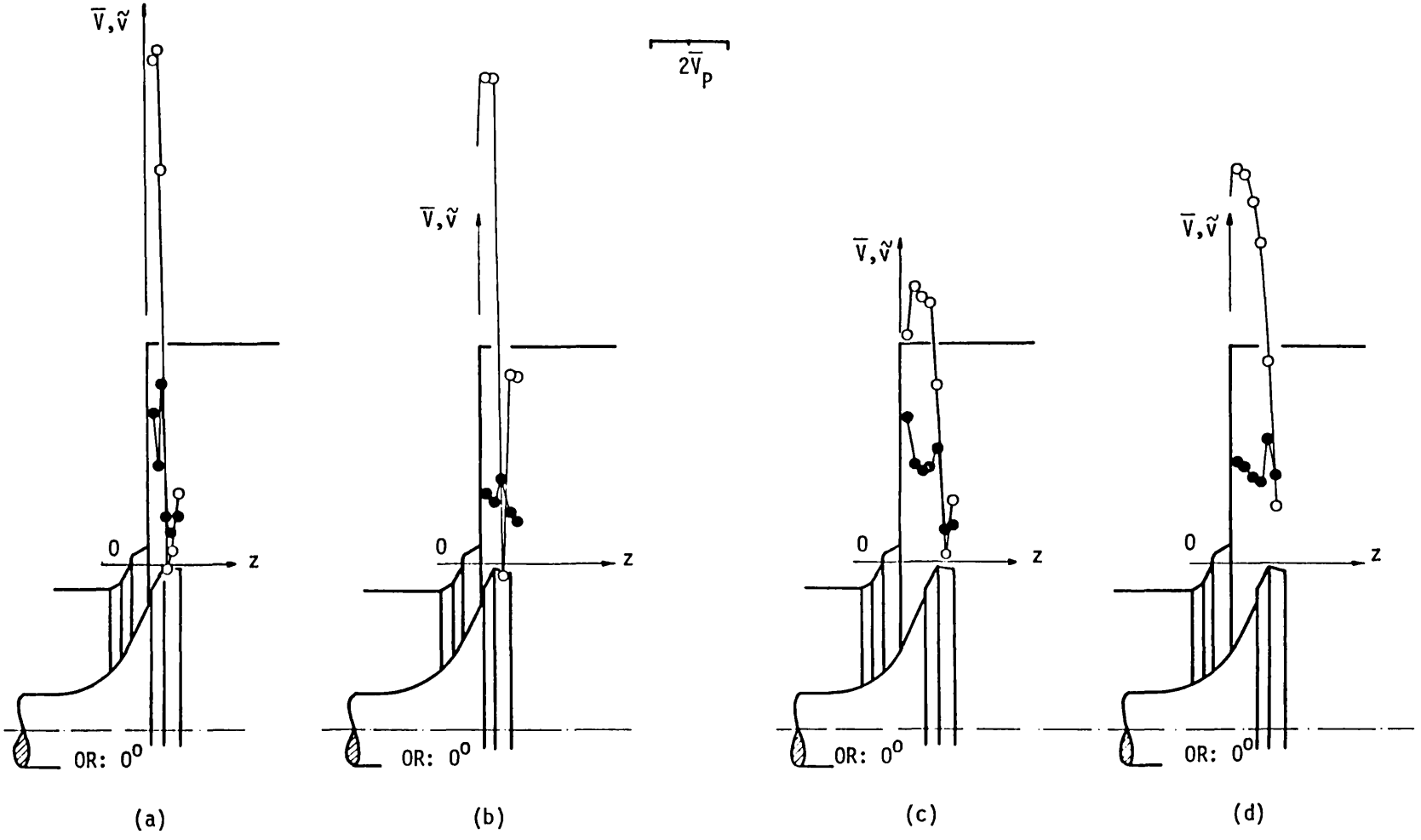

Fig. 5.16 Radial velocity distribution at the valve exit along the 0^{o} measurement plane. a) L = 4 mm, steady flow, b) L = 4 mm, $\theta = 29^{o}$, operating valve, c) L = 7 mm, steady flow, d) L = 7 mm, $\theta = 47^{o}$, operating valve, 916 rpm

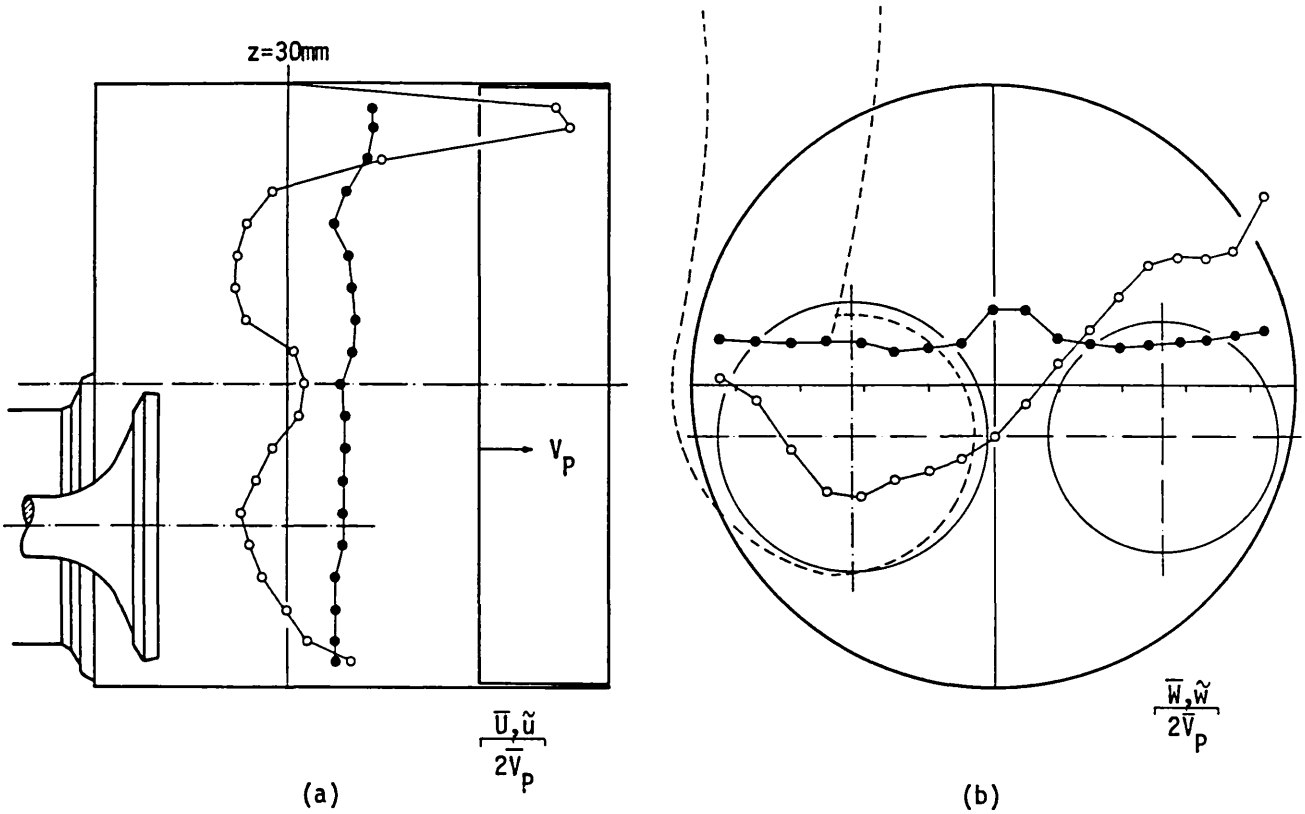

Fig. 5.17 Axial (a) and swirl (b) velocity distribution at z = 30 mm and $\theta = 72^{o}$ (L = 10 mm). Engine flow, n = 916 rpm

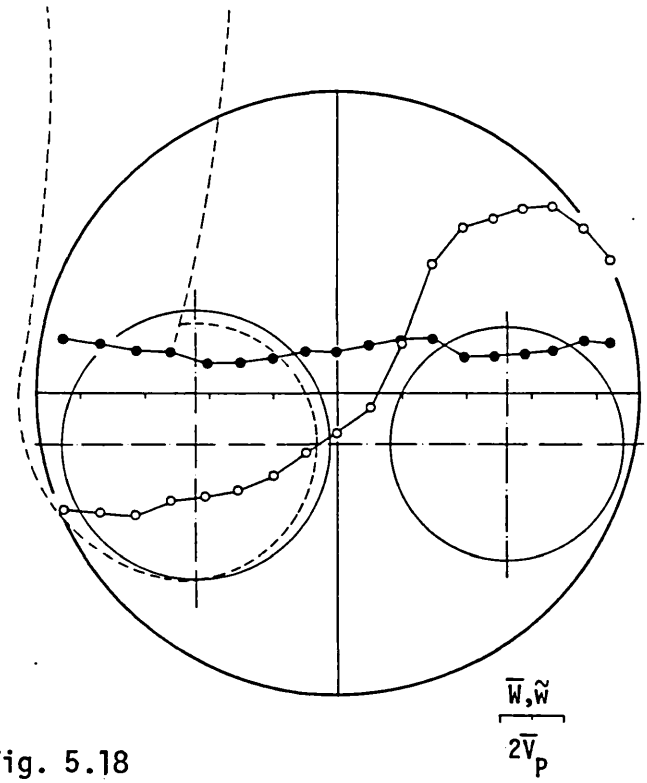

Fig. 5.18
Swirl velocity distribution at z = 47 mm and $\theta = 166^{o}$ (L = 7 mm). Engine flow, 916 rpm

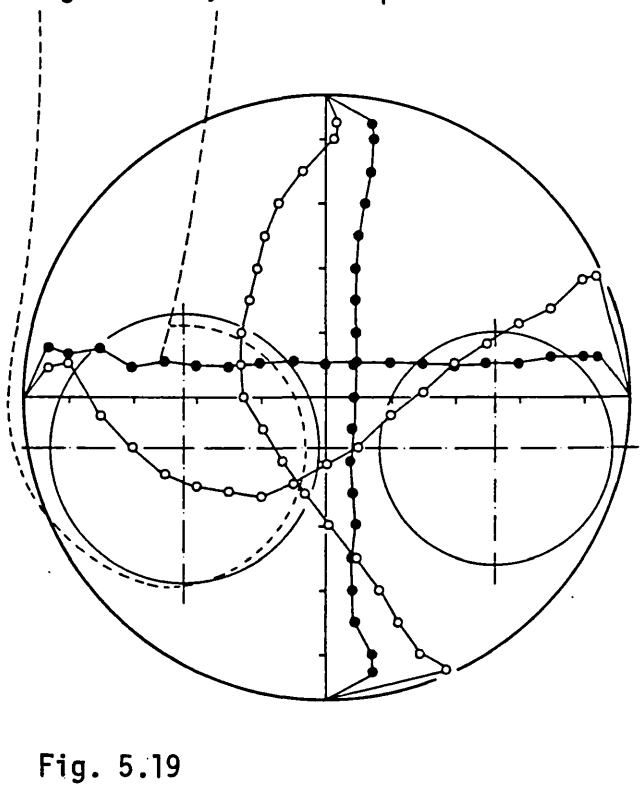

Fig. 5.19
Swirl velocity distribution at z = 47mm. Steady flow, L = 7 mm

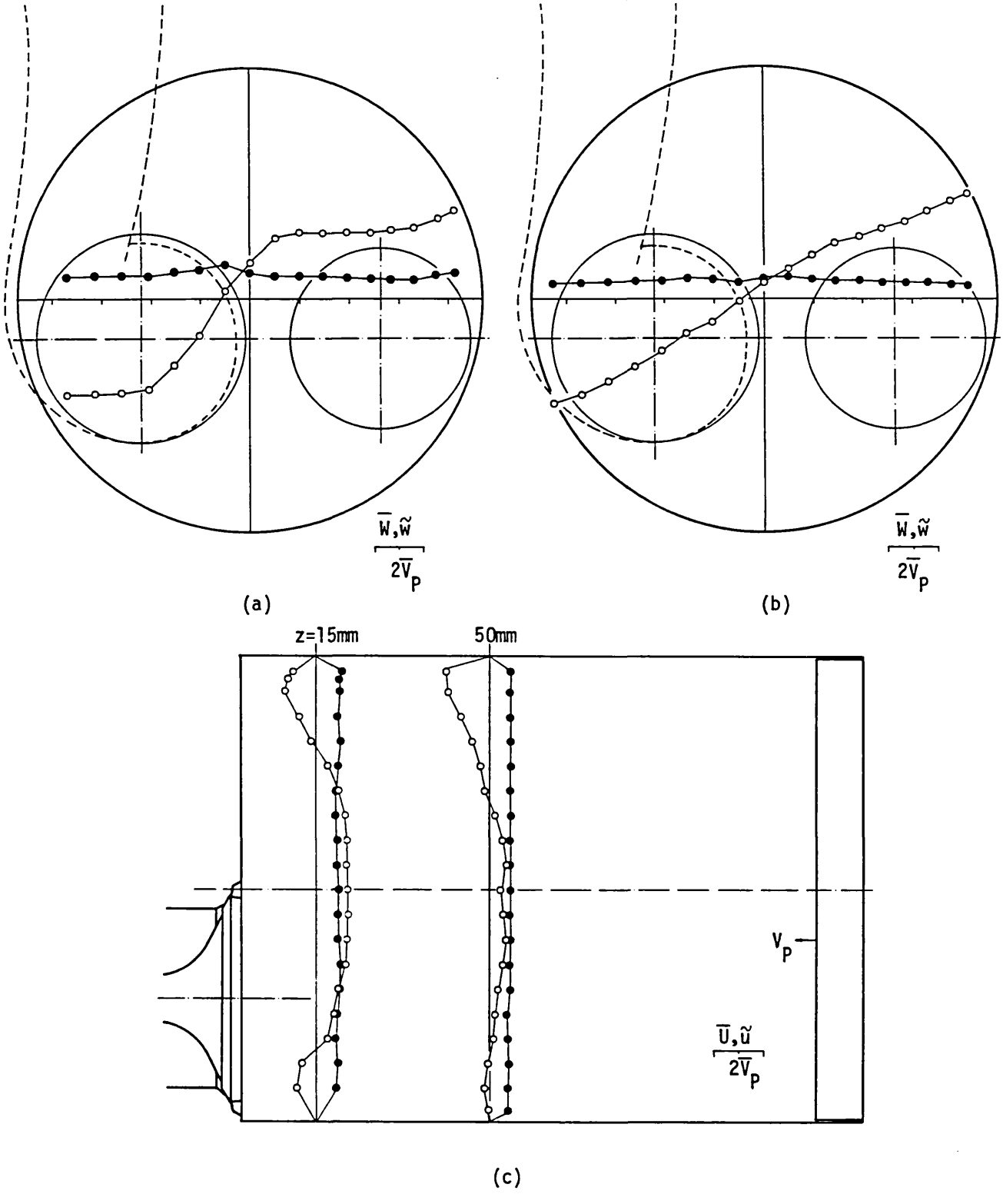

Fig. 5.20 Velocity distribution at $\theta = 220^{o}$ (IVC). a) Swirl component, z = 15 mm, b) Swirl component, z = 50 mm, c) Axial component, z = 15 and 50 mm.

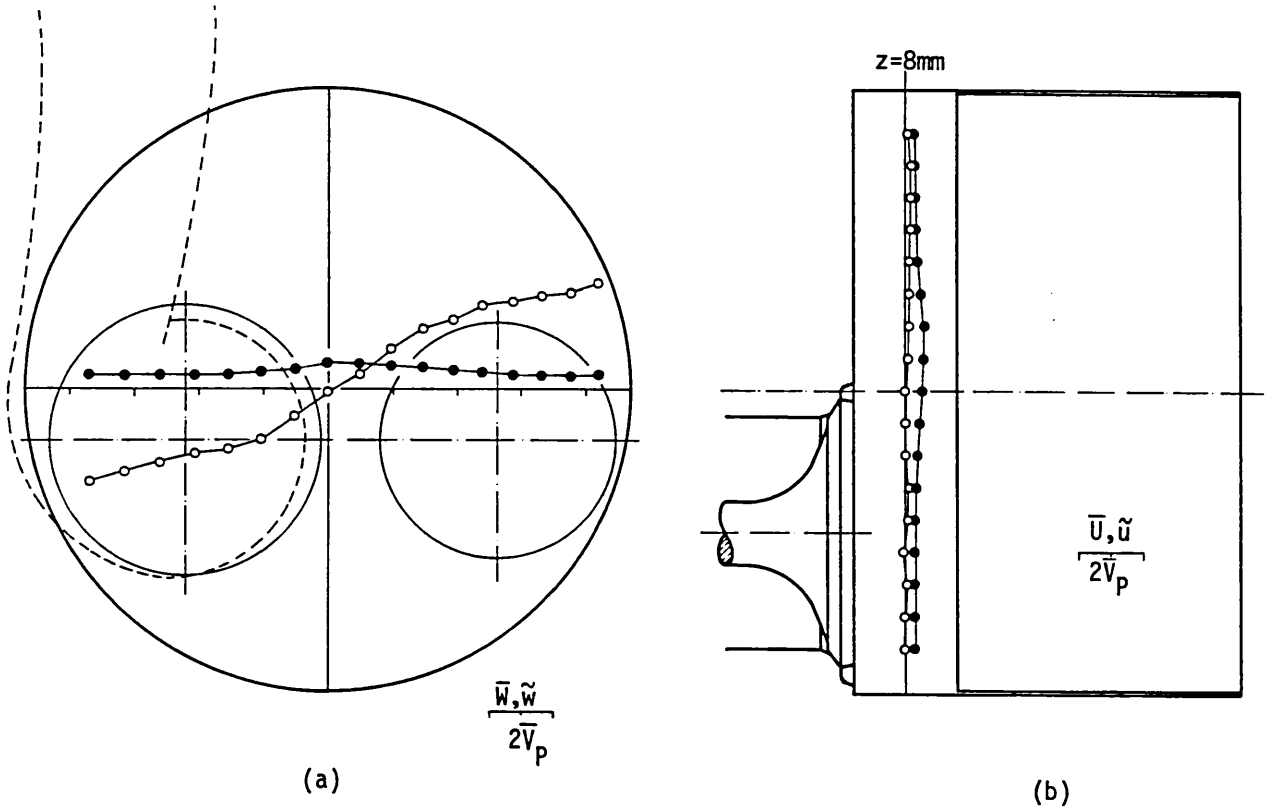

Fig. 5.21 Swirl (a) and axial (b) velocity distribution at z = 8 mm and $\theta = 360^{o}$ (TDC)

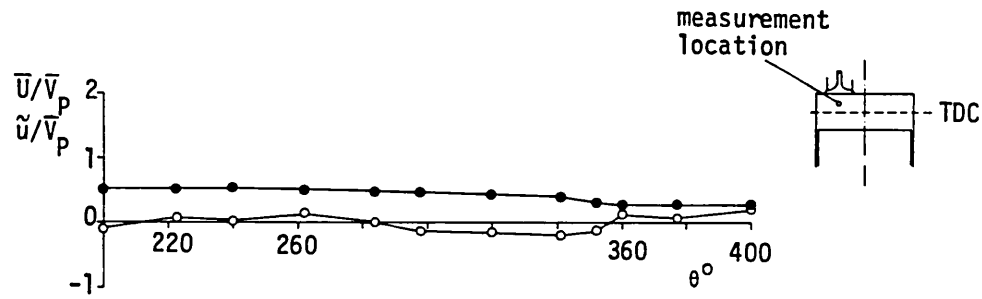

Fig. 5.22 Temporal variation of the axial mean and rms velocity at a point in the clearance volume (z = 8 mm, r = 20 mm) from $\theta = 200^{o}$ to $\theta = 400^{o}$

CHAPTER 6

CLOSURE

This last chapter of the thesis is divided into two sections. The first outlines the main findings and achievements of the present study and discusses the significance of the conclusions presented at the end of each chapter. The second section suggests future research, based on the findings and the experience acquired from this work.

6.1 ACHIEVEMENTS AND CONCLUSIONS

This thesis has presented in-cylinder velocity field measurements obtained by laser Doppler anemometry in a variety of model and production engine and engine-like configurations. Emphasis has been given to the accuracy and detail of the velocity measurements in order to minimise the ambiguities associated with the study and understanding of the complex, turbulent and time-dependent flowfields.

A main characteristic of the investigation is the organised structure of the research and the wide spectrum of flow configurations examined. In order to achieve the principal objective of this thesis, namely the in-depth understanding of the in-cylinder flow processes, a systematic study of the effect of isolated parameters on the in-cylinder flowfield was carried out starting from the study of axisymmetric steady flow simulations of the intake stroke and leading, through a gradual approach of increasing complexity, to the study of the valve exit and in-cylinder flowfields in a motored production engine. The benefit from this approach has been demonstrated by the relative ease with which the results of the production engine flow investigation were obtained and analysed.

An important contribution to engine flow research came from the results of the production and high speed engine investigations. The similarities with those of the present and previous studies in simplified engine simulations provided the basis for justification of the "model engine" concept and removed ambiguities with respect to their relevance to realistic engine configurations.

Another characteristic of the research was the continuous interaction of the experimental work with a parallel computational research programme. A good example of the contribution of this cooperation to the study of the in-cylinder flow phenomena is the understanding of the mechanism of turbulence augmentation observed with the central directed port configuration.

Finally the development of the measurement systems and the successful design of high speed realistic engines with full optical access for in-cylinder LDA measurements is a useful contribution to engine flow research from an engineering standpoint. The resulting hardware can be used for the application of a variety of laser diagnostic techniques which will, hopefully, lead to even better understanding of the in-cylinder flow processes.

The results of this experimental study have been extensively discussed in the previous chapters. In the following paragraphs an overview is given of the main conclusions and of their implications to engine research and design.

The flow at the exit of the intake valve of a reciprocating engine was found to be nearly quasi-steady and the valve jet velocities to scale with the instantaneous piston speed in the range of 200 to 900 rpm. The implication of this finding is that relatively simple steady flow tests can be used to study the valve flow characteristics and to provide velocity data for input to multi-dimensional engine flow calculations, thus removing ambiguities with respect to lack of accurate boundary conditions. This investigation also showed that the interaction of the in-cylinder flow-field with the flow at the valve exit may become important in some extreme cases of piston-crown geometry. This indicated that the valve flow cannot always be decoupled from the in-cylinder flow and suggests that future computational studies may need to include part of the intake port in the solution domain. The effect of valve/port geometry on the valve flowfield has also been examined. The results demonstrated the importance of the geometric details on the valve performance and pointed out that possible flow separation at the valve gap may lead to valve jet velocities higher than those expected by assuming a uniform velocity distribution at the valve exit. This finding isolated a parameter which may have been one of the reasons for the underprediction of the maximum in-cylinder velocities during induction by the computational methods.

These flow characteristics at the exit of the intake valve are relevant to engine speeds below 1000 rpm, where compressibility and resonance effects in the induction system were absent. These phenomena are likely, however, to play an important role at high engine speeds and their effects should be investigated.

The in-cylinder flowfield during early induction was shown to depend largely on the induction system geometry and to consist of a system of vortices which scale with the instantaneous piston position. The implication of this feature is that the in-cylinder flow during induction and downstream of the valve cannot be simulated by steady flow experiments. This, however, does not rule out their usefulness for some qualitative information and comparative studies between various induction system geometries, particularly when they are performed with detailed velocity field measurements rather than global diagnostic methods. The structure of the induction-generated flow was found to be important for the shaping of the flow at IVC. Three discrete cases were identified and resulted in different flow patterns at the end of induction with subsequent implications for the TDC flowfield. In the first case, the multi-vortex structure generated by simple cylindrical ports, either off-centre or axisymmetrically located with respect to the cylinder axis, decayed by the end of induction through the exchange of momentum between the counter-rotating vortices and resulted in a near uniform velocity field and turbulence intensity distribution at IVC with magnitudes around 0.7 $\overline{V}_p$. The second case was characterised by a single dominant vortex in the axial plane of symmetry generated by a central intake port with a shrouded valve and, as the cylinder charge tended to conserve its angular momentum, resulted in a well defined mean rolling flow pattern at IVC. Similarly, in the third case, the angular momentum imparted to the cylinder charge in the tangential plane through the swirl-producing ports was conserved throughout induction and resulted in an axially stratified swirl flow pattern at IVC which also induced axial and radial pressure gradients resulting in the formation of a weak toroidal vortex in the axial plane. In all these cases turbulence production took place mainly at the shear layers of the intake valve jet and was transported to other areas of the cylinder space with little differences in intensity between these flow configurations.

The effect of piston geometry on the shaping of the intake flow, although important during the early stages of induction, was found to be less important to the flow at IVC. It is during compression that the combustion chamber geometry, together with the flow structure at the end of induction, becomes important and determines the mean and turbulent characteristics of the TDC flowfield. In the case of a disc-type combustion chamber and in the absence of significant flow structures at IVC the compression process was nearly one-dimensional and resulted in a near-zero mean flow at TDC. Turbulence produced by the compression stresses was counterbalanced by dissipation which resulted in a net decay and near isotropic turbulence field at TDC. The distribution of turbulence intensity in the TDC clearance was not uniform, exhibiting spatial variations of 20 to 35%, depending on engine speed, and the average turbulence intensity did not scale with engine speed increasing from 0.45 $\overline{V}_p$ at 200 rpm to 0.59 $\overline{V}_p$ at 2000 rpm. The mean velocity field did not seem to be influenced by engine speed and remained close to zero over this speed range.

The presence of the strong rolling vortex at IVC, generated by the central directed port, led to an entirely different flow development during compression. In this case the piston motion increased the velocity gradients associated with the rolling vortex and enhanced turbulence production which counterbalanced dissipation and led to nearly double turbulence intensity at TDC than all other intake port configurations. This increase of TDC turbulence through the mean flow, however, was achieved at the expense of the volumetric efficiency of the engine. For a practical configuration, the use of inclined valves (pentroof chamber) or appropriately designed directed ports may give rise to similar mechanisms of turbulence augmentation with less impact to the breathing capacity of the engine.

Finally the tangential mean flow pattern generated by the swirl-producing ports was found to persist throughout compression although the angular momentum of the cylinder charge decayed by 30 to 50% depending on swirl level and velocity distribution and on combustion chamber geometry. The main swirl flow characteristics of the induction flowfield persisted during compression and did not lead always to solid body rotation at TDC as often assumed. The effect of swirl on TDC turbulence in a disc-type chamber was to reduce its intensity to average values of $\sim 0.35\ \overline{V}_p$, even

at an engine speed of 900 rpm. When a squish piston was present, however, the interaction of swirl and compression squish led to high swirl velocities and a complex in-bowl vortical structure and increased turbulence intensity at TDC of compression to more than 1 $\bar{V}_p$. Turbulence generation in this case was mainly controlled by the squish flow characteristics and was little influenced by the swirl level.

A distinct characteristic of the in-cylinder swirl flow in both model and production engines was a low frequency oscillation of the swirl velocity near the cylinder axis which was manifested as a helical trajectory of the swirl centre. This feature was almost suppressed with a squish piston which prevented the development of large scale motions during early induction. This suggests means of reducing the low frequency turbulent velocity fluctuations by imposing small length scales on the in-cylinder flowfield. This would eventually lead to a reduction of the combustion cyclic variations but the possibility of application of this principle is a matter of further research.

The summary of the achievements and conclusions of this experimental investigation has shown that the objectives of this study have been, to a large extent, accomplished. It cannot be argued, however, that the research subject has been exhausted and new questions have been raised. The following section summarises these points and highlights some of the areas where further research is required.

6.2 SUGGESTIONS FOR FURTHER WORK

The areas of engine flow research which have been shown to require the attention of future experimental work can be divided into three categories. The first is related to the study of the precombustion flowfield, the second to its interaction with the combustion process and the third to the development of the experimental methods necessary for these investigations.

In the first category, the effect of operating and geometric parameters of the engine on the precombustion flowfield requires further investigation.

In particular the study of the effect of engine speed on the in-cylinder flow should be extended to speeds higher than those of this work and should include the study of effects on the valve exit and in-cylinder flowfields during induction. The effect of induction swirl and compression squish on the scaling of the TDC mean and turbulent flowfields also requires investigation since these parameters influence the mechanisms of turbulence production and decay. These studies will provide information on the cause of the non-linear dependence of TDC turbulence on engine speed observed in this work and on the extent to which the present results can be extrapolated to higher engine speeds and different intake port and combustion chamber configurations. Similar investigations should be performed in relation to the flow inside the intake port and manifold in model and production engine configurations to determine their effect on the in-cylinder flowfield. The reduction of volumetric efficiency with engine speed should be taken into account by scaling parameters, such as the "relative intake volume flow rate" as suggested by Lancaster (1976), and the effect of intake flow throttling on the TDC flowfield should also be studied since only rarely do production engines operate with a wide open throttle.

Another aspect of the in-cylinder flow which has not been examined in this thesis is the interaction of the precombustion flowfield with fuel injection. The further development of high-speed direct-injection Diesel engines depends on the understanding of the fuel-spray formation and its mixing with the air charge. This process, however, involves two-phase flow phenomena and the available measurement techniques are in a development stage. A simplified approach is recommended to deal separately with liquid fuel injection in constant volume vessels and, thereby, to improve understanding of the spray formation and with gaseous injection in motored engines to study the spray/flow interaction. The latter should include the study of the "fuel" concentration as well as velocity fields, and to this end, optical techniques such as Rayleigh and Raman scattering should be further developed to be applied in reciprocating engines.

The difficulties associated with the probing of engine combusting flows suggest that research on the influence of the precombustion flowfield on combustion itself should also make use of simplification. The concepts of constant-volume combustion bombs and of rapid compression machines appear to be ideal for the development of the necessary experi-

mental techniques as well as for the study of the influence of mean and turbulent flow characteristics on flame propagation, cyclic variability and efficiency of the combustion process.

Laser based diagnostics are currently the most suitable experimental methods for the study of both, precombustion and combustion flowfields in reciprocating engines. Further development of these techniques and simultaneous application of global and local measurement methods is expected to provide the engine flow research with the tools necessary for the study of the in-cylinder flow phenomena. Laser Doppler anemometry is likely to remain the basic method for velocity field measurements but more thought and effort should be devoted to the measurement of turbulence scales and the understanding of cyclic variations.

It is believed that the results of the proposed systematic experimental studies, supported by parallel theoretical investigations, will assist the better understanding of the flow processes in reciprocating internal combustion engines and will provide basic knowledge for the design of high performance, fuel efficient and clean emissions engines.

REFERENCES

ABDEL-GAYED, R.G., AL-KHISHALI, K.J. and BRADLEY, D. (1984)
"Turbulent burning velocities and flame straining in explosions", Proc. R. Soc., London, A391, 393.

AHMADI-BEFRUI, B. (1985a)
Private Communication.

AHMADI-BEFRUI, B. (1985b)
"Analysis of flow evolution in the cylinders of motored reciprocating engines", Ph.D. Thesis, University of London.

AHMADI-BEFRUI, B., GOSMAN, A.D., LOCKWOOD, F.C. and WATKINS, A.P. (1981)
"Multidimensional calculation of combustion in an idealised homogeneous charge engine: A progress report", SAE Paper 810151.

AHMADI-BEFRUI, B., ARCOUMANIS, C., BICEN, A.F., GOSMAN, A.D., JAHANBAKHSH, A. and WHITELAW, J.H. (1982)
"Calculations and measurements of the flow in a motored model engine and implications to open-chamber direct-injection engines", Proc. Symp. on Three Dimensional Turbulent Shear Flows, St. Louis.

ALCOCK, J.F. (1934)
"Air swirl in oil engines", Proc. I. Mech. E., 128.

ALCOCK, J.F. and SCOTT, W.M. (1962)
"Some more light on Diesel combustion", Proc. I. Mech. E., (AD), No. 5.

AMANN, C.A. (1985)
"Classical combustion diagnostics for engine research", SAE Paper 850395.

ANNAND, W.J.D. (1969)
"Engine breathing-Aerodynamics of low speed flow through inlet valves and ports for reciprocating engines", Automobile Engineer, 59.

ANNAND, W.J.D. and ROE, G.E. (1974)
"Gas flow in the internal combustion engine", Foulis, U.K.

ARCOUMANIS, C. (1983)
"Velocity and concentration fields in reciprocating model engines", Ph.D. Thesis, University of London.

ARCOUMANIS, C., BICEN, A.F. and WHITELAW, J.H. (1982a)
"Measurements in a motored four-stroke reciprocating model engine", J. Fluids Engng., 104, 235.

ARCOUMANIS, C., BICEN, A.F. and WHITELAW, J.H. (1982b)
"Effects of inlet parameters on the flow characteristics in a four-stroke model engine", SAE Paper 820750.

ARCOUMANIS, C., BICEN, A.F., VLACHOS, N.S. and WHITELAW, J.H. (1982c)
"Effects of flow and geometry boundary conditions on fluid motion in a motored I.C. model engine", Proc. I. Mech. E., 196, 4.

ARCOUMANIS, C., BICEN, A.F. and WHITELAW, J.H. (1983)
"Squish and swirl-squish interaction in motored model engines", J. Fluids Engng., 105, 105.

ARCOUMANIS, C., BICEN, A.F., VAFIDIS, C. and WHITELAW, J.H. (1984a)
"Three dimensional flow field in four-stroke model engines", SAE Paper 841360.

ARCOUMANIS, C., BICEN, A.F. and WHITELAW, J.H. (1984b)
"The application of LDA to four-stroke motored model engines" in "Laser Anemometry in Fluid Mechanics", eds R. Adrian et al, Ladoan, Lisbon.

ARCOUMANIS, C. and WHITELAW, J.H. (1985)
"Fluid mechanics of internal combustion engines: A review", Proc. Symposium on Flows in Reciprocating Engines, ASME Winter Meeting, Miami Beach, Florida.

ARNOLD, M.J., TINDAL, M.J. and WILLIAMS, T.J. (1972)
"Measurement of induction gas velocities in a reciprocating engine cylinder", SAE Paper 720115.

ASANUMA, T. and OBOKATA, T. (1972)
"Decay of air swirl motion in an engine cylinder", JARI Tech. Memo., No. 10.

BALL, W.F., PETTIFER, H.F. and WATERHOUSE, C.N.F. (1983)
"Laser Doppler velocimeter measurements of turbulence in a direct-injection diesel combustion chamber", Proc. International Symposium on Combustion in Engineering, Vol. 1, I. Mech. E., Paper C52/83, 163-174.

BALLAL, D.R. and LEFEBVRE, A.H. (1975)
"The structure and propagation of turbulent flames", Proc. R. Soc. London, A344, 217-234.

BICEN, A.F. (1983)
"Air flow characteristics of model internal-combustion engines", Ph.D. Thesis, University of London.

BIRD, G.L. (1985)
"The Ford 2.5 litre high speed direct injection Diesel engine - Its performance and future possibilities", SAE Paper 850262.

BLUMBERG, P.N., LAVOIE, G.A. and TABACZYNSKI, R.J. (1979)
"Phenomenological models for reciprocating internal combustion engines", Prog. Energy Combust. Sci., 5, 123.

BORMAN, G. (1985)
"Reciprocating engine combustion research needs", SAE Paper 850398.

BRANDL, F., REVERENCIC, I., CARTELLIERI, W. and DENT, J.C. (1979)
"Turbulent air flow in the combustion bowl of a D.I. Diesel engine and its effect on engine performance", SAE Paper 790040.

BRANDSTATTER, W., JOHNS, R.J.R. and WIGLEY, G. (1985)
"The effect of inlet port geometry on in-cylinder flow structure", SAE Paper 850499.

BRITISH STANDARDS INSTITUTION (1964)
"Methods for the measurement of fluid flow in pipes", B.S. 1042, Part 1.

BUCHHAVE, P. (1979)
"The measurement of turbulence with the burst-type laser Doppler anemometer - Errors and correction methods", State University of New York, Technical Report No. TRL-106.

BUTLER, T.D., CLOUTMAN, L.D., DUKOWICZ, J.K. and RAMSHAW, J.D. (1979)
"CONCHAS: An Arbitrary Lagrangian-Eulerian computer code for multi-component chemically reactive fluid flow at all speeds", Los Alamos Scientific Laboratories Report No. LA-8129-MS.

BUTLER, T.D., CLOUTMAN, L.D., DUKOWICZ, J.K. and RAMSHAW, J.D. (1981)
"Multidimensional numerical simulation of reactive flow in internal combustion engines", Prog. Energy Comb. Sci., 7, 293.

BUTLER, T.D., AMSDEN, A.A., O'ROURKE, P.J. and RAMSHAW, J.D. (1985)
"KIVA: A comprehensive model for 2D and 3D engine simulations", SAE Paper 850554.

CHAPMAN, M. (1979)
"Two-dimensional numerical simulation of inlet manifold flow in a four cylinder internal combustion engine", SAE Paper 790244.

CHANAUD, R.C. (1965)
"Observations of oscillatory motion in certain swirling flows", J. Fluid Mech., 21, 111-127.

CLERK, D. (1921)
"Cylinder actions in gas and gasoline engines", SAE Journal, 8, 523.

COGHE, A. and GHEZZI, U. (1981)
"Measurement and analysis of turbulence in internal combustion engines", Presented at the First IEA Conference on New Energy Conservation Technologies and their Commercialisation, Berlin.

COGHE, A., FERRARI, G., AGOSTONI, G., BRIOSCHI, C., BRUNELLO, G., CALDERINI, F., GUARNERI, C. and VOLPI, A. (1980)
"Velocity measurements on the motored single cylinder Fiat engine", CNPM Report NT-8053.

COGHE, A., GAMMA, F., MAURI, M., BRUNELLO, G., CALDERINI, F. and FERRI DEGLI ANTONI, L. (1985)
"In-cylinder air motion measurements by laser velocimetry under steady-state flow conditions", SAE Paper 850123.

COLE, J.B. and SWORDS, M.D. (1978)
"Optical studies of turbulence in an internal combustion engine", Seventeenth Symposium (International) on Combustion, The Combustion Institute, 1295.

COLE, J.B. and SWORDS, M.D. (1980)
"An investigation of the ignition process in a lean-burning engine using conditionally sampled laser-Doppler anemometry", SAE Paper 800043.

COLE, J.B. and SWORDS, M.D. (1981)
"On the correlation between gas velocity and combustion pressure fluctuations in a spark-ignition engine", Eighteenth Symposium (International) on Combustion, The Combustion Institute, 1837.

COLE, J.B., SWORDS, M.D. and TROMANS, P.S. (1980)
"A proposed method of measuring turbulence length scales using laser-Doppler anemometry and photon correlation", J. Phys. D: Appl. Phys., 13, 1137.

DANESHYAR, H. and FULLER, D.E. (1982)
"Mixture motion in an engine cylinder", BL Colloquium on Combustion in IC Engines.

DAVIS, G.C. and KENT, J.C. (1979)
"Comparison of model calculations and experimental measurements of the bulk cylinder flow processes in a motored PROCO engine", SAE Paper 790290.

DENNISON, E.S., KUCHLER, T.C. and SMITH, D.W. (1931)
"Experiments on the flow of air through engine valves", Trans. ASME, (OGP-53-6), 53, 79.

DENT, J.C. and SALAMA, N.S. (1975)
"The measurement of the turbulence characteristics in an internal combustion engine cylinder", SAE Paper 750886.

DICKSEE, C.B. (1949)
"Open combustion-chamber Diesel engines in Britain", SAE Quarterly Transactions, 3, No. 1, 89.

DIMOTAKIS, P. (1976)
"Single scattering particle laser Doppler measurements of turbulence", Paper 10, AGARD Conference No. 193, Applications of Non-Intrusive Instrumentation in Fluid Flow Research.

DURAO, D.F.G. (1976)
"The application of laser anemometry to free jets and flames with and without recirculation", Ph.D. Thesis, University of London.

DURAO, D.F.G., LAKER, J. and WHITELAW, J.H. (1980)
"Bias effects in laser Doppler anemometry", J. Phys. E.: Sci. Instrum., 13, 442.

DURST, F. and KREBS, H. (1984)
"LDA-optics developments for measurements in internal combustion engines", Proc. Second International Symposium on Applications of Laser Anemometry to Fluid Mechanics, Lisbon.

DURST, F., MELLING, A. and WHITELAW, J.H. (1981)
"Principles and Practice of Laser-Doppler Anemometry", Second Edition, Academic Press, London.

DYER, T.M. (1985)
"New experimental techniques for in-cylinder engine studies", SAE Paper 850396.

EKCHIAN, A. and HOULT, D.P. (1979)
"Flow visualisation study of the intake process of an internal combustion engine", SAE Paper 790095.

EL-TAHRY, S.H. (1982)
"A numerical study on the effects of fluid motion at inlet-valve closure on subsequent fluid motion in a motored engine", SAE Paper 820035.

EL-TAHRY, S.H. (1984)
"Reynolds stress model to engine flow calculations", in Flows in Internal Combustion Engines-II, ASME, New York, 39-46.

ENGELMAN, H.W. (1973)
"Design of a tuned intake manifold", ASME Paper 73-WA/DGP-2.

FANSLER, T.D. (1985)
"Laser velocimetry measurements of swirl and squish flows in an engine with a cylindrical piston bowl", SAE Paper 850124.

FISHER, G.L. (1983)
"Through-the-piston combustion photography on a direct-injection Diesel engine", Ricardo Consulting Engineers, Report DP83/1367.

FITZGEORGE, D. and ALLISON, J.L. (1962)
"Air swirl in a road vehicle Diesel engine", Proc. I. Mech. E., (AD), No. 4.

FOUNTI, M. (1983)
"Model furnace and heat exchanger flows", Ph.D. Thesis, University of London.

FRASER, R., PACK, C.J. and SANTAVICCA, D.A. (1984)
"An LDV system for turbulence length scale measurements", ASME 105th Winter Annual Meeting, New Orleans, LA.

FUKUTANI, I. and WATANABE, E. (1982)
"Air flow through poppet inlet valves - Analysis of static and dynamic flow coefficients", SAE Paper 820154.

GANY, A., LARREA, J.J. and SIRIGNANO, W.A. (1980)
"Laser Doppler velocimetry measurements in a motored I.C. engine simulator", AIAA Paper 80-0079.

GEORGE, W.K. (1975)
"Limitations to measuring accuracy inherent in the laser Doppler signal", Proc. LDA-Symposium, Copenhagen.

GERBER, A., CHARNAY, G. and BIDAULT, M. (1985)
"Comparisons between steady and unsteady flows in cylinders of an internal combustion engine", SAE Paper 850121.

GOSMAN, A.D. (1983)
"Flow processes in cylinders", to be published in Thermodynamics and Gas Dynamics of Internal Combustion Engines, Vol. 2, J.H. Horlock and D. Winterbone Eds., Oxford University Press.

GOSMAN, A.D. (1985)
"Multidimensional modelling of cold flows and turbulence in reciprocating engines", SAE Paper 850344.

GOSMAN, A.D., MELLING, A., WHITELAW, J.H. and WATKINS, A.P. (1978)
"Axisymmetric flow in a motored reciprocating engine", Proc. I. Mech. E., 192, 11.

GOSMAN, A.D., TSUI, Y.Y. and WATKINS, A.P. (1984)
"Calculation of three-dimensional air motion in model engines", SAE Paper 840229.

GOSMAN, A.D., TSUI, Y.Y. and VAFIDIS, C. (1985)
"Flow in a model engine with a shrouded valve - A combined experimental and computational study", SAE Paper 850498.

GOSMAN, A.D. and JOHNS, R.J.R. (1978)
"Development of a predictive tool for in-cylinder gas motion in engines", SAE Paper 780315.

GRASSO, F. and BRACCO, F.V. (1983)
"Computed and measured turbulence in axisymmetric reciprocating engines", AIAA J., 21, No. 4, 601.

GREAVES, G., WANG, C.H.T. and KYRIAZIS, G.A. (1980)
"Inlet port design and fuel injection rate requirements for direct injection Diesel engines", Proc. FISITA Conference.

GRIFFIN, M.D., ANDERSON, J.D. and DIWAKAR, R. (1976)
"Navier-Stokes solutions of the flowfield in an internal combustion engine", AIAA Journal, 14, No. 12, 1665.

HAGHGOOIE, M., KENT, J.C. and TABACZYNSKI, R.J. (1982)
"Turbulent time-scale measurements in a spark-ignition engine using hot wire anemometry and fast response ion probes", Proc. Symposium on Flows in Internal Combustion Engines, ASME Winter Annual Meeting, Phoenix.

HAGHGOOIE, M., KENT, J.C. and TABACZYNSKI, R.J. (1984)
"Intake valve cylinder boundary flow characteristics in an internal combustion engine", Comb. Sci. Tech., 38, 49.

HAYDER, M.E., VARMA, A.K. and BRACCO, F.V. (1984)
"A limit to TDC turbulence intensity in internal combustion engines", Submitted for publication to the AIAA Journal.

HEITOR, M.V., LAKER, J.R., TAYLOR, A.M.K.P. and VAFIDIS, C. (1984)
"Instruction manual for the FS "Model 2" Doppler-frequency counter", Imperial College, Mech. Eng. Dept. Report FS/84/10.

HIROTOMI, T., NAGAYAMA, I., KOBAYASHI, S. and YAMAMASU, M. (1981)
"Study of induction swirl in a spark ignition engine", SAE Paper 810496.

HOESEL, H. and RODI, W. (1977)
"New biasing elimination method for laser Doppler velocimeter counter processing", Rev. Sci. Instrum., 48, 910.

HORVATIN, M. and HUSSMANN, A.W. (1969)
"Measurement of air movement in internal combustion engine cylinders", DISA Information, No. 8.

JOHNS, R.J.R. (1984)
"A unified method for calculating engine flows", ASME Paper No. 84-DGP-18.

JOHNSTON, S.C., ROBINSON, C.W., RORKE, W.S., SMITH, J.R. and WITZE, P.O. (1979)
"Application of laser diagnostics to an injected engine", SAE Paper 790092.

KASTNER, L.S., WILLIAMS, T.J. and WHITE, J.B. (1963)
"Poppet inlet valve characteristics and their influence on the induction process", Proc. I. Mech. E., 178, 955.

KYRIAKIDES, S.C. (1984)
"Cylinder air motion in direct injection Diesel engines", Ph.D. Thesis, University of London.

LANCASTER, D.R. (1976)
"Effects of engine variables on turbulence in a spark-ignition engine", SAE Paper 760159.

LANCASTER, D.R., KRIEGER, R.B., SORENSON, S.C. and HULL, W.L. (1976)
"Effects of turbulence on spark-ignition engine combustion", SAE Paper 760160.

LIOU, T.-M. and SANTAVICCA, D.A. (1982)
"Cycle resolved LDV measurements in a motored I.C. engine", Proc. Symposium on Applications of Laser Velocimetry, ASME Winter Annual Meeting, Phoenix.

LIOU, T.-M. and SANTAVICCA, D.A. (1983)
"Cycle resolved turbulence measurements in a ported engine with and without swirl", SAE Paper 830419.

LIOU, T.-M. and SANTAVICCA, D.A. (1985)
"Cycle resolved LDV measurements in a motored I.C. engine", J. Fluids Engng, 107, 232.

LIOU, T.-M., HALL, M., SANTAVICCA, D.A. and BRACCO, F.V. (1984)
"Laser Doppler velocimetry measurements in valved and ported engines", SAE Paper 840375.

LUCK, C.E. (1906)
"The pressure drop through poppet valves", ASME Trans., 27, 232.

MARTIN, J.K., WITZE, P.O. and BORGNAKKE, C. (1984)
"Multiparameter conditionally sampled laser velocimetry measurements during flame propagation in a spark ignition engine", 20th Symposium (International) on Combustion, Ann Arbor, MI.

MARTIN, J.K., WITZE, P.O. and BORGNAKKE, C. (1985)
"Combustion effects on the preflame flow field in a research engine", SAE Paper 850122.

MATTAVI, J.N., GROFF, E.G. and MATEKUNAS, F.A. (1979)
"Turbulence, flame motion and combustion chamber geometry - Their interactions in a lean-combustion engine", General Motors Research Laboratories, Report GMR-2884.

McLAUGHLIN, D.K. and TIEDERMAN, W.G. (1973)
"Biasing correction for individual realisation of laser anemometer measurements in turbulent flows", Phys. Fluids, 16, 2082.

MELLING, A. (1973)
"The influence of velocity gradient broadening on mean and rms velocities measured by laser anemometry", Imperial College, Mech. Eng. Dept., Report HTS/73/33.

MELLING, A. and WHITELAW, J.H. (1975)
"Optical and flow aspects of particles", Proc. LDA Symposium, Copenhagen.

MELLING, A. and WHITELAW, J.H. (1976)
"Design of laser Doppler anemometers for reciprocating engines", Imperial College, Mech. Eng. Dept., Report CHT/76/6.

MONAGHAN, M.L. and PETTIFER, H.F. (1981)
"Air motion and its effect on Diesel engine performance and emissions", SAE Paper 810255.

MORSE, A.P. (1977)
"The effect of crank-angle broadening on laser Doppler measurements in reciprocating engines", Imperial College, Mech. Eng. Dept., Report FS/77/8.

MORSE, A.P., WHITELAW, J.H. and YIANNESKIS, M. (1979)
"Turbulent flow measurements by laser Doppler anemometry in motored piston-cylinder assemblies", J. Fluids Engng., 101, 208.

MORSE, A.P., WHITELAW, J.H. and YIANNESKIS, M. (1980a)
"The influence of swirl on the flow characteristics of a reciprocating piston-cylinder assembly", J. Fluids Engng., 102, 478.

MORSE, A.P., WHITELAW, J.H. and YIANNESKIS, M. (1980b)
"The flow characteristics of a piston-cylinder assembly with an off-centre open port", Proc. I. Mech. E., 194, 31.

MORSE, A.P. and WHITELAW, J.H. (1981)
"Measurements of the in-cylinder flow of a motored four-stroke reciprocating engine", Proc. R. Soc. Lond., A377, 309.

MUKERJEE, T., PRZEKWAS, A.J., SINGHAL, A.K., DUGGAL, V.K. and KUO, T.W. (1984)
"Three-dimensional modelling of in-cylinder processes in D.I. Diesel engine", SAE Paper 840227.

NAMAZIAN, M. and HEYWOOD, J.B. (1982)
"Flow in the piston-cylinder-ring crevices of a spark-ignition engine: Effect on hydrocarbon emissions, efficiency and power", SAE Paper 820088.

NUTTING, E.M. and LEWIS, G.W. (1918)
"Air flow through poppet valves", NACA Tech. Rep. No. 24.

OHIGASHI, S., HAMAMOTO, Y. and TANABE, S. (1972)
"Swirl - Its measurement and effect on combustion in a Diesel engine", Proc. I. Mech. E., C134, 129.

OLDENGARM, J., VAN KRIEKEN, A.H. and RATERINK, H.J. (1976)
"Development of a rotating grating and its use in laser velocimetry", Proc. ISL/AGARD Workshop on Laser Anemometry, 603, St. Louis, France.

OLDFIELD, S.G. and WATSON, N. (1983)
"Exhaust valve geometry and its effect on gas velocity and turbulence in an exhaust port", SAE Paper 830151.

PATTERSON, D.J. (1967)
"Cylinder pressure variations, a fundamental combustion problem", SAE Trans., 75, Paper 660129.

PETTIFER, H.F. (1982)
"Interaction of port design and injection rate for a D.I. Diesel", SAE Paper 820358.

RAMOS, J.I. and SIRIGNANO, W.A. (1980a)
"Axisymmetric flow model with and without swirl in a piston-cylinder arrangement with idealised valve operation", SAE Paper 800284.

RAMOS, J.I. and SIRIGNANO, W.A. (1980b)
"Axisymmetric flow model in a piston-cylinder arrangement with detailed analysis of the valve region", SAE Paper 800286.

RASK, R.B. (1978)
"Velocity measurements inside the cylinder of a motored internal combustion engine", Third International Workshop on Laser Velocimetry, Purdue University.

RASK, R.B. (1979)
"Laser Doppler anemometer measurements in an internal combustion engine", SAE Paper 790094.

RASK, R.B. (1981)
"Comparison of window, smoothed-ensemble and cycle-to-cycle data reduction techniques for laser Doppler anemometer measurements of in-cylinder velocity", Proc. Symp. on Fluid Mechanics of Combustion Systems, Colorado.

RASK, R.B. (1984)
"Laser Doppler anemometer measurements of mean velocity and turbulence in internal combustion engines", General Motors Report GMR-4839.

RENSHAW, J. and WIGLEY, G. (1979)
"In-cylinder swirl measurements by laser anemometer in a production Diesel engine", AERE, Harwell, Report R9646.

REYNOLDS, W.C. (1980)
"Modelling of fluid motions in engines: An introductory overview", in "Combustion Modelling in Reciprocating Engines", Mattavi, J.N. and Amann, C.A. eds., Plenum Press, p. 69.

RICARDO, H.R. (1922)
"Recent research work on the internal combustion engine", Transactions SAE, 17, Pt. 1.

SEMENOV, E.S. (1963)
"Studies of turbulent gas flow in piston engines", Otdelenie Tekhnicheskikh Nauk, No. 8, 1958. (NASA Technical Translation F-97, 1963).

SMITH, J.R. (1982)
"Turbulent flame structure in a homogeneous-charge engine", SAE Trans., 89, Paper 820043.

SWORDS, M.D., KALGHATGI, G.T. and WATTS, A.J. (1982)
"An experimental study of ignition and flame development in a spark ignited engine", SAE Paper 821220.

TABACZYNSKI, R.J. (1982)
"Effects of inlet and exhaust system design on engine performance", SAE Paper 821577.

TABACZYNSKI, R.J. (1983)
"Turbulence measurements and modelling in reciprocating engines - An overview", I. Mech. E., International Conference on Combustion Engineering, 1, Paper C51/83.

TANABE, S., HAMAMOTO, Y. and OHIGASHI, S. (1978)
"Swirl in a four-stroke cycle engine cylinder", Bulletin of the JSME, 21, No. 152, 287.

TANAKA, K. (1929)
"Air flow through suction valve of conical seat", Aeronautical Research Institute Report, Tokyo Imperial University.

TAYLOR, C.F. (1977)
"The internal combustion engine in theory and practice", Vol. 1, MIT Press.

TIERNEY, W.T., MITCHELL, E. and ALPERSTEIN, M. (1975)
"The Texaco controlled-combustion system - A stratified charge engine concept review and current status", Paper No. C1/75, Power Plants and Future Fuels, Instn. Mech. Engrs.

TINDAL, M.J., WILLIAMS, T.J. and EL KHAFAJI, A.H.A. (1974)
"Gas flow measurements in engine cylinders", SAE Paper 740719.

TINDAL, M.J. and WILLIAMS, T.J. (1977)
"An investigation of cylinder gas motion in the direct injection Diesel engine", SAE Paper 770405.

TINDAL, M.J., WILLIAMS, T.J. and ALDOORY, M. (1982)
"The effect of inlet port design on cylinder gas motion in direct injection Diesel engines", Proc. Symposium on Flows in Internal Combustion Engines, ASME Winter Annual Meeting, Phoenix.

TROLINGER, J.D., BENTLEY, H.T., LENNERT, A.E. and SOWLS, R.E. (1974)
"Application of electro-optical techniques in Diesel engine research", SAE Trans., Paper 740125, 633.

UZKAN, T., BORGNAKKE, C. and MOREL, T. (1983)
"Characterisation of flow produced by a high-swirl inlet port", SAE Paper 830266.

WAKISAKA, T., HAMAMOTO, Y., OHIGASHI, S. and HASHIMOTO, M. (1979)
"Measurements of air swirl and its turbulence characteristics in the cylinder of an internal combustion engine", I. Mech. E., Paper C91/79.

WATKINS, A.P. (1973)
"Calculation of flow and heat transfer in the combustion chamber of a reciprocating engine", M.Sc. Thesis, University of London.

WATKINS, A.P. (1977)
"Flow and heat transfer in piston/cylinder assemblies", Ph.D. Thesis, University of London.

WATTS, R. and SCOTT, W.M. (1969)
"Air motion and fuel distribution requirements in high-speed direct injection engines", Proc. I. Mech. E., 184, Pt. 3J, Paper 17.

WIGLEY, G. and HAWKINS, M.G. (1978)
"Three-dimensional velocity measurements by laser anemometry in a Diesel engine under steady state inlet flow conditions", SAE Paper 780060.

WIGLEY, G., PATTERSON, A.C. and RENSHAW, J. (1981)
"Swirl velocity measurements in a firing production Diesel engine by laser anemometry", Proc. Symp. on Fluid Mechanics of Combustion Systems, ASME Spring Meeting, Boulder.

WIGLEY, G. and GLANZ, R. (1984a)
"Application of laser anemometry to Diesel engine port flow development", S.I.A. Conference on Diesel Engines for Automotive Applications, Lyon, France.

WIGLEY, G. and GLANZ, R. (1984b)
"A laser anemometer system for engine flow studies", Proc. Second International Symposium on Applications of Laser Anemometry to Fluid Mechanics, Lisbon.

WILLIAMS, T.J. and TINDAL, M.J. (1980)
"Gas flow studies in direct injection Diesel engines with re-entrant combustion chambers", SAE Paper 800027.

WINSOR, R.E. and PATTERSON, D.J. (1973)
"Mixture turbulence - A key to cyclic combustion variation", SAE Paper 730086.

WITZE, P.O. (1977)
"Measurements of the spatial distribution and engine speed dependence of turbulent air motion in an I.C. engine", SAE Paper 770220.

WITZE, P.O. (1978)
"Application of laser velocimetry to a motored internal combustion engine", Third International Workshop on Laser Velocimetry, Purdue University.

WITZE, P.O. (1980a)
"A critical comparison of hot-wire anemometry and laser Doppler velocimetry for I.C. engine applications", SAE Paper 800132.

WITZE, P.O. (1980b)
"Influence of air motion variation on the performance of a direct-injection stratified-charge engine", I. Mech. E. Paper C394/80.

WITZE, P.O. (1981)
"Comparisons between measurement and analysis of fluid motion in internal combustion engines", Sandia National Laboratories, Report SAND81-8242.

WITZE, P.O. (1982)
"The effect of spark location on combustion in a variable-swirl engine", SAE Paper 820044.

WITZE, P.O. and DYER, T.M. (1984)
"Laser measurement techniques applied to turbulent combustion in piston engines", ASME 105th Winter Annual Meeting, New Orleans, LA.

WITZE, P.O. and VILCHIS, F.R. (1981)
"Stroboscopic laser shadowgraph study of the effect of swirl on homogeneous combustion in a spark-ignition engine", SAE Paper 810226.

WITZE, P.O., MARTIN, J.K. and BORGNAKKE, C. (1983)
"Measurements and predictions of the precombustion fluid motion and combustion rates in a spark ignition engine", SAE Paper 831697.

WITZE, P.O., MARTIN, J.K. and BORGNAKKE, C. (1984a)
"Conditionally-sampled velocity and turbulence measurements in a spark ignition engine", Comb. Sci. Tech., 36, 301.

WITZE, P.O., MARTIN, J.K. and BORGNAKKE, C. (1984b)
"Fluid motion during flame propagation in a spark ignition engine", SAE Paper 840377.

WOOD, G.B., HUNTER, D.U., TAYLOR, E.S. and TAYLOR, C.F. (1942)
"Air flow through intake valves", Transactions of SAE, 50, 212.

WOODS, W.A. and KHAN, S.R. (1965)
"An experimental study of flow through poppet valves", Proc. I. Mech. E., 180, 32.

YANTA, W.J. (1973)
"Turbulence measurements with a laser Doppler velocimeter", Naval Ordinance Labs., White Oak, Silver Spring, Report NOLTR 73-94.

YIANNESKIS, M. (1982)
"Flow in reciprocating engine cylinders and curved ducts", Ph.D. Thesis, University of London.